Université du Québec
Institut National de la Recherche Scientifique
Centre Énergie, Matériaux et Télécommunications

Electrospun NASICON nanofibers as solid electrolytes for lithium batteries

Par

Andrea La Monaca

Thèse présentée pour l'obtention du grade de

Philosophiae Doctor (Ph.D.)

en Sciences de l'Energie et des Materiaux

Jury d'évaluation

Président du jury et examinateur interne	Prof. Shuhui Sun INRS-EMT, Université du Québec
Examinateur externe	Prof. Jinhyuk Lee Département de Génie des Matériaux Université McGill
Examinateur externe	Prof. Xia Li Département de Génie Chimique et des Matériaux Université Concordia
Directeur de recherche	Prof. Federico Rosei INRS-EMT, Université du Québec
Codirecteur de recherche	Prof. Ashok Vijh IREQ, Hydro-Québec

Acknowledgments

First and foremost, I would like to thank my supervisor, Prof. Federico Rosei and my co-supervisor during the initial stages of my PhD, Prof. Karim Zaghib. They have been essential in the very first part of my project; with their professional lead and remarkable experience, they helped me outlining my research path and achieving publication.

I would also like to acknowledge the invaluable contribution of Prof. Ashok Vijh, also known as the "father of electrochemical physics"; he mentored me and vastly helped me to go through the several challenges of my project. Additionally, I want to thank him for stepping in as my co-supervisor in the final stage of my PhD.

I would like to thank Dr. Andrea Paolella, who has been my scientific guide since day one. He helped me going through this challenging PhD journey, providing both scientific and personal support.

I would also like to thank all the researchers and technicians, not only of Hydro-Quebec, who helped me facing the everyday challenges in lab. A special thanks goes to Gabriel, Sylvio, Alina, Hendrix, Giovanni and Sergey, who were by my side during most of the scientific work of these years.

Thank you also to all the other students I met at both Hydro-Quebec and INRS, with who I shared highs and lows while sipping a coffee, doing a BBQ or playing soccer.

I am exceptionally grateful to my beloved parents who always supported me, encouraged me and have been so close to me all the time, despite being more than 7000 km away. I want to extend my gratefulness to all the other members of my family and all my friends who are also far away. They probably do not know how important they have been during this PhD journey.

Last but not least, the most special *thank you* goes to Marta, who was by my side even when I struggled the most, showing love and affection all the time. We have been through incredibly difficult times during these years but her support was unconditional. I would also like to extend this special thanks to my newly adopted cat, who provided an unbelievable psychological support, especially while we were locked in our apartment because of the pandemic.

Andrea

Résumé

Pour réduire notre dépendance aux combustibles fossiles et tirer le meilleur parti des sources d'énergie renouvelables, le développement de dispositifs de stockage et de conversion d'énergie plus performants est essentiel. Les batteries au lithium à l'état solide (ASSLB) sont probablement l'une des technologies les plus prometteuses. Leur fonctionnement est basé sur les mêmes principes que les batteries lithium-ion (LIB), toutefois, les ASSLB présentent un électrolyte solide, qui remplace tant le séparateur que l'électrolyte liquide. L'électrolyte solide permet l'utilisation tant d'une cathode dense que de Li métallique comme anode, obtenant ainsi des densités d'énergie plus élevées et une meilleure sécurité par rapport aux LIB. Malgré cela, les ASSLB ne sont pas encore prêtes pour la distribution commerciale, car elles présentent des problèmes intrinsèques qui doivent être résolus, tels que la formation d'interfaces électrolyte/électrode homogènes ou la faible conductivité ionique à température ambiante.

Cette thèse porte sur l'étude de diverses propriétés des matériaux NASICON (Natrium Superionic Conductor) à base de lithium. Nous nous sommes initialement concentrés sur l'optimisation de la synthèse à l'état solide de $Li_{1+x}Al_xTi_{2-x}(PO_4)_3$ (LATP), en évaluant les effets de l'utilisation des précurseurs TiO_2 rutile et anatase sur la cristallisation du LATP et sur la conductivité ionique des pastilles préparées par *hot-pressing*.

Une stratégie alternative pour synthétiser LATP est la méthode sol–gel, qui peut être couplée à la technique d'électrospinning pour fabriquer des nanofibres céramiques. Dans ce travail, nous rapportons qu'une pression de 150 MPa appliquée à une membrane nanofibreuse de LATP avant la calcination est une méthode efficace pour améliorer sa conductivité ionique, ce qui en fait un bon candidat pour le développement d'électrolytes céramiques et de polymères composites.

Devant l'impossibilité d'adapter directement la méthode de préparation du LATP à la synthèse des nanofibres de $Li_{1.5}Al_{0.5}Ge_{1.5}(PO_4)_3$ (LAGP), nous avons développé une nouvelle méthode de synthèse basée sur des précurseurs à base de chlorures. Les nanofibres de LAGP ont été caractérisées sous forme d'une membrane céramique nanofibreuse et d'une charge pour électrolytes polymères à base d'oxyde de polyéthylène, montrant des résultats prometteurs en termes de propriétés physiques et électrochimiques.

Enfin, l'influence d'une substitution partielle de Ge par Ti sur la synthèse et les propriétés des nanofibres électrofilées de LAGP a été étudiée. L'ajout de Ti s'est avéré être une stratégie efficace pour

améliorer tant la pureté que la morphologie des nanofibres. De plus, la conductivité ionique au-dessus de 40 °C est améliorée lorsque des nanofibres LAGP avec Ti sont utilisées comme charges.

Mots-clés : Batteries au lithium à l'état solide; Électrolyte solide; Électrolyte polymère composite; LATP; LAGP; NASICON; Conductivité ionique; Electrospinning; Sol–gel; Hot-pressing

Abstract

To reduce our addiction to fossil fuels and better exploit the renewable sources of energy, more efficient electrochemical storage and conversion devices must be developed. All-solid-state lithium batteries (ASSLBs) are presumably one of the most promising technologies. Their operation is based on the same principles of lithium-ion batteries (LIBs), however, ASSLBs feature a solid electrolyte, which replaces both the separator and the liquid electrolyte. The solid electrolyte enables the use of both a dense cathode and metallic Li as anode, thus achieving higher energy densities and better safety than LIBs. However, ASSLBs are not yet ready for commercial deployment, as they come with intrinsic issues that must be addressed, such as the formation of homogeneous electrolyte/electrode interfaces or the low ionic conductivity at room temperature.

This thesis is focused on the investigation of several properties of Li-based NASICON (Natrium Superionic Conductor) materials. We initially focused on the optimization of the solid-state synthesis of $Li_{1+x}Al_xTi_{2-x}(PO_4)_3$ (LATP), by studying the effects of the use of rutile and anatase TiO_2 precursors on LATP crystallization and on the ionic conductivity of the resulting pellets, prepared by hot-pressing.

An alternative strategy to synthesize LATP is the sol–gel method, which can be coupled with the electrospinning technique to fabricate ceramic nanofibers. In this work, a 150 MPa pressure applied on a nanofibrous LATP membrane before calcination is proposed as an effective method to improve its ionic conductivity, thus making it a good candidate for the development of ceramic and composite polymer electrolytes.

Since LATP preparation method could not be directly adapted to the synthesis of $Li_{1.5}Al_{0.5}Ge_{1.5}(PO_4)_3$ (LAGP) nanofibers, we developed a new synthesis route, based on chloride precursor materials. LAGP nanofibers were characterized in the form of full-ceramic nanofibrous membrane and of fillers for polyethylene oxide-based polymer electrolytes, showing promising results in terms of physical and electrochemical properties.

Finally, the influence of a partial substitution of Ge with Ti on the synthesis and properties of electrospun LAGP fibers was investigated. The addition of Ti proved to be an effective strategy to improve both the purity and the morphology of the nanofibers. Moreover, the ionic conductivity above 40 °C is enhanced when Ti-substituted LAGP nanofibers are used as fillers.

Keywords: All-solid-state lithium batteries (ASSLBs); Solid electrolyte; Composite polymer electrolyte; LATP; LAGP; NASICON, Ionic conductivity; Electrospinning; Sol–gel; Hot-pressing.

Table of contents

List of figures

List of tables

Abbreviations

Abbreviation	*Meaning*
1D	One-dimensional
3D ED	Three-dimensional Electron Diffraction
acac	Acetylacetone
ACN	Acetonitrile
AcOH	Acetic acid
ADF-STEM	Annular Dark-field Scanning Electron Microscopy
aLATP	Anatase-based LATP
ASSLB	All-solid-state lithium battery
CE	Composite Electrolyte
CQ	Quadrupolar Coupling Constant
DMF	N,N-dimetylformammide
EDS	Energy Dispersive X-ray Spectroscopy
EIS	Electrochemical Impedance Spectroscopy
EtOH	Ethylic alcohol
GPE	Gel-polymer electrolytes
H2O	Deionized water
HRTEM	High-resolution Transmission Electron Microscopy
HTXRD	High-temperature X-ray Diffraction
iPrOH	Isopropyl alcohol
LAGP	$Li_{1.5}Al_{0.5}Ge_{1.5}(PO_4)_3$
LAGTP	$Li_{1.5}Al_{0.5}Ge_{1.5-x}Ti_x(PO_4)_3$
LAGTP01	$Li_{1.5}Al_{0.5}Ge_{1.4}Ti_{0.1}(PO_4)_3$
LAGTP02	$Li_{1.5}Al_{0.5}Ge_{1.3}Ti_{0.2}(PO_4)_3$
LAGTP03	$Li_{1.5}Al_{0.5}Ge_{1.2}Ti_{0.3}(PO_4)_3$
LATP	$Li_{1.3}Al_{0.3}Ti_{1.7}(PO_4)_3$
LATPnf	LATP nanofibers
LIB	Lithium-ion battery
LiPON	Lithium-phosphorus oxynitride
LISICON	Lithium Superionic Conductor
LiTFSI	Lithium bis(trifluoromethanesulfonyl)imide
LLATO	$Li_{0.33}La_{0.557}Ti_{1-x}Al_xO_3$
LLTO	$Li_{0.33}La_{0.557}TiO_3$
LLZO	$Li_7La_3Zr_2O_{12}$

LZO	$La_2Zr_2O_7$
MAS-NMR	Magic Angle Spinning NMR
MEEP	Poly[bis(methoxy-ethoxy-ethoxy)phosphazene]
Na/S	Sodium/Sulfur
NASICON	Sodium Superionic Conductor
NMR	Nuclear Magnetic Resonance
NTs	Nanotubes
PAN	Poly(acrylonitrile)
PE	Polymer Electrolyte
PEC	Poly(ehylene carbonate)
PEO	Polyethylene Oxide
pLATPnf	Pressed LATP nanofibers
PMMA	Poly(methyl methacrylate
PPA	Phenylphosphonic acid
PPC	Poly(propilene carbonate)
PPO	Poly(propylene oxide)
PSi	Polysiloxane
PVC	Poly(vinyl chloride)
PVdF	Poly(vinylidene difluoride)
PVdF-HFP	Poly(vinylidene fluoride-co-hexafluoropropylene)
PVP	Poly(vinylpirrolidone)
rLATP	Rutile-based LATP
SEI	Solid Electrolyte Interphase
SEM	Scanning Electron Microscopy
Tg	Glass-transition temperature
TGA	Thermogravimetric Analysis
THF	Tetrahydrofuran
XPS	X-ray Photoelectron Spectroscopy
XRD	X-ray Diffraction
ZEBRA	Zeolite Battery Research Africa

1 Introduction

1.1 Overview

Fossil fuels, including coal, oil and natural gas, have powered global economy since industrial revolution, and currently supply about 80% of the world's energy requirement. However, their extraction and combustion have increased the amount of anthropogenic greenhouse gases, such as CO_2, which are the major responsible for global warming. Global energy-related CO_2 emissions decreased by 5.8 % in 2020, owing to the major economic recession due to the Covid-19 pandemic (**Figure 1.1**). Despite the small and temporary decline, however, current projections for 2022 foresee an increase of the global energy demand above pre-Covid-19 levels, driving CO_2 emissions towards the largest single increase of the last decade as soon as the demand for coal, oil and gas rebound with economy.[1] According to the last assessment report of the Intergovernmental Panel on Climate Change, in the absence of major action to reduce emissions, global mean temperature is set to rise by 3.7 to 4.8 °C by 2100. Even by reducing the emission of greenhouse gases, global warming would continue to happen for at least several more decades, and the risk of potential overshoots in temperature is concrete. Maintaining a global temperature increase below 1.5 °C as compared to pre-industrial levels is vital, since it would limit the frequency and intensity of extreme events, such as heavy precipitations, droughts, floods, ocean acidification, species extinctions. Moreover, human adaptation will be less difficult.[2]

In this framework, a shift towards a low-carbon economy is mandatory. Demand for renewables energies increased by 3% in 2020 and kept increasing during 2021 across all key sectors, i.e. power, heating, industry and transport. The power sector is growing of about 8% in terms of demand for renewables reaching 8300 TWh, the largest year-on-year growth on record in absolute terms.[1] Although fossil fuels are set to remain a significant source of energy and materials for decades, a technological revolution is needed to transit to affordable, accessible and sustainable energy sources. Renewable energies are good candidates to gradually replace fossil fuels, however, their unpredictability and unreliability prevented their unquestioned use. Solar radiation, wind, and waves are arguably the most tangible energy sources at our disposal, despite being variable in time and diffuse in space. Nuclear reactors provide a constant energy source with associated problems of radioactive waste disposal. Geothermal energy is restricted in location. All these energy sources require or at least

benefit from energy storage.[3] The development and integration of energy storage devices is thus crucial for an efficient use and a widespread diffusion of renewable energies.

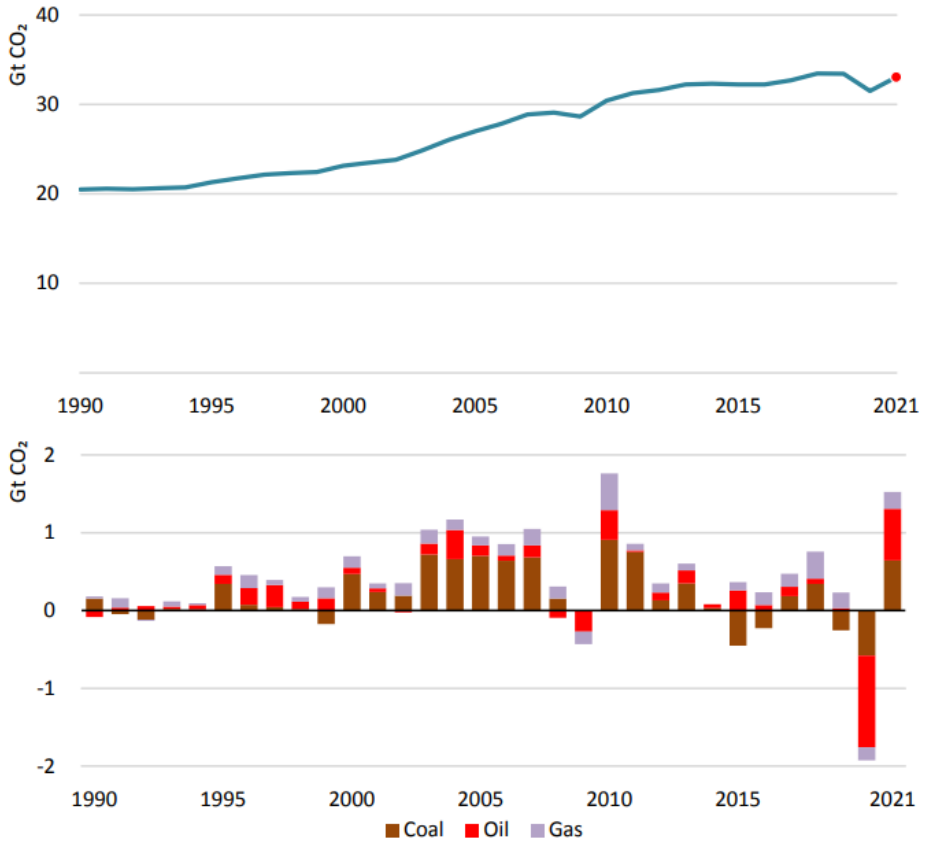

Figure 1.1 (a) Evolution of global energy-related CO_2 emissions from 1990 to 2021 and (b) their change compared to the previous year. The impact of every fuel is shown. *Reproduced with permission.*[1]

Energy storage for large-scale applications can be carried out with four different technologies: mechanical, electrical, chemical, and electrochemical. Pumped hydroelectric systems account for around 95% of all active storage installations worldwide, corresponding to a throughput capacity of over 181 GW with an energy efficiency of 70-80%. However, pumped hydroelectric is a location-dependent storage system, as needs both geographical height and water availability. Its characteristics along with those of other energy storage systems are displayed in **Figure 1.2** in terms of power rating, which identifies potential applications, and duration of discharge. In general, electrochemical energy storage is characterized by several advantageous features, including pollution-free operation, high efficiency, flexible power and energy to meet different grid functions, long cycle life, and low maintenance. Batteries represent an excellent energy storage technology for the integration of renewable resources. Their compact size makes them well suited for transportation and application,

they can reduce variations in local solar output and mitigate output fluctuations at wind farms. Although the high cost is limiting the market penetration, the modularity and scalability of different battery systems will certainly lead to a drop in costs in the coming years. Today, sodium/sulfur (Na/S) battery technology is the only commercially mature, large-scale battery technology available for power plants and residential applications, with a few hundred installations worldwide, accounting for 530 MW of discharge power capacity. Other interesting battery technologies are currently emerging or being revived for stationary applications because of their potential low cost (redox-flow) and enhanced performance (lithium-ion) (**Figure 1.2**).[4]

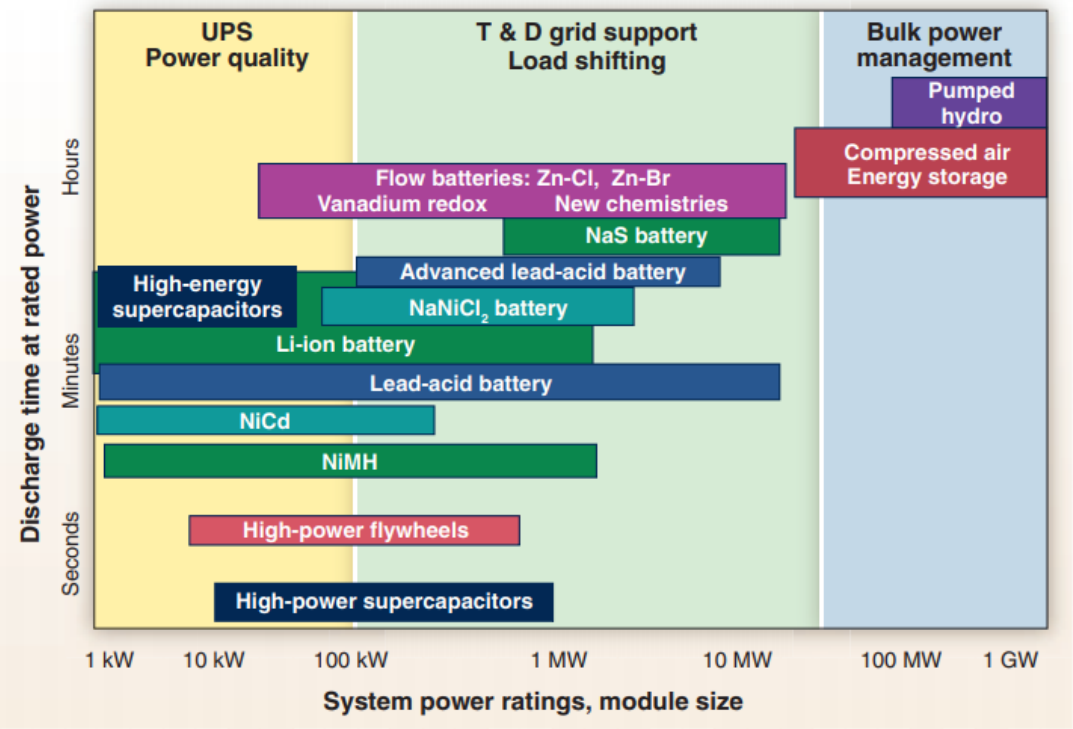

Figure 1.2 Comparison of discharge time and power rating for various EES technologies. ***Reproduced with permission.***[4] ***(Copyright 2011 Science).***

1.1.1 Lithium-ion batteries

The lithium-ion battery (LIB) first commercialized by Sony in 1991, was formerly known as "rocking chair" or "shuttle" battery because of the Li^+ ions moving back and forth between the electrodes.[5] Commercial LIBs are composed of a graphite (Li_xC_6) anode and a layered-oxide ($Li_{1-x}MO_2$) cathode, where M is most of the time Co but can also be Ni or Mn. Between the electrode, a polyolefin-based separator soaked in a liquid electrolyte is placed to prevent short-circuits and ensure Li-ion transport. A schematical illustration of a conventional LIB is depicted in **Figure 1.3**.

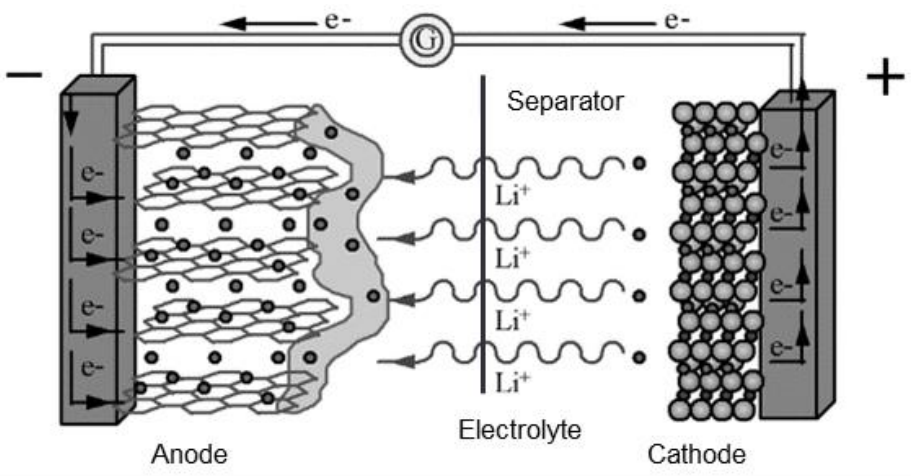

Figure 1.3 Schematic illustration of a conventional lithium-ion battery.

Conventional LIBs store about 180 Wh kg^{-1} at an average voltage of 3.8 V, which is only 5 times higher than typical energy densities of older lead-acid batteries. To achieve such a marginal improvement, an actual revolution in materials science was required. Nowadays, billions of lithium-ion cells are produced and regularly used to power smartphones, tablets, laptops and several other portable electronic devices. The state-of-the-art LIBs, can deliver volumetric and gravimetric energy up to 770 Wh L^{-1} and 260 Wh Kg^{-1}, respectively. However, the energy density of conventional LIBs is already close to the limit, as predicted by Janek et al. (**Figure 1.4**).[6] LIBs are expected to be the leading technology for electric vehicle applications during the next years, with their manufacturing going from 747 GWh (2020) to about 2500 GWh by 2025.[7] With current technology however, this is not sustainable as cobalt is expensive and not so abundant in the earth crust. It also presents political and ethical issues because of the way it is mined in Africa. However, LIBs' major issues concern the safety, as the presence of both a combustible electrolyte and an oxidizing agent poses a risk of thermal run-away reactions resulting in fires or explosions. Lithium-ion batteries would also need to reduce their carbon footprint, which is currently between 60 and 170 kg CO_2 per kWh.[8] The use of lithium is another aspect to consider when moving to a so important increase of LIBs production. The replacement of all the world's 1.2 billion cars and lorries with electric or plugin hybrid vehicles would use up to 30% of the world's known reserves of lithium. But lithium is also unlimitedly accessible in sea water and obtaining it from there is also a more environmental-friendly process than conventional mining. New and efficient recycling processes could also ease lithium exploitation.[9]

At the current state, LIB is the only concrete and mature technology available to answer the energy storage demand during the next decade. However, all the issues cited above must be overcome to

achieve such a universal deployment and this is not an easy task. The research community has already started looking beyond LIBs, thus confirming that the quest for the next-generation energy storage technology is ongoing.

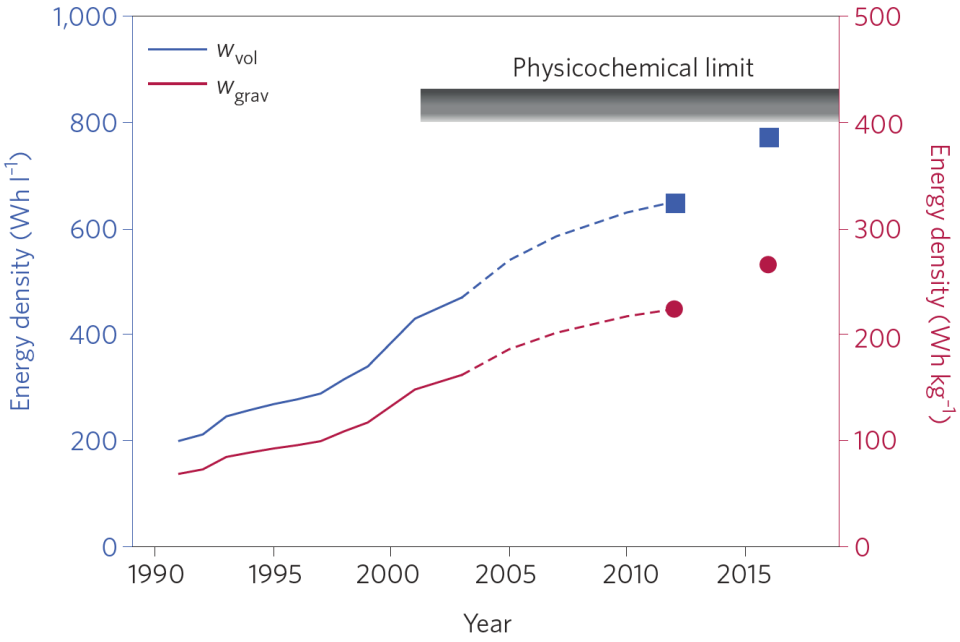

Figure 1.4 Energy density of the standard cylindrical 18650 LIB cell from 1991 to 2016. ***Reproduced with permission.***[6] ***(Copyright 2016 Nature Publishing Group).***

1.1.2 Next-generation lithium metal batteries

From the performance point of view metallic lithium is the ultimate choice for the anode in Li^+-based rechargeable batteries (**Figure 1.5**). It is indeed characterized by the highest theoretical capacity (3860 mAh g^{-1}; 2061 mAh cm^{-3}) and the lowest electrochemical potential (-3.04 V versus the standard hydrogen electrode) compared to all the other anode materials.[10] The advantages of employing metallic Li as anode material for the development of secondary batteries were well known way before the first LIB was commercialized. In fact, graphite was used as host material for lithium ions specifically to solve the issues that came up with metallic lithium. During the 1970s Stanley Whittingham developed the first Li-based secondary battery while working at Exxon.[11] Then, in the late 1980s, Moli Energy was the first company that developed and commercialized Li metal batteries. The technology was based on a MoS_2 cathode and excess Li as anode. The device proved to be stable for hundreds of cycles, thus millions of cylindrical-type cells were sold to the market. However, several accidents began to occur, including fires caused by dendrite formation, which finally led to the recall of all the marketed cells.[11] As a result, the commercialization of Li metal batteries has been suspended. Since then, several

scientific studies tried to solve the safety issues affecting this technology, but without success. Only the introduction on the market of polymer electrolyte-based batteries by Bolloré in 2011 has partially revived the quest for novel battery technologies based on Li metal.[12]

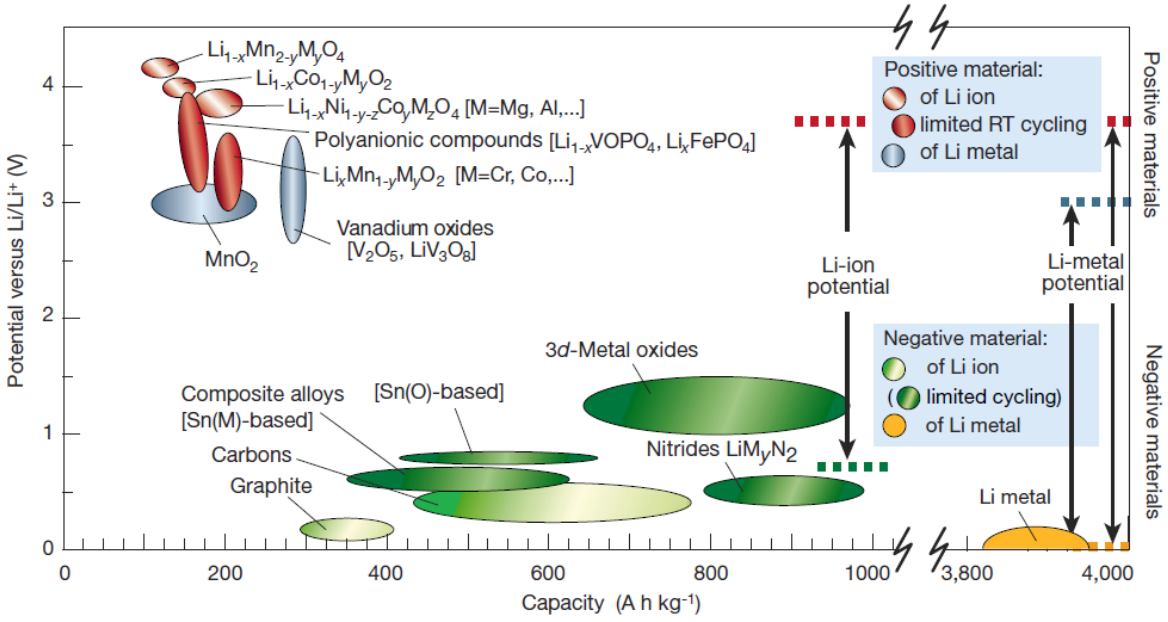

Figure 1.5 Voltage versus capacity for positive- and negative-electrode materials commercially employed in LIB or proposed as candidates for next-generation Li-metal batteries. ***Reproduced with permission.***[13] ***(Copyright 2001 Nature Publishing Group).***

As mentioned in the previous subchapter, LIBs are approaching their intrinsic limits and a new paradigm for secondary batteries is becoming a necessity.[6] Currently, state-of-the-art Li-ion batteries can deliver specific energies up to 260 Wh kg^{-1}. Just by replacing the graphite-based anode with metallic Li and maintaining the same layered-oxide cathode, the specific energy results doubled, reaching about 440 Wh kg^{-1}. Moving to new chemistries, such as Li–S and Li–air systems, can further boost the specific energy to ~650 Wh kg^{-1} and ~950 Wh kg^{-1}, respectively (**Figure 1.6a**).[10]

Despite the performance improvements, Li metal is still far from being the perfect anode material. Several challenges characterize the use of Li in secondary batteries, most of which are related to safety and stability over cycling. Both these aspects are fundamentally associated with the deposition of Li, which similarly to many other metals, can occur in dendritic form.[14] Dendrite formation is reported as the main cause of cell short-circuit, which often leads to thermal runaways, fires and explosions. The Li uneven deposition is also detrimental for achieving a stable cyclability of the cell over time. It indeed leads to an increase of cell resistance and a decrease of Coulombic efficiency over cycling, which correspond to an ongoing capacity fading.[10,15]

A profound knowledge of Li interface and its electrochemical deposition is needed to make metallic Li a suitable anode for next-generation devices. That is why studies have been oriented towards the understanding of the solid electrolyte interphase (SEI) formation. The SEI is a passivation layer formed on the anode surface during cell's first cycles and is mostly made of decomposition products of the electrolyte. Hence, a crucial aspect of a stable and safe Li metal battery is the formation of a stable SEI and its endurance throughout the whole battery life. Another major issue of Li anode is the dendrite growth, which is a typical occurrence during high-current electroplating of metals, such as Li, Cu, Ni and Zn. Dendritic deposition inevitably leads to the perforation of the thin LIB's separator, thus short-circuiting the cell and causing its thermal runaway and potential explosion. Additionally, while most of the intercalation anodes used in commercial LIBs, such as graphite, feature a relatively small volume change (c.a. 10%), Li metal undergoes a virtually infinite volume change during operation. All the phenomena cited above are strongly connected one to each other (**Figure 1.6c**). During plating, metallic Li undergoes a significant volume expansion, which can produce fractures in the fragile SEI (step 1). Li dendrite growth is thus promoted through the SEI's cracks (step 2).

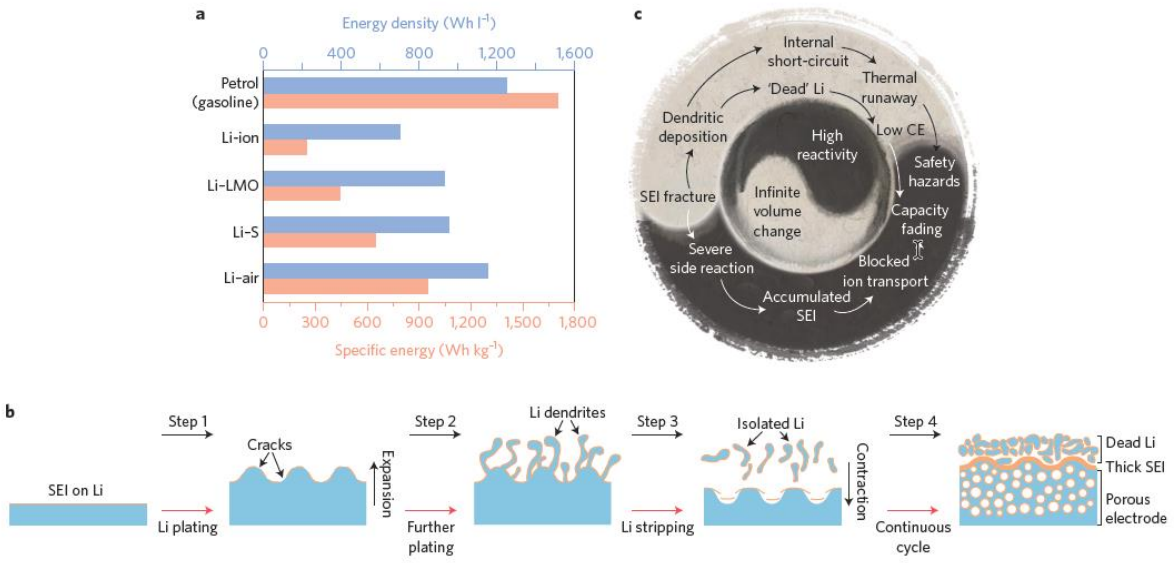

Figure 1.6 (a) Bar chart showing the gravimetric (pink) and volumetric (blue) energy densities of petrol (gasoline) and typical Li batteries. (b) Schematic showing the steps of Li stripping/plating process, including the initial formation of cracks (step 1) and dendrites (step 2) during plating, and the formation of dead Li (step 3) during stripping. Continuous cycling results in accumulated dead Li, thick SEI and porous Li electrode (step 4). (c) Correlations among the different challenges in the Li metal anode. *Reproduced with permission.*[10] *(Copyright 2017 Nature Publishing Group).*

During Li stripping, volume contraction further stresses the SEI, which fractures even more. Once dendrites are formed, subsequent stripping from the dendrites themselves or from their roots can produce 'dead' Li, which is electrically isolated from the substrate; hence non-reactive (step 3). During

continuous cycling, the process is repeated several times, thus leading to a porous electrode, a thick SEI and a significant amount of dead Li, which all cause the irreversible capacity fading of the cell.[10] To deal with these issues, various strategies have been proposed during the last few decades. Several studies focused on the optimization of liquid electrolytes, especially using additives to improve the formation of the SEI. Fluorinated compounds, such as HF, have been used as additives to form a dense and uniform layer on Li surface, however the protective effect tends to wear off after some cycles. $LiNO_3$ has been widely reported as additive for ether electrolytes, especially for Li–S applications.[16] Combined with Li polysulfide proved to be effective at stabilizing Li deposition and preventing dendrites formation in ether electrolytes.[17] Electrolytes with a high Li salt concentration have been also proposed as a strategy to suppress dendrite formation. At the same time, they have been effective at reducing the dissolution of Li polysulfide, which is a major problem in Li–S batteries. However, increasing the amount of Li salt greatly affect the total cost of the electrolyte.

Another interesting approach is the interface engineering, such as fabricating an artificial SEI that acts as a strong physical barrier against dendrite propagation or using chemically stable and mechanically strong scaffolds to reinforce the SEI formed during electrochemical cycling.

While all the strategies proposed above aim to optimize the current technology by modifying the liquid electrolyte or the anode surface, a more fundamental approach consists into replacing the liquid electrolyte with a solid ion-conductive material, which can mechanically hinder the dendrite growth as well as Li volume changes without affecting the SEI. However, shifting from the current commercial LIB technology towards an all-solid-state device is certainly a significant leap, which requires deep theoretical studies as well as profound experimental investigations.

1.2 All-solid-state lithium batteries

The replacement of the commercial liquid electrolyte with a solid equivalent is the first step towards next-generation all-solid-state lithium batteries (ASSLBs). The lack of flammable media is certainly beneficial for the safety of the battery, which as described above is the major concern of LIBs. However, flammability and potential explosion are not the only issues characterizing LIBs. Both organic solvents and Li salt, which are the main components of the liquid electrolyte, are often responsible for side reactions during cycling that lead to capacity fading and aging. On this aspect, using a solid electrolyte is expected to be beneficial for achieving longer device lifetimes. Solid materials are indeed characterized by a slower reactivity compared to liquids. This aspect enabled solid-

state microbatteries to successfully complete more than 10000 cycles,[18] however there is no guarantee that this property can be maintained scaling up the device. Other aging phenomena observed in LIBs, such as gas evolution from the cathode materials, can occur in solid-state cells as well.[19,20] Moreover, the solid nature of the electrolyte itself can introduce or intensify other aging mechanisms, e.g. mechanical degradation, which can greatly affect the cell lifetime.[21] From the economical point of view, electrolyte filling and wetting process and the subsequent formation procedure have a great impact on the final cost of the device.[22] Thus, using a solid electrolyte can also simplify the assembly procedure and reduce the costs. Shifting to a solid-state electrolyte, however, is not only advantageous for the absence of a flammable liquid material, but also for the final performance of the device. Using a solid material that acts as both an electrical insulator and a Li-ion conductor, thus replacing both the separator and the electrolyte, hugely decreases both the weight and the volume of the cell. Additionally, as mentioned in the previous subchapter, it enables the use of metallic Li as anode, which doubles, at least, the gravimetric energy density of the cell. The higher electrochemical stability of some solid electrolytes compared to the commercial liquid counterparts, also allows the use of high-capacity (sulfur; oxygen) or high-voltage ($LiNi_{0.5}Mn_{1.5}O_4$, $LiNi_xMn_yCo_zO_2$) cathodes, which can further increase the energy density. Cathode formulation is also relatively different compared to the conventional ones used in LIBs. In a LIB the cathode is usually porous to a certain degree, thus enabling the permeation of the liquid electrolyte, which acts as bridge among all the cell elements. In an ASSLB the cathode is dense, hence it must contain an additive able to create ionic pathways to effectively connect all the cathode particles to the electrolyte. This additive is often made of the same material as the solid electrolyte. This aspect is also beneficial to improve the interface compatibility between cathode and solid electrolyte. This leads to a different assembly design if compared to LIBs, as displayed in **Figure 1.7**. Commercial LIBs are characterized by a parallel stacking of single galvanic cells to form a cell stack. Several cell stacks are then serially connected to achieve the battery pack. ASSLBs however can be assembled by serially stacking the galvanic cells and then doing parallel connection of the cell stacks into a denser battery pack. This approach leads to a minor use of current collectors and to an optimized packaging design. In addition, pressure vents and cooling systems are not required in ASSLBs, since no flammable materials are involved, therefore no gas generation is expected. Also, the ionic conductivity of solid electrolyte materials is usually higher when the temperature increases.[23] Additionally, the thermal properties as well as chemical and electrochemical stabilities and mechanical resistance of most solid electrolytes are in general better than those of liquid media. Therefore, the

ASSLB technology will not only go beyond the intrinsic limits of LIBs, but it will boost the development of new battery architectures, such as integrated and flexible batteries.[24,25]

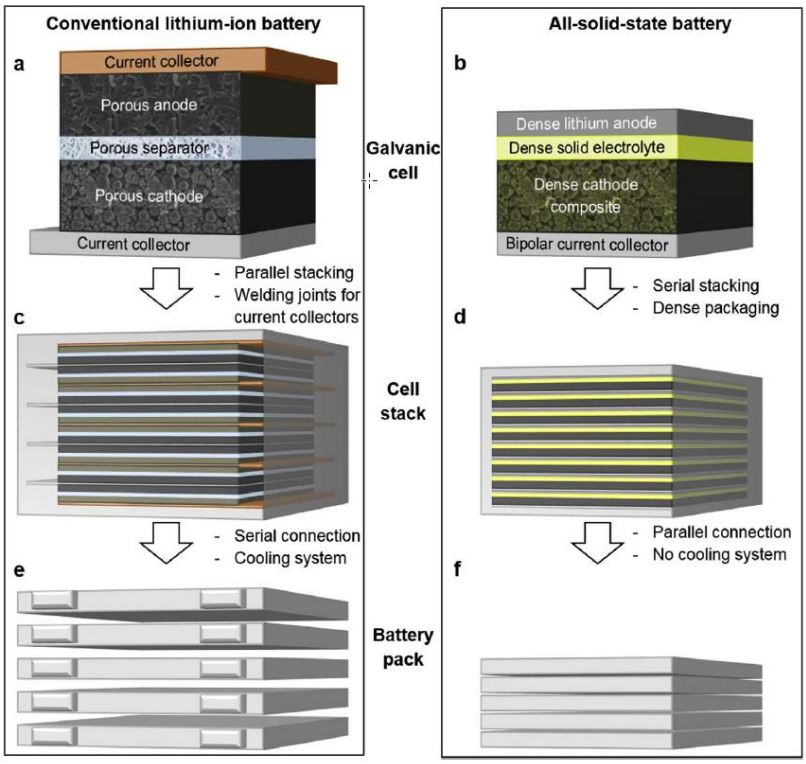

Figure 1.7 Comparison of conventional LIB and next-generation ASSLB at the galvanic cell, cell stack, and battery pack levels. ***Reproduced with permission.***[23] ***(Copyright 2018 Elsevier).***

1.3 Solid electrolytes

1.3.1 Historical outline

The solid electrolytes developed for battery applications mainly fall into two categories: inorganic ceramics and organic polymers. The first has presumably been the first to be discovered. In 1960, the fast transport of a Na-ions was observed for the first time in a ceramic-based β-alumina ($Na_2O{\cdot}11Al_2O_3$), which was then successfully used in high-temperature sodium-sulfur batteries for stationary applications, belonging to molten-salt battery category.[12] In 1973, Fenton et al. studied polymer electrolytes for the first time. They found that the complex formed between poly(ethylene oxide) (PEO) and alkali metal salts had the property of conducting ions.[26] Since then, several theories have been proposed to explain the mechanism of ion-conduction in PEO-based electrolytes, and several other polymer electrolytes have been developed.[27]

The ZEBRA (Zeolite Battery Research Africa) cell, developed during the 1980s by Zeolite Battery Research Africa Project group, was a lower-temperature variant of previously developed molten-salt batteries, based again on Na-ion conductive β-alumina.[28] Since the 1990s, several inorganic materials displaying a fast ionic conduction have been discovered and later proposed for LIB applications, such as lithium-phosphorus oxynitride (LiPON) fabricated as a thin-film electrolyte by Bates et al.[29] Several other ion-conducting ceramics were investigated during the same years, like perovskite-type,[30] sodium superionic conductor (NASICON)-type,[31] garnet-type,[32] and sulfide-type[33] materials. After Fenton's discovery in 1973,[26] the research of a polymer-based electrolyte advanced. Various polymer materials, such as poly(vinylidene fluoride) (PVdF),[34,35]poly(vinylidene fluoride-co-hexafluoropropylene) (PVdF-HFP),[36,37] poly(methyl methacrylate) (PMMA),[38–40] and poly(acrylonitrile) (PAN)[41,42] have been increasingly investigated for the development of either all-solid-state polymer or gel polymer electrolytes for lithium-ion batteries. More recently, several hybrid formulations featuring both organic and inorganic materials have been investigated. Both passive and ion-conductive fillers have been reported to enhance the properties of polymer electrolytes, hence introducing a new class of materials usually referred to as composite or hybrid electrolytes.

The main features of the three different classes of solid Li^+-conductive materials, i.e. ceramic, polymer and composite electrolytes, are displayed in **Figure 1.8** and compared with liquid counterparts commercially used in LIBs.

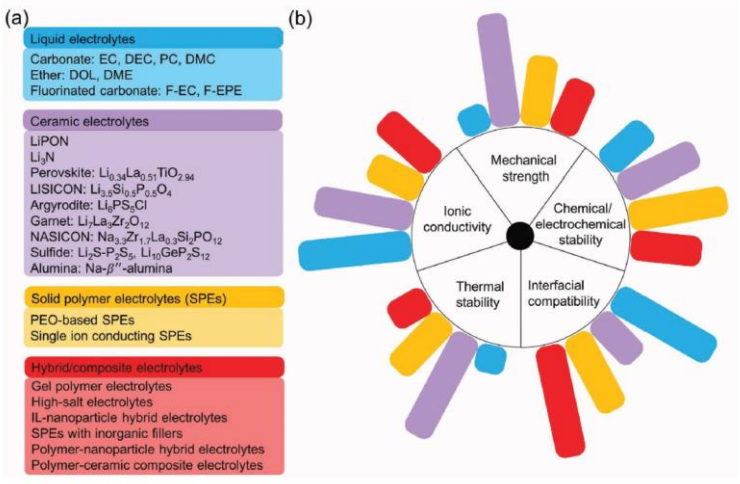

Figure 1.8 (a) Common electrolyte systems for liquid, ceramic, polymer and composite electrolytes for lithium-based batteries. (b) Main physico-chemical properties of liquid, ceramic, polymer and composite electrolytes. ***Reproduced with permission.***[12] ***(Copyright 2018 Royal Society of Chemistry).***

1.3.2 Ceramic inorganic electrolytes

In general, the main advantage of ceramic electrolytes resides in the mechanical properties. The excellent mechanical strength and the extreme hardness make them the safer option when metallic lithium is used as anode. They easily prevent the dendritic growth as well as any potential short circuit. From the safety point of view, they are usually characterized by a good thermal stability thus keeping the electrodes separate even in case of thermal runaway. Regarding the ionic conductivity, important progress has been made in the last decades. While most proposed materials are characterized by a room-temperature ionic conductivity in the order of 10^{-7}–10^{-4} S cm^{-1}, values closer and closer to liquid electrolytes have been reported for sulfide-based materials (10^{-3}–10^{-2} S cm^{-1}). Nevertheless, ceramic electrolytes have still some major drawbacks that need to be addressed. The chemical and electrochemical stability is often a major concern. Ti-containing compounds, such as $Li_{0.33}La_{0.557}TiO_3$ (LLTO) and $Li_{1.3}Al_{0.3}Ti_{1.7}(PO_4)_3$ (LATP), are electrochemically unstable at low potential, since Ti^{IV} can be easily reduced to Ti^{III}. The synthesis process of sulfides is often challenging, since they are reportedly reactive towards moisture, thus hindering the industrial upscale. However, the main issue of all inorganic electrolytes is arguably the interfacial compatibility with the electrodes. From a mechanical point of view, finding a good surface contact between two solid materials is very challenging, and requires the use of high pressure and high temperature treatments, which greatly increases the costs. From a chemical and electrochemical point of view, several reactions at the interface with high-voltage cathode materials and metallic lithium have been reported for various ceramic electrolytes.

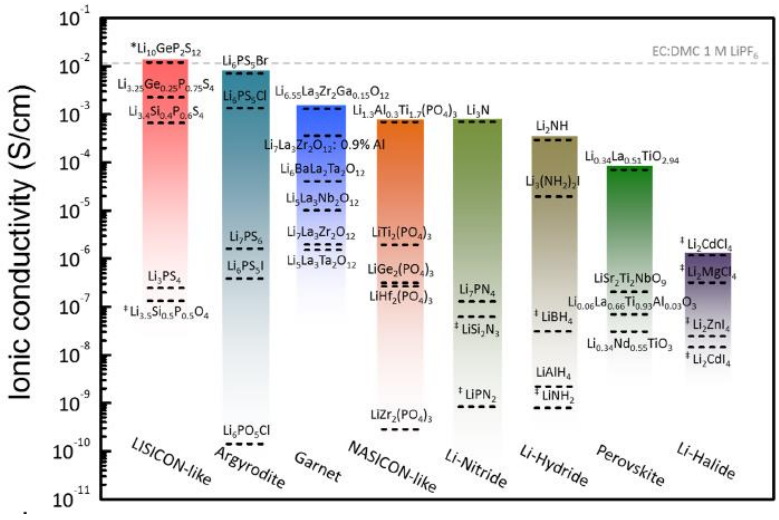

Figure 1.9 Reported total ionic conductivity of solid-state lithium-ion conductors at room temperature. ***Reproduced with permission.***[43] ***(Copyright 2016 American Chemical Society).***

A brief description of the main families of ceramic materials investigated as solid electrolyte is reported below. Before going through them, however, it is worth noting that at present no material has still been elected as the ultimate solid electrolyte for future batteries, since all the compounds investigated to date possess advantages and disadvantages.

Nitride materials. Glassy lithium-phosphorous-oxynitride (LiPON) solid electrolyte was introduced by Bates et al. in 1992.[44] Thin-film batteries with Li anodes and LiPON electrolytes demonstrated thousands of cycles,[45,46] hence it still represents a good candidate to develop future thin-film batteries. However, the poor mechanical stability and the low ionic conductivity of LiPON at room temperature (2×10^{-6} S cm^{-1}) greatly hinder its practical use in batteries.[29,47,48]

Single-crystal lithium nitride (Li_3N) consists of hexagonal Li_2N layers connected by pure Li layers through N–Li–N bridges.[49] The ionic conductivity of single-crystal Li_3N is in the order of 10^{-3} S cm^{-1} at room temperature. This high value is mainly due to the presence of Li^+ vacancies within the planar Li_2N layers. In recent years, only a few researchers have focused on Li_3N as a solid-state electrolyte because of its low electrochemical decomposition potential (0.445 V) and poor stability, which prevent its practical application in batteries.[48]

LISICON and thio-LISICON materials. Li^+ super ionic conductors (LISICON) and thio-LISICON compounds are characterized by structures similar to γ-Li_3PO_4, with an orthorhombic unit cell and *Pnma* space group, where all cations are tetrahedrally coordinated. Lithium ions diffuse between LiO_4 tetrahedra, where they are located, and interstitial sites present in the PO_4 network. Aliovalent substitution of P^V by Si^{IV} or Ge^{IV} giving rise to new compositions such as $Li_{3+x}(P_{1-x}Si_x)O_4$,[50,51] can lead to fast lithium-ion conduction.[43] LISICON-type electrolytes are characterized by a high thermal stability and near-zero vapor pressure in addition to stability in the presence of water and aqueous electrodes.[51,52] Despite the marked stability, few LISICON electrolytes have been reported compared with other ceramic electrolytes. The main reason is their ionic conductivity at room temperature, which is too low for practical applications (10^{-7} S cm^{-1}).[51] Additionally, they suffer from instability when in contact with Li and air.[53] Substituting O by S in $Li_{3+x}(P_{1-x}Si_x)O_4$ to form $Li_{3+x}(P_{1-x}Si_x)S_4$, leads to the thio-LISICON family. This substitution is reported to further increase lithium-ion conductivity by 3 orders of magnitude at room temperature.[54] In fact, materials like $Li_{10}MP_2S_{12}$ (M = Si, Ge, or Sn)[33,55,56] and $Li_{11}Si_2PS_{12}$ possess the highest reported lithium-ion conductivities for ceramic solid electrolytes, above 10^{-2} S cm^{-1} at room temperature.[57] These values are in the same order of magnitude as those of commercial liquid electrolytes currently used in LIBs. However, sulfide in thio-

LISICON materials easily reacts with the moisture in the atmosphere, producing harmful H_2S gas. Additionally, Ge-based compounds are prone to be reduced at low potentials.[47]

Argyrodite. Lithium argyrodite is a recently proposed class of fast Li-ion conductors, isostructural to Cu- and Ag-argyrodite materials and best described by the general formula Li_6PS_5X (with X = Cl, Br, or I). The structure is characterized by tetrahedral close packing of anions (cubic unit cell with space group $F\bar{4}3m$). Phosphorus atoms are located in tetrahedral interstices, forming a network of PS_4 tetrahedra, as observed in the thio-LISICON structure. Li ions are randomly distributed over the remaining tetrahedral interstices, i.e. 48h and 24g sites, and rapidly diffuse through them. The highest ionic conductivity has been reported by Deiseroth et al.,[58] corresponding to 7×10^{-3} S cm^{-1} at room temperature. It is worth noting that the substitution of sulfur by oxygen tends to decrease the ionic conductivity, as already observed for LISICON and thio-LISICON materials. First reported data on Li_6PS_5X (X = Cl, Br, I) argyrodite structures show that the electrochemical stability windows are as wide as 0−7 V versus Li/Li$^+$.[59]

Perovskites. Perovskite structure can be described with a general formula ABO_3, with a cubic unit cell and space group $Pm\bar{3}m$. Alkaline-earth or rare-earth elements are usually found in A-sites at the corners of a cube while B ions, which are typically transition metals are located at the center. Oxygen atoms occupy the face-center position. Lithium can be introduced through aliovalent doping on the A site of the perovskite structure.[43] Inaguma et al. developed several materials with the general formula $Li_{3x}La_{2/3-x}TiO_3$ by means of aliovalent substitution of both metal ions, thus reporting high bulk Li-ion conductivities of 10^{-3} S cm^{-1} and total conductivities as high as 7×10^{-5} S cm^{-1} at room temperature, attracting considerable interest.[30] Despite its high conductivity at room temperature, LLTO is not suitable to be used as solid electrolyte in Li-based batteries, since it rapidly undergoes Li$^+$ insertion with the simultaneous reduction of Ti^{IV} to Ti^{III} when in direct contact with metallic Li, thus giving rise to high electronic conductivity.[43]

Garnet. Several oxides materials derived from the ideal garnet structure and characterized by the general formula $A_3B_2(XO_4)_3$ (cubic unit cell and space group $Ia\bar{3}d$) have been reported.[60] Garnet-like compounds were studied for the first time as solid electrolytes by Weppner et al.[61] Especially, $Li_7La_3Zr_2O_{12}$ (LLZO) has been given much attention because of its high stability in contact with metallic Li.[32] LLZO structure is characterized by dodecahedral LaO_8 and octahedral ZrO_6. Li ions can be located in two different sites, corresponding to tetrahedral 24d site and distorted octahedral 96h site and usually referred to as Li1 and Li2, respectively. The Li2 site is vacant in the ideal garnet

structure. The disordering and partial occupation of the Li atoms at the Li2 site is a crucial factor for having fast Li-ion conduction.[62] Besides high bulk Li-ion conductivity, corresponding to 5×10^{-4} S cm^{-1} at room temperature, this material also exhibits excellent thermal performance and chemical stability against molten lithium, air and moisture.[63]

NASICON. The expression "Na^+ super ionic conductors" (NASICON) was firstly introduced by Hong and Goodenough in 1976 to denote the Na^+ transport abilities of the solid solution $Na_{1+x}Zr_2Si_xP_{3-x}O_{12}$.[64] During the years, the term has been broadly used to indicate a family of phosphates materials characterized by the general formula $AMM'(PO_4)_3$, where the A-site is usually occupied by alkali ions or alkaline-earth ions while M and M' stand for transition metal ions with oxidation states between II and V. Given the growing interests over the last decades in finding a performing Li^+ conductor to be used as solid electrolyte for electrochemical applications, lithium was soon substituted for sodium as a charge carrier.[65]

The general formula of Li-based NASICON compounds corresponds to $Li_{1+x}M^{III}_xM^{IV}_{2-x}(PO_4)_3$ with M^{III} = Cr, Al, Ga, Sc, Y, In, or La and M^{IV} =Ti, Ge, Sn, Hf, or Zr. The structure is generally characterized by a rhombohedral unit cell and space group $R\bar{3}c$., as shown in **Figure 1.10**, consisting of isolated MO_6 octahedra, which share a corner with PO_4 tetrahedra.[31,66] Li ions can occupy two different sites in the structure: the Li1 sites (Wyckoff position 6b) that are 6-fold coordinated located directly between two MO_6 octahedra, and the Li2 sites (Wyckoff position 18e) that are 8-fold coordinated and located between two columns of MO_6 octahedra. In $LiM^{IV}_2(PO_4)_3$ compounds Li ions are located exactly at the Li1 sites. Partial substitution of M^{IV} with M^{III} leads to additional occupation of further positions by Li ions. It was commonly assumed that these positions corresponded to Li2 sites, however Li2 cavity is very large compared to the ionic radius of Li^+. Recent research identified a new Li3 site (Wyckoff position 36f) within Li2 cavity, which is in better agreement with experimental results.[67] Lithium migration occurs via hopping between Li1 and Li3 sites, and partial occupancies of lithium ions on those two sites are crucial for fast lithium-ion conduction, especially as vacancies are required at the intersection of the conduction pathways to enable three-dimensional diffusion within the structure.[68,69]

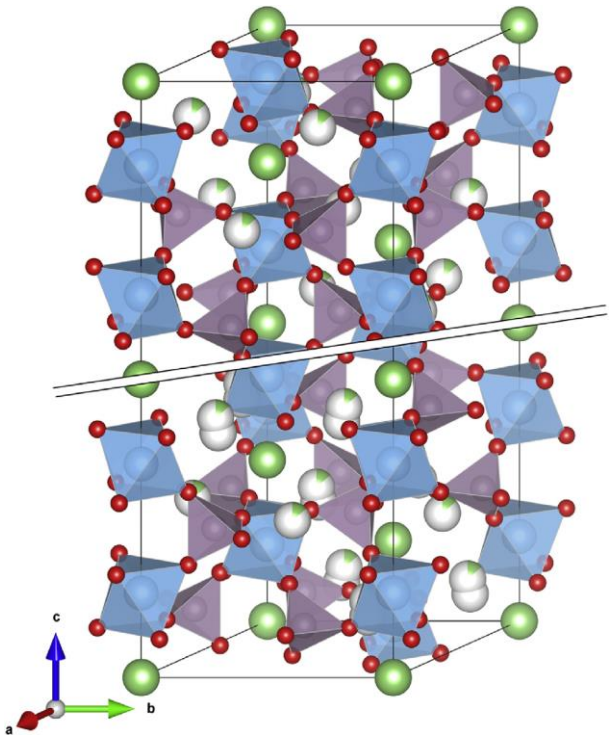

Figure 1.10 Rhombohedral structure of $Li_{1.5}Al_{0.5}Ti_{1.5}(PO_4)_3$, Red spheres: O, blue octahedra: $(Al/Ti)O_6$, purple octahedra: PO_4. Top half shows Li2 sites occupied, while in the bottom half additional lithium occupy Li3. *Reproduced with permission.*[70] *(Copyright 2018 Elsevier).*

The strategies for improving ionic conductivities usually fall into two different paths. First, modifying the size of the network can greatly influence lithium-ion transport. Given that the bottleneck of lithium-ion conduction resides between Li1 and Li3 sites, a common approach involves increasing the bottleneck size by using larger M ions, e.g. shifting from $M = Ge^{IV}$ (0.53 Å), to Ti^{IV} (0.605 Å) and Hf^{IV} (0.71 Å) can increase lithium-ion conductivity up to 4 orders of magnitude (**Figure 1.11a**). Additionally, the activation energy of lithium-ion conduction decreases linearly while increasing the bottleneck size between the Li1 and Li3 sites, which further supports the importance of achieving an optimal bottleneck sizes for mobile ions. Second, the aliovalent substitution of M^{IV} with M^{III} cations such as Al^{III} and Sc^{III} can greatly enhance the ionic conductivity by increasing both the Li ions concentration and their mobility (**Figure 1.11b**).[43] That is why the most studied Li-based NASICON structures are Al-doped $LiTi_2(PO_4)_3$ and $LiGe_2(PO_4)_3$. While the undoped compounds have relatively poor Li-ion conductivities, in the order of 10^{-6} S cm^{-1} at room temperature, the aliovalent substitution of Ti^{IV} and Ge^{IV} by Al^{III} proved to be an effective strategy to increase the ionic conductivity of 2-3 orders of magnitude.[71] The highest conductivities at room temperature reported to date are 1.3×10^{-3} S cm^{-1} for $Li_{1.3}Al_{0.3}Ti_{1.7}(PO_4)_3$ (LATP)[31] and 2.8×10^{-4} S cm^{-1} for $Li_{1.5}Al_{0.5}Ge_{1.5}(PO_4)_3$ (LAGP), as displayed in **Table 1.1**.[69,70,72]

Table 1.1 Ionic conductivities of NASICON $Li_{1+x}M^{III}_xM^{IV}_{2-x}(PO_4)_3$ materials.[70]

	Ge^{IV} (53 pm)	Hf^{IV} (71 pm)	Ti^{IV} (60.5 pm)	Zr^{IV} (72 pm)
Al^{III} (53.5 pm)	2.8×10^{-4}	-	1.3×10^{-3}	-
Cr^{III} (61.5 pm)	1.2×10^{-4}	5.3×10^{-7}	3.9×10^{-4}	5.9×10^{-7}
Eu^{III} (117 pm)	-	-	6×10^{-5}	-
Fe^{III} (64.5 pm)	3×10^{-5}	1.7×10^{-4}	5.2×10^{-4}	1.4×10^{-7}
Ga^{III} (62 pm)	4.4×10^{-5}	-	2.6×10^{-4}	-
In^{III} (80 pm)	9.2×10^{-6}	1.4×10^{-4}	4×10^{-4}	8.2×10^{-8}
La^{III} (103.2 pm)	-	-	5.3×10^{-4}	-
Lu^{III} (86.1 pm)	-	9.8×10^{-5}	-	-
Sc^{III} (74.5 pm)	2.6×10^{-5}	8.6×10^{-5}	8.8×10^{-4}	-
Y^{III} (90 pm)	-	9.2×10^{-5}	6.1×10^{-4}	7.1×10^{-5}

The aliovalent substitution is effective only to a certain extent, in fact stoichiometries with higher Al contents (≥ 0.6) often leads to the formation of non-conductive secondary phases, e.g. $AlPO_4$.[31,68,73] Besides the good ionic conductivity, LATP and LAGP are characterized by high chemical stability, being unaffected by the presence of both air and water.[71] They are also electrochemically stable at high potentials, thus being suitable for coupling with high-voltage cathode materials.[74] However, both materials have still some drawbacks that need to be addressed.

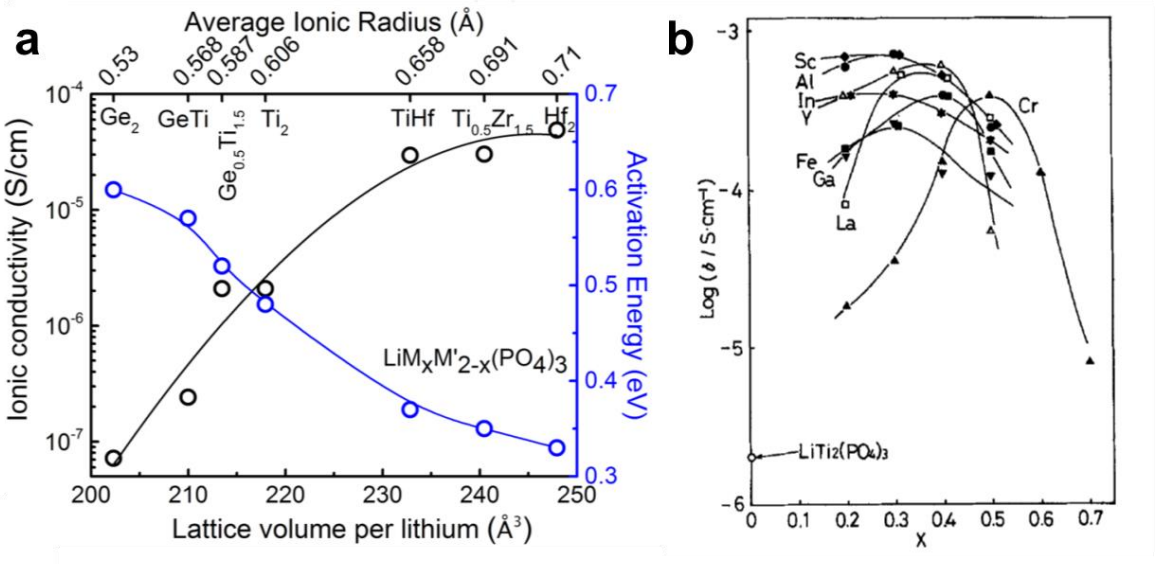

Figure 1.11 (a) Lithium-ion conductivity and activation energy of NASICON $Li_{1+x}M^{III}_xM^{IV}_{2-x}(PO_4)_3$ with different cationic radii at room temperature as a function of lattice volume per lithium atom. *Reproduced with permission.*[43] *(Copyright 2016 American Chemical Society).* (b) Variation of the ionic conductivity of $Li_{1+x}M^{III}_xTi_{2-x}(PO_4)_3$ at room temperature with the degree of substitution (X). *Reproduced with permission.*[31] *(Copyright 1990 IOP Publishing).*

The presence of Ge^{IV} or Ti^{IV} make them susceptible to the electrochemical reduction when low potentials are employed. This is a major concern when they are in contact with metallic Li, which easily causes their reduction to Ge^{III} and Ti^{III}, respectively, thus generating electrical conduction between the electrodes.[74] While the electrochemical reduction of Ti^{IV} in contact with Li is universally accepted, Ge^{IV} reactivity seems to still be an ambiguous topic.[75,76]

Several different synthesis methods have been developed to achieve LATP and LAGP solid electrolytes. They can be generally divided into two main categories: solid- and liquid-based approaches.

Solid-state synthesis is a conventional method to prepare LATP and LAGP electrolytes, and more in general inorganic materials. Aono et al. used it for the first time to achieve Li-based NASICON materials.[31,77,78] Generally, the chemical precursors are mixed and ball milled. Then several heat treatments (calcination and sintering) enable the achievement of pure and dense solid electrolyte. However, very high temperatures (700–1200 °C) and long dwell times (>12h) are often necessary to reduce the impurity content and maximize the density. Solid state reactions are indeed intrinsically slow because, although an optimal mixing of precursor materials at the level of individual particles can be achieved, thanks to several milling steps, on the atomic level they are usually very inhomogeneous. A good atomic level mixing of the reactants can be achieved either by counterdiffusion of ions between different particles or by liquid- or gas phase transport, thus to enable atoms of the different elements in the correct ratio to react and form the desired product. In a typical solid-state synthesis, four aspects must be optimized: 1) the starting materials, which ideally should be of accurately known stoichiometry, pure and reactive; 2) mixing of reactants. As mentioned above, reactants must be brought into contact as efficiently as possible. Reducing the particle size of the reactants and achieving an intimate mixing by a high-energy mechanical milling technique (ball milling, planetary milling, etc.); 3) the container must be inert towards the reactants and thermally stable at the temperature employed for the heat treatment in order to avoid contaminations; 4) the firing schedule, which should avoid the volatilization of one or more reactants and should feature temperatures at which the precursors react on a reasonable timescale.[79] The samples prepared with a solid-state method are usually characterized by a highly crystalline structure, large grains, fewer grain boundaries, great ionic conductivity, and high density. However, the high temperatures used often cause lithium loss and the formation of secondary phases,[80] which have a negative impact on the Li-ion conductivity.

Another standard solid-based synthesis approach to prepare NASICON-type electrolytes is the melt-quenching method.[81–84] This enables the achievement of a glass-ceramic material characterized by a very high ionic conductivity, as reported for a LAGP electrolyte displaying a value of 4.22×10^{-3} S cm^{-1} at room temperature.[85] However, this method requires even higher temperatures (≈1500 °C) compared to solid-state synthesis in order to melt the precursors. The melt is then quenched at room temperature to obtain an amorphous glass. Final sintering crystallizes the material. Besides the high temperatures needed, this method is greatly affected by the chemical precursors and the sintering conditions.

Among liquid-based methods, sol–gel provides an efficient synthetic path for the achievement of crystalline LATP and LAGP solid electrolytes.[73,86–90] The precursors materials are dissolved in a suitable solvent to obtain first a colloidal solution, then a gel network. The heat treatment of the gel removes volatile components and organic side groups, enabling the crystallization of the final product. The major advantage of the sol–gel synthesis is the possibility to achieve pure materials employing lower temperatures and shorter time than those needed for solid-state and melt-quenching methods. Sol–gel method has been largely employed in this thesis, thus it will be described in detail in **Chapter 1.4.1**.

A variation of the sol–gel approach, known as Pechini process, is characterized by the dissolution of the precursor materials in water and most importantly by the introduction of an alpha-hydroxycarboxylic acid, such as citric acid.[91,92] Citric acid acts as chelating agent to form a cross-linked network. After subsequent polymerization and calcination, nano-sized particles can be achieved.

The coprecipitation method has been reported as valid synthetic path for the LATP and LAGP solid electrolytes.[93–95] It is based on the dissolution of the precursor materials in an aqueous solution and their simultaneous precipitation upon pH adjustment or freeze drying. The obtained powder is then treated at intermediate or high temperature to crystallize the final product. The use of water instead of organic solvents lowers the costs of the process, and as the other liquid-based methods is characterized by lower calcination and sintering temperature. However, the high costs associated with the required chemicals and the relatively common secondary phases detected using this approach, often prevent its application.

Another liquid-based synthesis is represented by the hydrothermal/solvothermal method. Generally, the precursor materials are placed in a PTFE-lined cylinder along with water or an organic solvent; their solubility is P,T-dependant. The sealed cylinder is then heated in a temperature range of 100–

500 °C; its pressure is controlled either externally or by the degree of filling to achieve the crystallization of the final material.[79] Few studies report the successful use of hydrothermal/solvothermal methods for the synthesis of NASICON-type LATP.[96–99]

1.3.3 Organic polymer electrolytes

A polymer electrolyte comprises at least a polymer matrix and a lithium salt, which is needed to provide ionic conductivity. To be suitable for practical applications in lithium polymer batteries, a polymer electrolyte must possess some specific properties:[100,101] 1) High ionic conductivity. While liquid electrolytes are usually characterized by an ionic conductivity of 10^{-2}–10^{-3} S cm^{-1}, polymer electrolytes should possess conductivities approaching 10^{-4} S cm^{-1} at room temperature. 2) High Li^+ transference number. A Li^+ transference number close to unity is ideal for electrolyte systems, since it can reduce the polarization during the charge/discharge process.[102] An effective strategy to increase the Li^+ transference number is to reduce the mobility of anions. This can be achieved by anchoring the anions to the polymer backbone, thus achieving single-ion conducting polymer electrolyte,[103–106] or by introducing anion receptors that selectively complex them in the electrolyte.[107,108] 3) Good mechanical strength. Polymer electrolytes should be strong enough to oppose to lithium dendrite growth without being brittle like ceramics. Moreover, they should be able to elastically cushion the stress due to the process of manufacture, cell assembly, storage and usage. Adding inorganic fillers or physical supports and crosslinking, are all feasible strategies to improve the dimensional stability of polymer electrolytes. 4) Wide electrochemical stability window. The oxidation potential of the electrolyte must be higher than the insertion potential of Li^+ in the cathode and the reduction potential must be lower than that of metallic lithium in the anode. 5) Optimal chemical and electrochemical stability. Polymer electrolytes should be inert to the materials employed for other battery components, such as anode, cathode, current collectors, additives, and battery packaging. They should also be thermally stable even in case of electrical abuse, such as short-circuit and overcharge, and in case of fire.[27]

Dry polymer electrolytes. Conventional solid polymer electrolytes, made of a lithium salt dissolved into a polymer matrix, are often referred to as dry polymer electrolytes. A dry polymer electrolyte is a typical ion-coupled system, in which ion transport only occurs in amorphous regions above the glass-transition temperature (T_g), assisted by the segmental motion of chains. The ion transport in an ion-coupled system is affected by two factors: 1) the amount of amorphous phase in the polymer matrix, since several polymers are semi-crystalline; 2) the T_g of the polymer employed, since the mobility of

polymeric chains increases above the glass transition. Moreover, the polymer employed should be able to effectively dissolve lithium salts. From this perspective, some of the best candidates are presumably the polyethers, which are also characterized by a good electrochemical stability. Polyethers dissolve lithium salts by interacting with the metal ions through the ether oxygens. In this class of polymers, PEO, which is based on a $–CH_2–CH_2–O–$ chemical structure, is undoubtedly the most promising material thanks to the flexibility of its chains, enabled by the low T_g, which is equal to -64 °C. In addition, the strong donor character of the oxygen atoms enables a prompt solvation of Li^+ ions. The ionic conductivity of PEO-based electrolytes significantly improves after 65 °C, which corresponds to the melting point of PEO. PEO is also commercially available in a relatively pure state and at reasonable cost. However, being a semi-crystalline polymer at room temperature, the crystalline domains greatly hinder the transport of Li^+ ions. That is why the ionic conductivity at room temperature of PEO-based electrolytes is relatively low, usually around 10^{-6}–10^{-8} S cm^{-1}. Adding plasticizers, forming cross-linked or blocked polymers and incorporating inorganic ceramic fillers are all effective strategies to decrease the crystallinity of PEO and thus improve the ionic conductivity at room temperature of PEO-based solid electrolytes. Other polymers with a low T_g have also been investigated, such as poly(propylene oxide) (PPO),[109,110] poly[bis(methoxy-ethoxy-ethoxy)phosphazene] (MEEP),[111,112] polysiloxane (PSi),[113,114] etc., which remain completely amorphous at ambient temperature. PPO is commonly used as a polymer matrix for ionic conduction, similarly to PEO. The solvation of lithium ions in MEEP is attributed to both the ether oxygens and the nitrogen atoms in the polymer backbone.[27,115,116]

In polymer electrolytes, the choice of the lithium salt is crucial. Lithium salts employed for the development of polymer electrolytes have usually been already tested in liquid media, since the requirements are similar, i.e. high solvability, good electrochemical stability, high thermal stability and a pronounced ability for form a stable SEI. The most studied ones are $LiClO_4$, $LiBF_4$, $LiPF_6$, $LiAsF_6$, $LiCF_3SO_3$ and $LiN(CF_3SO_2)_2$. The mobility of the ions of these lithium salts is in the following order: $LiBF_4>LiClO_4>LiPF_6>LiAsF_6>LiCF_3SO_3>LiN(CF_3SO_2)_2$, while their dissociation constants follow this order: $LiN(CF_3SO_2)_2>LiAsF_6>LiPF_6>LiClO_4>LiBF_4>LiCF_3SO_3$.[117]

Gel polymer electrolytes. Gel polymer electrolytes (GPEs) are prepared by incorporating a certain amount of liquid plasticizer and/or solvent into a dry polymer electrolyte. This was first attempted by Feuillade et al. in 1975,[118] by adding an aprotic solution containing an alkali metal salt to a polymer matrix. Given the addition of a liquid component, the major contribution to Li^+ transport is not related

to the segmental motion of polymer chains and Li^+ hopping mechanism as in dry polymer electrolyte, but it mainly occurs in the gelled and/or liquid phase. Especially when the material is characterized by a connected porosity, the ionic conductivity of the GPE depends almost entirely by the properties of the trapped liquid medium. Since the ionic conductivity of the GPE no longer depends by the polymer's ability to complex Li^+ ions, several other polymers can be selected, since they mostly act as supporting network. Polymers reported in the literature include PEO,[119,120] polyvinyl chloride (PVC),[121] PAN,[122] PMMA,[123] PVdF,[124] and PVdF-HFP copolymer.[125] However, often GPEs based on a single polymer matrix are not able to fulfill all the requirements listed above. For example, PMMA-base electrolytes are characterized by low mechanical strength, PAN-based electrolytes undergo passivation at the interface with metallic lithium,[126] fluorine groups in PVdF- and PVdF-HFP-based electrolytes react with metallic lithium, thus producing LiF, which is responsible for safety hazard.[127] Several strategies to improve the properties of the polymer matrices have been proposed, such as blending, copolymerizing, crosslinking and compounding. The addition of inorganic fillers is presumably the most effective and versatile strategy to improve the mechanical strength and interfacial stability of polymer electrolytes in general. This approach leads to a new class of electrolyte commonly referred to as composite or hybrid electrolyte, which are described in detail in the next subchapter.

1.3.4 Composite electrolytes

Although several studies report the use of purely inorganic solid electrolytes or organic polymer electrolytes for ASSLBs, in the last few decades a growing research interest has been turned to the composite electrolytes, which aim to combine the advantages and eliminate the drawbacks of both inorganic and organic solid electrolytes. Usually, the addition of inorganic ceramic components to polymer electrolytes leads to enhanced mechanical strength and improved ionic conductivity. Several polymers, such as PEO, PAN, PMMA and PVdF, have been employed as polymer matrices to achieve composite electrolytes for lithium batteries. Using a polymer to develop composite materials is advantageous for several reason: 1) because of their mechanical properties, polymers can help increasing the flexibility and reducing the brittleness of solid electrolytes; 2) the presence of the polymer enables the achievement of a better interface with the electrodes thus reducing the interfacial resistance; 3) polymers are usually easier to process and more cost-effective, thus being more convenient for future large-scale manufactures.[116,128]

Inorganic fillers. The key advantages of adding inorganic fillers to polymer electrolytes arise from the following specific aspects: 1) the reduction of polymer's crystallinity in favour of the more conductive amorphous phase; 2) the enhancement of the interfacial stability between electrolyte and electrodes; 3) the improvement of the Li^+ transference number. During the last forty years, several materials have been tested as filler in polymer electrolytes, but in general, they can be classified into two main categories, according to their ability of conducting Li^+ ions: inert and active fillers.

Most of the inert fillers reported to date are spherical particles made of oxide ceramics, such as aluminum oxide (Al_2O_3), silicon dioxide (SiO_2) and titanium oxide (TiO_2). In 1982, Weston et al. were the first investigating the application of Al_2O_3 as filler in a PEO-$LiClO_4$ polymer electrolyte.[129] They reported that the addition of 10 vol.% of α-alumina greatly improved the mechanical stability of the polymer electrolyte. Later, Croce and coworkers noted that the addition of Al_2O_3 and TiO_2 particles to a PEO-$LiClO_4$ polymer electrolyte positively affects the ionic conductivity of the electrolyte.[130] Following studies further investigated the interaction between the inorganic fillers and PEO, which is behind the ionic conductivity improvement. It has been observed that both Al_2O_3 and TiO_2 could act as cross-linking centers for the polymeric chains of PEO, which hinder its recrystallization and decreases its crystallinity. Hence, inorganic fillers behave like plasticizer, decreasing the crystallinity of PEO and enhancing its ability of transporting Li^+ ions.[131] However, another phenomenon involving the interface particle-polymer, could contribute to the ionic conductivity improvement of the composite electrolyte. This has been explained using Lewis acid-base theory: given that polyether matrix and Li counterion (e.g. ClO_4^-) can act as Lewis base centers and both Lewis acids and bases are present on the surface of ceramic particles, various acid-base interactions may involve the Li^+ ion, which is considered a hard acid.[132,133] SiO_2 has also been reported as filler to effectively improve the ionic conductivity of PEO- $LiClO_4$ polymer electrolytes. Thanks to the numerous hydroxyl groups on the surface, SiO_2 particles can form a stable interface with the polymer matrix, thus reducing its crystallinity and consequently increasing the Li^+ conductivity and transference number of the electrolyte. Moreover, a wider electrochemical stability window (up to 5 V) could be achieved.[134–136]

Active fillers are usually made of ceramic materials characterized by an ionic conductivity comparable or higher than the one of the polymer-Li salt system. They can actively contribute to the Li^+ ions transport, thus further boosting the ionic conductivity of composite electrolytes, especially at room temperature. Perovskite-type,[137,138] garnet-type,[139–147] and NASICON-type[148–156] ceramics have been widely used as fillers to develop composite polymer electrolytes for ASSLBs. For example, Xu et al.

reported that the addition of $Li_{3/8}Sr_{7/16}Ta_{3/4}Zr_{1/4}O_3$ perovskite to a PEO-LiTFSI polymer electrolyte enables the achievement of an ionic conductivity of 5.4×10^{-5} and 3.5×10^{-4} S cm^{-1} at 25 and 45 °C, respectively, thanks to the strong interaction between the F^- of $TFSI^-$ anion and the surface Ta^{5+} of the perovskite particles.[137] Garnet-type fillers received particular attention during recent years, as they provided deep insight on the understanding of the preferential Li^+ ions path through the composite electrolyte. Zheng et al. observed that the dominant ionic path is strongly connected to the amount of $Li_7La_3Zr_2O_{12}$ ceramic phase used for the preparation of a PEO/LLZO/$LiClO_4$ composite electrolyte. When small amounts of ceramic filler are used (e.g. 5 wt.%) Li^+ ions preferentially migrate through the PEO phase, while increasing the inorganic content to 20 wt.% leads to a more balance transport, i.e. in both the polymeric and inorganic phases. A 50 wt.% addition of LLZO enables a preferential migration of Li^+ ions in the ceramic phase, because of the continuous network provided by LLZO fillers.[139,140] Particle size has also a significant impact on the conductivity of the composite electrolyte, as demonstrated by Zhang et al.[147] They investigated the addition of LLZTO particles of different size, i.e. 40 nm, 400 nm, and 10 μm to a Li-salt-free PEO electrolyte, reporting room-temperature ionic conductivities of 2.1×10^{-4} S cm^{-1}, 1.3×10^{-5} S cm^{-1}, and 3.8×10^{-6} S cm^{-1}, respectively. PEO-LITFSI-LLZTO composite electrolytes from "ceramic-in-polymer" to "polymer-in-ceramic" ratios have been also reported, particularly emphasizing their optimal dendrite-suppressing capability.[145,146] NASICON-type ceramics were the first active fillers to be tested in a composite polymer electrolyte in 2002. Specifically, Zhang et al. added glassy LATP to a PEO-based polymer electrolyte, reporting a room-temperature conductivity of 1.7×10^{-4} S cm^{-1}.[148] More recently, the effect of the addition of LATP fillers to a PEO-$LiClO_4$ electrolyte has been compared to that of inert fillers, such as TiO_2 and fumed silica.[149] After excluding a potential effect of a different PEO's crystallinity, the authors proved that the improvement in terms of ionic conductivity is related to an active role of LATP particles in Li^+ ion transport. Moreover, they observed that the maximum in conductivity occurs at the interphase between particles and polymer, which can form a fast percolation path for Li^+ ions when the LATP content is relatively low (10 wt.%). Another interesting approach consists in vertically aligning LATP nanoparticles in a PEO matrix. With this strategy, Zhai et al. achieved an ionic conductivity 3.6 times higher than that of the composite electrolyte with randomly dispersed nanoparticles.[154] Similar results have been reported by the same research group with vertically aligned LAGP nanoparticles blended into a flexible PEO/PEG matrix, achieving an ionic conductivity 6.9 times higher than that with randomly dispersed LAGP.[155] All these findings revealed that a specific amount of fillers is necessary to properly boost the ionic conductivity of the composite

electrolyte. If the inorganic content is too low, the ionic transport prevalently occurs in the polymer-Li salt system, since the repeated hopping between polymeric phase and inorganic particles results in a slower conduction path. On the contrary, too high inorganic content could lead to the formation of agglomerates, thus being unable to hinder the crystallization of the polymer phase. The proper amount of fillers must be identified in order to form continuous ion-conductive paths through the electrolyte and at the same time favour the formation of the polymer amorphous phase.

1.4 Coupling sol–gel and electrospinning: a strategy to achieve inorganic ion-conductive fibers

Coupling the sol–gel method with the electrospinning technique enables a facile approach to achieve fibers made of potentially any inorganic material.[157,158] This approach has been and is currently used to prepare ion-conductive fibers for different applications. We described this technique and its potential applications in a small review entitled "*Electrospun ceramic nanofibers as 1D solid electrolytes for lithium batteries*",[159] in which the main focus was the fabrication of nanofibers made of Li-ion conductive materials and their application as dense ceramic electrolytes or inorganic fillers for composite polymer electrolytes. Before further exploring this approach, some theoretical notions of the sol–gel method and the electrospinning technique must be introduced.

1.4.1 Sol–gel

The main drawback of solid-state syntheses is that reactants are not mixed on an atomic scale. However, various methods that allow to achieve atomic scale mixing of reactants exist. Most of them require low-temperature treatments to synthesize the desired phase, thus they are often referred to as *chimie douce* (soft chemistry) methods, although a final treatment at high temperature may be needed to improve purity and crystallinity, especially for ceramic products. A significant advantage, compared to other synthetic routes, is the achievement of products possessing high homogeneity, which often leads to improved properties and better understanding of their dependence on structure, compositions and dopants. In addition, non-powder precursors can be used, so as to not constrain the synthetic path in terms of morphology and application of the final product. For example, it is possible to achieve fibers or coatings, directly from the synthesis. Soft chemistry methods, however, have some drawbacks that often limit their use. The reactants can be costly and difficult to handle, for example; several waste products are often produced, such as processing solvents and by-products; additionally, the optimization of a specific synthetic route is not always directly applicable to the synthesis of a parent

structure. These aspects often hinder the employment of such methods in large-scale production.[79] Sol–gel approach belongs to this category, being based on the preparation of an initial solution that enables a close mixing of all reactants in a liquid phase.

The first reported examples of sol–gel processing are the studies on silica gels carried out by Ebelmen[160,161] and Graham[162] in the mid-1800s. They observed that the hydrolysis of tetraethyl orthosilicate ($Si(OC_2H_5)_4$), under acidic conditions, produced SiO_2 in the form of a "glass-like material".[160] Additionally, the viscous gel could be manipulated to obtain fibers, monolithic optical lenses or composites.[161] However, drying times of 1 year or more were necessary to avoid the silica fracturing into a fine powder, which greatly lowered the technological interests. Between the 1950s and 1960s, Roy and co-workers used the sol–gel method to successfully synthesize several ceramic oxide compositions, based on Al, Si, Ti, Zr, etc. and characterized by a very high chemical homogeneity.[163–166] Meanwhile, Iler's work on silica chemistry paved the way to the development of the commercial Ludox spheres made of colloidal silica powders and produced by DuPont's.[167,168]

While several definitions of sol–gel synthesis have been proposed during years, a more general one is universally accepted today. This definition states that a sol-gel process is a colloidal route used to synthesize ceramics with an intermediate stage including a sol and/or a gel state. Nowadays, the sol–gel term is not used to describe a unique path but a vast category of synthetic approaches based on common principles, as schematically illustrated in **Figure 1.12**.[169]

The first step of any sol–gel synthesis is the choice of precursors materials. Since sol–gel is a synthetic method based on chemical interactions, selecting different precursors and procedures can promote different synthetic routes, thus achieving different products. Afterword, a common option is dispersing the colloidal particles into a stable sol before transforming it into a gel. A polymer could also be used to achieve a stable polymeric gel. Both sols and gels can be processed in various ways to achieve different morphologies and applications: they can be spinned into fibers or transformed by several techniques into coating materials. Colloidal particles can also be conventionally treated by cold-pressing, hot-pressing and sintering to produce the desired ceramic. Additionally, controlled gelation and drying can be employed to avoid fractures in the final material. The size of the pores can be controlled as well by supercritical drying or by the use of surfactants.

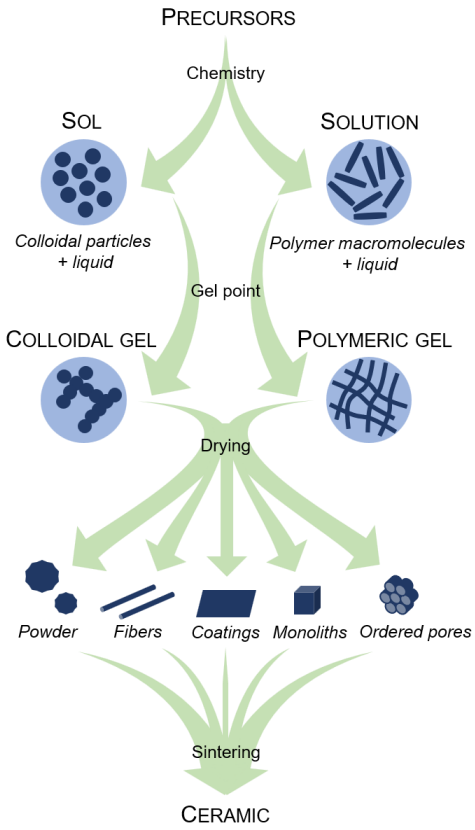

Figure 1.12. Simplified chart of sol–gel processes.[169]

Sol–gel method possesses several advantages compared to conventional solid-state synthesis techniques. It enables the production of hybrid organic/inorganic materials, which do not exist naturally and are impossible to obtain with conventional synthetic paths. More importantly, the temperatures employed in the very first steps of the process are considerably lower than those of conventional solid-state methods. This aspect is crucial for achieving pure products, since it greatly reduces the interactions between the material and the container walls, thus minimizing the risk of contaminations and by-products. Therefore, products characterized by a high purity can be easily achieved by using pure precursor materials. Other fundamental advantages characterize the sol–gel process, such as the control on the kinetics of each step of the chemical reaction, due to the low temperatures and the dilute conditions employed. This enables a high degree of control on the nucleation and growth of the material, which is crucial to achieve particles with a desired shape, size and size distribution. Moreover, the structure of the material can be easily controlled to achieve amorphous or semi-vitreous states. Several glasses, impossible to achieve by the standard melt-quench method, have been easily achieved by sol–gel, which allows to also tailor the distribution of pores and

crystalline domains to a certain extent. The greatest drawback of the sol–gel approach is probably the cost of precursor materials. Especially high-purity alkoxides, which are probably the most used reactants for this technique. Some of them however can be synthesized quite easily, while some others, such as Zr and Ti ones, are already employed industrially, which greatly lowered their cost. For most of the large-scale productions, sol–gel method can not compete with conventional high-temperature processes, which can usually rely on very inexpensive raw materials and well optimized procedures. However, sol–gel approach becomes more and more interesting when used in the field of highly advanced ceramics. Additionally, it can be coupled with several other techniques to tailor the morphology, the structure and the corresponding properties of the final product. For example, a casting or a spinning technique can be integrated into the synthetic process to easily achieve ceramic coatings or fibers, respectively.[169]

1.4.2 Electrospinning

Electrospinning is currently the only fabrication technique that enables the achievement of continuous fibers with diameters in the order of nanometers. While the technique mainly employs natural and synthetic polymers, polymeric alloys and solutions, it can also feature the addition of chromophores, nanoparticles, active agents, precursor materials, ceramics and metals to the electrospinning solution. Moreover, the electrospinning setup can be easily modified to achieve complex structures, such as core–shell or hollow fibers, or specific fiber alignments on a substrate.[170]

The term "electrospinning" is a blend word from "electrostatic" and "spinning" and was introduced around 1993. However, the initial studies and patents on this technique date to the beginning of the 1900s. Among them, Formhals developed and patented an apparatus for producing artificial filaments.[171] A milestone for the development of electrospinning was the work conducted in 1969 by Taylor on the conical shape of electrically driven jets,[172] later referred to by following researchers as "Taylor cone". Only in the late 1900s and early 2000s an upsurge of research on electrospinning has been recorded, as a result of the growing interest in nanotechnology. Electrospinning thus became a simple and versatile technique to prepare polymeric fibers with high surface area and nano-sized diameter, breaking new grounds for future technologies and applications.[159]

The process. Electrospinning appears as a very simple, thus easily controllable technique for fabricating fibers with diameters down to the nanometer range. In a typical electrospinning process (**Figure 1.13**), a solution or melt is pushed through a nozzle with an inner diameter of about 100 μm,

using a syringe connected to a syringe pump in order to control the flow rate. By means of a power supply, a high voltage, up to 30 kV, is applied to the nozzle, which thus acts as electrode. In a laboratory setup, a counter electrode is then placed at about 8-25 cm from the nozzle, to collect the electrospun fibers, thus also referred to as collector. The voltage applied to the nozzle causes a cone-shaped deformation of the drop of solution on the nozzle, the Taylor cone.[172]

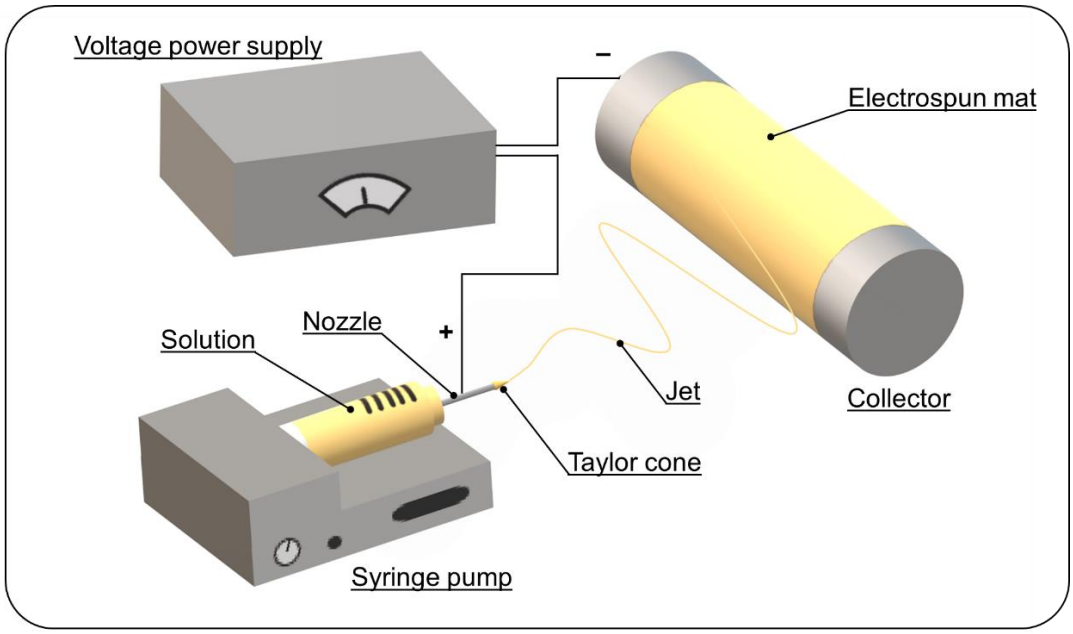

Figure 1.13 Schematic illustration of a typical electrospinning setup.

When the electrical field applied reaches a critical value the cone becomes a rapid whipping jet, which moves towards the collector while being continuously stretched during an unstable and chaotic flight. During this process, the solvent evaporates quickly (or the melt solidifies), resulting in the deposition of dry, randomly distributed polymeric fibers on the collector. After a prolonged deposition period, a nonwoven mat is obtained. Hence, the electrospinning process is not as simple as appears, but it is as a matter of fact a very complex balance of physical instabilities. One of them derives form the liquid strand itself, known as Rayleigh instability.[173] Others are induced by the coupling of the liquid strand with the electric field, thus related to the transport of charges into the liquid strand, i.e. the axisymmetrical instability and the whipping instability. The axisymmetrical instability causes a modulation of the surface charge density, which results in the formation of beads, aligned along the fiber as pearls on a string (**Figure 1.14a**). This can be prevented by changing the spinning parameters. Whipping (or bending) instabilities cause a lateral deformation relative to the axis of the fiber, which results into the formation of loops in the horizontal plane (**Figure 1.14b**). This kind of instability can

be enhanced by increasing the electrical conduction of the solution, thus minimizing the formation of high charge densities along the fibers.[170]

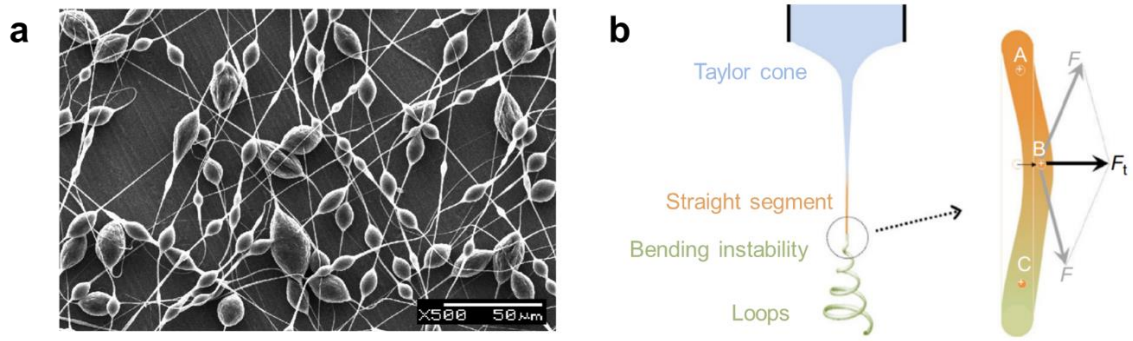

Figure 1.14 (a) SEM micrographs of PBS electrospun products (solvent: chloroform). *Reproduced with permission.*[174] *(Copyright 2008 John Wiley and Sons).* (b) Schematic illustration of perturbations causing the bending instability. A, B, and C represent three similarly charged parts of the jet where B has been perturbed from the symmetrical axis. *Reproduced with permissions.*[175] *(Copyright 2017 Elsevier).*

Parameters. The effect of the parameters on the formation of fibers is a crucial aspect of the electrospinning process. Usually, we can distinguish three different categories of parameters: solution (or molecular) parameters, process parameters and ambient parameters. The first category embraces all the variables related to the physico-chemical properties of the spinned solution, such as concentration and molecular weight of the polymer, viscosity of the solution and rheological and electrical properties of the solvent system. For fiber formation to occur, a minimum polymer concentration is needed. Increasing the concentration usually results in the increase of fiber diameters, until the formation of the fibers is hindered by the inability of maintaining a constant flow at the tip of the needle. The same observations have been reported for the viscosity of the solution, which is directly correlated to its concentration. The molecular weight of the polymer is a measure of the number of entanglements of polymer chains in a solution, thus reflecting its viscosity. Hence, even at low concentrations, increasing the molecular weight of the polymer can ensure a sufficient level of viscosity to produce a uniform jet during electrospinning. However, the molecular weight also affects the rheological and electrical properties of the solution, such as surface tension, conductivity and dielectric strength. In the second group, all the parameters we can change by directly acting on the electrospinning setup are included, such as the solution flow rate, the applied voltage and the distance between the nozzle and the collector, but also the collector shape and motion, the nozzle inner diameter and the angle between the nozzle and collector. The flow rate of the solution, controlled by the syringe pump, is an important process parameter since it affects the jet velocity. A lower flow rate

is usually preferable as the solvent can evaporate more easily before reaching the collector. High flow rates can result in the formation of beads and in wet fibers. A slight influence of the flow rate on the morphological properties of the collected fibers has also been reported. A crucial process parameter is the voltage applied to the nozzle. A threshold voltage must indeed be attained to observe the formation of fibers. However, the influence of higher voltages on the fiber diameter is ambiguous. An increase of diameters was reported in several studies, since higher voltages can lead to more polymer ejection. Other researchers however reported that high voltages can favour the narrowing of the jet, thus a decrease of fiber diameter. While certainly an influence exists, it is presumably related to the electrical properties of the spinned solution. While the nozzle to collector distance does not affect the electrospinning as significantly as other parameters, a minimum distance must be ensured to give the solvent enough time to evaporate. Also, beads have been observed when the collector is either too close or too far from the tip of the nozzle. Finally, the collector material, shape and motion can greatly influence the morphology of the fibers. For example, a cylindrical collector rotating at high speed can lead to aligned fiber. The ambient parameters, which can be controlled too in some specific conditions, include temperature and humidity. Since an inverse relationship between temperature and viscosity exists, increasing the ambient temperature can lead to smaller fiber diameters. The ambient humidity can affect the evaporation of the solvent as well as the electrical properties of the spinning solution.

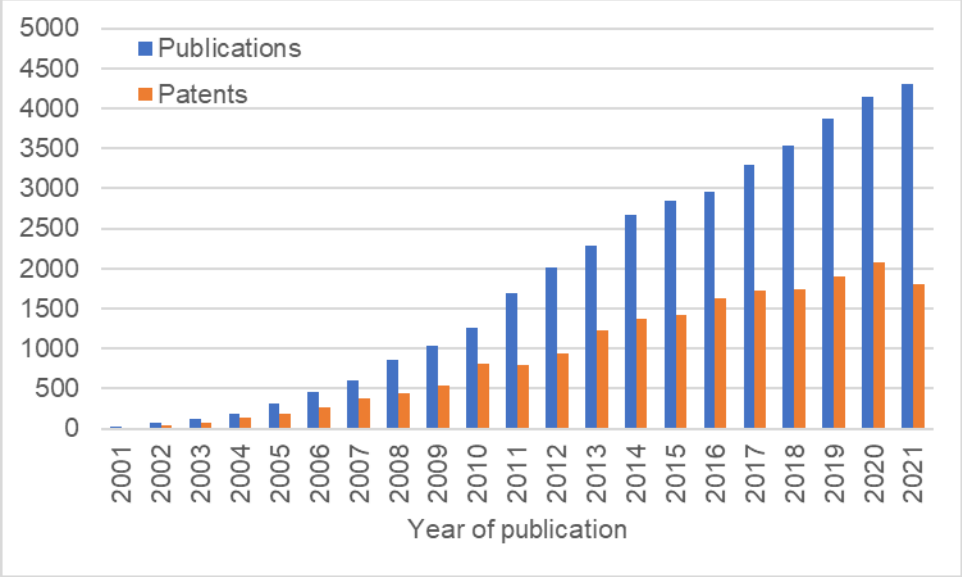

Figure 1.15. Number of scientific publications and patents per year (2001–2021) with the keyword "electrospinning". (Source: Scopus)

1.4.3 Inorganic ion-conductive nanofibers as electrolytes and fillers

An effective method to achieve ion-conductive ceramic fibers by electrospinning is to employ a sol–gel approach.[157,158] To use sol–gel for electrospinning, a solution with both sol–gel precursors and a polymer carrier is prepared. All the components must be perfectly soluble in the selected solvent system to obtain a homogeneous distribution of the precursors and stable electrospinning. Therefore, after the solution parameters and the ratio between the polymer and precursor materials are optimized, the prepared solution is electrospun to obtain precursor nanofibers. In the sol–gel synthesis, a high-temperature calcination step is finally performed to remove the polymer and all the organic side groups and crystallize the product. Owing to the void space within the fibrous network, product crystallization is confined within each fiber; thus, the final product retains the nanostructured morphology. The typical steps are displayed in **Figure 1.16.**

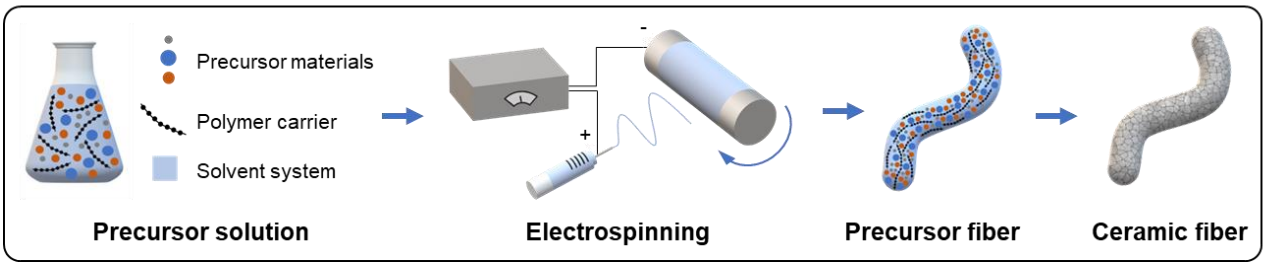

Figure 1.16 Schematic illustration of the synthesis process of ceramic fibers by electrospinning.

Since 2015, several Li^+-conductive ceramic fibers have been fabricated by this synthetic approach. Their synthetic conditions and main properties are summarized in **Table 1.2**. Perovskite-type[176–188] and garnet-type[189–196] fibers have been widely investigated, especially in the last few years, as both inorganic fillers and as base for dense inorganic electrolytes. Some studies on NASICON materials have also been reported.[197–199]

Table 1.2. Synthesis parameters and properties of ceramic Li-conductive fibers fabricated by electrospinning and employed in solid electrolytes.

Inorganic material	*Polymer carrier*[a]	*Solvent system*[b]	*Calcination conditions*	*Fiber diameter*	*Electrolyte composition*[c]	*Ionic conductivity (S cm^{-1})*	*Ref.*
$Li_{0.33}La_{0.557}TiO_3$	PVP	H_2O/iPrOH/AcOH	1000 °C (3h)	100–200 nm	LLTO pellet	4.37×10^{-6} (RT)	[176]
	PVP	DMF/AcOH	800 °C (2h)	140 nm	PAN/$LiClO_4$+15 wt% LLTO	2.4×10^{-4} (RT)	[177]
	PVP	DMF/AcOH	800 °C (2 h)	138 nm	PAN/$LiClO_4$+3 wt% LLTO	6.05×10^{-5} (30 °C)	[178]
	PVP	DMF/AcOH	800 °C (2 h)	1 μm	PEO-LiTFSI+5 wt% LLTO	5.53×10^{-5} (25 °C)	[179]
	PVP	DMF/AcOH	800 °C (2 h)	110 nm	PEO/LiTFSI+15 wt% LLTO	2.4×10^{-4} (25 °C)	[180]
	PVP	DMF/AcOH	800 °C (2 h)	500 nm	PEO/PPC/LiTFSI+8 wt% LLTO	5.66×10^{-5} (25 °C)	[181]
	PVP	DMF/AcOH	900 °C (3 h)	199 nm	PEO-LiTFSI+LLTO mat	1.6×10^{-4} (24 °C)	[182]
	PVP	DMF/AcOH	800 °C (2 h)	140 nm	PAN/$LiClO_4$+10 wt% LLTO	3.6×10^{-4} (RT)	[184]
	PVP	H_2O/iPrOH/AcOH	900 °C (3 h)	260 nm	PEO/$LiClO_4$+3 wt% LLTO	3.1×10^{-6} (RT)	[183]
	PVP	DMF/AcOH	900 °C (3 h)	200–300 nm	PVdF/$LiClO_4$+10 wt% LLTO NTs	1.7×10^{-3} (20 °C)	[185]
	PVP	DMF/AcOH	800 °C (2 h)	250 nm	PEC/LiTFSI+5 wt% LLTO	7.91×10^{-5} (25 °C)	[186]
	PVP	DMF/H_2O/iPrOH/AcOH	900 °C (2 h)	92 nm	PVdF-HFP/LiTFSI+30 wt% LLTO	3.8×10^{-4} (RT)	[187]
$Li_{0.33}La_{0.557}Ti_{1-x}Al_xO_3$	PVP	DMF/H_2O/iPrOH/AcOH	900 °C	155 nm	PVdF-HFP/LiTFSI+30 wt% LLATO	4×10^{-4} (25 °C)	[188]
$Li_7La_3Zr_2O_{12}$	PVP	H2O/iPrOH/AcOH	700 °C (2.5 h)	-	-	-	[189]
	PVP	DMF/AcOH	800 °C (2 h)	138 nm	PEO/LiTFSI+LLZO mat	2.5×10^{-4} (RT)	[190]
	PVP	DMF/iPrOH/AcOH	700 °C (1h)	100–276 nm	PAN/$LiClO_4$+5 wt% LLZO	1.31×10^{-4} (20 °C)	[191]
	PVP	DMF	700 °C (2 h)	100–200 nm	PEO/LiTFSI+10 wt% LLZO	2.39×10^{-4} (25 °C)	[192]
	PVP	DMF/H_2O/EtOH/AcOH	700 °C (3 h)	200 nm	-	-	[193]
	PVP	DMF/AcOH	750 °C (2.5 h)	100 nm	PVdF-HFP/LiTFSI+10 wt% LLZO	9.5×10^{-4} (20 °C)	[194]
	PVP	DMF	850 °C (2 h)	-	PPC/LiTFSI+7.5 wt% LLZO	1.59×10^{-4} (RT)	[195]
$Li_{6.28}La_3Zr_2Al_{0.24}O_{12}$	PVP	DMF/AcOH	800 °C (3 h)	-	PVdF/PEC/LiTFSI/SN+20 wt% Al-LLZO	3.91×10^{-4} (25 °C)	[196]
$Li_6Zr_2O_7$	PVP	H_2O/EtOH	750 °C (1 h)	100 nm	Ceramic fibers	1.27×10^{-5} (200 °C)	[200]
$La_2Zr_2O_7$	PVP	DMF	1000 °C (8 h)	200–300 nm	PPC/LiTFSI+10wt% LZO	1.2×10^{-4} (RT)	[201]
$Li_{1.4}Al_{0.4}Ti_{1.6}(PO_4)_3$	PVdF-HFP	DMF/THF/acac	850 °C (2 h)	270 nm	Ceramic mat	3×10^{-7} (RT)	[197]
$Li_{1.3}Al_{0.3}Ti_{1.7}(PO_4)_3$	PVdF-HFP	DMF/THF/acac	850 °C (2 h)	0.4–1 μm	Ceramic mat	3×10^{-5} (25 °C)	[198]
$Li_{1.5}Al_{0.5}Ge_{1.5}(PO_4)_3$	PVP	EtOH	700 °C (2 h)	300–800 nm	PEO/LiTFSI+10 wt% LAGP	7.14×10^{-6} (20 °C)	[199]
$Li_{1.5}Al_{0.5}Ge_{1.2}Ti_{0.3}(PO_4)_3$	PVP	EtOH/acac	700 °C (2 h)	-	PEO/LiTFSI+10 wt% LAGTP	5.3×10^{-6} (20 °C)	[202]

[a] PVP: poly(vinylpyrrolidone) ; [b] DMF: N,Ndimetyformammide; H_2O: deionized water, EtOH: ethyl alcohol; iPrOH: isopropyl alcohol; AcOH: acetic acid; THF: tetrahydrofuran; acac: acetylacetone; [c] NTs: nanotubes; PEC: poly(ethylene carbonate); PPC: poly(propilene carbonate)

$Li_{0.33}La_{0.557}TiO_3$. Liu et al. investigated the properties of LLTO nanowires for use as a ceramic filler for polymer electrolytes.[177] As reported in **Table 1.2**, they used poly(vinylpyrrolidone) (PVP) as a polymer carrier and a binary solvent consisting of dimethylformamide (DMF) and acetic acid (AcOH). The optimal condition for calcination were found to be 2 h at 800 °C. The average diameter of the calcined fibers decreased from 520 in the as-spun fibers to 140 nm by heating at 800 °C. A 15 wt.% nanowire content improved the ionic conductivity of a polyacrylonitrile-lithium perchlorate (PAN-$LiClO_4$) electrolyte by approximately three orders of magnitude, whereas an LLTO-nanoparticle-filled PAN-$LiClO_4$ electrolyte exhibited an improvement of only one order of magnitude. In contrast to the case of nanoparticles, ceramic nanofibers created a 3D ion-conducting pathway, which improved the long-range Li^+ transport (**Figure 1.17**).

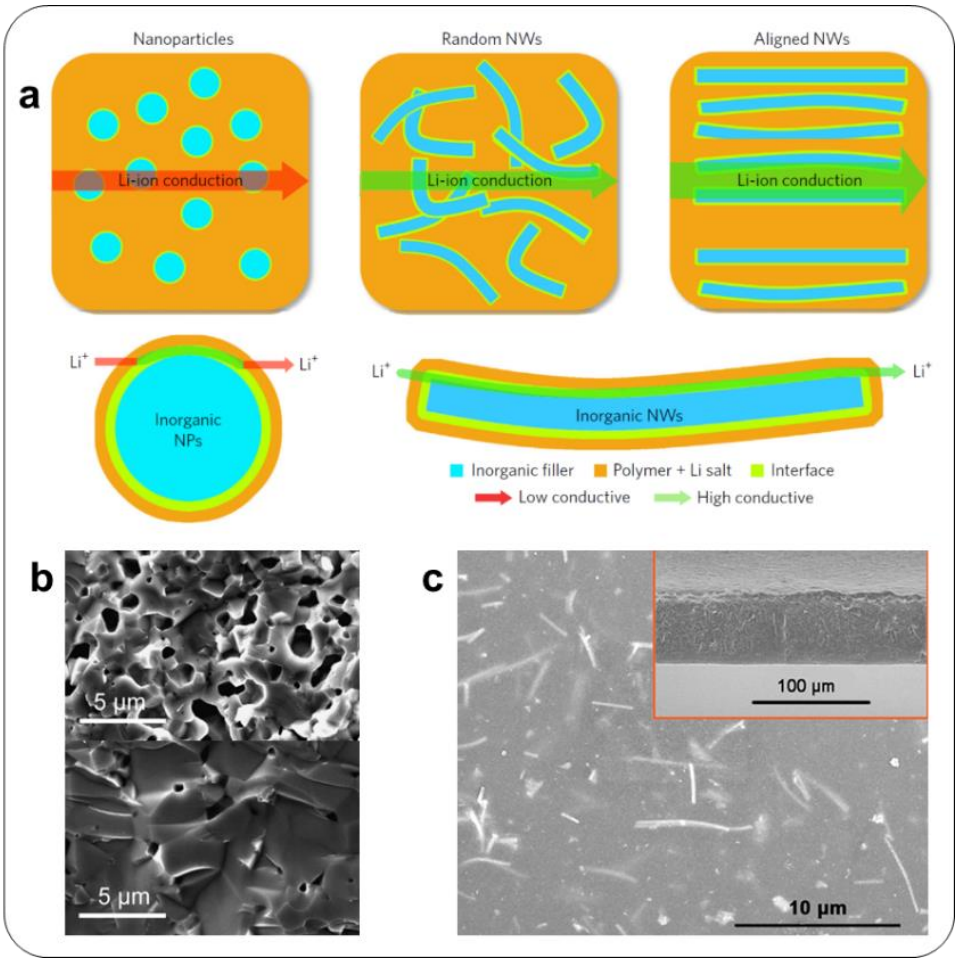

Figure 1.17 (a) Possible Li-ion conduction pathways in composite polymer electrolyte. *Reproduced with permission.*[178] *(Copyright 2017 Nature Publishing Group).* (b) Cross-sectional SEM image of pellet made of conventional sol–gel LLTO (top) and LLTO nanofibers (bottom). *Reproduced with permission.*[176] *(Copyright 2015 Elsevier).* (c) Morphology of composite polymer electrolyte with 15 wt% nanowire filler. *Reproduced with permission.*[177] *(Copyright 2015 American Chemical Society).*

According to Wieczorek et al.,[132] the ionic conductivity enhancement may be partly attributed to the strong affinity between $ClO4^-$ and acidic groups on the surface of nano-oxides, which facilitates the $LiClO4^-$ dissociation and increases the concentration of Li^+. Moreover, Liu et al. proposed that the high number of vacancies on the LLTO surface is beneficial for Li^+ hopping mechanism, thus further improving its ionic transport.[177] In the same year, Yang et al. reported the potential application of LLTO nanowires as an inorganic solid electrolyte for lithium batteries.[176] They synthesized them by electrospinning a water-based sol and performing a calcination step for 3 h at 1000 °C. The resulting polycrystalline fibers, which consisted of the pure tetragonal phase, had diameters of 100‑200 nm. Yang et al. successfully prepared pellets from LLTO nanowires; they reported higher density and improved ionic conductivity compared to those of pellets made of LLTO particles synthesized by a conventional sol–gel route. Cross-sectional images are shown in **Figure 1.17b**. Interesting results on LLTO nanofibers were reported by Liu et al.,[178] who investigated the effect of fiber alignment on the ionic conductivity of composite polymer electrolytes using interdigitated Pt electrodes (**Figure 1.17a**). They synthesized the LLTO nanofibers by spinning the precursor solution directly onto the Pt electrode and then calcined the fibers for 2 h at 800 °C. They showed that when well-aligned perpendicularly oriented nanowires were used, the conductivity was one order of magnitude larger than that of randomly oriented nanowires. The calculated surface conductivity of the nanowires was on the order of 10^{-2} S cm^{-1} at 30 °C, which is close to the typical values for liquid systems, indicating that the improved conductivity results from the absence of crossing junctions in the aligned sample. Moreover, they confirmed the previously proposed effect of LLTO surface vacancies on Li^+ transport.[177] They observed a smaller ionic conductivity enhancement when using inert ceramic fillers (ZrO_2 nanowires) instead of LLTO nanowires, thus showing the benefits of using highly ion-conductive fillers.[178] Recently, several other studies on the use of LLTO nanowires as a ceramic filler for the development of PEO,[179,180,182,183] PEO/PPC,[181] PAN,[184] PVdF,[185] PEC[186] and PVdF-HFP[187] based electrolytes have been reported. All the fiber-filled electrolytes showed improved ionic conductivity and Li^+ transference number, wider electrochemical stability window and enhanced mechanical strength compare to pristine or particle-filled electrolytes.

$Li_7La_3Zr_2O_{12}$. Few studies on the preparation of LLZO nanowires by electrospinning have been reported to date.[189–195] A water-based sol was electrospun using either nitrate or acetate precursor salts and PVP; then, after electrospinning, the effect of calcination time on the morphology and structure of the LLZO fibers was investigated. The optimal time was found to be 2.5 h; at shorter times, the

main phase was still $La_2Zr_2O_7$, whereas the fibers started to coalesce to form larger ligament-like structures after 3 h (**Figure 1.18a**).[189] However, it takes at least 3 h to produce a pure cubic LLZO phase. Later studies reported the electrospinning of a DMF-based sol with nitrate precursors and PVP as a polymer carrier.[190,191] Unlike the previous work, the pure cubic LLZO phase was obtained after only 1–2 h of calcination. Moreover, despite the short calcination time, a good fiber morphology was maintained, and no coalescence into the ligament-like structure was observed (**Figure 1.18b**).

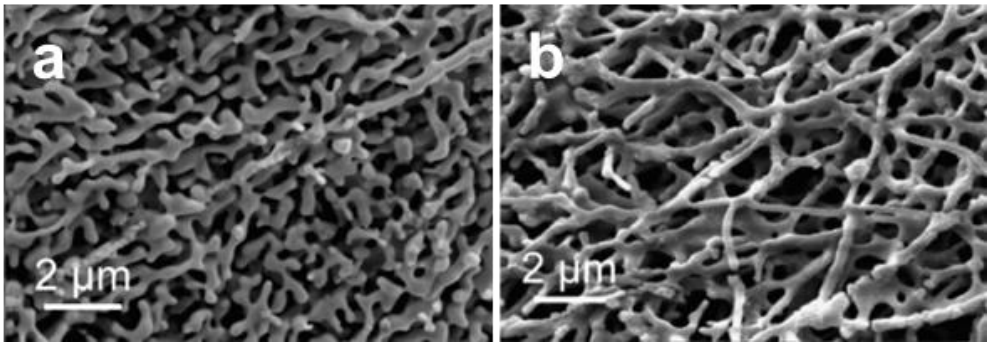

Figure 1.18 SEM images of electrospun LLZO calcined at 700 °C. (a) Ligament-like structure obtained by using aqueous precursors after a 3 h calcination step; (b) nanofibers prepared using DMF-based precursors and calcined for 1 h. *Reproduced with permission.*[191] *(Copyright 2017 American Chemical Society).*

Fu et al. then poured a solution of PEO-LiTFSI onto the ceramic mat to achieve a hybrid ceramic-polymer electrolyte with enhanced mechanical properties and fast Li^+ conduction. In addition, they demonstrated effective suppression of lithium dendrite growth by successfully cycling Li symmetric cells for 1000 h.[190] Yang et al. added various quantities of LLZO nanowires to a PAN-$LiClO_4$ electrolyte, and the highest ionic conductivity was obtained when 5 wt.% of the filler was used; this value is approximately three orders of magnitude higher than that of plain PAN-$LiClO_4$.[191] Al- and Ta-doped LLZO were also synthesized and investigated, yet the ionic conductivity of the corresponding composite polymer electrolytes was similar to that of electrolytes prepared with undoped LLZO. A recent study of LLZO nanowires as a ceramic filler for a PEO-LiTFSI electrolyte was reported by Wan et al.[192] The resulting hybrid electrolyte was characterized by a better ionic conductivity and an effective suppression of lithium dendrite growth. LLZO fibers have been used as filler for PVdF-HFP and PPC based electrolytes as well. Improved room-temperature ionic conductivity and electrochemical stability window have been reported.[194,195]

NASICONs. An interesting work that features the synthesis of a NASICON-based nanofibrous material with high ionic conductivity is that of Lancel et al.[197] They reported the synthesis of $Li_{1.4}Al_{0.4}Ti_{1.6}(PO_4)_3$ (LATP) nanofibers to fabricate a composite membrane for lithium air batteries.

Here a DMF/tetrahydrofuran (THF) binary solvent was used to dissolve the precursors and polymer carrier. As in the other cases, PVP has been investigated as a polymer carrier, but when it was used, the microstructure of the electrospun fibers was too dense, resulting in coalescence and morphology loss after calcination.[203] Hence, PVdF-HFP was used as the polymer carrier, and the electrospun fibers were then calcined for 2 h at 800–950 °C to obtain a pure LATP phase. The ionic conductivity of the resulting nanofibrous mat was 3×10^{-7} S cm^{-1}, which is lower than that of the bulk material. This is because of the mat porosity, which was estimated to be close to 60%. The mat was then impregnated with a solution of PVdF-HFP to obtain a watertight membrane for use as a separator in aqueous lithium air batteries (**Figure 1.19**).

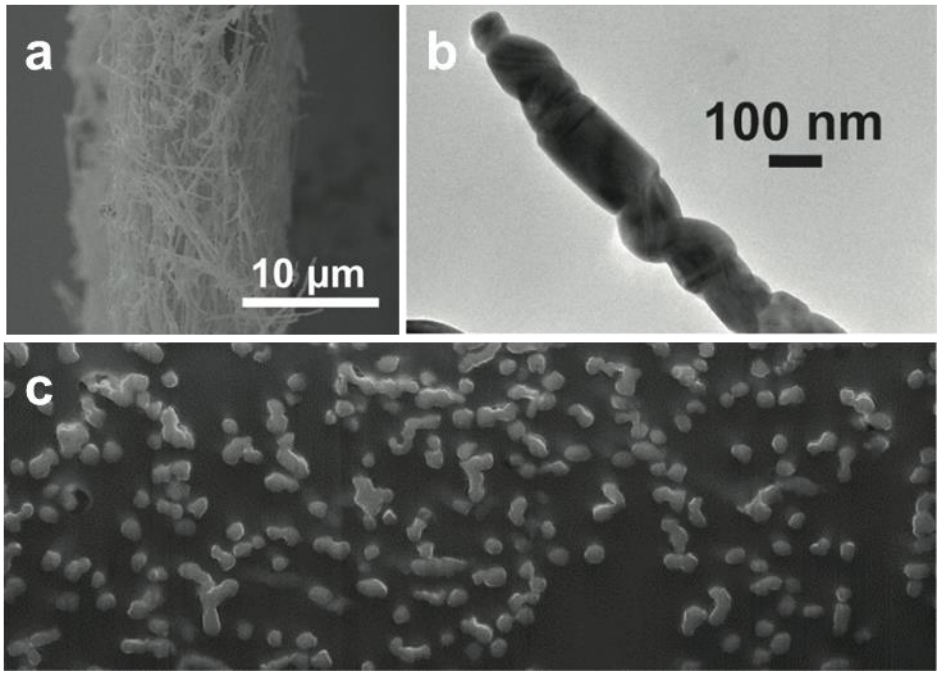

Figure 1.19 (a) Cross-sectional SEM image of self-standing LATP membrane after electrospinning and calcination. (b) Transmission electron microscopy images of isolated fibers (c) Cross-sectional field emission gun SEM image of a hybrid LATP/PVdF-HFP membrane. ***Reproduced with permission.***[197] ***(Copyright 2017 American Chemical Society).***

Despite it does not involve the electrospinning technique, the work carried out by He et al. deserves to be mentioned.[204] The authors fabricated a flexible Li^+ conductive glass-ceramic LAGP fiber by a melt-spinning technique. They claimed a significant reduction of pores and defects of the crystalline phase, compared to conventional solid-state and electrospinning methods. The LAGP glass-ceramic fibers, annealed at 825 °C for 6h, showed an ionic conductivity of 8.8×10^{-3} S cm^{-1} at room temperature. We investigated NASICON nanofibers fabricated by electrospinning based on both LATP and LAGP. The results are reported in details in **Chapters 5**, **6** and **7**.

Others. Lithium zirconate is a class of materials studied mainly for energy and environmental applications owing to their good ionic conductivity and high lithium content. Precursor salts and PVP were dissolved in a binary solvent of water and ethanol (4:6 mass ratio), which was then electrospun to obtain $Li_6Zr_2O_7$ nanofibers.[200] Pure-phase $Li_6Zr_2O_7$ nanofibers were obtained after the precursor fibers were calcined for 1 h at 750 °C. The authors of this study reported a negligible grain boundary resistance; thus, they speculated that the ionic conductivity of the nanofibers will be higher than that of the bulk material. Jing et coworkers reported the synthesis of ceramic lanthanum zirconate ($La_2Zr_2O_7$, LZO) fibers by calcining the electrospun precursor fibers at 1000 °C for 8 h. Compared to LLZO, LZO is has higher thermal and chemical stability, while maintaining the strong Lewis-acidity nature. The CE based on PPC and, cellulose and LZO fibers showed improved mechanical properties and room-temperature electrochemical performance.[201]

2 Aim of the thesis

As discussed in **Chapter 1** the global energy crisis needs prompt interventions. Batteries and other energy storage and conversion systems can certainly be instrumental for better exploiting sustainable energy resources, thus reducing our addiction to fossil fuels. However, more efficient and safe devices, such as ASSLBs, are necessary to perform a plausible replacement of fuel-based engines and furnaces in the automotive and stationary field, respectively. In this work, Li-based NASICON-type ceramic materials are synthesized with various methods to achieve different morphologies. Then, they are proposed as basis to develop solid electrolytes in order to address some of the main issues that are still affecting ASSLBs.

The aim of the thesis is described below as a list of different objectives, which however are part of the same optimization work made on NASICON materials.

1. **Improvement of the solid-state synthesis of LATP.** LATP is a valid Li^+ ion-conductive material to develop dense fully-inorganic electrolyte for lithium-based batteries. However, some fundamental aspects of its crystallization are still unknown; therefore, its synthesis can still be optimized by reducing calcination time and temperature and improving the density of the pellets with different techniques. This part of the work evolved through the following steps:
    - *Optimization of the precursor materials.* The effects of using different precursors, such as rutile and anatase TiO_2 as source of Ti for the solid-state synthesis of LATP, were investigated.
    - *Optimization of the calcination temperature.* Different calcination temperatures were tested to identify the value at which the highest density and ionic conductivity are achieved.
    - *Characterization of the powders. In-situ* high-temperature X-ray diffraction (HTXRD) was used as main characterization technique to thoroughly understand the crystallization mechanism of LATP.
    - *Preparation of dense ceramic electrolytes.* Dense pellets were prepared by hot-pressing at different temperatures.
    - *Evaluation of the ionic conductivity.* The ionic conductivity was measured by electrochemical impedance spectroscopy (EIS) to evaluate bulk and grain-boundary contributions.

2. **Effect of the fiber morphology on the properties of LATP.** A synthesis approach to fabricate LATP nanofibers, which consists of coupling sol–gel and electrospinning, was selected after a thorough research in the literature. From reported works, fiber morphology has proven to be beneficial to achieve denser inorganic pellets, as well as to enhance the properties of polymer electrolyte when ceramic fibers are used as fillers. The work proceeded through the following steps:
    - *Optimization of stoichiometry and electrospinning process.* The most conductive stoichiometry was selected and the electrospinning parameters have been adapted to the composition.
    - *Influence of the density on the conductivity.* A pressing step was introduced in the fabrication process of the nanofibrous ceramic mat in order to control the porosity and evaluate the impact of the density on the ionic conductivity of the sample.
    - *Influence of the fiber morphology on the properties of LATP.* By means of different characterization techniques, the effect of the arrangement of LATP crystallites into a nanofibrous network was investigated.

3. **Enhancing PEO-based polymer electrolytes through the addition of LAGP nanofibers.** The method used for the fabrication of LATP nanofibers was not directly applicable to LAGP, thus a novel chloride-based synthetic approach was developed. LAGP nanofibers were tested as both nanofibrous ceramic mat and as fillers for polymer electrolytes, showing promising results. This project proceeded through the following points:
    - *Optimization of synthetic method and electrospinning process.* Several Ge precursors were tested to directly apply the synthetic approach used for the fabrication of LATP fibers; however, all the attempts were unsuccessful. A novel chloride-based synthesis was developed, which entailed deep modifications of the electrospinning parameters.
    - *Evaluation of the influence of the calcination temperature.* Different calcination temperatures were tested to evaluate their effects on the morphology and purity of LAGP nanofibers.
    - *Investigation of the properties of porous nanofibrous mats.* The ceramic nanofibrous mats achieved using different calcination temperatures were characterized by different techniques. The relation between calcination temperature, density and ionic conductivity was assessed.

- *LAGP nanofibers as fillers for PEO-based composite electrolytes.* The addition of different amounts of LAGP nanofibers to a PEO-based electrolyte was performed. The ionic conductivity of the composite electrolytes was measured by EIS.

4. **Improving the purity and morphology of LAGP nanofibers by Ti substitution.** The purity and morphology of the previously synthesized LAGP nanofibers could be improved. Therefore, we investigated the effect of a partial substitution of Ge with Ti. The addition of stabilized Ti butoxide, thanks to its high viscosity, can be beneficial for the stability of the electrospinning process, thus leading to an improved fiber morphology. Moreover, it could help the crystallization of the NASICON phase during the calcination step. The following steps were carried out:
    - *Optimization of synthetic method and electrospinning process.* By combining the method used for the preparation of LAGP nanofibers and the stabilization of Ti precursor, LAGTP nanofibers were successfully synthesized.
    - *Investigation of different amounts of Ti doping.* Different amounts of Ti precursor were added to the spinning solution to achive different stoichiometry.
    - *Characterization of LAGTP nanofibers.* The structural and morphological properties have been investigated and compared to those of the undoped LAGP.
    - *LAGTP nanofibers as fillers for PEO-based composite electrolytes.* The same amount of different samples of LAGTP nanofibers were added to a PEO-based electrolyte. The ionic conductivities of the composite electrolytes were measured by EIS and compared to that of the LAGP-filled electrolyte.

2.1 Thesis organization

The thesis is divided into eight chapters, which are organized as follows:

Chapter 1 The energy crisis issue is introduced. Background information on the state-of-the-art LIBs and ASSLBs are provided, with particular focus on the use of ceramic ion-conductive fibers to develop solid electrolytes.

Chapter 2 The aim and the objectives of the thesis are presented.

Chapter 3 The experimental details are provided. The materials as well as the different synthetic methods are thoroughly described. Finally, the characterization techniques employed for all the steps of this project are listed.

Chapter 4 The influence of the use of rutile and anatase TiO_2 on the solid-state synthesis of LATP is investigated.

Chapter 5 The effect of pressure on the properties of LATP nanofibers prepared by electrospinning and subsequent calcination is described.

Chapter 6 A novel synthetic method to fabricate LAGP nanofibers by electrospinning is introduced. The characterization of the achieved ceramic nanofibers as both ceramic mat and fillers in PEO-based polymer electrolytes is described.

Chapter 7 The effect of the partial substitution of Ge with Ti on the properties of electrospun LAGP fibers is presented. Then, Ti-substituted LAGP nanofibers were added as fillers in PEO-based polymer electrolytes and their effects are also discussed.

Chapter 8 Here the conclusions and some perspectives on the subjects of the thesis are reported. Moreover, an outlook on potential future studies related to the thesis results is proposed.

3 Experimental

3.1 Materials

For the solid-state synthesis of LATP, lithium carbonate (Li_2CO_3), aluminum oxide (Al_2O_3), ammonium phosphate dibasic ($(NH_4)_2HPO_4$), rutile and anatase titanium oxide (TiO_2) were purchased from Sigma Aldrich and used as precursor materials.

For the synthesis of LATP fibers, lithium nitrate ($LiNO_3$, reagent grade, Sigma-Aldrich), aluminum nitrate nonahydrate ($Al(NO_3)_3 \cdot 9H_2O$, ≥98%, Sigma-Aldrich), titanium butoxide ($C_{16}H_{36}O_4Ti$, 97%, Sigma-Aldrich), and phenylphosphonic acid (PPA) ($C_6H_7O_3P$, 98%, Sigma-Aldrich) were used as precursor materials. Poly(vinylidene fuoride-co-hexa-fluoropropene) (PVDF–HFP) (Sigma Aldrich) was used as polymer carrier for the electrospinning process. N,N-Dimethylformamide (DMF) (C_3H_7NO, anhydrous, 99.8%, Sigma-Aldrich), tetrahydrofuran (THF) (C_4H_8O, anhydrous, ≥99.9%, Sigma-Aldrich) were used to dissolve the materials above, while acetylacetone ($C_5H_8O_2$, Sigma-Aldrich, ≥99%) was use to stabilize titanium butoxide and prevent its hydrolysis reaction.

To synthesize LAGP fibers, lithium chloride (LiCl, anhydrous, 99%, Alfa Aesar), aluminum chloride ($AlCl_3$, anhydrous, 99.99%, Sigma-Aldrich), germanium(IV) chloride ($GeCl_4$, 99.99%, Sigma-Aldrich), and phenylphosphonic acid (PPA) ($C_6H_7O_3P$, 98%, Sigma-Aldrich) were used as precursor materials. Polyvinylpyrrolidone (PVP) (Mw ~1,300,000, Sigma-Aldrich) and ethanol (EtOH) (C_2H_5OH, anhydrous, ≤0.005% H_2O, Sigma-Aldrich) were used as polymer carrier and solvent, respectively.

For the synthesis of $Li_{1.5}Al_{0.5}Ge_{1.5-x}Ti_x(PO_4)_3$ (LAGTP) fibers, the materials employed for LAGP synthesis have been used, with the addition of titanium butoxide ($C_{16}H_{36}O_4Ti$, 97%, Sigma-Aldrich), previously stabilized in acetylacetone ($C_5H_8O_2$, Sigma-Aldrich, ≥99%).

Polyethylene oxide (PEO) (Mw 100,000, Sigma-Aldrich), lithium bis(trifluoromethylsulphonyl)imide (LiTFSI) ($LiC_2F_6NO_4S_2$, >98%, 3M HQ-115) and acetonitrile (ACN) (CH_3CN, 99.8% anhydrous, Sigma-Aldrich) were used to prepare the composite polymer electrolyte.

3.2 Solid-state synthesis of $Li_{1.5}Al_{0.5}Ti_{1.5}(PO_4)_3$ ceramic electrolytes

In a standard solid-state synthesis, stoichiometric amounts of Li_2CO_3, Al_2O_3, TiO_2, (rutile or anatase) and $(NH_4)_2HPO_4$ were placed in a zirconia vial together with four zirconia balls (diameter: 12.7 mm) and ball milled in a SPEX mixer for 15 minutes. The fine powder was then heated in an alumina

crucible at 550 °C for 2 hours and subsequently at 700 °C for 2 hours with a heating rate of 5 °C min^{-1} in air atmosphere.

3.3 Characterization of $Li_{1.5}Al_{0.5}Ti_{1.5}(PO_4)_3$ powders and pellets

The morphological characterization was carried out using a Lyra 3 scanning electron microscope (SEM) by Tescan. Elemental composition analysis was performed using a windowless energy dispersive spectrometer (EDS) Extreme by Oxford instruments. To acquire cross section SEM images, pellets have been prepared with an Ar Ion Milling IM4000 Plus (Hitachi), using a 6 kV ion beam energy and a fast 30 ° rotation for 4 hours.

X-ray diffraction was performed using a high temperature X-ray diffractometer (HTXRD) by Rigaku, equipped with a CuKα radiation source. A mixture of Li_2CO_3, Al_2O_3, TiO_2, and $(NH_4)_2HPO_4$ was heated at 3 °C/min from room temperature to 700 °C (dwelling time: 2 hours) in ambient atmosphere. Scanning was performed in 0.04 ° steps at a 6.14 °/min rate.

Electrochemical impedance spectroscopy (EIS) was carried out using a BioLogic VMP potentiostat/galvanostat by applying an AC perturbation of 5 mV in a frequency range of 1 MHz–50 mHz from 20 to 80 °C. Prior to EIS measurements, pellets have been prepared by hot-pressing 0.75 g of LATP powders at 56 MPa and 750 °C for 1 hour between graphite foils using a titanium-zirconium-molybdenum die. They were then placed between stainless steel blocking electrodes in 2032-type coin cells.

Density values of aLATP and rLATP hot-pressed pellets were calculated using the following equation:

$$d\ (\%) = \left(\frac{wv}{d_{th}}\right) \times 100$$

where w and v are the weight and the volume of the sample respectively, and d_{th} is the theoretical density of LATP (estimated to be equal to 2.9 g cm^{-3}).

3.4 Synthesis of electrospun NASICON nanofibers

First, the precursor materials and a polymer carrier are dissolved in a suitable solvent system to achieve a stable and clear precursor solution. Then, the solution is electrospun by a NanoNC eSrobot machine to deposit the precursor fibers onto a collector. Finally, the precursor fibers are calcined to crystallize

the final product in the form of ceramic fibers and simultaneously remove the remnant volatile components, the organic side groups and the polymer carrier.

3.4.1 Synthesis of $Li_{1.3}Al_{0.3}Ti_{1.7}(PO_4)_3$ nanofibers

In a typical procedure, 160 mg of PVDF−HFP and stoichiometric amounts of lithium nitrate (3.64 mmol, 0.276 g), aluminum nitrate (0.84 mmol, 0.315 g), and PPA (8.40 mmol, 1.328 g) were added to 8 mL of DMF:THF (1:1 v/v) and dissolved by magnetically stirring the solution overnight. A stoichiometric amount of titanium butoxide (4.76 mmol, 1.62 mL) was then added to the main solution, after being previously stabilized in 2 equivalents of acetylacetone (0.93 mL). For the sake of reproducibility, all the steps have been carried out inside a dry room. The viscous *sol* was then loaded in a plastic syringe and electrospun by using a 20 μL/min flow rate and applying 15 kV to the needle by means of a high voltage power supply. The fibers were deposited onto a cylindrical rotating collector (300 rpm rotation angular speed) wrapped in aluminum foil and connected to a secondary high-voltage power supply, to apply -2 kV to favor the fiber deposition. A distance of 10 cm between needle and collector was used to let the solvents evaporate. After about 6 hours, a dry white yellowish membrane was collected and dried at 75 °C overnight to remove potential solvent traces. Several circular samples with 20 mm diameter were cut from the dried membrane using a puncher and stacked to achieve a suitable thickness (150-200 μm). The stacked samples were then pressed using a hydraulic press at 150 MPa to reduce their porosity. Both the pressed and the non pressed samples were calcined at 850 °C for 2 h with a heating rate of 5 °C min^{-1} between quartz plates to achieve pressed LATP nanofibers, hereafter referred to as LATPnf and pLATPnf, respectively.

3.4.2 Synthesis of $Li_{1.5}Al_{0.5}Ge_{1.5}(PO_4)_3$ nanofibers

To prepare LAGP nanofibers, 300 mg of PVP and stoichiometric amounts of lithium chloride (3.9 mmol, 0.174g), aluminum chloride (1.3 mmol, 0.173 g), and PPA (7.8 mmol, 1.233 g) were added to 10 mL of EtOH and dissolved by magnetically stirring the solution overnight. A 5 % excess of lithium chloride, compared to the stoichiometric amount, has been used to compensate the lithium loss during high-temperature treatments. A stoichiometric amount of germanium chloride (3.9 mmol, 445 μL) was then added to the precursor solution. All the steps have been carried out inside a glove box (Ar atmosphere, $H_2O \leq 0.1$ ppm, $O_2 \leq 0.1$ ppm). The obtained viscous solution appeared clear and homogeneous with a viscosity suitable for electrospinning. The solution was then loaded in a plastic syringe and electrospun. A flow rate of 15 μL/min was used to push it through a 27-gauge needle, to

which 13 kV were applied by means of a high voltage power supply. The fibers were deposited onto a cylindrical rotating collector (50 rpm rotation angular speed) wrapped in aluminum foil and placed at 10 cm from the needle to let the solvent evaporate. To favor fiber deposition, -2 kV were applied to the rotating collector by means of a secondary high-voltage power supply. After about 6 hours, a dry white membrane was collected and dried at 50 °C overnight to remove potential solvent traces. Several circular samples with 20 mm diameter were cut from the dried membrane using a puncher, stacked to achieve a suitable thickness (100–200 μm), placed between Si_3N_4 plates and then calcined at 700, 800 and 900 °C for 2 h with a heating rate of 5 °C min^{-1} under constant air flow. The samples are hereafter referred to as LAGP 700, LAGP 800 and LAGP 900.

3.4.3 Synthesis of $Li_{1.5}Al_{0.5}Ge_{1.5-x}Ti_x(PO_4)_3$ nanofibers

Stoichiometric amounts of lithium chloride (1.95 mmol, 0.0868 g), aluminum chloride (0.65 mmol, 0.0867 g), and PPA (3.9 mmol, 0.6165 g) were added to 5 mL of EtOH and dissolved by magnetically stirring the solution overnight. A 5 % excess of lithium chloride, compared to the stoichiometric amount, has been used to compensate the lithium loss during high-temperature treatments. Stoichiometric amounts of germanium chloride and titanium butoxide were then added to the precursor solution to achieve 3 different Ge:Ti molar ratios, i.e. 1.4:0.1, 1.3:0.2 and 1.2:0.3. Titanium butoxide has been previously stabilized in 2 equivalents of acetylacetone. All the steps have been carried out inside a glove box (Ar atmosphere, $H_2O \leq 0.1$ ppm, $O_2 \leq 0.1$ ppm). The obtained pale-yellow solution appeared clear and homogeneous with a viscosity suitable for electrospinning. The solution was then loaded in a plastic syringe and electrospun at a flow rate of 10–15 μL/min. A 25-gauge needle was used, to which a 13–15 kV voltage was applied by means of a high voltage power supply. The fibers were deposited onto a cylindrical rotating collector (50 rpm rotation angular speed) wrapped in aluminum foil and placed at 10 cm from the needle to let the solvent evaporate. To favor fiber deposition, -2kV were applied to the rotating collector by means of a secondary high-voltage power supply. Electrospinning has been carried out at a constant temperature of 20 °C and a relative humidity of 40%. After about 4 hours, a dry white to pale-yellow membrane was collected and dried at 50 °C overnight to remove potential solvent traces. Several circular samples with 16 mm diameter were cut from the dried membrane using a puncher, stacked and placed between Si_3N_4 plates. Then they were calcined at 700 °C for 2 h with a heating rate of 5 °C min^{-1} under constant air flow. According to the Ti content, i.e. 0.1, 0.2 or 0.3, the ceramic samples are referred to as LAGTP01, LAGTP02 and LAGTP03.

3.5 Fabrication of PEO-LiTFSI-NASICON nanofibers composite polymer electrolytes

First, 0.6 g of PEO and 0.3 g of LiTFSI were dissolved in 3.1 g of ACN, resulting in an EO/Li+ ratio of 13:1. Then, various amounts of LAGP 700 nanofibers, i.e. 1, 5, 10 and 20 wt.% of the weight of the final dry product, were added as fragments and magnetically stirred until completely dispersed in the form of fibers. The viscous solution was then cast onto a stainless-steel foil using an automatic film coater and dried at 50 °C for 12 h to achieve a PEO-LiTFSI-LAGP nanofibers composite electrolyte, hereinafter referred to as CE-LAGPf followed by the percentage amount of fibers. A filler-free PEO-LiTFSI electrolyte as well as a PEO-LiTFSI-LAGP particles composite electrolyte were prepared by following the same procedure for the sake of comparison. They are hereinafter called PE and CE-LAGPp respectively. The same procedure has been used to prepare also composite polymer electrolytes based on LAGTP fibers. A 10 wt.% amount of LAGTP01, LAGTP02 and LAGTP03 (in respect to the weight of the final dry product) was added to the polymer matrix, to achieve PEO-LiTFSI-LAGTP nanofibers composite electrolytes, hereinafter referred to as CE-LAGTP followed by the content of Ti. For the sake of comparison, PE, CE-LAGPf and a specifically prepared composite electrolyte with $Li_{1.5}Al_{0.5}Ti_{1.5}(PO_4)_3$ nanofibers, were selected. All the steps needed to prepare the electrolytes have been carried out inside a dry room.

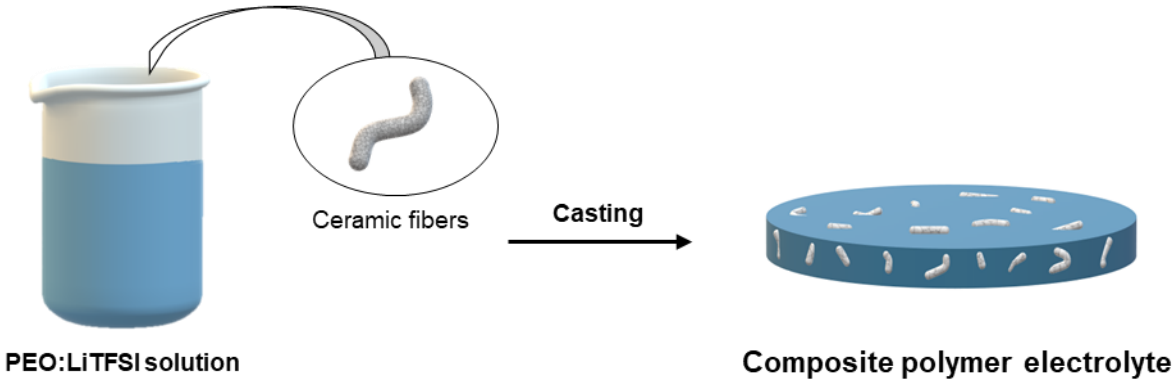

Figure 3.1 Schematic illustration of the preparation of a composite polymer electrolyte with ceramic fibers as fillers.

3.6 Characterization of ceramic nanofibers and composite electrolytes

Porosity values of ceramic nanofibrous samples were calculated using the following equation:

$$p(\%) = 100 - \left[\left(\frac{wv}{d_{th}}\right) \times 100\right]$$

where w and v are the weight and the volume of the sample respectively, and d_{th} is the theoretical density of the materials, estimated to be equal to 2.9 and 3.49 g cm^{-3} respectively for LATP and LAGP.

X-ray diffraction (XRD) patterns were acquired using a Rigaku SmartLab or a Rigaku MiniFlex X-ray diffractometer equipped with a Cu K_α rotating anode (operating at 40 kV and 15-150 mA) and D\teX Ultra 1D silicon strip detector. The diffraction patterns were collected at room temperature in the Bragg–Brentano geometry over the angular range: $2\theta = 10°$-$100°$, with a step size of 0.01°. XRD data analysis was carried out using PDXL 2.8.4.0 software from Rigaku.

Scanning electron microscopy (SEM) images and energy dispersive X-ray spectra (EDS) were acquired using a Hitachi FlexSEM SU1000 scanning electron microscope and a Hitachi SU7000 equipped with an Ultim Max Oxford Instrument EDS at different accelerating voltages (5 kV–20 kV). Prior to the observation with the FlexSEM SU1000, the samples were sputter-coated with a thin layer of gold (ca. 3 nm) to increase the electronic conductivity.

^{7}Li, ^{27}Al and ^{31}P solid-state Magic Angle Spinning (MAS) NMR spectra were recorded at room temperature in 500 MHz WB Bruker AVANCE NEO NMR spectrometer (Larmor frequency of 194.38, 130.33 and 202.48 MHz for ^{7}Li, ^{27}Al and ^{31}P, respectively) equipped with 4 mm triple resonance probe. Single pulse NMR experiments were used to acquire MAS NMR spectra at a spinning speed of 4 kHz for ^{7}Li and of 15 kHz for ^{27}Al and ^{31}P. 16 scans with $\pi/2$ pulse of 3 μs and relaxation delay of 10 s were collected for ^{7}Li NMR. 64 scans with $\pi/2$ pulse of 2.85 μs and relaxation delay of 10 s were collected for ^{27}Al NMR. 16 scans with $\pi/2$ pulse of 2.3 μs and relaxation delay of 100 s were collected for ^{31}P NMR. The fitting of ^{7}Li NMR spectra was done with the Bruker Topspin 4.1 build-in module SOLA.

High-resolution transmission electron microscopy (HRTEM) images and annular dark-field scanning electron microscopy (ADF-STEM) images were carried out using a Talos F200S G2 microscope (Thermo Fischer Scientific) working at 200 kV. Energy-dispersive X-ray spectroscopy (EDS) maps were acquired with a double windowless silicon drift detector.

Three-dimensional electron diffraction (3D ED)[42] data were collected with a Zeiss Libra TEM operating at 120 kV and equipped with a LaB_6 source. Data acquisition was performed in STEM mode after defocusing the beam to achieve parallel illumination of the sample. A beam size of about 150 nm in diameter was obtained by inserting a 5 μm C2 condenser aperture.[43] The data was recorded using an ASI Timepix detector, able to register the arrival of single electrons and to deliver a pattern that is

virtually background-free. 3D ED data were taken from six fragments belonging to the main trigonal phase. Fragments had a typical pseudo-hexagonal platelet habit and diameter comparable with the beam size. 3D ED data were collected with a precessing beam (precession angle 1°), in fixed steps of 1° and for a total range from 90° to 116°. The camera length was 180 mm, corresponding to a maximum resolution of 0.75 Å. The data was analyzed using ADT3D software.[44] The *ab initio* structure solution was obtained by direct methods implemented in the software SIR2014,[45] using a kinematical approximation: I_{hkl} proportional to F^2_{hkl}.

X-ray photoelectron spectra (XPS) were acquired using a VG Escalab 220i-XL spectrometer equipped with a hemispherical analyzer, applying a Twin Anode X-Ray Source. The binding energy was calibrated by reference to the C 1s peak (284.8 eV).

Thermogravimetric analyses (TGA) have been performed using a TA instruments TGA 550 analyzer in a temperature range of 25-640 °C with a heating rate of 10 °C/min under N_2 atmosphere.

Electrochemical impedance spectroscopy (EIS) was carried out on three samples of each kind with a BioLogic VMP potentiostat/galvanostat by applying an AC perturbation of 5 mV in a frequency range of 1 MHz–50 mHz from 20 to 80 °C. Prior to EIS measurements, ceramic samples were sputter-coated with a thin layer of Pt (ca. 30 nm) on both sides to improve the electrical contact. All the samples were then placed between stainless steel blocking electrodes in 2032-type coin cells.

4 Influence of rutile and anatase TiO_2 precursors on the solid-state synthesis of a $Li_{1.5}Al_{0.5}Ti_{1.5}(PO_4)_3$ ceramic electrolyte

This chapter is based on the paper "*Influence of rutile and anatase TiO_2 precursors on the synthesis of a $Li_{1.5}Al_{0.5}Ti_{1.5}(PO_4)_3$ electrolyte for solid-state lithium batteries*" published on the *Journal of the Electrochemical Society, 2022, 169, 040515*.[205]

4.1 Background

As largely discussed in **Chapter 1**, the replacement of flammable liquid electrolyte with inorganic solid electrolytes is beneficial not only for the safety of the final battery, but also for its energy density, since enables the use of metallic lithium as anode. Among all the ceramic materials proposed, the NASICON-like Al-doped $LiTi_2(PO_4)_3$ (LATP) is one of the most promising because of a high ionic conductivity, in the order of 10^{-4} S cm^{-1}, and a good chemical stability in ambient conditions. Moreover, it can be synthesized starting from relatively inexpensive precursor materials through different processes. A facile method to synthesize NASICON-like LATP is by a solid-state approach, which consists in mixing oxide-based precursor materials and alternate ball-milling and high temperature steps until achieving a high purity phase. This category of synthesis methods is characterized by high-energy and expensive steps; hence, they are considered less suitable for a potential industrial production. It is thus desirable to optimize the procedure to achieve a more efficient synthesis.[23,206]

In this chapter, we investigated how different polymorphs of TiO_2 can affect the synthesis and the properties of a $Li_{1.5}Al_{0.5}Ti_{1.5}(PO_4)_3$ electrolyte. Specifically, we synthesized LATP by a solid-state method using anatase TiO_2 as Ti source, and hereafter referred to as aLATP. We replicated the same synthesis except using rutile TiO_2 instead (the final product denoted rLATP). We studied the crystallization of both materials using *in situ* HTXRD. By combining HTXRD data, SEM images and EIS results, we evaluated the influence of the two phases of TiO_2 on the synthesis, and on the properties and performance of the synthesized LATP electrolytes.

4.2 Results and discussion

SEM imaging was used to investigate the morphology of rLATP and aLATP (**Figure 4.1**). Both samples consist of cubic and irregular crystallites, which tend to form agglomerates of several microns in size. The irregular shape is related to the temperature used for the synthesis, i.e. 700 °C.[207,208] When

a temperature of 950 °C is used, resulting crystals are predominantly cubic shaped in both samples (**Figure 4.1c,f**). EDS analysis of both samples confirmed the formation of LATP with an even elemental distribution without apparent segregation of secondary phases (**Figure 4.1g,h)**.

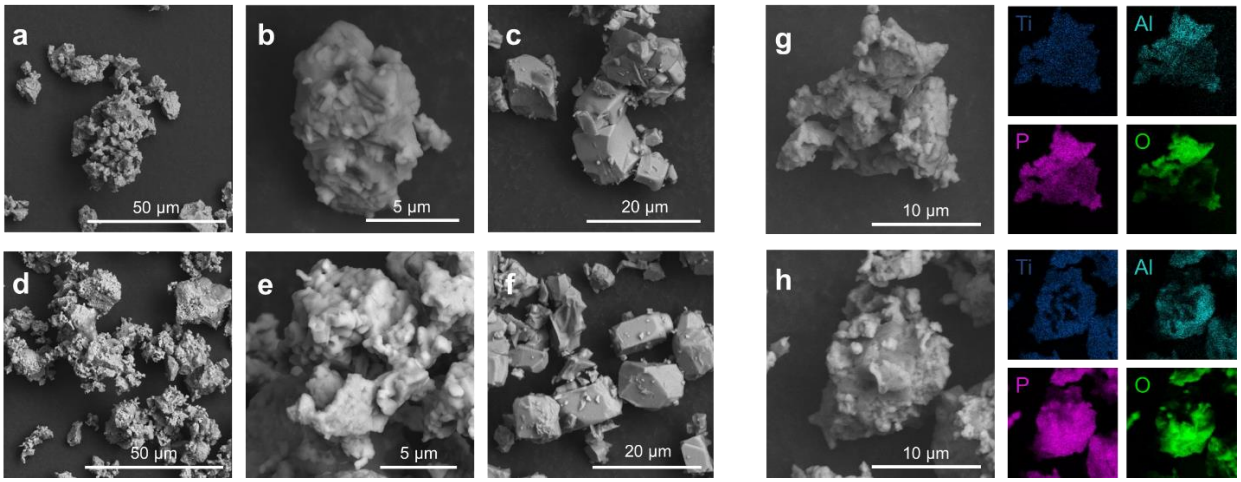

Figure 4.1 SEM images of aLATP synthesized at (a,b) 700 °C and (c) 950 °C and rLATP synthesized at (d,e) 700 °C and (f) 950°C. SEM-EDS analysis and corresponding elemental mapping of (g) aLATP and (h) rLATP.

HTXRD has been performed on both samples to have a deep insight on LATP crystallization and how it is influenced by the presence of rutile and anatase phases. The evolutions of XRD patterns of both samples are displayed in **Figure 4.2**. The initial XRD patterns differ because of the Ti precursor used (**Figure 4.3**). When the temperature increases, the XRD patterns of both samples evolve: the peaks ascribed to intermediate product, such as Li_3PO_4 and biphosphammite $(NH_4)H_2PO_4$ start to appear between 100 and 200 °C in the patterns of both samples.

Then, peaks corresponding to precursor materials, rutile and anatase included, start to decrease in intensity and LATP rhombohedral phase appears. Specifically, in the diffractogram of aLATP acquired at 378 °C, peaks corresponding to the NASICON phase (space group $R\bar{3}c$) of $Li_{1.2}Al_{0.2}Ti_{1.8}(PO_4)_3$ (PDF card: 01-084-5450) started appearing. In a similar temperature range, no peaks are detected in the rLATP pattern, as displayed in **Figure 4.4a**. When the temperature reaches 583 °C, we observed the appearance of the LATP phase also in the rLATP pattern, while in the aLATP pattern collected in the 592-622 °C range the corresponding peaks are already very intense (**Figure 4.4b**).

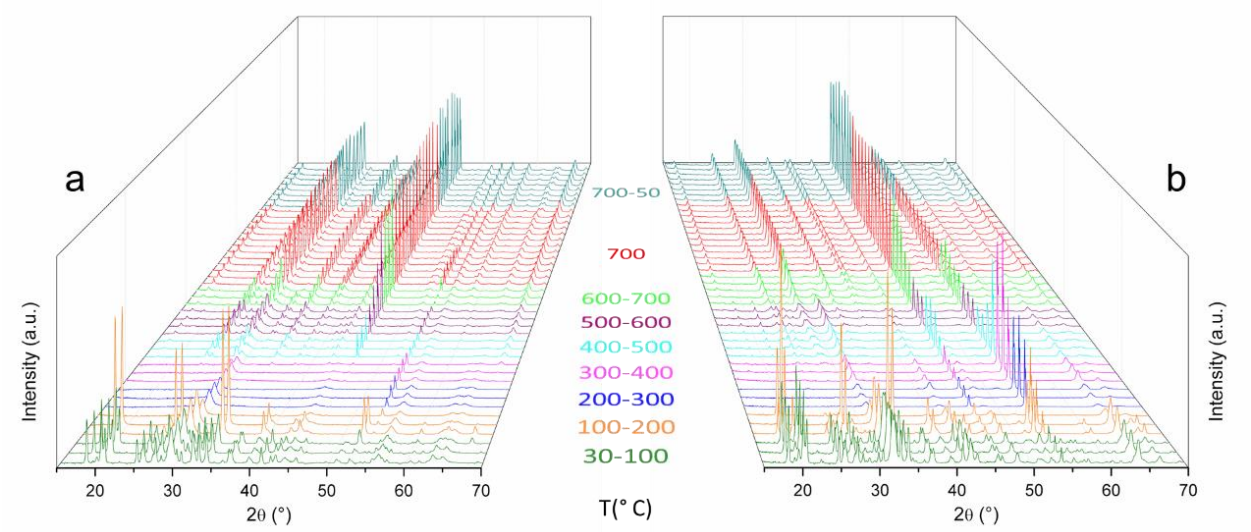

Figure 4.2 HTXRD analyses of (a) aLATP and (b) rLATP performed in a temperature range of 30-700 °C with a dwell time of 2 hours. XRD patterns acquired while cooling down the samples from 700 to 50 °C are displayed too.

When the temperature reached 700 °C, aLATP phase is characterized by a higher degree of crystallinity and less impurity phases than rLATP. However, after dwelling at 700 °C for 2 hours, rLATP become purer and more crystalline, displaying only a few low-intensity peaks ascribable to $Li_4P_2O_7$ and Li_3PO_4 while, several peaks associated with $AlPO_4$ and $Li_4P_2O_7$ have been identified in the aLATP diffractogram acquired after the 2-hour dwelling at 700 °C (**Figure 4.4c,d**). Both samples were cooled down to room temperature for the final XRD analyses. The patterns did not change significantly from their 700 °C counterparts, and this verifies their stability (**Figure 4.4c,d**).

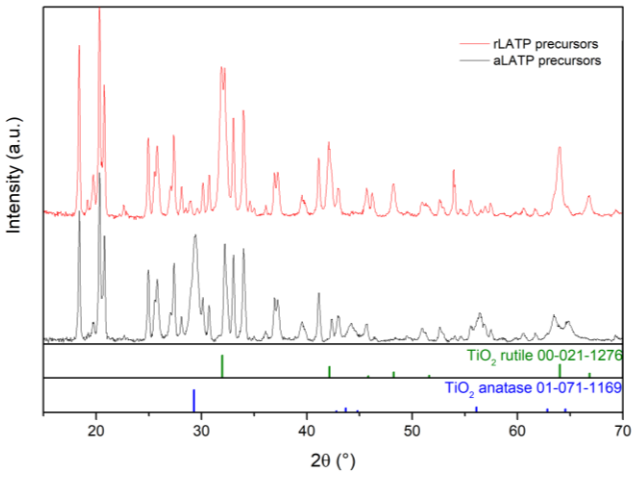

Figure 4.3 XRD patterns of the precursor materials used for the synthesis of aLATP and rLATP.

At 300 °C, only TiO_2 XRD patterns appear in the samples. This indicates that at 300 °C all the precursors have become amorphous except for TiO_2, and that TiO_2 is the last one to react (**Figure 4.5**). The use of anatase or rutile phase of TiO_2 does not affect the reaction routes of the synthesis. Between 127-327 °C, the formation enthalpy and Gibbs energy of anatase TiO_2 are about 6.2kJ/mol higher than those of rutile TiO_2.[209] Assuming an Arrhenius-type reaction rate, this difference causes a four-fold faster kinetics for anatase TiO_2 reactions at 327 °C, in good agreement with our observation that LATP appears sooner with anatase TiO_2 than with rutile TiO_2.

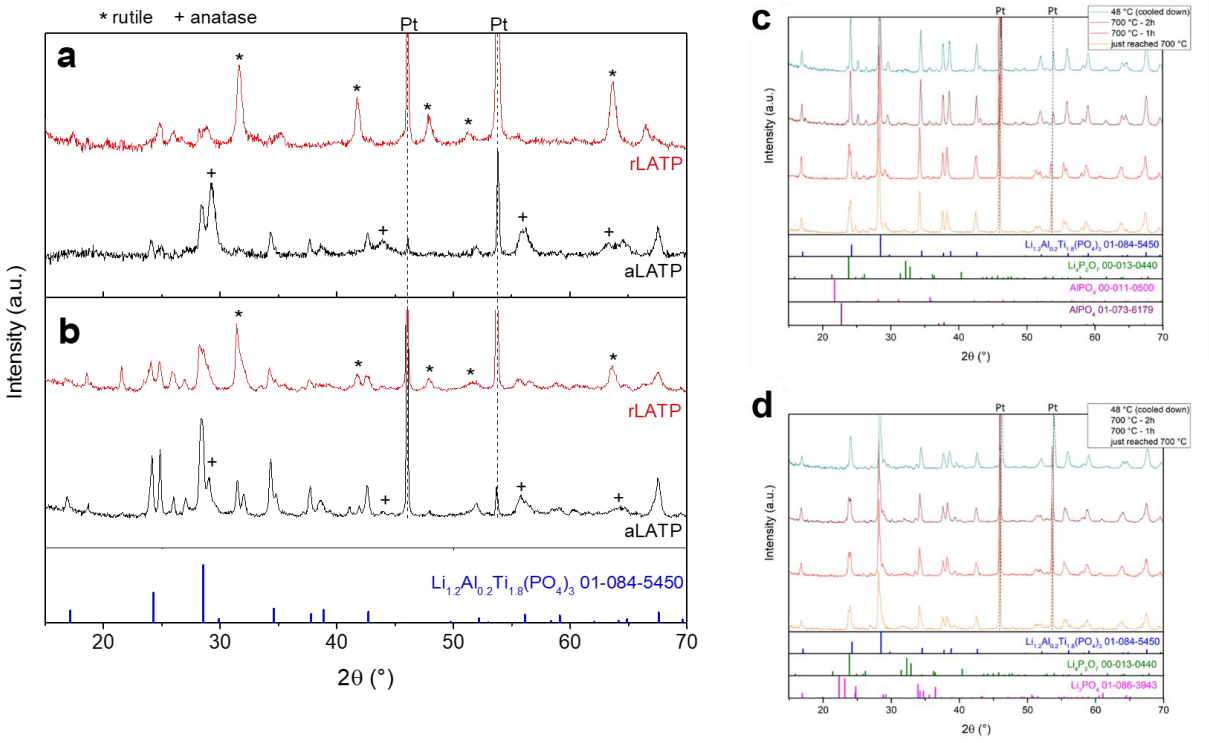

Figure 4.4 XRD patterns acquired in a temperature range of (a) 378-408 °C for aLATP and 370-400 °C for rLATP, and (b) 592-622 °C for aLATP and 583-613 °C for rLATP. ((*): TiO_2 rutile; (+): TiO_2 anatase; Pt peaks derive from the crucible). XRD patterns acquired on (c) aLATP and (d) rLATP, when the temperature just reached 700 °C, after dwelling at the same temperature for 1 and 2 hours, and after cooling down.

Pellets have been prepared with both aLATP and rLATP by hot-pressing the corresponding powders at 750 °C under 56 MPa. The density of both aLATP and rLATP pellets, estimated by using their weight and dimensions, resulted equal to 90 % of the theoretical value. To evaluate the ionic conductivity, each sample has been painted with silver ink and placed in a coin cell between stainless steel blocking electrodes (**Figure 4.6a**).

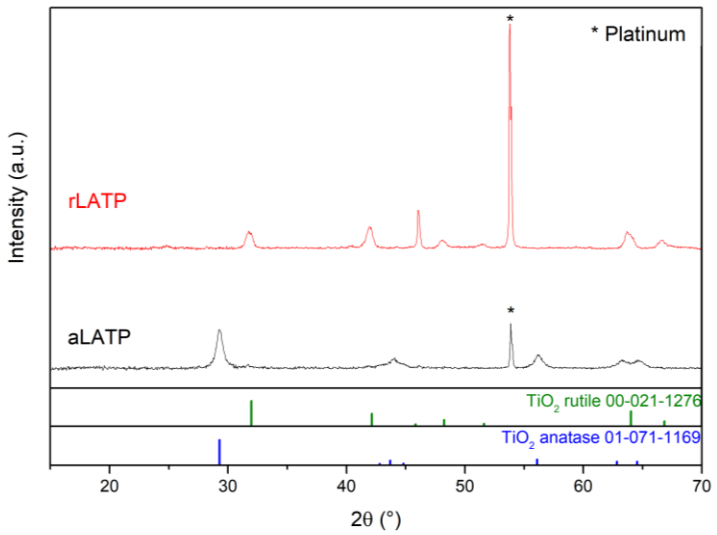

Figure 4.5 XRD patterns acquired in a temperature range of 285-315 °C for aLATP and 277-307 °C for rLATP. ((*): platinum).

EIS spectra were acquired in the 20-80 °C temperature range. The resulting Nyquist plots consist of two semicircles: the first one was acquired at high frequency, while the second one, can be observed in the mid-low frequency region and appears small and partly convoluted with the double layer capacitance arising at the electrodes. Similar findings were reported for hot-pressed LLZO by Tenhaeff et al., who were not able to associate this small semicircle with any distinct phenomenon.[210] Thus, we selected an equivalent circuit made of resistors (R) and constant phase elements (CPE), which represent the resistive and the non-ideal capacitive contributions of each phenomenon. Specifically, the equivalent circuit $R_0(R_{gb}CPE_{gb})(R_{low}CPE_{low})CPE_{el}$ depicted in **Figure 4.6b**, was used to model the experimental data of both samples, where R_0 is the circuit resistance, external to the sample, R_{gb} and CPE_{gb} are associated with the ionic transport at grain boundaries, R_{low} and CPE_{low} represent the low-frequency unidentified semicircle and CPE_{el} is related to the double layer capacitance of the electrodes. We can confidently exclude the presence of intra-grain contributions, since it appears as a scientific consensus that the bulk conductivity of NASICON materials can be identified only at very low temperatures, from -100 to 10 °C.[85,87,211,212] Moreover, the capacitive contribution of the first semicircle is equal to 10^{-9} F, which is within the typical range of grain boundary phenomena.[213] On these premises, we can evaluate the total ionic conductivity (σ), which mainly derive from the ionic transport occurring at grain boundaries for both samples. **Figure 4.6c** displays the representative Nyquist plots resulting from EIS analyses carried out at 20, 50 and 80 °C. By fitting them, we can calculate the total ionic conductivity of both aLATP and rLATP pellets. From the resulting values,

shown in **Figure 4.6d** in the form of Arrhenius plot, aLATP appears more conductive than rLATP throughout the temperature range. The slope of the Arrhenius plot expressed in the linear form $\ln(\sigma) = \ln(A) - E_a/RT$, has been used to calculate the activation energy, which corresponds to 0.44 (±0.01) eV and 0.40 (±0.02) eV for aLATP and rLATP, respectively (**Table 4.1**). Both values are in good agreement with those reported in the literature.[212,214] The ionic conductivity of aLATP at 20 °C is equal to 1.5×10^{-4} S cm^{-1}, about twice that of rLATP (8.5×10^{-5} S cm^{-1}).

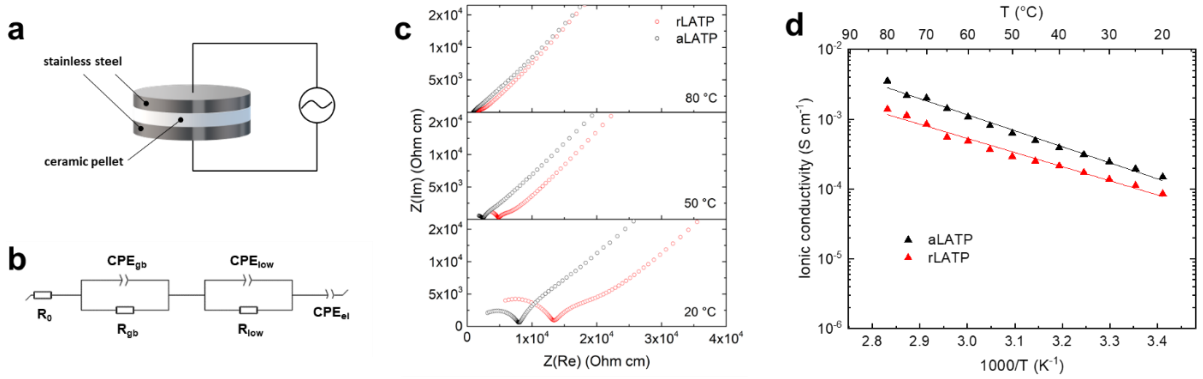

Figure 4.6 (a) Scheme of the setup used for EIS analysis of aLATP and rLATP. (b) Equivalent circuit used for EIS data fitting. Representative (c) EIS spectra at 20, 50 and 80 °C and (d) Arrhenius plot in a temperature range of 20-80 °C of aLATP and rLATP.

This difference is mainly due to a less efficient ionic conduction at the grain boundaries of rLATP. The origin of this different contribution could be related to a slightly different morphology of the particles. As discussed above, no significant differences in the morphology of the crystallites of the two samples have been observed. However, as displayed in **Figure 4.1**, aLATP crystallites appear slightly more uniform in the shape, which could be beneficial to achieve a tighter packing.

Table 4.1 Average grain size, density and ionic conductivity with corresponding activation energy measured at 20 °C of aLATP and rLATP pellets.

	Average grain size (Å)	*Density*	*σ (S cm⁻¹)*	*E_a (eV)*
aLATP	76	90 %	1.5×10^{-4}	0.44 (±0.01)
rLATP	197	90 %	8.5×10^{-5}	0.40 (±0.02)

To verify this hypothesis, we took cross-section SEM images on both aLATP and rLATP hot-pressed pellets. At low magnification (**Figure 4.7a,b**), we did not observe any significant difference between the two pellets. Hence, we acquired high magnification images by selecting the most representative areas of both samples. This allowed us to estimate the local porosity of the pellets, which is strongly

related to the effectiveness of the densification process. Moreover, we can observe the potential presence of fractures, which are detrimental for the achievement of fast ionic conduction. After investigating several areas of both samples, the most representative ones are shown in **Figure 4.7c,d**. While the local porosity is similar in both samples, i.e 9-10 %, which well correlates with the pellets' density, aLATP densification appears more uniform, which ensures a better contact between particles and consequently a more effective Li conduction at the interface. Meanwhile, rLATP is characterized by fractures and larger pores, probably arising from a less efficient packing of the particles during the hot-pressing step. Pores and fractures could stem from the different average particle size calculated from the diffraction data of the pellets. In fact, rLATP is characterized by slightly bigger particles (**Table 4.1**), which can negatively affect its densification process. This phenomenon generates several bottlenecks along the path of Li ions, thus slowing down their transport between the electrodes and negatively affecting the final conductivity of the rLATP pellet. To exclude any potential influence of pellets' composition on the ionic conductivity values, we acquired XRD patterns of both aLATP and rLATP pellets (**Figure 4.7e**).

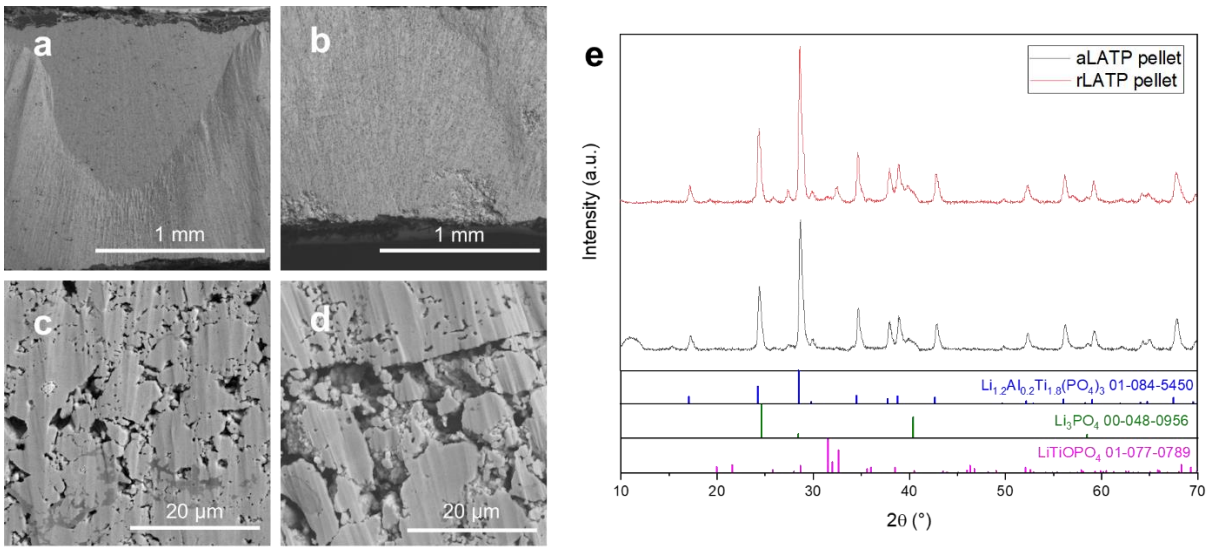

Figure 4.7 Cross-section SEM images of (a,c) aLATP and (b,d) rLATP pellets densified at 750 °C by hot-pressing, acquired after EIS analyses, and (e) corresponding XRD patterns.

We did not observe any unexpected evolution of LATP peaks, however peaks associated with the impurity phases of $LiTiOPO_4$ and Li_3PO_4 were detected in both samples. The peaks appear slightly more intense in the rLATP pattern, which correlates well with its low ionic conductivity measured by EIS. Hupfer et al. reported that small percentages of $LiTiOPO_4$ can be beneficial for the ionic conductivity of LATP, especially when low sintering temperatures are used;[215] however, this

phenomenon was observed with the simultaneous presence of $AlPO_4$ impurity phase, which we did not detect. Since, in our study, both aLATP and rLATP display a similar composition, we can assert that the main contribution to the difference observed in the ionic conductivity behavior is presumably associated with their morphology as demonstrated by cross-section SEM analysis.

4.3 Conclusions

In summary, we investigated the effects of anatase and rutile as Ti source for the solid-state synthesis of a LATP electrolyte. From a morphological point of view, no significant differences were observed in the crystallites of the prepared samples. The crystallization of LATP has been then studied by *in situ* HTXRD. We observed that aLATP starts forming at a lower temperature while rLATP displays less impurity phases. After hot-pressing the corresponding powders, the ionic conductivity of the densified pellets has been measured: aLATP has a higher conductivity, mainly because of a lower grain boundary resistance. Hence, anatase TiO_2 should be chosen for lower synthesis temperature and higher conductivity, while rutile TiO_2 is the choice for purer crystals. Current trends focus on optimizing known solid electrolyte materials rather than searching for alternatives. In this framework, every achievement and detail, e.g. selecting the best precursor materials as well as the proper synthesis temperature, can be helpful to lower the cost and improve the current methods. This aspect is crucial for the industrial scale up of solid electrolyte synthesis, which is a mandatory step for the future deployment of all-solid-state batteries. We thus believe that our findings can represent an important contribution towards the development of more efficient and less expensive syntheses for Ti-based solid electrolytes.

5 Effect of pressure on the properties of solid electrolyte made of electrospun ceramic $Li_{1.3}Al_{0.3}Ti_{1.7}(PO_4)_3$ nanofibers

This chapter is based on the paper "*Effect of pressure on the properties of a NASICON $Li_{1.3}Al_{0.3}Ti_{1.7}(PO_4)_3$ nanofiber solid electrolyte*" published on *Journal of Materials Chemistry A, 2021, 9, 13688-13696*.[198]

5.1 Background

As introduced in **Chapter 1.4**, recently ceramic one-dimensional (1D) structures have been widely investigated for developing novel solid electrolytes for ASSLBs (**Table 1.2**). Specifically, nanofibers and nanowires have been mainly employed as inorganic fillers for polymer-based composite electrolytes, exhibiting better lithium-ion conduction and mechanical properties compared to their nanoparticle counterparts. Additionally, they have been studied as basis to develop fully ceramic pellets, resulting in denser and better conductive electrolytes. Lancel et al. reported the synthesis of ceramic $Li_{1.4}Al_{0.4}Ti_{1.6}(PO_4)_3$ fibers by electrospinning and subsequent calcination, which have been then used as inorganic component into a hybrid membrane for lithium–air batteries.[197] The ionic conductivity reported for the ceramic membrane (3×10^{-7} S cm^{-1}) is significantly lower than the bulk conductivity value previously achieved for the same structure (10^{-4} S cm^{-1}),[31] because of the typical high porosity of electrospun materials. Here we adapt the synthetic procedure employed by Lancel et al. to achieve the most conductive $Li_{1.3}Al_{0.3}Ti_{1.7}(PO_4)_3$ stoichiometry. With the aim of reducing the porosity of the ceramic membrane, the effect of applying a 150 MPa pressure to the electrospun membrane, prior to the heat treatment has been investigated. We thus report how the pressing process affects the morphology of the membrane as well as the structure and the physico/chemical properties of the ceramic material. Despite the presence of some impurity phases and a less homogeneous substitution of Ti^{4+} by Al^{3+}, the pressed LATP nanofibers showed an increased ionic conductivity and a much smaller activation energy compared to pristine LATP fibers.

5.2 Results and discussion

Using a hydraulic press, various loads have been applied to stacked samples of precursor fibers to identify the value at which the porosity is being reduced without compromising fiber morphology and mechanical integrity of the sample during the heat treatment. A trade-off value was identified at 150 MPa, which reduces the porosity of the ceramic sample from 85 % to 60 % without affecting its

integrity and morphology. Applying a pressure higher than 150 MPa results in a denser sample, which is however more prone to fracture during the heat treatment (**Figure 5.1**). Fractures could arise from a reduced ability to accommodate the decrease in volume, as well as from gaseous side products generated at high temperature trying to escape from the sample. After the pressing step, pLATPnf samples were calcined at 850 °C for 2h with a heating rate of 5 °C min^{-1}. The selected temperature and time allowed to achieve an almost pure LATP phase with the sought NASICON structure, without compromising the fiber shape. The fibers tend to coalesce when severe heating conditions are used, as already reported.[189] The area of the sample has halved during the heating treatment. The observed shrinkage is due to the decomposition and loss of the polymer and organic side products, and to the simultaneous crystallization of LATP. The results presented and discussed below for pLATPnf are compared to those of non-pressed LATP nanofibers samples, simply referred to as LATPnf, which have been prepared by following the same procedure, except for the pressing step.

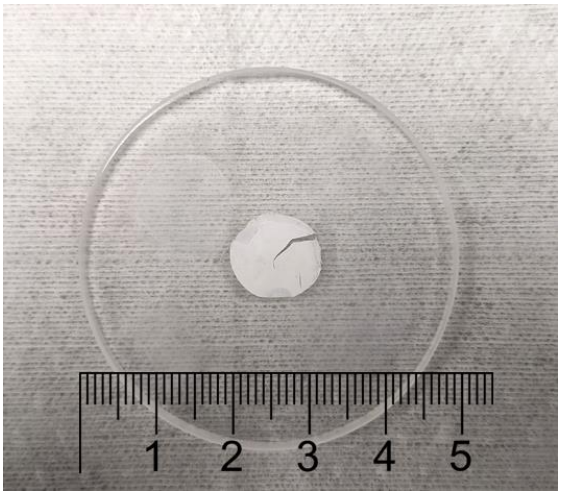

Figure 5.1 LATP fiber sample pressed at 300 MPa and calcined at 850 °C for 2h.

SEM images of LATP precursor fibers, LATPnf and pLATPnf are displayed in **Figure 5.2**. The as spun precursor fibers are characterized by a diameter ranging from 700 nm to 2 μm (**Figure 5.2a**). After calcination, the fiber diameter decreased to a range of 0.4–1 μm (**Figure 5.2b**). LATPnf maintained the 1D morphology because the separation of the fibers ensures that crystal growth occurs only inside each single fiber. This also allows to control the crystallites' size by using the fiber confinement as a template. **Figure 5.2c** clearly shows how the pressure applied to pLATPnf greatly decreases the porosity and thus increases the number of contact points among the fibers, which is beneficial for the ionic conductivity of the final material. In terms of morphology, the nanofibers are still easily discernible, and the coalescence is minimized. However, there is almost no spatial separation

among the nanofibers, hence crystal growth is not as confined as for LATPnf. **Figure 5.2d,e** shows how this affects the final dimension of crystalline domains composing the fibers, ranging from 100 to 250 nm in LATPnf while reaching 600 nm in pLATPnf. A different crystal shape can also be noticed: while LATPnf are composed of cubic-shaped crystallites, typical of the NASICON phase,[208,216,217] pLATPnf are mostly made of spherical crystallites. These structures were previously observed by Schell et al. when temperatures lower than or equal to 800 °C are employed for a 10h calcination step of sol–gel synthesized LATP. Although the temperature used for pLATPnf is higher than the reported one, the lower time of calcination (2h) could have played an important role in the crystal growth, thus affecting the shape of crystalline domains.[207]

XRD patterns of both LATPnf and pLATPnf are shown in **Figure 5.2f**. The main peaks in both samples are ascribable to the rhombohedral NASICON-like structure (space group $R\bar{3}c$) of $Li_{1.3}Al_{0.3}Ti_{1.7}(PO_4)_3$ (PDF card 00-066-0868). The absence of an Al-containing secondary phase is the first evidence of the successful aliovalent substitution of Ti^{4+} by Al^{3+}. The substitution is also confirmed by the lattice parameters, shown in **Table 5.1**, which are lower than those reported for $LiTi_2(PO_4)_3$, due to the smaller size of Al^{3+} compared to Ti^{4+}.[31] In particular, the lattice parameters measured for pLATPnf are in excellent agreement with those reported by Aono et al. for $Li_{1.3}Al_{0.3}Ti_{1.7}(PO_4)_3$ stoichiometry, while for LATPnf, the *c* parameter is larger. Since the variation of *c* parameter with Al content is more important than that of *a*/*b* parameter, a higher value could suggest a slightly lower degree of substitution.[31]

Table 5.1 Cell parameters of LATPnf and pLATPnf compared to $LiTi_2(PO4)$.

	a(A), b(A)	*c(A)*
$LiTi_2(PO_4)_3$ [31]	8.512	20.858
LATPnf	8.4906(3)	20.8518(10)
pLATPnf	8.49266(18)	20.8068(7)

As shown in **Figure 5.2f**, neither secondary phases nor impurity phases were detected in the LATPnf pattern, which thus consists of pure LATP fibers. Low intensity peaks were instead detected in the pLATPnf pattern and can be attributed to small amounts of TiP_2O_7 and $LiTiPO_5$. They are common side products in LATP high temperature synthesis procedures, resulting both from the decomposition and incomplete reaction of starting materials.[197,218,219] $LiTiPO_5$ has a similar stoichiometry and is often considered a reaction intermediate of $LiTi_2(PO_4)_3$.[220,221]

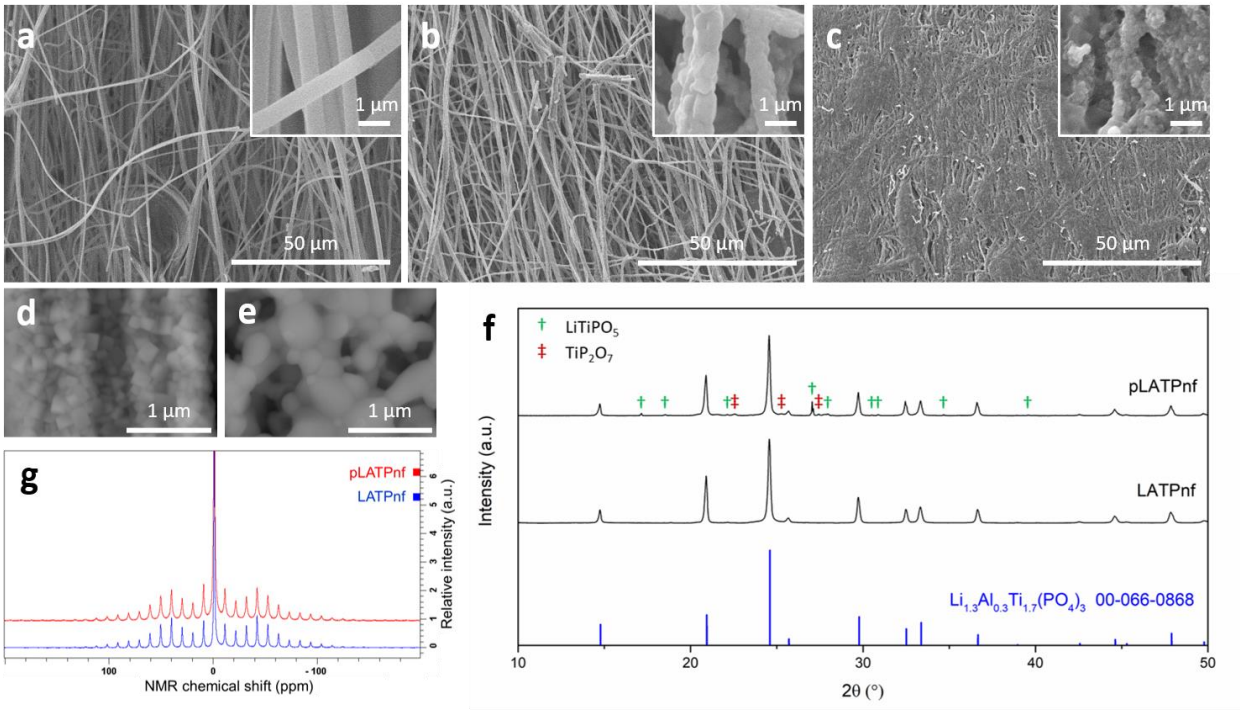

Figure 5.2 SEM images of (a) LATP precursor fibers, (b) LATPnf and (c) pLATPnf (corresponding magnification in the inset). High magnification SEM images of crystallites composing (d) LATPnf and (e) pLATPnf. (f) XRD patterns of pLATPnf and LATPnf. (†: $LiTiPO_5$; ‡: TiP_2O_7). (g) ^7Li MAS NMR spectra of pLATPnf and LATPnf.

The formation of TiP_2O_7, along with TiO_2, could be also ascribed to a partial volatilization of Li_2O during the heating process,[218] however the mild conditions used are not sufficient to cause such loss of lithium. No peaks related to $AlPO_4$ and TiO_2 were detected, in accordance with previous reports on sol–gel syntheses of LATP.[222,223] This aspect confirms the successful aliovalent substitution and suggests that no thermal decomposition of LATP structure occurred. As reported elsewhere, the high porosity of electrospun precursor fibers is beneficial for decreasing the time and temperature of calcination.[176,224] This was also confirmed by LATPnf synthesis, which required a calcination step of 2 hours at 850 °C to achieve a pure NASICON-like phase, meaning a less severe heat treatment compared to reported studies on sol–gel synthesis of bulk LATP.[89,222,223] The impurity phases detected in pLATPnf are probably related to its higher density, which requires more severe heating conditions to complete the synthesis of the final product. Increasing temperature and/or time of calcination would have surely been beneficial in terms of purity, however, as mentioned above, fibers undergo coalescence when severe heating conditions are used, leading to the complete loss of their morphology. For the sake of comparison, we decided to maintain the same heating conditions for both samples, as a trade-off between morphology and purity.

To investigate the lithium location within the NASICON structure, ^{7}Li MAS NMR spectra of LATPnf and pLATPnf were recorded (**Figure 5.2g**). Spectra of both samples can be described as a combination of two components centered at -1.1 ppm with quadrupolar coupling constant (C_Q) values equal to 45 kHz and 5 KHz and η = 0.1. Based on data reported by Arbi et al. those signals can be assigned to Li ions located at M1 and M3 sites.[225] The relative integral intensities of the components in both samples are 85:15, respectively. We did not observe any substantial differences between LATPnf and pLATPnf, thus the pressure does not appear to affect lithium location within the structure.

To better understand how the different phases are arranged in the pLATPnf fiber morphology, we acquired EDS maps of both LATPnf and pLATPnf and the results are displayed in **Figure 5.3**. More in detail, **Figure 5.3a** shows the morphology of a single LATP fiber with the corresponding mapping of the main elements, namely Al, Ti, P and O, showing that an even elemental distribution and thus a homogenous phase were obtained for the LATPnf sample. Conversely, a less uniform elemental distribution is observed in the pLATPnf one (**Figure 5.3b,c**). Specifically, Al and Ti content vary widely, meaning that different stoichiometry and/or phases are present in the sample, in agreement with XRD patterns. Given that no Al-containing phase has been detected by XRD analysis, the uneven Al distribution discernible in **Figure 5.3b** is presumably related to different degrees of aliovalent substitution of Ti^{4+} by Al^{3+}.

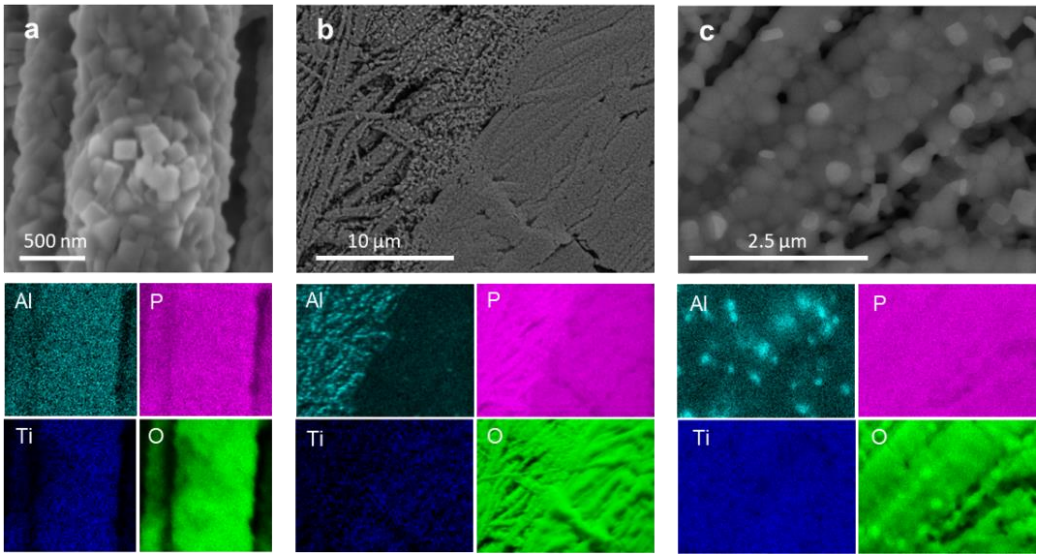

Figure 5.3 SEM-EDS analysis and corresponding elemental mapping of (a) LATPnf and (b,c) pLATPnf.

This is confirmed by the opposite pattern displayed for the Ti distribution in the corresponding mapping. The Al-content across the sample is greatly influenced by the density of the fibers. **Figure 5.3b** proves that Al substitution is less significant in denser areas, where consequently, a higher Ti content is observed. Thus, less dense areas are mainly made of Al-rich LATP, whereas denser ones, which are poor in Al, presumably contain also TiP_2O_7 and $LiTiPO_5$ impurity phases. As already reported, the confined space of the fiber reduces the diffusion distance of precursor materials, thus being beneficial to achieve an even distribution of the ionic species during the calcination step.[176] This advantageous effect is minimized by some margin in the pressed areas, where fibers are often clustered, thus partially resembling the bulk material.

HAADF-STEM imaging was performed to investigate the morphology of the individual fibers, and the results are shown in **Figure 5.4**, which displays a single LATP polycrystalline fiber, composed of small cubic-shaped crystallites as already detected by SEM imaging (**Figure 5.2d**). Darker areas are attributed to pores formed along the fiber during the calcination step. A small cluster of fibers, isolated from the pLATPnf sample, has also been investigated (**Figure 5.4b**). Crystalline domains are less evident here, probably due to the larger thickness of the cluster compared to single fibers. No dark spots are observed in the analysis, proving that the pressure applied before the calcination step affects both intra-fiber and inter-fiber porosity. **Figure 5.4c** shows a HRTEM image acquired on the border of a LATPnf crystallite. The good crystallinity for the whole sample as observed by XRD is here confirmed within a single grain. The fast Fourier transform (FFT) pattern (inset in **Figure 5.4c**) shows the reflections corresponding to the [1,1,1] orientation of the NASICON structure.

Three-dimensional electron diffraction data, displayed in **Figure 5.4d,e**, confirmed a rhombohedral structure. No reflection indicating lattice modulation was observed. Extinctions were consistent with the $R\bar{3}c$ space group. Crystal structure solution confirmed the model reported by Aono et al.,[31] based on a framework of TiO_6 octahedra and PO_4 tetrahedra. Potentials likely corresponding to Li atoms in position 6*b* (0,0,0) were clearly visible in the *ab initio* solution.

XPS spectra were acquired to further explore the elemental composition of LATP fibers. Survey spectra of LATPnf and pLATPnf samples (**Figure 5.5a**) show the presence of the base elements, i.e. Ti, Al, P and O. Al doping in LATPnf sample corresponds to the desired stoichiometry, since the ratio of the atomic concentrations of Al and Ti is close to 1:5, while a 2:5 ratio results from pLATPnf analysis.

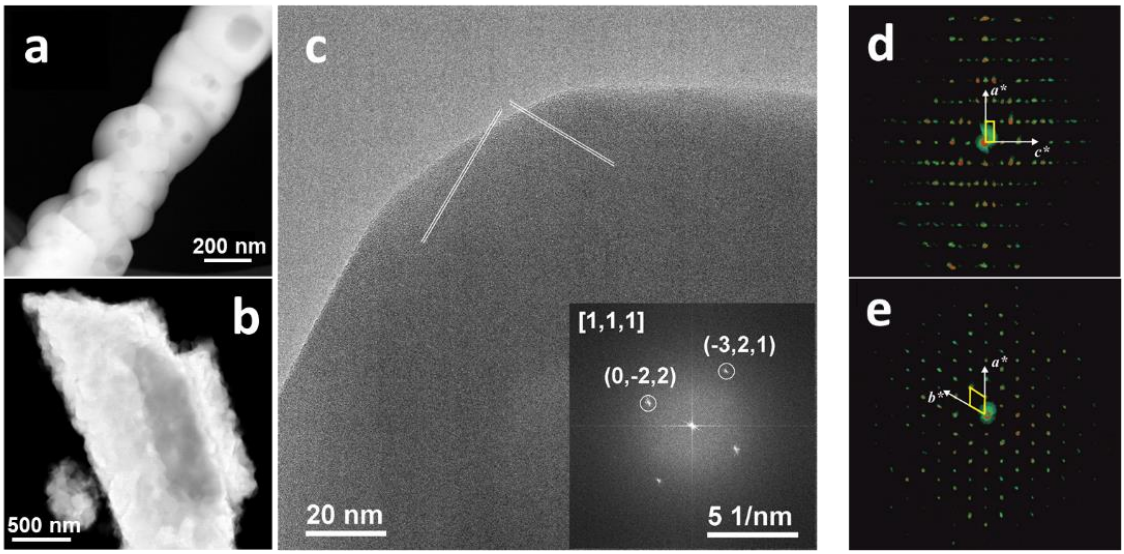

Figure 5.4 HAADF-STEM image of (a) an isolated fiber of LATPnf and (b) a cluster of fibers of pLATPnf. (b) HRTEM image of a crystallite close to [1, 1, 1] orientation and corresponding FFT image (inset). Reconstruction of a 3D ED data set projected along (d) *b and (e) *c**. Projections of the reciprocal vectors are sketched in white and cell edges are sketched in yellow. Extinctions *okl*: *l* = 2*n* are due to the *c*-glide plane.**

Since XPS provides quantitative information of the sample's surface composition, the higher Al:Ti ratio observed for pLATPnf could result from the uneven elemental distribution already observed during the EDS analysis. This unevenness is presumably related to the pressure step which locally increased the density of the sample. The higher density hinders the substitution of Ti^{4+} by Al^{3+}, causing the presence of Al-free impurity phases, i.e. TiP_2O_7 and $LiTiPO_5$. Accordingly, less dense areas are richer in Al. High-resolution spectra of Al 2p and Ti 2p are displayed in **Figure 5.5b**. As expected, Al 2p spectra show only one peak at a binding energy of ~74 eV.[56] For both samples the Ti 2p spectrum shows two evident peaks. Each of them has been deconvoluted into two peaks. Those at higher binding energy, centered at ~460 eV and ~466 eV, correspond to Ti^{4+} $2p_{3/2}$ and Ti^{4+} $2p_{1/2}$ respectively.[83,226] At lower binding energies, i.e. ~463 eV and ~458 eV, two small peaks can be attributed to Ti^{3+}.[83,226] According to the intensity of the peaks, in both samples the amount of Ti^{3+} was about 10% and presumably originates from the surface reduction of Ti^{4+} to Ti^{3+} by reducing gases produced during the calcination step.[83] Since we did not further anneal, Ti^{3+} formed during calcination does not oxidize back to Ti^{4+}.[83]

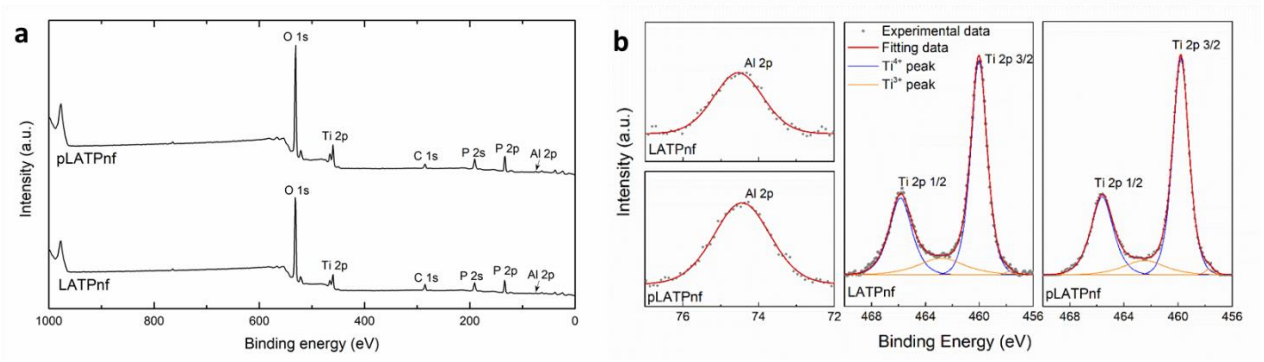

Figure 5.5 XPS survey spectra of LATPnf and pLATPnf samples. (b) High resolution spectra of Al 2p and Ti 2p regions. (c) Schematic illustration of the effect of the pressure on the Al content and distribution in pLATPnf.

EIS analysis of both LATPnf and pLATPnf samples was performed to measure the ionic conductivity. Each sample was placed in a coin cell between stainless steel blocking electrodes (**Figure 5.6a**) and EIS data have been acquired at a temperature ranging from 20 °C to 80 °C. The fitting of EIS spectra was performed by using the equivalent circuit depicted in **Figure 5.6b**. The resulting total impedance was used to calculate the ionic conductivity of both samples at different temperatures, displayed as Arrhenius plot in **Figure 5.6d**. The slope of the Arrhenius plots has been used to calculate the activation energy of both LATPnf and pLATPnf, yielding 0.37 ± 0.02 eV and 0.19 ± 0.02 eV respectively. Both results are in good agreement with the values reported in the literature for LATP.[67,223,227,228] The lowest value of pLATPnf could be related to the locally higher degree of Al substitution as well as to the better connection between LATP grains.[229–231] Regarding the ionic conductivity, LATPnf sample showed a value equal to 5×10^{-7} S cm^{-1} at 25 °C, which is slightly higher than the one reported by Lancel et al.[197] The pressure applied to pLATPnf proved to be highly beneficial for the ionic conductivity of the final electrolyte. Because of the higher density and the increased number of contact points, the pLATPnf sample is characterized by a two order of magnitude higher ionic conductivity at 25 °C, i.e. 3×10^{-5} S cm^{-1}.

Four-point probe measurements were acquired to rule out a potential electronic contribution to the total conductivity due to the presence of Ti^{3+} (**Figure 5.5b**). The data shows that the electronic conductivity of pLATPnf is negligible when compared to the total conductivity of the sample (**Figure 5.7a**). Equivalent measurements on LATPnf were not possible as this sample is not mechanically suitable for testing with this technique (**Figure 5.7b**). Al-rich LATP areas and $LiTiPO_5$ impurity phases could play a role in enhancing LATP's ionic conductivity. Al contents higher than 0.3 indeed proved to be beneficial for the ionic transport, as showed by both computational methods and single crystal impedance studies.[230,232]

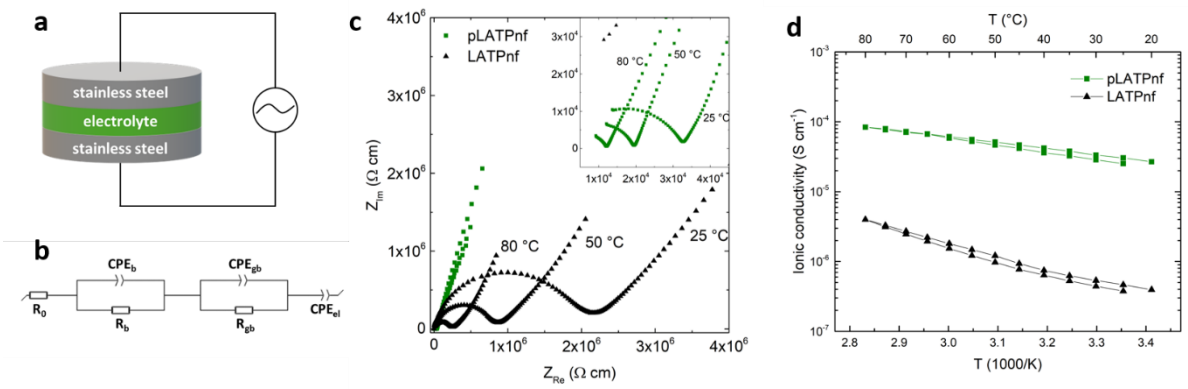

Figure 5.6 (a) Scheme of the EIS analysis setup. (b) Equivalent circuit used to fit EIS data. (c) EIS spectra of LATPnf and pLATPnf at 25 °C, 50 °C and 80 °C; a magnification of pLATPnf high frequency data is shown in the inset. (d) Arrhenius plot comparing LATPnf and pLATPnf ionic conductivities in the 20-80 °C temperature range. Two consecutive scans in opposite directions have been performed.

Additionally, Hupfer et al. reported that a 5% addition of $LiTiPO_5$ improves LATP's conductivity of almost one order of magnitude.[215] The direct ion conduction pathways provided by the fiber morphology, the numerous fiber contact points due to the pressing step and the potential contribution of impurity phases resulted in a more effective Li-ion transport in pLATPnf. Li ions are not restricted to move inside a single fiber as mostly happens in LATPnf sample, but they can hop more frequently between fibers leading to a more efficient conducting mechanism.

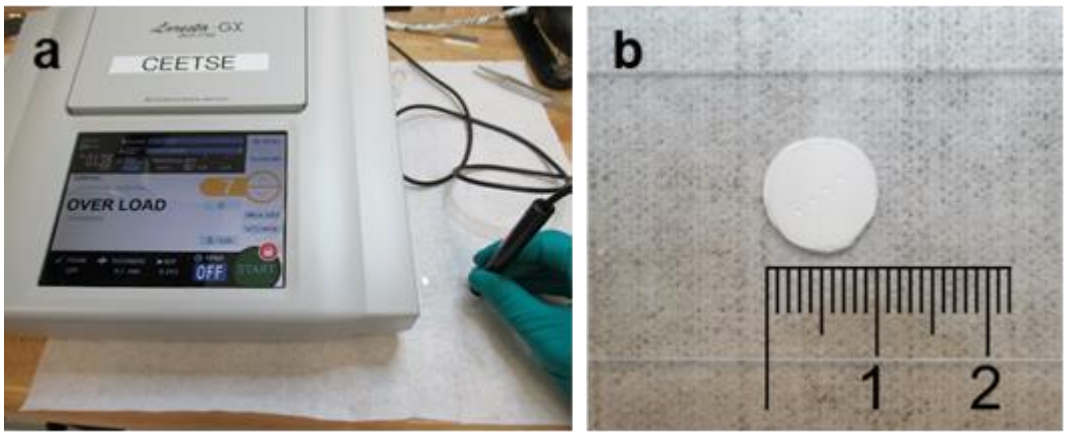

Figure 5.7 (a) Four-point probe test of pLATPnf. The value is out of the range of the instrument (>108 Ω/sq). (b) Indentations made by the PSP probe on LATPnf.

5.3 Conclusions and perspectives

LATP nanofibers have been synthesized by electrospinning and subsequent calcination at 850 °C for 2h. A 150 MPa pressure was applied on the pristine membrane, prior to the calcination step, and the effects on the properties of the final sample have been investigated. The morphological

characterization of LATPnf and pLATPnf samples showed that the density of the pristine membrane affects crystal growth during the calcination step. Different crystal shapes and sizes were detected in the pLATPnf sample as well as some impurity phases. These last evidences correlate with an uneven substitution of Ti with Al along pLATPnf sample. Whereas, Ti and Al contents are constant in LATPnf, they vary with the density by moving along the pLATPnf surface. Although the high porosity, typical of electrospun materials, proved to be beneficial for decreasing temperatures and times of calcination, the lower value measured for pLATPnf could be responsible for the impurity phases and the uneven elemental distribution. The higher density, coupled with the mild calcination conditions, presumably hinders the homogeneous diffusion of ions during crystal growth. Al ions appeared to be particularly affected by the local density of the sample, giving rise to Al-rich areas as well as Al-free impurity phases.

Even though the pressing step negatively affected the purity and homogeneity of LATP, it proved to be very beneficial for ionic transport across the solid electrolyte. The presence of impurity phases as well as the decrease of porosity (from 86% to 60%) led to a two order of magnitude higher ionic conductivity. The pLATPnf sample displayed a conductivity value equal to 3×10^{-5} S cm^{-1} at room temperature, which is only one order of magnitude lower than the one reported for bulk LATP. Despite this, LATPnf and pLATPnf are not suitable to be tested in a solid-state battery configuration, since their performance will not be comparable to that of a dense LATP pellet. However, the results achieved are promising for future application of NASICON fibers as both a base for developing ceramic electrolytes and an active filler/scaffold for composite polymer electrolytes. The mild conditions that allowed to achieve a pure and homogenous NASICON phase, compared to the synthesis of bulk materials by sol–gel processes, confirmed the beneficial effect of the high porosity and the fiber morphology. Most importantly the great influence that the applied pressure and thus the density of the precursor material have on the crystal growth can be, in our view, a significant contribution to the optimization of soft-chemistry methods (e.g. sol–gel, Pechini, hydrothermal), which aim to develop synthesis processes featuring less severe calcination steps, and thus more suitable for industrial upscale.

6 Properties and performance of electrospun NASICON $Li_{1.5}Al_{0.5}Ge_{1.5}(PO_4)_3$ fibers and their application as fillers in PEO-based electrolytes.

This chapter is based on the paper "*Synthesis of Electrospun NASICON $Li_{1.5}Al_{0.5}Ge_{1.5}(PO_4)_3$ Solid Electrolyte Nanofibers by Control of Germanium Hydrolysis*" published on *Journal of the Electrochemical Society, 2021, 168, 110512*.[199]

6.1 Background

The synthesis of Li-based NASICON materials is often performed by a solid-state method which exploits several long and high-temperature steps to achieve a pure and homogeneous phase, making the process very expensive and often unsuitable for scale-up. For this reason, a sol–gel approach has been proposed as a soft-chemistry alternative, even if occasionally yields less pure products. Other challenges are often encountered in the pelletizing step, where high pressure and sintering temperature are needed to achieve suitable densities. Some of these issues have already been addressed by coupling the sol–gel approach with electrospinning (**Chapter 1.4**), thus obtaining ceramic nanofibers and nanowires which often exhibit unusual properties. Moreover, ceramic fibers can be employed as active fillers to successfully improve the performance of composite polymer electrolyte, as already extensively reported.[177–188,190–192,194–196,201] Previous studies on the sol–gel synthesis of LAGP employed various precursor materials, both organic and inorganic, as Ge source.[69,86,88,90,91,233–239] Among them, germanium oxide has the advantage of being relatively inexpensive and stable at atmosphere conditions however, its low solubility in both water and organic solvents makes it unsuitable for electrospinning techniques.[235,236] Ge alkoxides are the most frequently used precursors for LAGP sol–gel syntheses, thanks to their good solubility in various organic solvents, which allows to easily obtain a homogeneous solution.[69,88,90,91,233,234,237–239] However, their reactivity towards even small traces of water greatly limits the use of other aqueous precursor salts, such as nitrates and acetates. Alkoxides instantaneously undergo hydrolysis and polycondensation reaction in the presence of even small amounts of water, leading to the formation and precipitation of Ge-O-Ge oligomers. These polycondensation products rapidly form a suspension which is not suitable for electrospinning since it negatively affects the homogeneity of the solution, hence the purity of the final material.[240] Germanium chloride has also been investigated as a source of Ge for soft chemistry methods. It is a valid alternative to alkoxides especially because of its low cost, however, it also reacts with water.[86] LAGP sol–gel syntheses reported in the literature were not directly applicable to electrospinning for

a variety of reasons, such as low concentration and viscosity, large amounts of additives, inhomogeneous solution, incompatibility with spinnable polymers. After testing different Ge-based materials, we succeeded in preparing a homogeneous and stable solution based on chloride precursors and suitable for the synthesis of LAGP nanofibers. Here we report a procedure to achieve LAGP nanofibers by electrospinning, as well as their application as filler to enhance the performance of a PEO:LiTFSI based electrolyte.

6.2 Results and discussion

Initially, the process used to synthesize LATP fibers[197,198] was adapted to achieve LAGP nanofibers. Ti butoxide was replaced with a stoichiometric amount of Ge butoxide, however, its addition to the precursor solution resulted in an opaque and viscous solution, as displayed in **Figure 6.1a** (right) along with the clear chloride-based one (left). This confirms the already observed instability of Ge alkoxides and reported previously in the presence of small traces of water.[240] Ge butoxide spontaneously underwent hydrolysis and condensation reaction because of the water contained in the used precursor salts (lithium and aluminum nitrates), leading to the formation of insoluble Ge-O-Ge oligomers.[240] Moreover, unlike several metal alkoxides,[241–246] Ge ones cannot be stabilized by chelation using acetylacetone, because of their lower tendency to form coordination compounds. The oligomers suspension makes the solution unsuitable for the electrospinning process, which is unstable, leading to coalesced fibers and beads (**Figure 6.1b,d**). Moreover, the material achieved exhibits a high content of GeO_2 after calcination due to Ge-O-Ge groups (**Figure 6.1e**). Conversely, the chloride-based approach led to a clear and homogeneous solution suitable to perform a stable electrospinning process thus achieving uniform beadless fibers.

Circular samples cut from the pristine electrospun membrane (**Figure 6.1c**) were calcined at 700 °C, 800 °C, and 900 °C for two hours under constant air flow. The temperature had a significant effect on the size and porosity of the ceramic samples. LAGP 700 samples displayed porosity values ranging from 79 to 83% and their area was about 50% that of the corresponding pristine ones. LAGP 800 porosities were 60% ca. while their area became 25% of what it was before the calcination step. A higher temperature is also detrimental for the mechanical integrity of calcined samples: while a temperature of 700 °C did not have any relevant effect on the integrity of the samples, at 800 °C two out of three samples displayed some fractures after heat treatment. At 900 °C all treated samples were damaged or broken. Hence the higher the temperature the faster and more significant is the shrinkage

during the calcination step, thus leading to smaller and less porous samples which are also more likely to break.

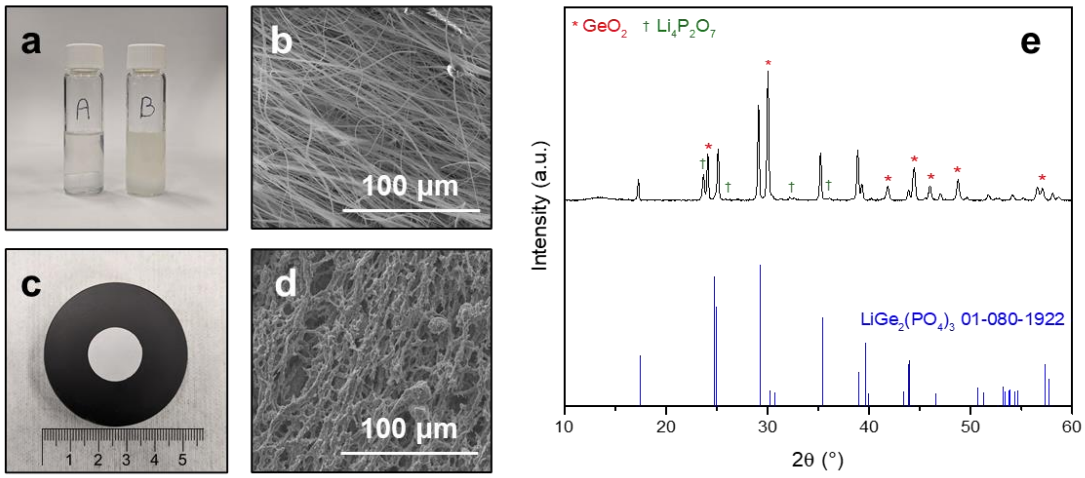

Figure 6.1 Pictures of (a) vials containing LAGP precursor solutions based on GeCl4 (left) and Ge butoxide (right) and (c) a circular sample made of LAGP electrospun nanofibers. SEM images of (b) LAGP precursor fibers and (d) LAGP ceramic fibers prepared by adapting the synthesis used for LATP (Section 2.2.1 and [1,2]) by replacing titanium butoxide with germanium butoxide. (e) Corresponding XRD pattern of LAGP fibers.

Figure 6.2 shows the morphological and structural evolution of LAGP fibers calcined at 700 °C, 800 °C and 900 °C. The diameter of as spun precursor fibers (**Figure 6.2a**) ranges from 300 to 800 nm. The range of diameters does not change after heat treatment at 700 °C. Using higher calcination temperatures (800 °C and 900 °C) is detrimental for the morphology of the sample, as the fibers start to coalesce. At 800 °C several fibers can still be identified by SEM imaging, as displayed in the inset in **Figure 6.2c**, while a temperature of 900 °C yields a dense sample following almost total coalescence of the fibers (**Figure 6.2d**). Although higher calcination temperatures tend to damage the fiber morphology, they are beneficial for the material crystallization and corresponding purity shown by the XRD patterns displayed in **Figure 6.2e**. The main peaks in each pattern can be attributed to the NASICON-like structure (space group $R\bar{3}c$) of $Li_{1.5}Al_{0.5}Ge_{1.5}(PO_4)_3$ (PDF card 04-022–7674). They become sharper by increasing the calcination temperature, meaning that LAGP crystallinity improves. Minor peaks in LAGP 700 and LAGP 800 patterns are related to impurity phases of $AlPO_4$, GeP_2O_7, and $Li_9Al_3(PO_4)_2(P_2O_7)_3$, while only traces of $AlPO_4$ and GeP_2O_7 resulted when 900 °C temperature is employed. The Li-rich $Li_9Al_3(PO_4)_2(P_2O_7)_3$ phase has been reported when Al-doping of 0.7 and higher are employed. However, its peaks are more intense when the temperature used for the heat treatment is decreased.[247] $AlPO_4$ is a common impurity phase for the sol–gel synthesis of LAGP,[86,88,239,247] while GeP_2O_7 is an intermediate product of LAGP crystallization.[248] These aspects are consistent with the

decrease of impurity peaks intensity when the calcination temperature is increased. Given the presence of impurity peaks in LAGP 700 and their decrease when higher temperatures are employed, a calcination temperature lower than 700 °C has not been tested.

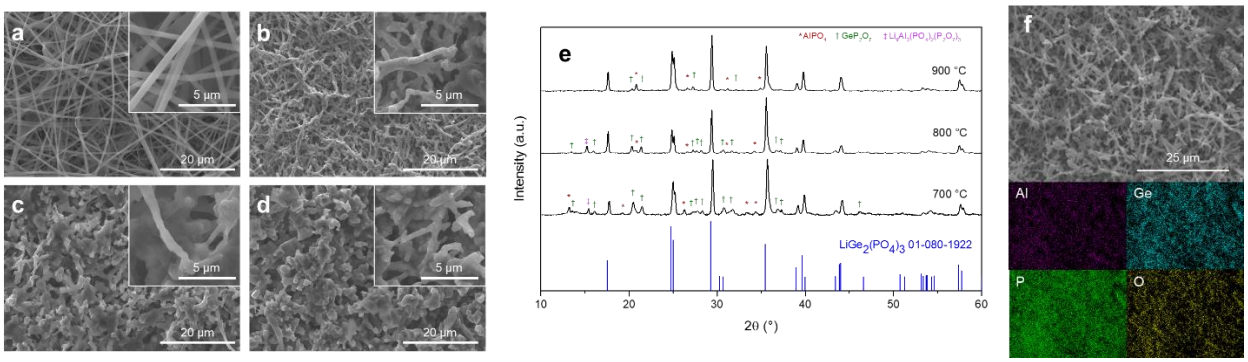

Figure 6.2 SEM images of (a) LAGP precursor fibers, (b) LAGP 700, (c) LAGP 800 and (d) LAGP 900 (high magnification details of the fibers in the inset). (e) XRD patterns of LAGP 700, LAGP 800 and LAGP 900. ((*): $AlPO_4$; (†): GeP_2O_7; (‡): $Li_9Al_3(PO_4)_2(P_2O_7)_3$). (f) SEM-EDS analysis and corresponding elemental mapping of LAGP 700.

Increasing the calcination time proved to not be an effective strategy for improving the purity of the materials (**Figure 6.3a**). Furthermore, the effect of a two-hour annealing step at 800 °C and 900 °C on LAGP 700 has been investigated. No major differences resulted when comparing SEM and XRD data to the sample directly calcined at the same temperature (**Figure 6.3b,d**). The measured values of the lattice parameters are in good agreement with those reported in the PDF card 04-022–7674 for $Li_{1.5}Al_{0.5}Ge_{1.5}(PO_4)_3$ and are displayed in **Table 6.1**. A marginal increase of parameter *a* with the increase of calcination temperature is observed. As expected, changes in parameter *c* are more relevant,[247] which results higher than the value reported for $LiGe_2(PO_4)_3$ in all three samples, which is ascribable to the substitution of Ge^{4+} (0.530 Å) by the larger Al^{3+} (0.535 Å). However, it is lower than the one reported for $Li_{1.5}Al_{0.5}Ge_{1.5}(PO_4)_3$ (PDF card 04-022–7674), which could be related to a slightly lower than expected degree of substitution.[247]

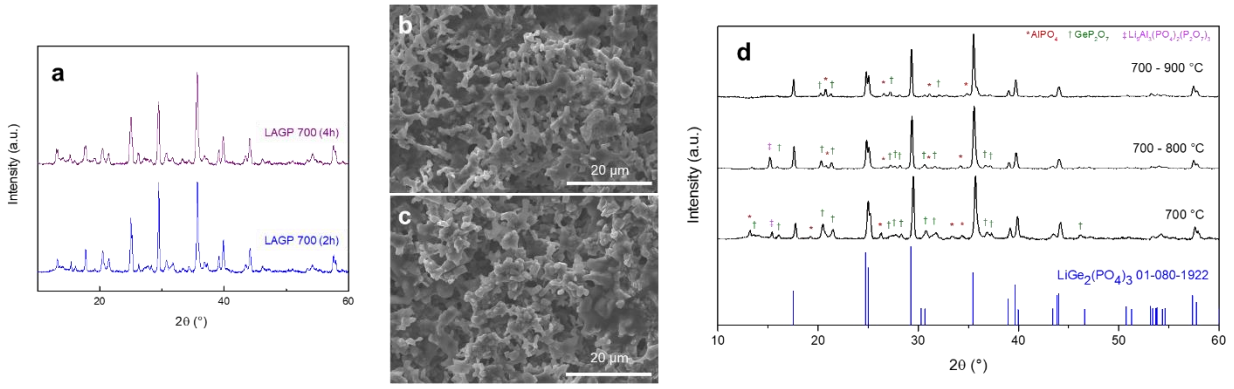

Figure 6.3 (a) Comparison of XRD patterns of LAGP fibers calcined at 700 °C for 2h and for 4h. SEM images of LAGP 700 after further annealing at (b) 800 °C and (c) 900 °C. XRD patterns of annealed LAGP 700-800 and LAGP 700-900 compared to LAGP 700. ((*): $AlPO_4$; (†): GeP_2O_7; (‡): $Li_9Al_3(PO_4)_2(P_2O_7)_3$).

To investigate the elemental distribution and localization of the phases detected by XRD, EDS mapping of Al, Ge, P and O was performed for LAGP 700 and is displayed in **Figure 6.2f**. The elemental distribution appears homogeneous across the sample. The impurity phases resulting from XRD peak assignment cannot be identified in the elemental maps, as no local concentration of Ge or Ti is evident. Since they did not form any cluster or agglomeration, their formation is probably not related to the local morphology and density of the sample, but they are only reaction intermediates of LAGP crystallization. They presumably could not be identified using this technique because of the resolution limit of the instrument. Additionally, EDS analysis excluded the possible presence of Cl ions stemming from the decomposition of the chloride-based precursor materials used for the synthesis, which could have remained in the final sample (**Figure 6.4**).

Table 6.1. Cell parameters of LAGP 700, LAGP 800, and LAGP 900 compared to $LiGe_2(PO_4)_3$ and $Li_{1.5}Al_{0.5}Ge_{1.5}(PO_4)_3$.

	a (Å), b (Å)	*c (Å)*
$LiGe_2(PO_4)_3$ (PDF card 01-080-1922)	8.275	20.470
$Li_{1.5}Al_{0.5}Ge_{1.5}(PO_4)_3$ (PDF card 04-022-7674)	8.261	20.621
LAGP 700	8.2591	20.482
LAGP 800	8.2676	20.562
LAGP 900	8.2725	20.545

We thus decided to further investigate the morphology and elemental distribution by TEM imaging and corresponding EDS mapping of smaller portions of LAGP samples, which are displayed in **Figure 6.5**.

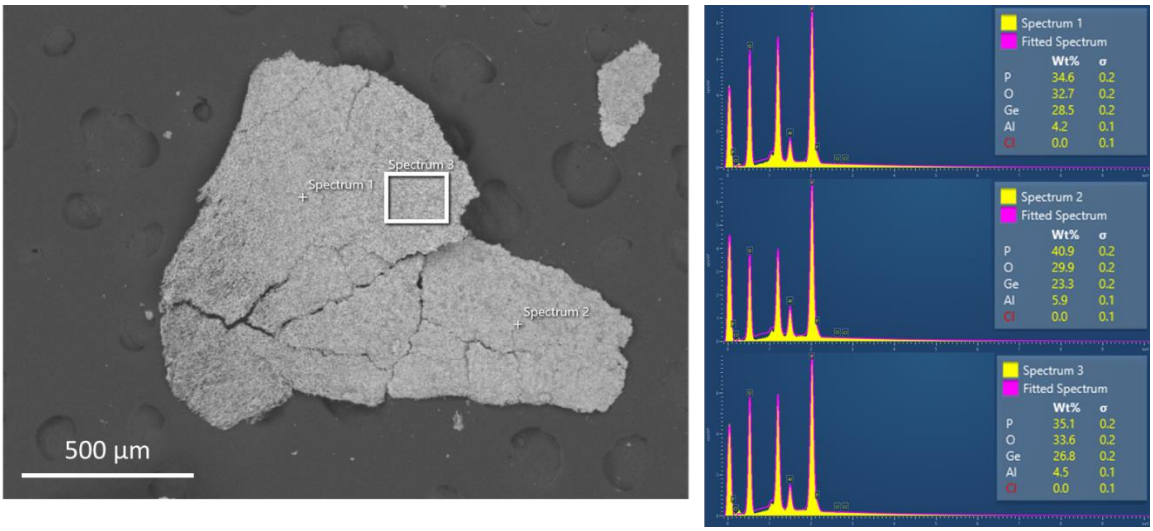

Figure 6.4 SEM/EDS analysis of LAGP 700 to exclude the presence of Cl^- ions.

Specifically, Al mapping correlates well with XRD results. Areas with higher Al concentration can be easily identified for all three samples (circled in white) and arguably correspond to the Al-rich impurity phases already identified in the XRD spectra, namely $AlPO_4$ and $Li_9Al_3(PO_4)_2(P_2O_7)_3$. This is also confirmed by the lower intensity displayed in the very same spots of Ge maps. In addition, by integrating EDS maps, we were able to quantify the elemental composition of all three samples. Particular attention has been devoted to the Al/Ge ratio. While LAGP 700 shows a value ranging from 0.15 to 1.40 by moving across the sample, LAGP 800 and LAGP 900 both feature a constant Al/Ge ratio of 0.33 as expected by the sought stoichiometry. These data certainly relate well with the impurity phases detected in the samples whose quantities are considerably higher in LAGP 700. Hence, the substitution of Ge by Al was effective and the sought stoichiometry was achieved, but the amount of impurities present in LAGP 700 is responsible for the inhomogeneous mapping of Ge and Al.

A comparison of ^7Li MAS NMR spectra of the three samples is shown in **Figure 6.6a**. All spectra can be described as a combination of three components centered at ~0 ppm. Similar to what was observed for LATP in previous work,[198] C_Q values of the first two components are equal to 50 kHz and 5 kHz. Those signals can be assigned to Li ions located at M1 and M3 sites of LAGP. The third component has significantly higher C_Q (165 kHz). Its relative population in the sample decreases with an increase of calcination temperature, as demonstrated by the decrease of spinning sidebands intensity from LAGP 700 to LAGP 900 in the region taken far from the central line (see insert in **Figure 6.6a**).

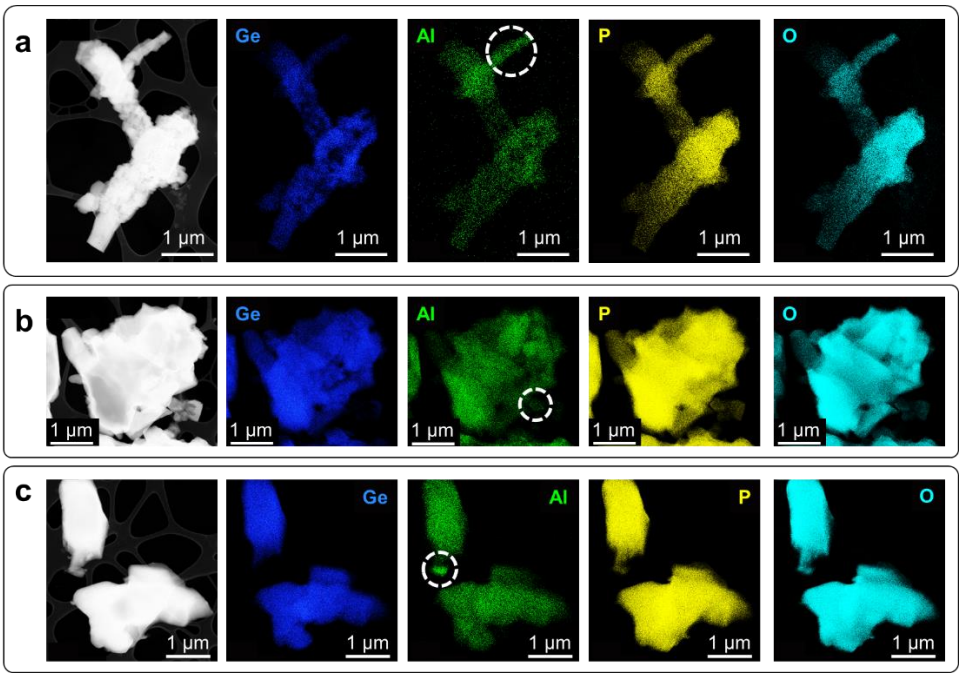

Figure 6.5 TEM-EDS characterization (first column) and corresponding elemental mapping of (a) LAGP 700, (b) LAGP 800 and (c) LAGP 900.

It can be assigned to $Li_9Al_3(PO_4)_2(P_2O_7)_3$, taking into account that signals of this compound are also detected in ^{27}Al and ^{31}P NMR spectra (**Figure 6.6b,c**)[249] and demonstrate the same trend with respect to the calcination temperature. Two small peaks at ~38 ppm (labeled A1 and A2) are observed in ^{27}Al NMR spectra of LAGP 800 and LAGP 900 in addition to signals of AlO_6 (LAGP) and $Li_9Al_3(PO_4)_2(P_2O_7)_3$. These two peaks may correspond to the two $AlPO_4$ phases.195 There is a significant overlap of the peaks in ^{31}P NMR spectra. Nevertheless, signals of $P(OGe)_{4-m}(OAl)_m$ with m = 0, 1, 2 and 3 can be identified at −42, −37, −32 and −27 ppm respectively. [225,249] The P0 peak in LAGP 900 sample has a much higher intensity than the same peak in the other two samples. A signal originating from $Li_9Al_3(PO_4)_2(P_2O_7)_3$ is also visible in the spectrum at −16 ppm. In addition to that, a small resonance, which can be assigned to $Li_4P_2O_7$,[249,250] is observed at −4 ppm. Its intensity increases with the increase of the calcination temperature. The signal of $AlPO_4$ (observed in ^{27}Al NMR) should be located between −25 and −35 ppm and probably overlap with P2 and P3 peaks, which agrees with the structure, being all characterized by crystallographically independent orthophosphate groups[249] Additionally, the GeP_2O_7 phase detected in XRD patterns should generate two signals in the same region, despite being characterized by a pyrophosphate group. This has been previously attributed to the small P-O-P value of the bridging angle, which displaces the peaks towards the Ge-ortophosphate range.[251]

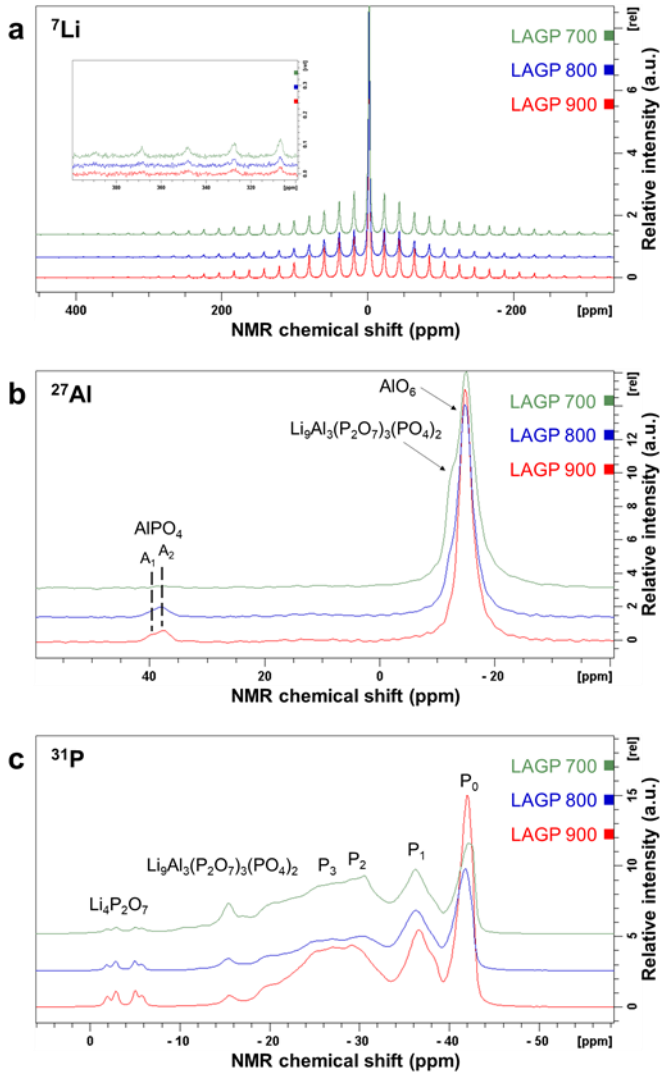

Figure 6.6 (a) ^{7}Li, (b) ^{27}Al and (c) ^{31}P MAS NMR spectra of LAGP 700, LAGP 800 and LAGP 900.

To evaluate the ionic conductivity of ceramic LAGP fibers, EIS analysis was performed on LAGP 700 and LAGP 800. The impossibility of achieving an intact LAGP 900 sample prevents us from assessing its electrochemical performance. Each LAGP ceramic sample was placed in a coin cell between stainless steel blocking electrodes (**Figure 6.7a**) to acquire EIS data between 20 °C and 80 °C. EIS spectra were fitted by using the equivalent circuit depicted in **Figure 6.7b** and the resulting impedance was used to calculate the ionic conductivity values displayed in **Figure 6.7c**. The ionic conductivity of both samples follows the Arrhenius law:

$$\sigma = Ae^{\left(-\frac{E_A}{RT}\right)}$$

Where σ, A, Ea, R, and T are the ionic conductivity, the pre-exponential factor, the activation energy, the gas constant, and the temperature, respectively. The slope of the Arrhenius plot expressed in the linear form $\ln(\sigma) = \ln(A) - E_A/RT$, has been used to calculate the activation energy, which corresponds to 0.407 (±0.003) eV for LAGP 700 and 0.349 (±0.007) eV for LAGP 800. Both values are in good agreement with those reported in the literature.[252] As demonstrated by Delaizir et al. the activation energy appears to be independent of the density,[233] while Yang et al. observed that a higher density corresponds to a slightly lower activation energy.[253]

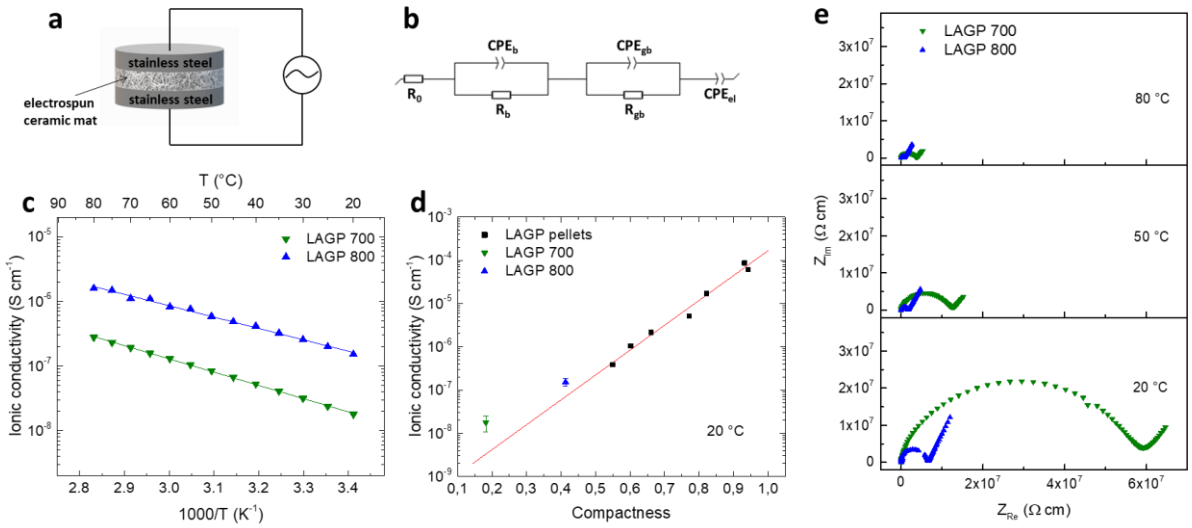

Figure 6.7 (a) Scheme of the setup used for EIS analysis of LAGP 700 and LAGP 800. (b) Equivalent circuit used for EIS data fitting. (c) Representative Arrhenius plot of LAGP 700 and LAGP 800 in a temperature range of 20 °C–80 °C. (d) Ionic conductivity at 20 °C vs density of LAGP 700 and LAGP 800 samples compared to data achieved with LAGP pellets by Delaizir et al.[233] (e) EIS spectra of LAGP 700 and LAGP 800 at 20 °C, 50 °C, and 80 °C.

Hence, the value we report for LAGP 800 is certainly related to its higher density (40% ca.) compared to LAGP 700 (20% ca.), as well as to its higher purity as observed in XRD data (**Figure 6.2e**). Higher density and purity are beneficial for the formation of numerous percolation pathways, thus leading to more effective Li-ion conduction. EIS spectra of LAGP 700 and LAGP 800 acquired at 20 °C, 50 °C, and 80 °C are shown in **Figure 6.7e** for comparison. Ionic conductivity values at 20 °C correspond to 1.9×10^{-8} S cm^{-1} and 1.5×10^{-7} S cm^{-1} for LAGP 700 and LAGP 800 respectively. At 50 °C they respectively become 8.5×10^{-8} S cm^{-1} and 5.9×10^{-7} S cm^{-1}, while at 80 °C they are equal to 2.8×10^{-7} S cm^{-1} and 1.6×10^{-6} S cm^{-1}. Although the low ionic conductivity at room temperature makes them unsuitable to be used as solid electrolyte as-is, their low density must be considered. As evidenced by data displayed in **Figure 6.7d**, where the ionic conductivity at 20 °C is plotted against the material density, LAGP 700 and LAGP 800 conductivity values are above the ones estimated by a linear fitting

of data reported by Delaizir et al. for LAGP pellets having densities ranging between 50 and 100% of LAGP's theoretical value.[233]

Among all the potential applications of ceramic ion-conductive nanofibers, one of the most interesting is as filler in composite polymer electrolytes. We thus investigated the effect of LAGP nanofibers when used as filler in PEO-based electrolytes. We selected LAGP 700 despite its lower purity because, being characterized by a more pronounced fiber morphology, it allows to emphasize the effects attributed to the elongated shape when compared to a conventional particle-shaped filler. After magnetically stirring selected amounts of LAGP nanofibers and nanoparticles into the polymer electrolyte slurry and coating them onto stainless-steel foils, SEM images were acquired (**Figure 6.8a-f**). A mix of secondary and back scattered electrons has been collected to emphasize the presence of ceramic fillers. As **Figure 6.8a-d** show, LAGP nanofibers are evenly distributed in the polymer matrix, hence their dispersion in the polymer slurry was homogeneous. Conversely, LAGP particles have a lower tendency to disperse well, thus forming some aggregates in the coatings visible as brighter spots (**Figure 6.8e,f**). An even distribution of the filler in the composite electrolyte is crucial to obtain good and reproducible values of ionic conductivity, since fillers can effectively hinder the crystallization of PEO. Their agglomeration however is often considered the cause of lower conductivity values.[149,152,254]

The thermal stability of fiber-based composite electrolytes was evaluated by TGA and compared to that of PE. The resulting data are displayed in **Figure 6.8g**. No weight losses related to residual solvent or to previously adsorbed water release have been detected before the actual thermal degradation. A typical two-step curve characterizes all the samples. The first step corresponds to the thermal degradation of PEO, whose onset in the filler-free electrolyte was estimated at 378 °C. Low amounts of LAGP nanofibers, such as 1 and 5%, do not appear to affect the degradation temperature of PEO, whereas in CE-LAGPf10 and CE-LAGPf20 the degradation onset decreased to 372 °C and 366 °C, respectively. This aspect is even more evident when the first derivative of the weight loss is plotted since the first peak, corresponding to the point of the greatest rate of PEO thermal degradation, shifted at lower temperature values for both CE-LAGPf10 and CE-LAGPf20. As reported, the addition of active fillers greatly affects PEO's crystallinity, which in turn can significantly affect its thermal degradation.[255] A second weight loss was detected just below 450 °C and we attribute it to the LiTFSI degradation process. Since the analyses have been carried out under a constant flow of N_2, the residual weight can be partly attributed to carbonaceous products, deriving from the thermal degradation of both PEO and LiTFSI in a non-oxidative atmosphere. Nevertheless, the residual

weight is proportional to the amount of LAGP fibers added to the polymer matrix, thus confirming their stability within the temperature range employed for the analysis.

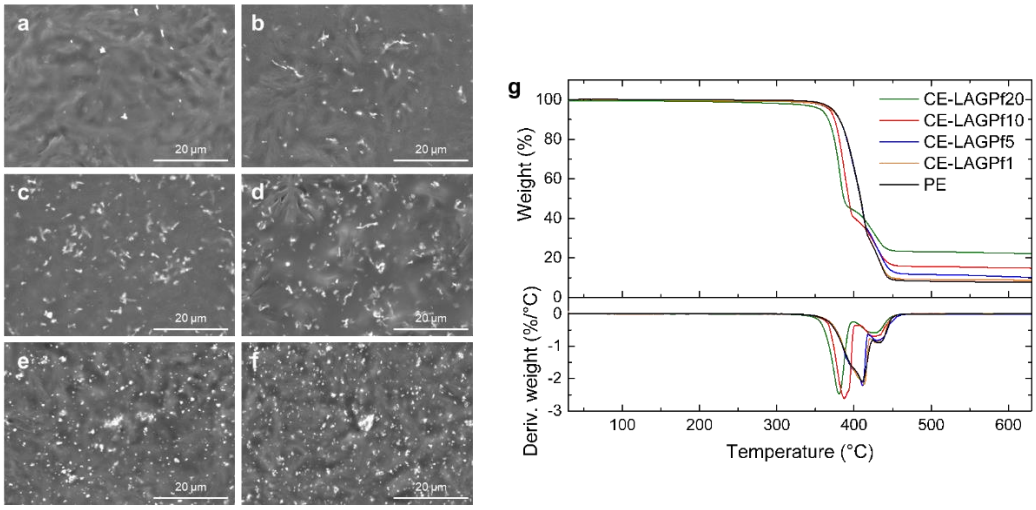

Figure 6.8 SEM images of (a) CE-LAGPf1, (b) CE-LAGPf5, (c) CE-LAGPf10, (d) CE-LAGPf20, (e) CE-LAGPp10 and (f) CE-LAGPp20 acquired by detecting both secondary and back-scattered electrons. (g) TGA/DTG curves of CE-LAGPf20, CE-LAGPf10, CE-LAGPf5, CE-LAGPf1 and PE.

EIS analyses were performed on composite electrolytes and on the LAGP-free polymer electrolyte to investigate the effect of the filler presence and morphology on Li-ion transport. The electrolyte was placed in a coin cell between stainless steel blocking electrodes before testing (**Figure 6.9a**). EIS spectra have been acquired in the 20 °C–80 °C temperature range and fitted using the equivalent circuit depicted in **Figure 6.9b**. As shown in **Figure 6.9c**, the impedance value of CE-LAGPf10 at 20 °C is about half of that of PE, while CE-LAGPp10 displays the same value as the filler-free electrolyte. The data acquired between 20 and 80 °C was used to draw the corresponding Arrhenius plots. CE-LAGPf10, CE-LAGPp10, and PE plots are compared and shown in **Figure 6.9d** to better emphasize the benefits of using fibers instead of particles as filler. LAGP particles are characterized by a purity higher than that of LAGP fibers (**Figure 6.10a**), which usually corresponds to an improved ionic conductivity. The three electrolytes here shown feature the typical 2-slope behavior due to the PEO transition from semi-crystalline to amorphous.[256,257] The first section—below the PEO melting point—is characterized by a linear relationship between conductivity and temperature, which means Li-ion conduction obeys the Arrhenius law, whereas the second region is related to segmental motion of PEO chains and is better fitted using the Vogel-Tammer-Fulcher equation.[256] The ionic conductivity of CE-LAGPf10 is higher than that of PE and CE-LAGPp10 in the whole temperature

range, but especially at 20 °C where corresponds to 7.14 × 10^{-6} S cm^{-1}, i.e. double that of PE (3.42 × 10^{-6} S cm^{-1}).

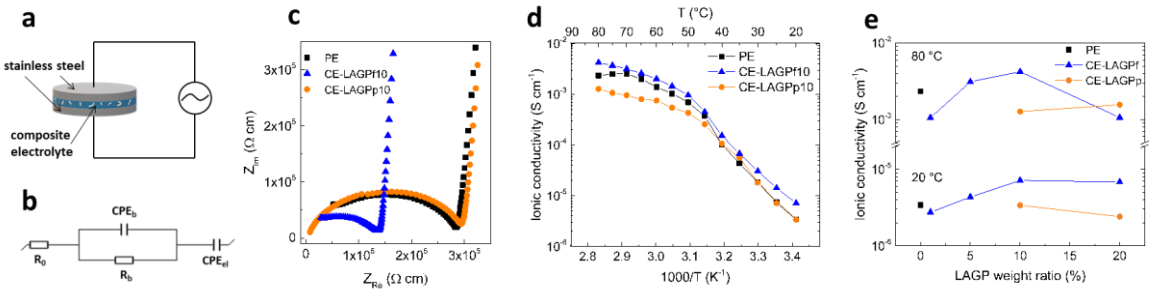

Figure 6.9 (a) Scheme of the setup used for EIS analysis of polymer and composite electrolytes. (b) Equivalent circuit used for EIS data fitting. Representative (c) EIS spectra at 20 °C and (d) Arrhenius plot in a temperature range of 20 °C–80 °C of CE-LAGPf10, CE-LAGPp10, and PE. (e) Ionic conductivity at 20 °C and 80 °C vs LAGP weight ratio.

The improvement observed is certainly due to the high conductivity at room temperature of LAGP NASICON material, reported as 2.8 × 10^{-4} S cm^{-1} for a 100% dense pellet (**Figure 6.7d**).[69,233] Additionally, this aspect well correlates with the results of both SEM imaging and TGA. The even distribution of fibers has proven to be beneficial to hinder the crystallization of PEO and thus achieving faster Li-ion conduction.[179,192,258,259] In the 20 °C–40 °C range the ionic conductivity of CE-LAGPp10 is about the same as the one of PE, meaning that the use of 10% LAGP particles as filler had no effect on the conduction mechanism. Unlike fibers which provide a continuous conduction path, a constant hopping of Li-ions from the polymer chain to the particles is needed when particle shaped fillers are used.[177,178] In the 50 °C–80 °C temperature range, the ionic conductivity is lower than that of PE. This can be attributed to the agglomeration observed before (**Figure 6.8e**), which leads to inhomogeneous Li-ion conduction across the composite electrolyte when PEO becomes amorphous.[177,192,256] The absence of agglomerates in CE-LAGPf10 allows to achieve conductivity values that are slightly higher than those of PE since evenly dispersed fibers do not hinder the mobility of PEO chains. When the amount of LAGP fibers is increased to 20% (**Figure 6.9e**), the ionic conductivity at 80 °C is comparable to the one of CE-LAGPp20 and both are lower than that of PE, which means that further increasing the amount of filler (both fibers and particles) has a negative effect at high temperature where polymer chains of amorphous PEO are very mobile and probably hindered by relatively large amounts of filler. However, at 20 °C the ionic conductivity of CE-LAGPf20 is still as high as the one of CE-LAGPf10, whereas the value recorded for CE-LAGPp20 is lower than that achieved by CE-LAGPp10. This could be again related to the tendency of LAGP particles to agglomerate. Arrhenius plots of all the electrolytes as well as the comparison of CE-

LAGPf20 and CE-LAGPp20 to PE are displayed in **Figure 6.10b,c**. The ionic conductivity values of all the electrolyte tested, acquired at 20, 50 and 80 °C are reported in **Table 6.2**.

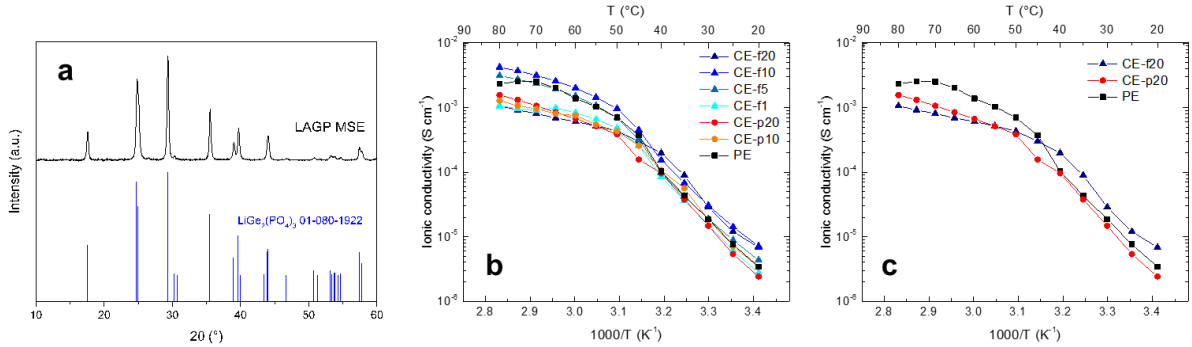

Figure 6.10 (a) XRD pattern of commercial LAGP particles (MSE). (b) Representative Arrhenius plots of (a) CE-LAGPf20, CE-LAGPf10, CE-LAGPf5, CE-LAGPf1, CE-LAGPp20, CE-LAGPp10 and PE and (b) of CE-LAGPf20, CE-LAGPp20 and PE in a temperature range of 20-80 °C.

Table 6.2 Ionic conductivity values at 20, 50 and 80 °C of all the electrolytes tested.

	Ionic conductivity (S cm⁻¹)		
	20 °C	*50 °C*	*80 °C*
CE-LAGPf20	6.83×10^{-6}	4.31×10^{-4}	1.06×10^{-3}
CE-LAGPf10	7.14×10^{-6}	9.61×10^{-4}	4.22×10^{-3}
CE-LAGPf5	4.34×10^{-6}	6.97×10^{-4}	3.12×10^{-3}
CE-LAGPf1	2.75×10^{-6}	4.82×10^{-4}	1.06×10^{-3}
PE	3.42×10^{-6}	6.99×10^{-4}	2.35×10^{-3}
CE-LAGPp20	2.41×10^{-6}	3.86×10^{-4}	1.56×10^{-3}
CE-LAGPp10	3.39×10^{-6}	4.31×10^{-4}	1.28×10^{-3}

6.3 Conclusions and perspectives

We report the successful synthesis of NASICON-like LAGP nanofibers by electrospinning. $GeCl_4$ was selected as Ge source to achieve a stable and homogeneous solution suitable for the electrospinning process. The subsequent calcination step led to full-ceramic nanostructured samples whose ionic conductivity proved to be above the expected value. We then used LAGP nanofibers as filler to develop PEO:LiTFSI-based composite electrolytes. The addition of 10% LAGP nanofibers

doubled the room temperature ionic conductivity of the filler-free polymer electrolyte, as the fibers provide longer ion-conductive paths and decrease PEO crystallinity. We expect that the conductivity can be further increased by optimizing the synthesis thus achieving LAGP nanofibers with a higher degree of purity. We believe that the process reported here can be a significant contribution to further optimizing the conditions of LAGP sol–gel synthesis methods. Sol–gel products are often characterized by a lower purity, however shorter heat treatments and lower temperatures are usually required to synthesize them. This last aspect is crucial to develop synthetic protocols suitable for largescale production. The integration of electrospinning into sol–gel syntheses proved to be a facile method to achieve ceramic ion-conducting LAGP fibers. Moreover, the addition of LAGP nanofibers to a PEO-based polymer electrolyte further evidenced that elongated fillers are able to provide enhanced performance compared to their particle-shaped counterpart, thus being suitable candidates to develop composite electrolytes for next-generation solid-state batteries.

7 Properties and performance of $Li_{1.5}Al_{0.5}Ge_{1.5-x}Ti_x(PO_4)_3$ ($0.1 \leq x \leq 0.3$) nanofibers: influence of Ti^{IV} substitution.

This chapter is based on the paper "*Influence of Ti^{IV} substitution on the properties of a $Li_{1.5}Al_{0.5}Ge_{1.5}(PO_4)_3$ nanofiber-based solid electrolyte*", published on *Nanoscale, 2022, 14, 5094-5101*.[202]

7.1 Background

Recently, materials with 1D morphology have been employed as a filler for composite electrolytes, proving to be more effective than their particle-like counterparts.[159] Nanofiber and nanowire fillers can reduce the number of particle/polymer junctions that lithium ions have to cross between the electrodes by forming longer ion-conductive continuous pathways.[177,178] Moreover, 1D fillers greatly improve the mechanical strength of the electrolyte, by acting as supporting scaffold.[192,260] Most of the works reported up to date were about the use of 1D fillers based on garnet[190–192,194,195,260] or perovskite materials,[177–180,183,185–187,261] while only few studies have focused on NASICON fibers.[197–199,204] On the basis of the results of our previous work on the synthesis of electrospun LAGP nanofibers[199] and reported data on LATP fibers,[197,198] we successfully synthesized pure and stable $Li_{1.5}Al_{0.5}Ge_{1.5-x}Ti_x(PO_4)_3$ ($0.1 \leq x \leq 0.3$) (LAGTP) nanofibers. We aim to gain insights on the effect of a partial substitution of Ge by Ti on the synthesis and the properties of a $Li_{1.5}Al_{0.5}Ge_{1.5}(PO_4)_3$ (LAGP) fiber-based electrolytes. Thus, the morphological and structural properties have been investigated and compared to those of plain LAGP fibers. In addition, we also propose their application as filler to enhance the performance of a PEO-based composite electrolyte for lithium metal batteries.

7.2 Results and discussion

Previous works on electrospun LATP nanofibers showed that pure NASICON-like materials can be easily achieved in the form of elongated structures by using a sol–gel approach coupled to the electrospinning technique.[198,227] We recently developed a new chloride-based synthesis for LAGP nanofibers (**Chapters 3.4.2 and 6**), which enables the facile achievement of Ge-based 2-dimensional materials starting from a stable solution.[199] However low calcination temperatures need to be employed to maintain the sought morphology, thus compromising the purity of the final product, as we observed that temperature ≥ 800 °C are crucial to minimize the presence of impurity phases. Hence, we studied how a partial substitution of Ge with Ti can affect both morphology and purity of

the final product. We prepared a precursor solution for LAGP, referred to as solution A in **Figure 7.1**. Then, we added Ti butoxide previously stabilized in acac (solution B in **Figure 7.1**). The addition of solution B makes the precursor solution more viscous, mainly because of the high viscosity of Ti butoxide. Increasing its amount results in even higher viscosities, which can certainly affect the electrospinning technique. Thus, process parameters have been slightly tuned to optimize the process for each precursor solution. The typical instabilities of the electrospinning process appear to be better balanced by the higher viscosities; thus, a more efficient formation of continuous fibers can be achieved. The acac used to chelate Ti butoxide did not significantly affect the electrospinning process, given the low amount used and the fact that its dielectric constant is similar to the one reported for EtOH.[262,263]

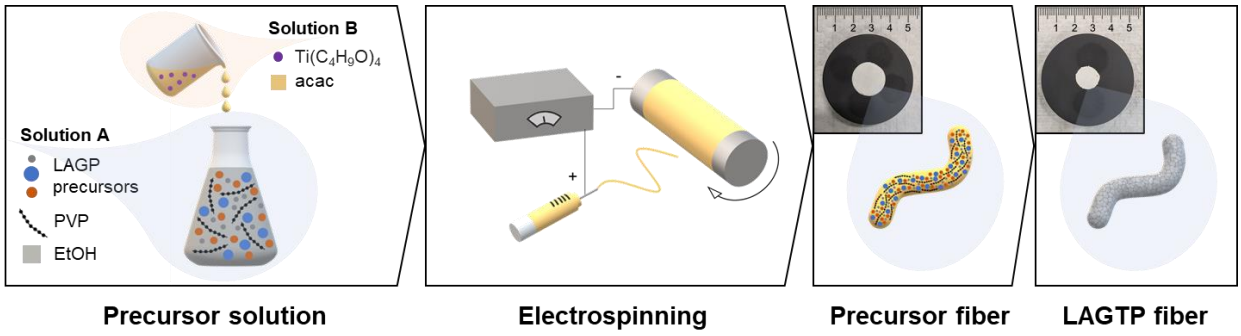

Figure 7.1 Schematic illustration of the fabrication process of LAGTP fiber.

After achieving the electrospun membranes, circular samples have been cut and calcined at 700 °C for 2 hours under constant air flow. As already observed for plain LAGP,[199] the temperature affects the mechanical integrity of the samples. After the heat treatment at 700 °C, all the samples remain intact, whereas increasing the temperature at 800 °C tends to cause fractures. No intact samples have been achieved at 900 °C. All three LAGTP ceramic samples calcined at 700 °C are characterized by a porosity equal to 93±3%.

Figure 7.2 displays the SEM images acquired on the pristine membranes and on LAGTP01, LAGTP02 and LAGTP03 calcined at 700, 800 and 900 °C. SEM images of LAGP nanofibers from our previous work were also included (**Figure 7.2a**) for the sake of comparison. No relevant differences can be observed in the morphology of the pristine membranes, which means the optimization of the parameters for electrospinning LAGTP precursor solutions has been successful. The effect of Ti addition can be observed in the calcined samples. As for LAGP, no coalescence occurs by calcining the samples at 700 °C. However, the coral-like structures that characterize LAGP

morphology disappear when Ti is added, resulting in well distinct fibers. Differences are even more obvious when the calcination temperature is increased: at 800 °C LAGP is characterized by fibers partially fused together and some coalesced areas, which lead to a closed porosity, while the morphology of all LAGTP samples appears unaltered. At 900 °C, the coalescence phenomenon appears in LAGTP samples too, however fibers are still easily discernible, conversely to what observed for LAGP, where only few fibers can be identified.[199] This phenomenon could be associated with a higher thermal and dimensional stability of LAGTP precursor fibers compared to LAGP ones, which prevents their coalescence at high temperature.

The structure of LAGTP samples was investigated by XRD analysis. Corresponding patterns are shown in **Figure 7.3a** and compared to that of LAGP nanofibers. The main phase in all LAGTP samples corresponds to the typical rhombohedral structure (space group $R\bar{3}c$) of NASICON-like materials.

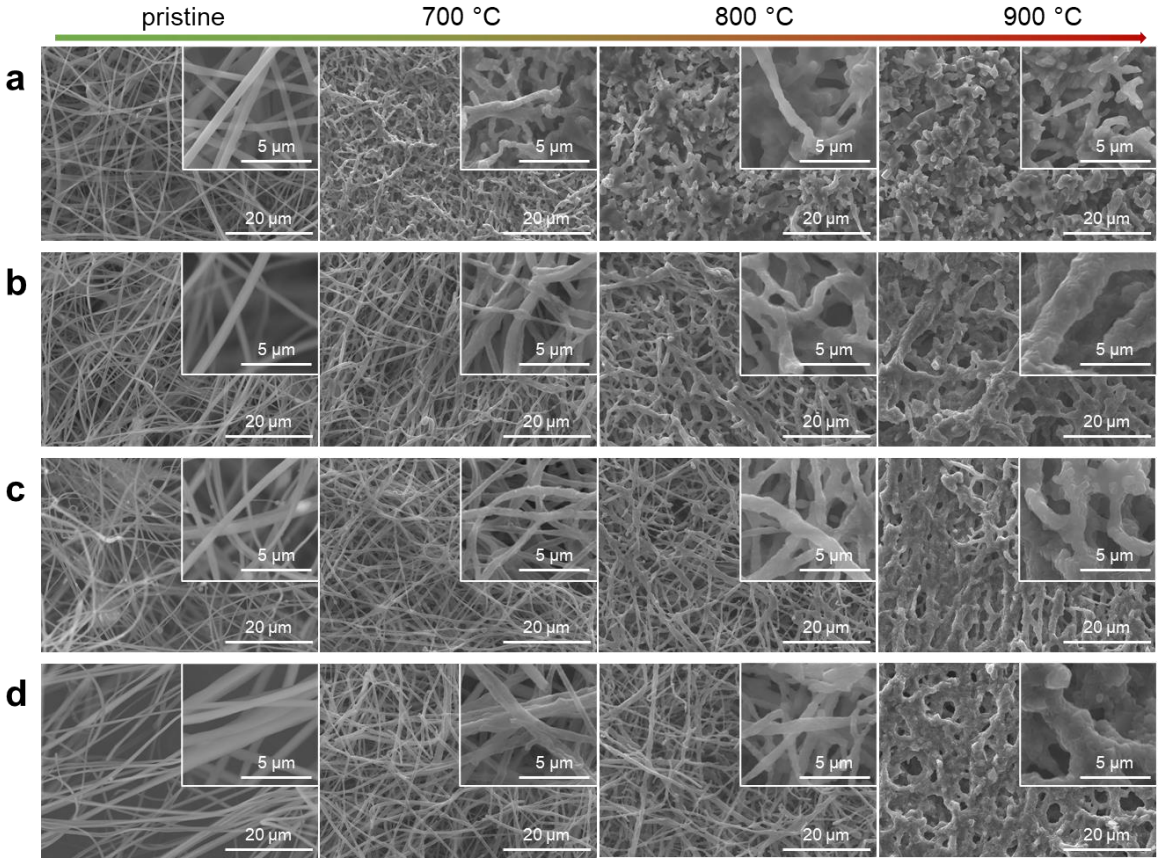

Figure 7.2 SEM images of pristine and calcined (a) LAGP, (b) LAGTP01, (c) LAGTP02 and (d) LAGTP03 (high magnification details of the fibers in the inset).

Minor peaks can be assigned to phosphate-based compounds, such as $Li_9Al_3(PO_4)_2(P_2O_7)_3$, $AlPO_4$, TiP_2O_7 and $Li_4P_2O_7$. Considering the low temperature and short time of calcination, a great improvement in terms of purity has been achieved. Comparing the XRD patterns of LAGTP samples with the one of LAGP prepared under the same conditions, we can see that, although some impurity phases ($Li_9Al_3(PO_4)_2(P_2O_7)_3$ and $AlPO_4$) are still present, their peaks are fewer and less intense. No peaks associated with GeP_2O_7 have been detected. A small peak around 24° is probably due to the presence of $Li_4P_2O_7$ traces, as confirmed later by ^{7}Li MAS-NMR. In LAGPT03 the small peak detected around 32.6° is ascribable to an impurity phase of TiP_2O_7, probably due to the increased Ti content, which caused a minor phase segregation. Both $Li_4P_2O_7$ and TiP_2O_7 are often reported as common secondary phases of Li-based NASICON materials.[247,264,265] Moreover, by increasing the amount of Ti addition, the samples become less crystalline as suggested by the broadening of the peaks and the appearance of a small hump at about 14°. Although increasing the calcination temperature proved to be beneficial for both purity and crystallinity of the NASICON phase, as shown in **Figure 7.3b,c**, the amorphous peak still grows with Ti content.

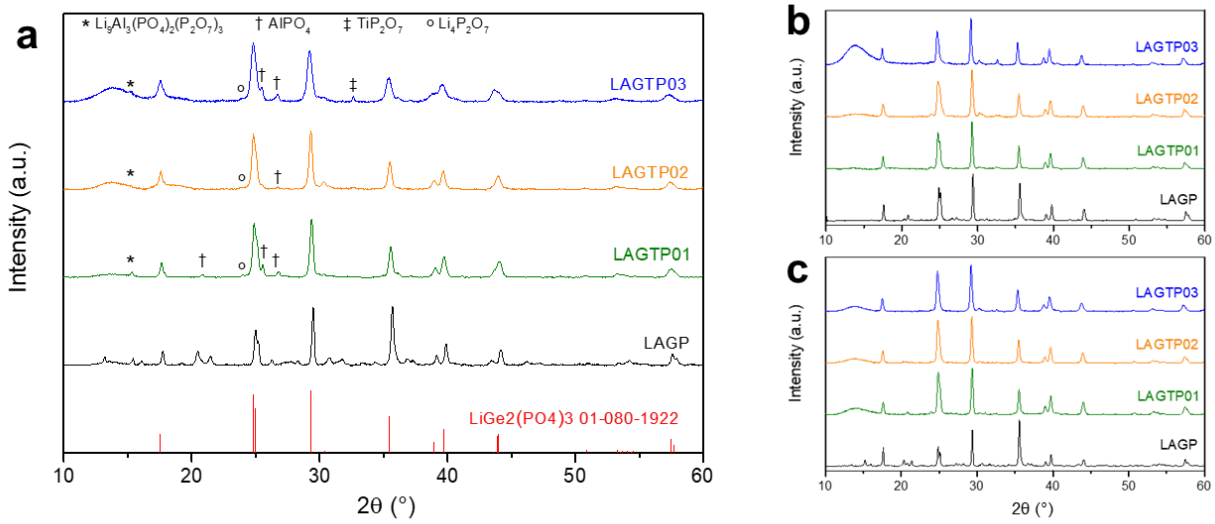

Figure 7.3 XRD patterns of LAGP, LAGTP01 LAGTP02 and LAGTP03 calcined at (a) 700 °C, (b) 800°C and (c) 900 °C. ((*): $Li_9Al_3(PO_4)_2(P_2O_7)_3$; (†): $AlPO_4$; (‡): TiP_2O_7; (°): $Li_4P_2O_7$).

EDS analysis was carried out to assess how the distribution of the elements, particularly of Al, Ge and Ti, changes across the sample when Ti content increases. **Figure 7.4a,b** show the elemental maps of LAGTP01 and LAGTP02. All the elements are uniformly distributed across both samples, except Al which seems to be more concentrated in fiber junctions. This could be related to a potentially lower

mobility of Al ions during LAGTP crystallization, which, associated with the fiber confinement, makes the three-dimensional diffusion less effective. These Al-rich areas could be also related to the impurities observed in the XRD patterns of both LAGTP01 and LAGTP02, specifically $Li_9Al_3(PO_4)_2(P_2O_7)_3$ and $AlPO_4$. Comparing LAGTP01 and LAGTP02, the latter appears to be characterized by fewer Al-rich areas, and thus a more homogeneous Al distribution. This aspect is in good agreement with what we observed in the XRD characterization, where LAGTP02 appeared as the purest sample. The elemental mapping of LAGTP03 is displayed in **Figure 7.4c**. Some Al-rich areas are noticeable, as observed for the other samples. Furthermore, some fibers appear rich in Ge and poor in Ti, which can be related to a competitive behaviour of the two elements during the crystallization process.

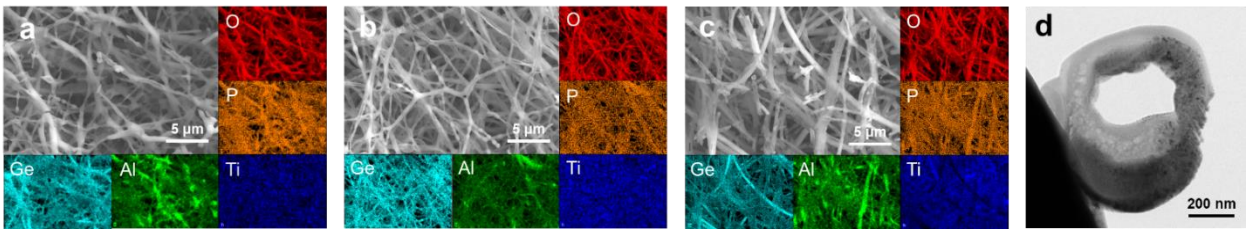

Figure 7.4 SEM/EDS analysis of (a) LAGTP01, (b) LAGTP02 and (c) LAGTP03. (d) Cross-sectional TEM image of a hollow LAGTP01 fiber.

This result correlates well with the presence of the TiP_2O_7 impurity observed in the XRD pattern of LAGTP03, which indicates a partial segregation of Ti in the form of a secondary phase. Ge-rich fibers are mostly visible in Ge and O mapping. We can speculate that they are mostly composed of an amorphous phase of germanium oxide, which is in good agreement with the hump observed in all the XRD patterns, especially in the LAGTP03 one.

During SEM analysis several hollow fibers have been detected in all three LAGTP samples. We thus acquired high-magnification cross-sectional TEM images on a single hollow fiber, as displayed in **Figure 7.4d** for LAGTP01. This phenomenon could be related to a high polymer content in the core part of some specific fibers, which coupled with a potentially low three-dimensional ionic diffusion due to the short calcination times employed, can produce cavities and hollow structures. The hollow structure of the fiber could derive from the crystallization mechanism of the NASICON phase; therefore, it could be also associated with different purity and elemental distribution on the material surface. To better assess these effects, we performed a local EDS analysis on both the inner and the outer surface of the same fiber. Different Ge/Ti ratios have been recorded, i.e. 18 and 5, in the inner and outer surface respectively. This can be ascribed to a higher concentration of Ti on the outer

surface of the fibers. The uneven distribution of Ge and Ti observed in a single hollow fiber could be related to a different mobility of the metal ions throughout LAGTP crystallization. Conversely, Al content appears constant throughout the fiber.

A comparison of the ^{7}Li MAS NMR spectra of the three LAGTP samples is shown in **Figure 7.5a**. All spectra can be described as a combination of three components centered at ~0 ppm. C_Q values of the first two components are equal to 50 kHz and 10 kHz. The corresponding signals can be assigned to the Li ions located at M1 and M3 sites of the NASICON structure. The third component is characterized by a significantly higher C_Q (165 kHz). Probably it's ascribable to some impurities, such as $Li_4P_2O_7$ and $Li_9Al_3(PO_4)_2(P_2O_7)_3$ whose signals have been also detected in ^{31}P NMR. Two peaks at -18 and 38 ppm are observed in ^{27}Al NMR spectra of all the samples (**Figure 7.5b**).[225] The first signal corresponds to AlO_6 units of LAGP (and, probably, of $Li_9Al_3(P_2O_7)_3(PO_4)_2$), while the second signal can be ascribed to AlO_4 units, typical of $AlPO_4$ structure. As opposed to what we previously observed with LAGP,[199] a single phase of $AlPO_4$ is presumably present as impurity in LAGTP samples. The amount of AlO_4 is slightly higher in LAGTP02, than in LAGTP01 and LAGTP03. In ^{31}P NMR, displayed in **Figure 7.5c**, signals of $P(OGe)_{4-m}(OAl)_m$ with m = 0, 1, 2 and 3 can be identified at -42, -37, -32 and -27 ppm respectively.[225] The fraction of P0 site is reducing with the increase of Ti content, from 40% in LAGTP01 to 27% in LAGTP02 and 18% in LAGTP03. Signals of $Li_4P_2O_7$ and $Li_9Al_3(P_2O_7)_3(PO_4)_2$ are also visible in the spectrum at -4 ppm and -16 ppm, respectively. Potential signals of $AlPO_4$, which resulted in ^{27}Al NMR spectra, should be located around -30 ppm and probably overlap with the peaks of P_2 and P_3 present in the same area.

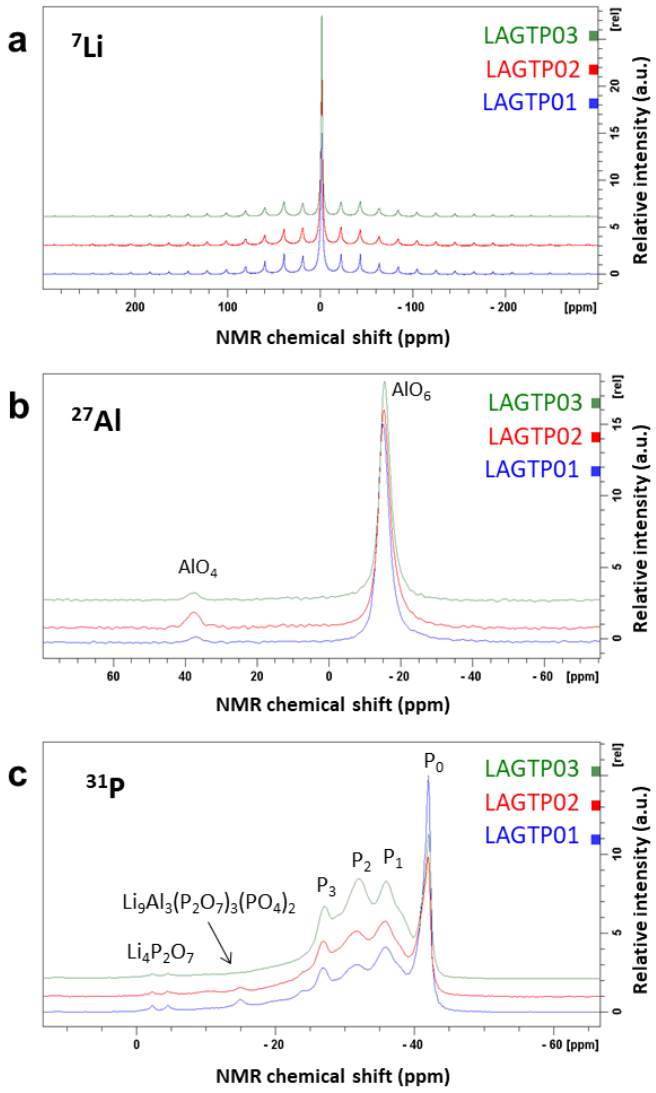

Figure 7.5 (a) ^{7}Li, (b) ^{27}Al and (c) ^{31}P MAS NMR of LAGTP01, LAGTP02 and LAGTP03.

It is worth noting that P_2 and P_3 signals are sharp and well-spaced, in contrast to what we observed in the ^{31}P NMR spectrum of LAGP.[199] This is probably due to the lower content of impurity phases detected in LAGTP samples, which results in a lower number of signals in that region. No relevant differences have been noticed in the spectra of the three samples analyzed, except for the expected reduction of P0 site ($P(OGe)_4$) with the increase of Ti content (fraction of P0 in LAGTP01, LAGTP02, and LAGTP03 equals to 40%, 27% and 18% respectively).

To estimate the ionic conductivity of ceramic LAGTP fibers, we performed EIS analysis on LAGTP01, LAGTP02 and LAGTP03 nanofibrous pellets. They have been placed in a coin cell between stainless steel blocking electrodes (**Figure 7.6a**) and tested in a temperature range of 20-80 °C. The corresponding Arrhenius plot is shown in **Figure 7.6b**, where the ionic conductivity values

are compared with those of plain LAGP. LAGTP02 is the only one displaying a conductivity higher than that of LAGP, while the values achieved for LAGTP01 and LAGTP03 are about 1/5 and 1/3 of LAGP's one. However, it is worth noting that the porosity values of LAGTP samples (93±3%), are significantly higher than the value reported for LAGP (81±2%).[199] The higher porosity is certainly detrimental for the final ionic conductivity of the samples, however, achieved values are in line with what we previously observed by plotting LAGP ionic conductivity against its density. Hence, it is plausible to assert that at equal porosity the ionic conductivity of LAGTP is higher than LAGP one.

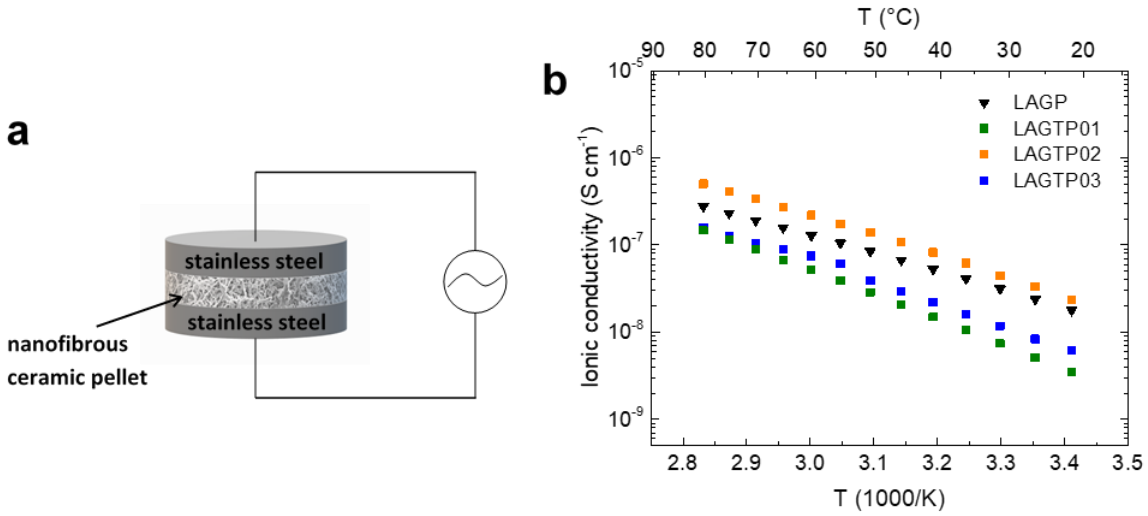

Figure 7.6 (a) Scheme of the setup used for EIS analysis of LAGTP nanofibrous pellets. (b) Arrhenius plot in a temperature range of 20-80 °C of ceramic LAGTP nanofibers compared to LAGP ones.

To evaluate the potential application of LAGTP nanofibers as fillers they have been added to a matrix of PEO:LiTFSI to achieve the corresponding composite electrolytes, i.e. CE-LAGTP01, CE-LAGTP02 and CE-LAGTP03. Only LAGTP nanofibers prepared at 700 °C were tested as fillers in order to compare the results with those we previously reported for LAGP nanofibers. Moreover, essential properties, such as density and ionic conductivity, were impossible to measure for the nanofibrous pellets prepared at 800 and 900 °C because of the formation of fractures during the calcination step. The dimensions of the nanofibers and their distribution into the polymer matrix have been investigated by SEM. The images are shown in **Figure 7.7a-e** along with those of CE-LAGP and CE-LATP. As mentioned above, while discussing the SEM images of ceramic LAGTP fibers (**Figure 7.2**), the addition of Ti has been beneficial for the morphology of the fibers. This improved morphology, allows them to maintain their integrity while dispersing them in the electrolyte slurry. LAGTP fillers are indeed characterized by a pronounced elongated shape that better resembles fibers when compared to LAGP ones (**Figure 7.7a**). Moreover, LAGTP fibers appear longer than LAGP

counterpart, approaching a length of 20 µm. These aspects are of great significance in regards of the electrochemical performance of the electrolytes. Longer and more uniformly shaped fibers can provide fast and continuous paths for ionic transport between the electrodes, thus improving the performance of the electrolyte at room temperature.

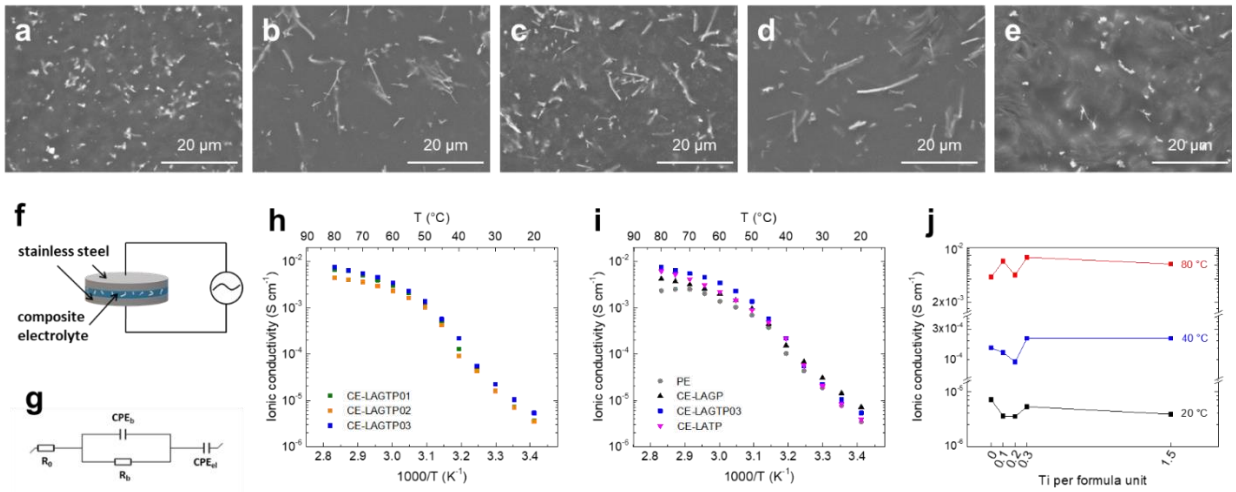

Figure 7.7 SEM images of (a) CE-LAGP, (b) CE-LAGTP01, (c) CE-LAGTP02, (d) CE-LAGTP03 and (e) CE-LATP. (f) Scheme of the setup used for EIS analysis of composite and polymer electrolytes. (g) Equivalent circuit used for EIS data fitting. Representative Arrhenius plot in a temperature range of 20-80 °C of (h) CE-LAGTP electrolytes and (i) LAGTP03 compared to PE, CE-LAGP and CE-LATP. (j) Ionic conductivity at 20, 40 and 80 °C vs. Ti content.

To investigate if the improved morphology and purity resulted in a faster ionic conduction, EIS analyses were performed on LAGTP based composite electrolytes. The results have been compared with those achieved with CE-LAGP and PE we previously reported,[199] and with CE-LATP, specifically prepared as reference. Each electrolyte was placed in a coin cell between stainless steel blocking electrodes, as per the setup shown in **Figure 7.7f**. EIS spectra, acquired between 20 and 80 °C, have been fitted using the equivalent circuit depicted in **Figure 7.7g**. Resulting data are displayed in the form of Arrhenius plot in **Figure 7.7h,i**. **Figure 7.7h** shows how the ionic conductivity of LAGTP samples changes with the temperature. All the plots have the characteristic two-slope behaviour, typical of PEO-based polymer electrolytes, where the two sections are divided by the PEO melting point. The best performing of the three LAGTP-based composite electrolytes, i.e. CE-LAGTP03 has been selected and compared with CE-LAGP, CE-LATP and PE (**Figure 7.7i**). At 20 °C, CE-LAGP, appears to be the most conductive, while CE-LAGTP03 is, as expected, right between CE-LAGP and CE-LATP, with an ionic conductivity of 5.3×10^{-6} S cm^{-1}. At 40 °C, CE-LAGTP03 is characterized by a higher ionic conductivity (2.2×10^{-4} S cm^{-1}) compared to both CE-LAGP and CE-LATP, which remains higher up to 80 °C, where it equals 7.5×10^{-3} S cm^{-1}. The presence of Ti appears

to positively affect the ionic transport above 40 °C. This aspect is more apparent in **Figure 7.7j**, where the ionic conductivity at 20, 40 and 80 °C is plotted against the Ti content per formula unit. While CE-LAGTP01 and CE-LAGTP02 are characterized by ionic conductivities lower than those of CE-LAGP, especially at low temperatures, the substitution of 20% of Ge by Ti improve the ionic transport. The effect is even more marked at higher temperatures and confirmed by the values achieved with CE-LATP. The partial substitution of Ge by Ti did not cause any significant improvement in ionic conductivity, compared to the unsubstituted LAGP. This was expected since, most of the reported Li1+xAlxGeyTi2-x-y(PO4)3 structures are characterized by ionic conductivity values lower or comparable to those reported for the Li1.5Al0.5Ge1.5(PO4)3 and Li1.3Al0.3Ti1.7(PO4)3 parent structures.[70,72,266] Moreover, while the improvement of the fillers' ionic conductivity could be beneficial for the conductivity of the composite electrolyte, it is not a foregone conclusion. In a composite polymer electrolyte, several other aspects can affect the final ionic conductivity, such as the interactions between fillers and polymer as well as the influence of the fillers' addition on the crystallinity of the polymer. Modifying the chemistry and the morphology of the ceramic fillers can have a significant impact on these phenomena.

7.3 Conclusions and perspectives

In summary, we investigated the effect of the partial substitution of Ge by Ti on the properties of LAGP nanofibers. We successfully synthesized ceramic LAGTP nanofibers by electrospinning and subsequent calcination. Regarding the morphology we observed more uniform and defined fibers with no coral-like structures. LAGTP fibers are also characterized by a higher purity when compared to plain LAGP ones. Ceramic fibers have been then dispersed in a polymer matrix to achieve composite polymer electrolytes. Ti substitution did not significantly affect the final ion-conduction properties of the composite electrolytes, although a minor increase of conductivity was observed above 40°C for CE-LAGTP03. While no big improvements are observed from the performance point of view, we believe that a partial substitution of Ge with Ti can be a suitable strategy to improve the purity of LAGP synthesized by solution-based methods, such as sol–gel. Moreover, the presence of Ti affects the crystallization of the NASICON phase, as demonstrated by the improved fiber morphology.

While most of the research efforts are dedicated to the discovery of the ultimate solid electrolyte for ASSLBs, the optimization of the already known materials is currently a valid alternative. In this framework, every detail enabling a more effective and efficient synthesis can boost progress along the

path towards the industrial production. We thus believe that the findings reported in this work can be a significant contribution for the ongoing optimization and the future development of the synthesis methods of NASICON based electrolytes.

8 Summary and outlook

In this chapter some general conclusions of this thesis are provided. In addition, some perspectives and suggestions for future works related to the projects of this thesis are discussed.

Solid electrolytes, either polymeric, ceramic or hybrid, proved to be a promising alternative to liquid electrolytes. Their development can certainly boost the technological achievement of all-solid-state devices, which can revolutionize the energy storage field. The integration of a solid layer between the battery's electrodes can be advantageous for the safety of the device, since it can mechanically prevent the growth of dendrites due to the uneven deposition of lithium. Moreover, replacing the organic and flammable liquid electrolyte, currently used in commercial LIBs, eliminates the risk of fire and explosion. However, the advantages are not only in terms of safety, but they concern the performance too. The potential introduction of metallic lithium as anode, which is safely feasible only in presence of a solid electrolyte, can at least double the energy density of the cell. Another improvement at the single cell level corresponds to the cathode formulation, which in LIBs must be porous to let the liquid medium penetrate in order to ensure a homogeneous ionic transport. In presence of a solid electrolyte, however, the cathode can be fabricated as a dense layer, with the addition of just an additive that ensures a good ionic conduction, such as particles of the electrolyte material itself. With this strategy, a generally denser cell can be achieved, which is significantly beneficial for the volumetric energy density of the device. As shown in **Figure 1.7**, the all-solid-state technology is advantageous also at cell stack and battery pack levels, since the removal of current collectors, cooling system and safety devices enables the achievement of a more compact device.

Polymer electrolytes have been continuously studied for decades; however, they compare unfavourably with the commercial liquid counterparts. Specifically, the performance at room temperature is lower than that provided by liquid electrolytes. Hence, polymer electrolytes are promising candidates for application at medium-high temperature, at which the polymer softens or melts, thus delivering better performance.

In this framework, inorganic electrolytes based on ceramic materials attracted considerable attentions. Despite the ultimate ceramic electrolyte has not been discovered yet, several promising classes of materials are currently under scientific investigation. All of them present several interesting properties, but they are still characterized by significant issues that hinder their commercial deployment. A common challenge with ceramic electrolytes is certainly the formation of a homogeneous and stable

interface with both electrodes. Additionally, the preparation of pure and dense pellets usually involves steps at high temperatures and pressures, which are complex and costly.

An interesting family of ion-conductive ceramics is represented by Li-based NASICON materials. Especially, LATP and LAGP structures have been investigated for their high ionic conductivity, good chemical stability and relatively low cost.

In this thesis, we focused at first on the optimization of the solid-state synthesis of LATP (**Chapter 4**). By using HTXRD technique, we investigated the effect of two different TiO_2 phases as precursor materials. We observed that, when anatase TiO_2 is used as Ti source, LATP starts crystallizing at a lower temperature, while the use of rutile TiO_2 ensures a purer product. These aspects, along with the morphology of the particles, affect the densification process during the hot-pressing step and thus the ionic conductivity of the resulting pellets. All these findings are crucial for the optimization of the synthetic process. Selecting the best precursor material and the proper synthesis temperature can lower the cost and improve the current methods, which are fundamental aspects for the achievement of the industrial upscale and the future deployment of all-solid-state batteries.

In the second part of this thesis, described in **Chapter 5**, we investigated the effects of the morphology on the properties of LATP electrolytes. On the basis of a synthetic approach, which combines sol–gel method and electrospinning technique, we optimized the stoichiometry to enhance the ionic conductivity. Then, we investigated the effects of a 150 MPa pressure, applied on the pristine membrane, prior to the calcination step. We observed that the higher density negatively affects purity, morphology and homogeneity of LATP. However, it resulted beneficial for achieving a high ionic conductivity of 3×10^{-5} S cm^{-1}, i.e. only one order of magnitude lower than that of the bulk material. LATP nanofibers thus proved to be a promising candidate as both a base for developing ceramic electrolytes and an active filler/scaffold for composite polymer electrolytes.

The promising results achieved in the previous part of the project led us to perform various attempts to directly adapt the method employed for the preparation of LATP to the synthesis of LAGP nanofibers. However, a suitable Ge precursor could not be found. Thus, we developed a novel synthesis, based on $GeCl_4$ as Ge source, to fabricate ceramic LAGP nanofibers. The full-ceramic mat showed an ionic conductivity above the expected value. LAGP nanofibers were then used as fillers for PEO:LiTFSI-based electrolytes, leading to an ionic conductivity that was double that of the filler-free polymer electrolyte, since they can provide long ion-conductive paths and decrease PEO

crystallinity. These findings confirmed that NASICON nanofibers are suitable fillers for the development of composite polymer electrolytes for lithium batteries.

In the last part of the project, we merged the interesting results achieved with both LATP and LAGP nanofibers, thus investigating the effect of the partial substitution of Ge by Ti on the properties of LAGP nanofibers. We observed that Ti-substitution enables the achievement of more uniform and defined fibers, as well as higher purity when compared to plain LAGP fibers. Hence, the addition of a Ti precursor evidently affects both the electrospinning process and the crystallization of LAGTP during the calcination step. Finally, LAGTP nanofibers were added to a PEO:LiTFSI-based electrolyte. Compared to the LAGP-filled electrolyte, the addition of LAGTP nanofibers did not lead to any significant improvement in terms of room-temperature ionic conductivity. However, above 40 °C a minor enhancement of the conductivity has been observed. While no big improvements are observed from the performance point of view, we believe that a partial substitution of Ge with Ti can be a suitable strategy to improve the purity of LAGP synthesized by solution-based methods, such as sol–gel.

8.1 Perspectives

Nowadays the research effort is mainly focused on the discovery of the ultimate solid electrolyte material. However, all the materials proposed up to now have advantages but also drawbacks that need to be addressed. This means that more resources should be invested into the optimization of currently known materials, and especially into finding suitable solutions to all the issues and challenges they present. While ceramic solid electrolytes are the most promising class of Li-ion conductive materials for the next-generation energy storage devices, they are still characterized by intrinsic issues that must be solved in order to achieve the commercial deployment of ASSLBs. Recently, materials characterized by ionic conductivities comparable to liquid media have been reported, which represent breakthrough discoveries; however, other aspects are crucial for achieving their industrial production as well as a perfectly operational battery, which are often overlooked. For example, while most researchers are racing towards reaching the highest ionic conductivity, more attention should be oriented towards improving the interface between solid electrolyte and electrodes, which is probably the most serious problem of the all-solid-state technologies. On this aspect, an effective strategy to achieve a better contact between the electrolyte and the electrodes, is the development of a composite polymer electrolyte. Polymers, for their intrinsic physical properties, such as flexibility and mechanical

strength, are optimal to achieve a stable and homogenous interface with the electrode's surface. Apply coatings of different materials on the ceramic pellet to form an interlayer between electrolyte and electrode can also be a suitable strategy.

In this framework, 1D or, more generally, nanostructured materials, can provide peculiar properties towards the development of advanced functional materials. The use of nanofibers and nanowires as active fillers for the development of composite polymer electrolytes is already a common practice. They proved to be beneficial for the improvement of the mechanical and the electrochemical properties of the electrolyte. However, there are several potential applications for ceramic nanostructured materials. Ceramic nanofibrous mats, for example, can be used as reinforcing scaffold in both electrolytes and electrodes, and at the same time they can provide fast and continuous paths for Li ions conduction. Nanowires can be used as basis to develop dense full-ceramic electrolytes, since they proved to be effective for achieving more efficient packings and thus higher densities.

Furthermore, various synthesis processes should be reconsidered while having in mind their potential industrial upscale. Most of the methods used for the synthesis of ceramic materials involve long high-temperature steps and high-energy mixing techniques, which are not suitable for large scale productions. Hence, already known synthetic routes should be optimized, while novel approaches involving easier and less expensive steps should be developed.

9 Bibliography

1 International Energy Agency, *Global Energy Review 2021*, 2021.

2 O. Hoegh-Guldberg, D. Jacob and M. Taylor, *Impacts of 1.5°C of Global Warming on Natural and Human Systems (An IPCC Special Report)*, 2018.

3 J. B. Goodenough and Y. Kim, *Chemistry of Materials*, 2010, **22**, 587–603.

4 B. Dunn, H. Kamath and J.-M. Tarascon, *Science*, 2011, **334**, 928–935.

5 T. Nagaura and K. Tozawa, *Progress in Batteries and Solar Cells*, 1990, **9**, 209.

6 J. Janek and W. G. Zeier, *Nature Energy*, 2016, 1, 1–4.

7 Federal Consortium for Advanced Batteries, *National Blueprint for Lithium Batteries 2021-2030*, 2021.

8 E. Emilsson and L. Dahllöf, *Lithium-Ion Vehicle Battery Production – Status 2019 on Energy Use, CO2 Emissions, Use of Metals, Products Environmental Footprint, and Recycling*, 2019.

9 M. Armand and J.-M. Tarascon, *Nature*, 2008, **451**, 652–657.

10 D. Lin, Y. Liu and Y. Cui, *Nature Nanotechnology*, 2017, **12**, 194–206.

11 K. Brandt, *Solid State Ionics*, 1994, **69**, 173–183.

12 L. Fan, S. Wei, S. Li, Q. Li and Y. Lu, *Advanced Energy Materials*, 2018, 8, 1–31.

13 J.-M. Tarascon and M. Armand, *Nature*, 2001, **414**, 359–367.

14 W. Xu, J. Wang, F. Ding, X. Chen, E. Nasybulin, Y. Zhang and J. G. Zhang, *Energy and Environmental Science*, 2014, **7**, 513–537.

15 B. Wu, S. Wang, J. Lochala, D. Desrochers, B. Liu, W. Zhang, J. Yang and J. Xiao, *Energy and Environmental Science*, 2018, **11**, 1803–1810.

16 D. Aurbach, E. Pollak, R. Elazari, G. Salitra, C. S. Kelley and J. Affinito, *Journal of The Electrochemical Society*, 2009, **156**, A694.

17 W. Li, H. Yao, K. Yan, G. Zheng, Z. Liang, Y. M. Chiang and Y. Cui, *Nature Communications*, 2015, **6**, 7436.

18 J. Li, C. Ma, M. Chi, C. Liang and N. J. Dudney, *Advanced Energy Materials*, 2015, **5**, 1–6.

19 T. Bartsch, F. Strauss, T. Hatsukade, A. Schiele, A. Y. Kim, P. Hartmann, J. Janek and T. Brezesinski, *ACS Energy Letters*, 2018, **3**, 2539–2543.

20 T. Inoue and K. Mukai, *ACS Applied Materials and Interfaces*, 2017, **9**, 1507–1515.

21 T. Famprikis, P. Canepa, J. A. Dawson, M. S. Islam and C. Masquelier, *Nature Materials*, 2019, **18**, 1278–1291.

22 T. Knoche, V. Zinth, M. Schulz, J. Schnell, R. Gilles and G. Reinhart, *Journal of Power Sources*, 2016, **331**, 267–276.

23 J. Schnell, T. Günther, T. Knoche, C. Vieider, L. Köhler, A. Just, M. Keller, S. Passerini and G. Reinhart, *Journal of Power Sources*, 2018, **382**, 160–175.

24 P. H. L. Notten, F. Roozeboom, R. A. H. Niessen and L. Baggetto, *Advanced Materials*, 2007, **19**, 4564–4567.

25 H. Nishide and K. Oyaizu, *Science*, 2008, **319**, 737–738.

26 D. E. Fenton, J. M. Parker and P. V. Wright, *Polymer*, 1973, **14**, 589.

27 L. Long, S. Wang, M. Xiao and Y. Meng, *Journal of Materials Chemistry A*, 2016, **4**, 10038–10039.

28 J. L. Sudworth, *Journal of Power Sources*, 2001, **100**, 149–163.

29 J. B. Bates, N. J. Dudney, G. R. Gruzalski, R. A. Zuhr, A. Choudhury, C. F. Luck and J. D. Robertson, *Journal of Power Sources*, 1993, **43**, 103–110.

30 Y. Inaguma, C. Liquan, M. Itoh, T. Nakamura, T. Uchida, H. Ikuta and M. Wakihara, *Solid State Communications*, 1993, **86**, 689–693.

31 H. Aono, E. Sugimoto, Y. Sadaoka, N. Imanaka and G. Y. Adachi, *Journal of the Electrochemical Society*, 1990, **137**, 1023–1027.

32 R. Murugan, V. Thangadurai and W. Weppner, *Angewandte Chemie - International Edition*, 2007, **46**, 7778–7781.

33 N. Kamaya, K. Homma, Y. Yamakawa, M. Hirayama, R. Kanno, M. Yonemura, T. Kamiyama, Y. Kato, S. Hama, K. Kawamoto and A. Mitsui, *Nature Materials*, 2011, **10**, 682–686.

34 Y. Saito, H. Kataoka, E. Quartarone and P. Mustarelli, *The Journal of Physical Chemistry B*, 2002, **106**, 7200–7204.

35 H. Kataoka, Y. Saito, T. Sakai, E. Quartarone and P. Mustarelli, *Journal of Physical Chemistry B*, 2000, **104**, 11460–11464.

36 S. Abbrent, J. Plestil, D. Hlavata, J. Lindgren, J. Tegenfeldt and Å. Wendsjö, *Polymer*, 2001, **42**, 1407–1416.

37 V. Arcella, A. Sanguineti, E. Quartarone and P. Mustarelli, *Journal of Power Sources*, 1999, **81–82**, 790–794.

38 G. B. Appetecchi, F. Croce and B. Scrosati, *Electrochimica Acta*, 1995, **40**, 991–997.

39 O. Bohnke, G. Frand, M. Rezrazi, C. Rousselot and C. Truche, *Solid State Ionics*, 1993, **66**, 97–104.

40 O. Bohnke, G. Frand, M. Rezrazi, C. Rousselot and C. Truche, *Solid State Ionics*, 1993, **66**, 105–112.

41 G. Dautzenberg, F. Croce, S. Passerini and B. Scrosati, *Chemistry of Materials*, 1994, **6**, 538–542.

42 R. XUE, H. HUANG, L. CHEN and K. WANG, *Solid State Ionics*, 1993, **59**, 1–4.

43 J. C. Bachman, S. Muy, A. Grimaud, H. H. Chang, N. Pour, S. F. Lux, O. Paschos, F. Maglia, S. Lupart, P. Lamp, L. Giordano and Y. Shao-Horn, *Chemical Reviews*, 2016, **116**, 140–162.

44 J. B. Bates, N. J. Dudney, G. R. Gruzalski, R. A. Zuhr, A. Choudhury, C. F. Luck and J. D. Robertson, *Solid State Ionics*, 1992, **53–56**, 647–654.

45 J. B. Bates, N. J. Dudney, D. C. Lubben, G. R. Gruzalski, B. S. Kwak, X. Yu and R. A. Zuhr, *Journal of Power Sources*, 1995, **54**, 58–62.

46 J. B. Bates, N. J. Dudney, B. Neudecker, A. Ueda and C. D. Evans, *Solid State Ionics*, 2000, **135**, 33–45.

47 C. Sun, J. Liu, Y. Gong, D. P. Wilkinson and J. Zhang, *Nano Energy*, 2017, **33**, 363–386.

48 R. Chen, W. Qu, X. Guo, L. Li and F. Wu, *Materials Horizons*, 2016, **3**, 487–516.

49 B. A. Boukamp and R. A. Huggins, *Physics Letters A*, 1976, **58**, 231–233.

50 Y. -W. Hu, I. D. Raistrick and R. A. Huggins, *Journal of The Electrochemical Society*, 1977, **124**, 1240–1242.

51 H. Y. P. Hong, *Materials Research Bulletin*, 1978, **13**, 117–124.

52 H. Kim, Y. Ding and P. A. Kohl, *Journal of Power Sources*, 2012, **198**, 281–286.

53 R. Bouchet, S. Maria, R. Meziane, A. Aboulaich, L. Lienafa, J. Bonnet, T. N. T. Phan, D. Bertin, D. Gigmes, D. Devaux, R. Denoyel and M. Armand, *Nature Materials*, 2013, **12**, 452–457.

54 M. Murayama, R. Kanno, M. Irie, S. Ito, T. Hata, N. Sonoyama and Y. Kawamoto, *Journal of Solid State Chemistry*, 2002, **168**, 140–148.

55 P. Bron, S. Johansson, K. Zick, J. Schmedt auf der Guenne, S. Dehnen and B. Roling, *Journal of the American Chemical Society*, 2013, 15694–15697.

56 J. M. Whiteley, J. H. Woo, E. Hu, K.-W. Nam and S.-H. Lee, *Journal of The Electrochemical Society*, 2014, **161**, A1812–A1817.

57 A. Kuhn, O. Gerbig, C. Zhu, F. Falkenberg, J. Maier and B. V. Lotsch, *Physical Chemistry Chemical Physics*, 2014, **16**, 14669–14674.

58 H.-J. Deiseroth, S.-T. Kong, H. Eckert, J. Vannahme, C. Reiner, T. Zaiß and M. Schlosser, *Angewandte Chemie*, 2008, **120**, 767–770.

59 S. Boulineau, M. Courty, J. M. Tarascon and V. Viallet, *Solid State Ionics*, 2012, **221**, 1–5.

60 V. Thangadurai, S. Narayanan and D. Pinzaru, *Chemical Society Reviews*, 2014, **43**, 4714–4727.

61 V. Thangadurai, H. Kaack and W. J. F. Weppner, *Journal of the American Ceramic Society*, 2003, **86**, 437–440.

62 C. A. Geiger, E. Alekseev, B. Lazic, M. Fisch, T. Armbruster, R. Langner, M. Fechtelkord, N. Kim, T. Pettke and W. Weppner, *Inorganic Chemistry*, 2011, **50**, 1089–1097.

63 C. Sun, J. Liu, Y. Gong, D. P. Wilkinson and J. Zhang, *Nano Energy*, 2017, **33**, 363–386.

64 J. B. Goodenough, H. Y.-P. Hong and J. A. Kafalas, *Materials Research Bulletin*, 1976, **11**, 203–220.

65 B. E. Taylor, A. D. English and T. Berzins, *Materials Research Bulletin*, 1977, **12**, 171–181.

66 V. Thangadurai, A. K. Shukla and J. Gopalakrishnan, *Journal of Materials Chemistry*, 1999, **9**, 739–741.

67 M. Monchak, T. Hupfer, A. Senyshyn, H. Boysen, D. Chernyshov, T. Hansen, K. G. Schell, E. C. Bucharsky, M. J. Hoffmann and H. Ehrenberg, *Inorganic Chemistry*, 2016, **55**, 2941–2945.

68 K. Arbi, J. M. Rojo and J. Sanz, *Journal of the European Ceramic Society*, 2007, **27**, 4215–4218.

69 M. Cretin and P. Fabry, *Journal of the European Ceramic Society*, 1999, **19**, 2931–2940.

70 A. Rossbach, F. Tietz and S. Grieshammer, *Journal of Power Sources*, 2018, **391**, 1–9.

71 R. DeWees and H. Wang, *ChemSusChem*, 2019, **12**, 3713–3725.

72 P. Maldonado-Manso, E. R. Losilla, M. Martínez-Lara, M. A. G. Aranda, S. Bruque, F. E. Mouahid and M. Zahir, *Chemistry of Materials*, 2003, **15**, 1879–1885.

73 Z. Liu, S. Venkatachalam and L. van Wüllen, *Solid State Ionics*, 2015, **276**, 47–55.

74 Y. Zhu, X. He and Y. Mo, *ACS Applied Materials and Interfaces*, 2015, **7**, 23685–23693.

75 X. Xu, Z. Wen, X. Wu, X. Yang and Z. Gu, *Journal of the American Ceramic Society*, 2007, **90**, 2802–2806.

76 H. Chung and B. Kang, *Chemistry of Materials*, 2017, **29**, 8611–8619.

77 H. Aono, E. Sugimoto, Y. Sadaoka, N. Imanaka and G. Adachi, *Journal of the Electrochemical Society*, 1989, **136**, 590–591.

78 H. Aono, E. Sugimoto, Y. Sadaoka, N. Imanaka and G. Adachi, *Bulletin of the Chemical Society of Japan*, 1992, **65**, 2200–2204.

79 A. R. West, *Solid State Chemistry and its Applications, 2nd Edition, Student Edition*, Wiley, 2014.

80 B. Key, D. J. Schroeder, B. J. Ingram and J. T. Vaughey, *Chemistry of Materials*, 2012, **24**, 287–293.

81 B. Yan, Y. Zhu, F. Pan, J. Liu and L. Lu, *Solid State Ionics*, 2015, **278**, 65–68.

82 J. Yang, Z. Huang, B. Huang, J. Zhou and X. Xu, *Solid State Ionics*, 2015, **270**, 61–65.

83 B. V. R. Chowdari, G. v. Subba Rao and G. Y. H. Lee, *Solid State Ionics*, 2000, **136–137**, 1067–1075.

84 X. Xu, Z. Wen, X. Yang, J. Zhang and Z. Gu, *Solid State Ionics*, 2006, **177**, 2611–2615.

85 J. S. Thokchom and B. Kumar, *Journal of Power Sources*, 2010, **195**, 2870–2876.

86 P. D. Kichambare, T. Howell and S. Rodrigues, *Energy Technology*, 2014, **2**, 391–396.

87 S. Breuer, D. Prutsch, Q. Ma, V. Epp, F. Preishuber-Pflügl, F. Tietz and M. Wilkening, *Journal of Materials Chemistry A*, 2015, **3**, 21343–21350.

88 M. Zhang, J. Li, K. Takahashi, O. Yamamoto, N. Imanishi, Y. Takeda, B. Chi and J. Pu, *Journal of The Electrochemical Society*, 2012, **159**, A1114–A1119.

89 M. Kotobuki and M. Koishi, *Ceramics International*, 2013, **39**, 4645–4649.

90 M. Kotobuki and M. Koishi, *Ceramics International*, 2015, **41**, 8562–8567.

91 M. Zhang, Z. Huang, J. Cheng, O. Yamamoto, N. Imanishi, B. Chi, J. Pu and J. Li, *Journal of Alloys and Compounds*, 2014, **590**, 147–152.

92 E. Zhao, F. Ma, Y. Jin and K. Kanamura, *Journal of Alloys and Compounds*, 2016, **680**, 646–653.

93 F. Ma, E. Zhao, S. Zhu, W. Yan, D. Sun, Y. Jin and C. Nan, *Solid State Ionics*, 2016, **295**, 7–12.

94 L. Huang, Z. Wen, M. Wu, X. Wu, Y. Liu and X. Wang, *Journal of Power Sources*, 2011, **196**, 6943–6946.

95 M. Kotobuki and M. Koishi, *Journal of Asian Ceramic Societies*, 2019, **7**, 551–557.

96 S. He, Y. Xu, B. Zhang, X. Sun, Y. Chen and Y. Jin, *Chemical Engineering Journal*, 2018, **345**, 483–491.

97 M. Fan, X. Deng, A. Zheng and S. Yuan, *Functional Materials Letters*, 2021, **14**, 2140002.

98 K. M. Kim, D. O. Shin and Y. G. Lee, *Electrochimica Acta*, 2015, **176**, 1364–1373.

99 C. Peng, Y. Kamiike, Y. Liang, K. Kuroda and M. Okido, *ACS Sustainable Chemistry and Engineering*, 2019, **7**, 10751–10762.

100 B. Scrosati and C. A. Vincent, *MRS Bulletin*, 2000, **25**, 28–30.

101 R. C. Agrawal and G. P. Pandey, *Journal of Physics D: Applied Physics*, 2008, **41**, 223001.

102 J. Y. Song, Y. Y. Wang and C. C. Wan, *Journal of Power Sources*, 1999, **77**, 183–197.

103 J. M. G. Cowie and G. H. Spence, *Solid State Ionics*, 1999, **123**, 233–242.

104 R. Meziane, J.-P. Bonnet, M. Courty, K. Djellab and M. Armand, *Electrochimica Acta*, 2011, **57**, 14–19.

105 Y. S. Zhu, X. W. Gao, X. J. Wang, Y. Y. Hou, L. L. Liu and Y. P. Wu, *Electrochemistry Communications*, 2012, **22**, 29–32.

106 Y. S. Zhu, X. J. Wang, Y. Y. Hou, X. W. Gao, L. L. Liu, Y. P. Wu and M. Shimizu, *Electrochimica Acta*, 2013, **87**, 113–118.

107 H. S. Lee, Z. F. Ma, X. Q. Yang, X. Sun and J. McBreen, *Journal of The Electrochemical Society*, 2004, **151**, A1429.

108 H. S. Lee, X. Q. Yang, C. L. Xiang, J. McBreen and L. S. Choi, *Journal of The Electrochemical Society*, 1998, **145**, 2813–2818.

109 D. Andersson, P. Carlsson, D. Engberg, L. M. Torell, L. Börjesson, R. L. McGreevy and W. S. Howells, *Physica B: Condensed Matter*, 1999, **266**, 126–130.

110 C. Vachon, C. Labreche, A. Vallee, S. Besner, M. Dumont and J. Prud'homme, *Macromolecules*, 1995, **28**, 5585–5594.

111 P. M. Blonsky, D. F. Shriver, P. Austin and H. R. Allcock, *Journal of the American Chemical Society*, 1984, **106**, 6854–6855.

112 J. Paulsdorf, M. Burjanadze, K. Hagelschur and H.-D. Wiemhofer, *Solid State Ionics*, 2004, **169**, 25–33.

113 Y. Karatas, R. D. Banhatti, N. Kaskhedikar, M. Burjanadze, K. Funke and H.-D. Wiemhöfer, *The Journal of Physical Chemistry B*, 2009, **113**, 15473–15484.

114 R. Hooper, L. J. Lyons, M. K. Mapes, D. Schumacher, D. A. Moline and R. West, *Macromolecules*, 2001, **34**, 931–936.

115 T. A. Luther, F. F. Stewart, J. L. Budzien, R. A. LaViolette, W. F. Bauer, M. K. Harrup, C. W. Allen and A. Elayan, *The Journal of Physical Chemistry B*, 2003, **107**, 3168–3176.

116 M. Dirican, C. Yan, P. Zhu and X. Zhang, *Materials Science and Engineering R: Reports*, 2019, **136**, 27–46.

117 M. Ue, *Journal of The Electrochemical Society*, 1994, **141**, 3336–3342.

118 G. Feuillade and Ph. Perche, *Journal of Applied Electrochemistry*, 1975, **5**, 63–69.

119 A. Chakrabarti, R. Filler and B. K. Mandal, *Solid State Ionics*, 2010, **180**, 1640–1645.

120 Y. Kim, *Solid State Ionics*, 2002, **149**, 29–37.

121 P. Vickraman and S. Ramamurthy, *Materials Letters*, 2006, **60**, 3431–3436.

122 H.-S. Min, J.-M. Ko and D.-W. Kim, *Journal of Power Sources*, 2003, **119–121**, 469–472.

123 P. Meneghetti, S. Qutubuddin and A. Webber, *Electrochimica Acta*, 2004, **49**, 4923–4931.

124 X. Wang, C. Gong, D. He, Z. Xue, C. Chen, Y. Liao and X. Xie, *Journal of Membrane Science*, 2014, **454**, 298–304.

125 Z. H. Li, C. Cheng, X. Y. Zhan, Y. P. Wu and X. D. Zhou, *Electrochimica Acta*, 2009, **54**, 4403–4407.

126 Z. Wang, B. Huang, H. Huang, L. Chen, R. Xue and F. Wang, *Electrochimica Acta*, 1996, **41**, 1443–1446.

127 H. S. Choe, J. Giaccai, M. Alamgir and K. M. Abraham, *Electrochimica Acta*, 1995, **40**, 2289–2293.

128 A. Mauger, M. Armand, C. M. Julien and K. Zaghib, *Journal of Power Sources*, 2017, **353**, 333–342.

129 J. Weston and B. Steele, *Solid State Ionics*, 1982, **7**, 75–79.

130 F. Croce, R. Curini, A. Martinelli, L. Persi, F. Ronci, B. Scrosati and R. Caminiti, *Journal of Physical Chemistry B*, 1999, **103**, 10632–10638.

131 E. Strauss, D. Golodnitsky, G. Ardel and E. Peled, *Electrochimica Acta*, 1998, **43**, 1315–1320.

132 W. Wieczorek, A. Zalewska, D. Raducha, Z. Florjańczyk and J. R. Stevens, *The Journal of Physical Chemistry B*, 1998, **102**, 352–360.

133 M. A. K. Lakshman Dissanayake, *Ionics*, 2004, **10**, 221–225.

134 K.-S. Ji, H.-S. Moon, J.-W. Kim and J.-W. Park, *Journal of Power Sources*, 2003, **117**, 124–130.

135 J. Xi, X. Qiu, X. Ma, M. Cui, J. Yang, X. Tang, W. Zhu and L. Chen, *Solid State Ionics*, 2005, **176**, 1249–1260.

136 D. Lin, W. Liu, Y. Liu, H. R. Lee, P.-C. Hsu, K. Liu and Y. Cui, *Nano Letters*, 2016, **16**, 459–465.

137 H. Xu, P. H. Chien, J. Shi, Y. Li, N. Wu, Y. Liu, Y. Y. Hu and J. B. Goodenough, *The Proceedings of the National Academy of Sciences*, 2019, **116**, 18815–18821.

138 J. Bae, Y. Li, J. Zhang, X. Zhou, F. Zhao, Y. Shi, J. B. Goodenough and G. Yu, *Angewandte Chemie - International Edition*, 2018, **57**, 2096–2100.

139 J. Zheng, M. Tang and Y. Y. Hu, *Angewandte Chemie - International Edition*, 2016, **55**, 12538–12542.

140 J. Zheng and Y. Y. Hu, *ACS Applied Materials and Interfaces*, 2018, **10**, 4113–4120.

141 M. Keller, G. B. Appetecchi, G. T. Kim, V. Sharova, M. Schneider, J. Schuhmacher, A. Roters and S. Passerini, *Journal of Power Sources*, 2017, **353**, 287–297.

142 W. Zhang, J. Nie, F. Li, Z. L. Wang and C. Sun, *Nano Energy*, 2018, **45**, 413–419.

143 K. Fu, Y. Gong, G. T. Hitz, D. W. McOwen, Y. Li, S. Xu, Y. Wen, L. Zhang, C. Wang, G. Pastel, J. Dai, B. Liu, H. Xie, Y. Yao, E. D. Wachsman and L. Hu, *Energy and Environmental Science*, 2017, **10**, 1568–1575.

144 Y. Gong, K. Fu, S. Xu, J. Dai, T. R. Hamann, L. Zhang, G. T. Hitz, Z. Fu, Z. Ma, D. W. McOwen, X. Han, L. Hu and E. D. Wachsman, *Materials Today*, 2018, **21**, 594–601.

145 H. Huo, Y. Chen, J. Luo, X. Yang, X. Guo and X. Sun, *Advanced Energy Materials*, 2019, **9**, 1–8.

146 L. Chen, Y. Li, S. P. Li, L. Z. Fan, C. W. Nan and J. B. Goodenough, *Nano Energy*, 2018, **46**, 176–184.

147 J. Zhang, N. Zhao, M. Zhang, Y. Li, P. K. Chu, X. Guo, Z. Di, X. Wang and H. Li, *Nano Energy*, 2016, **28**, 447–454.

148 X. W. Zhang, C. Wang, A. J. Appleby and F. E. Little, *Journal of Power Sources*, 2002, **112**, 209–215.

149 W. Wang, E. Yi, A. J. Fici, R. M. Laine and J. Kieffer, *Journal of Physical Chemistry C*, 2017, **121**, 2563–2573.

150 L. Yang, Z. Wang, Y. Feng, R. Tan, Y. Zuo, R. Gao and Y. Zhao, *Advanced Energy Materials*, 2017, **7**, 1701437.

151 X. Ban, W. Zhang, N. Chen and C. Sun, *Journal of Physical Chemistry C*, 2018, **122**, 9852–9858.

152 L. Liu, L. Chu, B. Jiang and M. Li, *Solid State Ionics*, 2019, **331**, 89–95.

153 X. Yu and A. Manthiram, *ACS Applied Materials and Interfaces*, 2020, **3**, 2916–1924.

154 H. Zhai, P. Xu, M. Ning, Q. Cheng, J. Mandal and Y. Yang, *Nano Letters*, 2017, **17**, 3182–3187.

155 X. Wang, H. Zhai, B. Qie, Q. Cheng, A. Li, J. Borovilas, B. Xu, C. Shi, T. Jin, X. Liao, Y. Li, X. He, S. Du, Y. Fu, M. Dontigny, K. Zaghib and Y. Yang, *Nano Energy*, 2019, **60**, 205–212.

156 C. Wang, Y. Yang, X. Liu, H. Zhong, H. Xu, Z. Xu, H. Shao and F. Ding, *ACS Applied Materials and Interfaces*, 2017, **9**, 13694–13702.

157 R. Ramaseshan, S. Sundarrajan, R. Jose and S. Ramakrishna, *Journal of Applied Physics*, 2007, **102**, 111101.

158 H. Wu, W. Pan, D. Lin and H. Li, *Journal of Advanced Ceramics*, 2012, **1**, 2–23.

159 A. la Monaca, A. Paolella, A. Guerfi, F. Rosei and K. Zaghib, *Electrochemistry Communications*, 2019, **104**, 106483.

160 M. Ebelmen, *Annales de chimie et de physique*, 1846, **16**, 129.

161 M. Ebelmen, *Comptes Rendus de l'Académie des Sciences*, 1847, **25**, 84.

162 T. Graham, *Journal of the Chemical Society*, 1864, **17**, 318–327.

163 D. M. Roy and R. Roy, *American Mineralogist*, 1954, **39**, 957–975.

164 R. Roy, *Journal of the American Ceramic Society*, 1956, **39**, 145–146.

165 R. Roy, *Journal of the American Ceramic Society*, 1969, **52**, 344–344.

166 G. J. McCarthy, R. Roy and J. M. McKay, *Journal of the American Ceramic Society*, 1971, **54**, 637–638.

167 R. K. Iler, *The Chemistry of Silica*, Wiley: New York, 1955.

168 L. L. Hench and J. K. West, *Chemical Reviews*, 1990, **90**, 33–72.

169 A. C. Pierre, *Introduction to Sol-Gel Processing*, Springer US, Boston, MA, 1998, vol. 1.

170 A. Greiner and J. H. Wendorff, *Angewandte Chemie - International Edition*, 2007, **46**, 5670–5703.

171 A. Formhals, Process and apparatus for preparing artificial threads, US1975504A, 1934, 1–4.

172 G. I. Taylor, *Proceedings of the Royal Society of London. A. Mathematical and Physical Sciences*, 1969, **313**, 453–475.

173 Lord Rayleigh, *Proceedings of the London Mathematical Society*, 1879, **s1-11**, 57–72.

174 Y. Liu, J.-H. He, J. Yu and H. Zeng, *Polymer International*, 2008, **57**, 632–636.

175 M. Yousefzadeh, in *Electrospun Nanofibers*, Elsevier, 2017, 277–301.

176 T. Yang, Y. Li and C. K. Chan, *Journal of Power Sources*, 2015, **287**, 164–169.

177 W. Liu, N. Liu, J. Sun, P. C. Hsu, Y. Li, H. W. Lee and Y. Cui, *Nano Letters*, 2015, **15**, 2740–2745.

178 W. Liu, S. W. Lee, D. Lin, F. Shi, S. Wang, A. D. Sendek and Y. Cui, *Nature Energy*, 2017, **2**, 17035.

179 L. Zhu, P. Zhu, Q. Fang, M. Jing, X. Shen and L. Yang, *Electrochimica Acta*, 2018, **292**, 718–726.

180 P. Zhu, C. Yan, M. Dirican, J. Zhu, J. Zang, R. K. Selvan, C. C. Chung, H. Jia, Y. Li, Y. Kiyak, N. Wu and X. Zhang, *Journal of Materials Chemistry A*, 2018, **6**, 4279–4285.

181 L. Zhu, P. Zhu, S. Yao, X. Shen and F. Tu, *International Journal of Energy Research*, 2019, **43**, 4854–4866.

182 K. Liu, R. Zhang, J. Sun, M. Wu and T. Zhao, *ACS Applied Materials and Interfaces*, 2019, **11**, 46930–46937.

183 K. Q. He, J. W. Zha, P. Du, S. H. S. Cheng, C. Liu, Z. M. Dang and R. K. Y. Li, *Dalton Transactions*, 2019, **48**, 3263–3269.

184 S. Hu, L. Du, G. Zhang, W. Zou, Z. Zhu, L. Xu and L. Mai, *ACS Applied Materials and Interfaces*, 2021, **13**, 13183–13190.

185 L. Xu, L. Zhang, Y. Hu and L. Luo, *Chemical Communications*, 2021, **57**, 11068–11071.

186 Y. Zhao, Y. Zheng, S. Cai, C. Hu, S. Chen, X. Liu, J. Liu and Z. Liu, *Thin Solid Films*, 2021, **734**, 1–10.

187 H. Yang, K. Tay, Y. Xu, B. Rajbanshi, S. Kasani, J. Bright, J. Boryczka, C. Wang, P. Bai and N. Wu, *Journal of The Electrochemical Society*, 2021, **168**, 110507.

188 H. Yang, J. Bright, B. Chen, P. Zheng, X. Gao, B. Liu, S. Kasani, X. Zhang and N. Wu, *Journal of Materials Chemistry A*, 2020, **8**, 7261–7272.

189 T. Yang, Z. D. Gordon, Y. Li and C. K. Chan, *Journal of Physical Chemistry C*, 2015, **119**, 14947–14953.

190 K. (Kelvin) Fu, Y. Gong, J. Dai, A. Gong, X. Han, Y. Yao, C. Wang, Y. Wang, Y. Chen, C. Yan, Y. Li, E. D. Wachsman and L. Hu, *Proceedings of the National Academy of Sciences*, 2016, **113**, 7094–7099.

191 T. Yang, J. Zheng, Q. Cheng, Y. Y. Hu and C. K. Chan, *ACS Applied Materials and Interfaces*, 2017, **9**, 21773–21780.

192 Z. Wan, D. Lei, W. Yang, C. Liu, K. Shi, X. Hao, L. Shen, W. Lv, B. Li, Q. H. Yang, F. Kang and Y. B. He, *Advanced Functional Materials*, 2019, **29**, 1–10.

193 T. Rosenthal, J. M. Weller and C. K. Chan, *Industrial and Engineering Chemistry Research*, 2019, **58**, 17399–17405.

194 Y. Li, W. Zhang, Q. Dou, K. W. Wong and K. M. Ng, *Journal of Materials Chemistry A*, 2019, **7**, 3391–3398.

195 M. Jing, H. Yang, Chong Han, F. Chen, L. Zhang, X. Hu, F. Tu and X. Shen, *Journal of The Electrochemical Society*, 2019, **166**, A3019–A3027.

196 T. H. Mengesha, S. L. Beshahwured, S.-H. Wu, Y.-S. Wu, R. Jose, S. J. Lue and C.-C. Yang, *ACS Applied Energy Materials*, 2021, **4**, 14554–14574.

197 G. Lancel, P. Stevens, G. Toussaint, M. Maréchal, N. Krins, D. Bregiroux and C. Laberty-Robert, *Langmuir*, 2017, **33**, 9288–9297.

198 A. La Monaca, G. Girard, S. Savoie, H. Demers, G. Bertoni, S. Krachkovskiy, S. Marras, E. Mugnaioli, M. Gemmi, D. Benetti, A. Vijh, F. Rosei and A. Paolella, *Journal of Materials Chemistry A*, 2021, **6**, 13688–13696.

199 A. la Monaca, G. Girard, S. Savoie, G. Bertoni, S. Krachkovskiy, A. Vijh, F. Pierini, F. Rosei and A. Paolella, *Journal of The Electrochemical Society*, 2021, **168**, 110512.

200 Y. Liu and X. Hua, *International Journal of Applied Ceramic Technology*, 2016, **13**, 579–583.

201 M.-X. Jing, H. Yang, C. Han, F. Chen, W.-Y. Yuan, B.-W. Ju, F.-Y. Tu, X.-Q. Shen and S.-B. Qin, *Ceramics International*, 2019, **45**, 18614–18622.

202 A. la Monaca, G. Girard, S. Savoie, R. Veillette, S. Krachkovskiy, F. Pierini, A. Vijh, F. Rosei and A. Paolella, *Nanoscale*, 2022, **14**, 5094–5101.

203 G. Lancel, PhD Thesis, Université Pierre et Marie Curie, 2016.

204 K. He, M. Z. Rong, B. Han, M. Q. Zhang, C. Zu, P. Xie, Y. Wang and B. Li, *RSC Advances*, 2019, **9**, 4157–4161.

205 A. la Monaca, W. Zhu, Z. Feng, G. Bertoni, D. Campanella, G. Girard, S. Savoie, A. G. Nita, D. Clement, H. Demers, A. Vijh, F. Rosei and A. Paolella, *Journal of The Electrochemical Society*, 2022, **169**, 040515.

206 M. Hou, F. Liang, K. Chen, Y. Dai and D. Xue, *Nanotechnology*, 2020, **31**, 132003.

207 K. G. Schell, E. C. Bucharsky, F. Lemke and M. J. Hoffmann, *Ionics*, 2017, **23**, 821–827.

208 E. jeong Yi, K. young Yoon, H. A. Jung, T. Nakayama, M. jung Ji and H. Hwang, *Applied Surface Science*, 2019, **473**, 622–626.

209 M. W. Chase, C. A. Davies, J. R. Downey, D. J. Frurip and A. N. McDonald, R. A. Syverud, *NIST JANAF Thermochemical Tables ver. 1.0*, 1985.

210 W. E. Tenhaeff, E. Rangasamy, Y. Wang, A. P. Sokolov, J. Wolfenstine, J. Sakamoto and N. J. Dudney, *ChemElectroChem*, 2014, **1**, 375–378.

211 A. Kubanska, L. Castro, L. Tortet, O. Schäf, M. Dollé and R. Bouchet, *Solid State Ionics*, 2014, **266**, 44–50.

212 M. Pogosova, I. Krasnikova, A. Sergeev, A. Zhugayevych and K. Stevenson, *Journal of Power Sources*, 2020, **448**, 227367.

213 Z. Huang, L. Chen, B. Huang, B. Xu, G. Shao, H. Wang, Y. Li and C. A. Wang, *ACS Applied Materials and Interfaces*, 2020, **12**, 56118–56125.

214 Q. Xu, C. L. Tsai, D. Song, S. Basak, H. Kungl, H. Tempel, F. Hausen, S. Yu and R. A. Eichel, *Journal of Power Sources*, 2021, **492**, 229631.

215 T. Hupfer, E. C. Bucharsky, K. G. Schell and M. J. Hoffmann, *Solid State Ionics*, 2017, **302**, 49–53.

216 W. Xiao, J. Wang, L. Fan, J. Zhang and X. Li, *Energy Storage Materials*, 2019, **19**, 379–400.

217 X. Shi, N. Ma, Y. Wu, Y. Lu, Q. Xiao, Z. Li and G. Lei, *Solid State Ionics*, 2018, **325**, 112–119.

218 Z. Luo, C. Qin, W. Xu, H. Liang, W. Lei, X. Shen and A. Lu, *Ceramics International*, 2020, **46**, 15613–15620.

219 R. Kahlaoui, K. Arbi, R. Jimenez, I. Sobrados, J. Sanz and R. Ternane, *Journal of Materials Science*, 2020, **55**, 8464–8476.

220 T. Hupfer, E. C. Bucharsky, K. G. Schell, A. Senyshyn, M. Monchak, M. J. Hoffmann and H. Ehrenberg, *Solid State Ionics*, 2016, **288**, 235–239.

221 A. Robertson, J. G. Fletcher, J. M. S. Skakle and A. R. West, *Journal of Solid State Chemistry*, 1994, 109, 53–59.

222 Y. Liang, Z. Lin, Y. Qiu and X. Zhang, *Electrochimica Acta*, 2011, **56**, 6474–6480.

223 E. C. Bucharsky, K. G. Schell, A. Hintennach and M. J. Hoffmann, *Solid State Ionics*, 2015, **274**, 77–82.

224 T. Yang, J. Zheng, Q. Cheng, Y.-Y. Hu and C. K. Chan, *ACS Applied Materials and Interfaces*, 2017, **9**, 21773–21780.

225 K. Arbi, W. Bucheli, R. Jiménez and J. Sanz, *Journal of the European Ceramic Society*, 2015, **35**, 1477–1484.

226 T. Yang, X. Liu, L. Sang and F. Ding, *Journal of Power Sources*, 2013, **244**, 43–49.

227 G. Lancel, P. Stevens, G. Toussaint, M. Maréchal, N. Krins, D. Bregiroux and C. Laberty-Robert, *Langmuir*, 2017, **33**, 9288–9297.

228 S. Wang, L. Ben, H. Li and L. Chen, *Solid State Ionics*, 2014, **268**, 110–116.

229 K. Arbi, S. Mandal, J. M. Rojo and J. Sanz, *Chemistry of Materials*, 2002, **14**, 1091–1097.

230 B. Zhang, Z. Lin, H. Dong, L. W. Wang and F. Pan, *Journal of Materials Chemistry A*, 2020, **8**, 342–348.

231 M. Pérez-Estébanez, J. Isasi-Marín, D. M. Többens, A. Rivera-Calzada and C. León, *Solid State Ionics*, 2014, **266**, 1–8.

232 D. Rettenwander, A. Welzl, S. Pristat, F. Tietz, S. Taibl, G. J. Redhammer and J. Fleig, *Journal of Materials Chemistry A*, 2016, **4**, 1506–1513.

233 G. Delaizir, V. Viallet, A. Aboulaich, R. Bouchet, L. Tortet, V. Seznec, M. Morcrette, J. M. Tarascon, P. Rozier and M. Dollé, *Advanced Functional Materials*, 2012, **22**, 2140–2147.

234 Z. Liu, S. Venkatachalam and L. van Wüllen, *Solid State Ionics*, 2015, **276**, 47–55.

235 G. B. Kunshina, I. v. Bocharova and E. P. Lokshin, *Inorganic Materials*, 2016, **52**, 279–284.

236 G. B. Kunshina, I. v. Bocharova and V. I. Ivanenko, *Inorganic Materials: Applied Research*, 2017, **8**, 238–244.

237 Y. Liu, J. Chen and J. Gao, *Solid State Ionics*, 2018, **318**, 27-34.

238 S. Zekoll, C. Marriner-Edwards, A. K. O. Hekselman, J. Kasemchainan, C. Kuss, D. E. J. Armstrong, D. Cai, R. J. Wallace, F. H. Richter, J. H. J. Thijssen and P. G. Bruce, *Energy and Environmental Science*, 2018, **11**, 185–201.

239 Y. C. Kim, K. N. Jung, J. W. Lee and M. S. Park, *Ceramics International*, 2020, **46**, 23200–23207.

240 V. Krishnan, S. Gross, S. Müller, L. Armelao, E. Tondello and H. Bertagnolli, *Journal of Physical Chemistry B*, 2007, **111**, 7519–7528.

241 H. Uchiyama, K. Takagi and H. Kozuka, *Colloids and Surfaces A: Physicochemical and Engineering Aspects*, 2012, **403**, 121–128.

242 W. Liu, J. Yang, H. Xu, Y. Wang, S. Hu and C. Xue, *Advanced Powder Technology*, 2013, **24**, 436–440.

243 D. M. Puri and R. C. Mehrotra, *Journal of The Less-Common Metals*, 1961, **3**, 253–258.

244 A. Léaustic, F. Babonneau and J. Livage, *Chemistry of Materials*, 1989, **1**, 240–247.

245 V. Krishnan, S. Gross, S. Müller, L. Armelao, E. Tondello and H. Bertagnolli, *Journal of Physical Chemistry B*, 2007, **111**, 7501–7518.

246 R.K. Mehrotra; R.C. Mehrotra, *Canadian Journal of Chemistry*, 1961, **39**, 795–798.

247 Z. Liu, S. Venkatachalam and L. Van Wüllen, *Solid State Ionics*, 2015, **276**, 47–55.

248 G. B. Kunshina, I. V Bocharova and V. I. Ivanenko, *Inorganic Materials: Applied Research*, 2017, **8**, 238–244.

249 Z. Liu, S. Venkatachalam, H. Kirchhain and L. van Wüllen, *Solid State Ionics*, 2016, **295**, 32–40.

250 S. V. Pershina, M. Y. Dzuba, S. G. Vlasova and Y. V. Baklanova, *Journal of Physics: Conference Series*, 2019, **1347**, 3–8.

251 E. R. Losilla, A. Cabeza, S. Bruque, M. A. G. Aranda, J. Sanz, J. E. Iglesias and J. A. Alonso, *Journal of Solid State Chemistry*, 2001, **156**, 213–219.

252 D. Safanama, N. Sharma, R. P. Rao, H. E. A. Brand and S. Adams, *Journal of Material Chemistry A*, 2016, **4**, 7718–7726.

253 J. Yang, Z. Huang, B. Huang, J. Zhou and X. Xu, *Solid State Ionics*, 2015, **270**, 61–65.

254 M. Dirican, C. Yan, P. Zhu and X. Zhang, *Materials Science and Engineering R: Reports*, 2019, **136**, 27–46.

255 G. Piana, F. Bella, F. Geobaldo, G. Meligrana and C. Gerbaldi, *Journal of Energy Storage*, 2019, **26**, 100947.

256 J. Lee, T. Howell, M. Rottmayer, J. Boeckl and H. Huang, *Journal of The Electrochemical Society*, 2019, **166**, A416–A422.

257 H. Zhang, C. Liu, L. Zheng, F. Xu, W. Feng, H. Li, X. Huang, M. Armand, J. Nie and Z. Zhou, *Electrochimica Acta*, 2014, **133**, 529–538.

258 P. Zhu, C. Yan, M. Dirican, J. Zhu, J. Zang, R. K. Selvan, C. C. Chung, H. Jia, Y. Li, Y. Kiyak, N. Wu and X. Zhang, *Journal of Materials Chemistry A*, 2018, **6**, 4279–4285.

259 X. Ao, X. Wang, J. Tan, S. Zhang, C. Su, L. Dong, M. Tang, Z. Wang, B. Tian and H. Wang, *Nano Energy*, 2021, **79**, 105475.

260 Y. Zhao, J. Yan, W. Cai, Y. Lai, J. Song, J. Yu and B. Ding, *Energy Storage Materials*, 2019, **23**, 306–313.

261 C. Yan, P. Zhu, H. Jia, J. Zhu, R. K. Selvan, Y. Li, X. Dong, Z. Du, I. Angunawela, N. Wu, M. Dirican and X. Zhang, *Advanced Fiber Materials*, 2019, **1**, 46–60.

262 Q. Yang, L. I. Zhenyu, Y. Hong, Y. Zhao, S. Qiu, C. E. Wang and Y. Wei, *Journal of Polymer Science, Part B: Polymer Physics*, 2004, **42**, 3721–3726.

263 D. R. Lide, *CRC Handbook of Chemistry and Physics, 84th Edition*, CRC Press, 2006.

264 K. M. Kim, D. O. Shin and Y. G. Lee, *Electrochimica Acta*, 2015, **176**, 1364–1373.

265 S. V. Pershina, B. D. Antonov, A. S. Farlenkov and E. G. Vovkotrub, *Journal of Alloys and Compounds*, 2020, **835**, 155281.

266 P. Zhang, M. Matsui, A. Hirano, Y. Takeda, O. Yamamoto and N. Imanishi, *Solid State Ionics*, 2013, **253**, 175–1

10 Appendix I: Sommaire récapitulatif

Nanofibres électrofilées de NASICON comme électrolytes solides pour batteries au lithium

10.1 Introduction

Les combustibles fossiles, notamment le charbon, le pétrole et le gaz naturel, alimentent l'économie mondiale depuis la révolution industrielle et fournissent actuellement environ 80 % des besoins énergétiques mondiaux. Cependant, leur extraction et leur combustion ont augmenté la quantité de gaz à effet de serre anthropiques, tels que le CO_2 (**Figure 10.1**), qui sont les principaux responsables du réchauffement climatique.

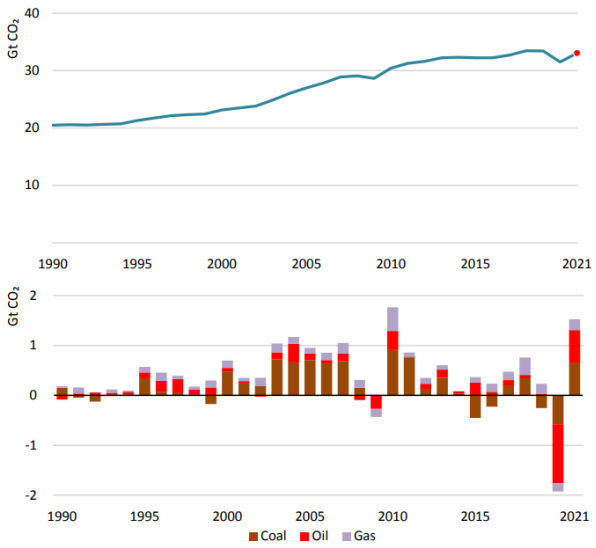

Figure 10.1 Évolution des émissions mondiales de CO_2 liées à l'énergie de 1990 à 2021 et (b) leur évolution par rapport à l'année précédente. L'impact de chaque carburant est indiqué. *Reproduction autorisée.* [1]

Selon le dernier rapport d'évaluation du *Intergovernmental Panel on Climat Change*, en l'absence d'action majeure pour réduire les émissions, la température moyenne mondiale est appelée à augmenter de 3,7 à 4,8 °C d'ici 2100. Même en réduisant les émissions de gaz à effet de serre, le réchauffement climatique continuerait de se produire pendant encore au moins plusieurs décennies, et le risque de dépassements potentiels de température est concret. Maintenir une augmentation de la température mondiale en dessous de 1,5 °C par rapport aux niveaux préindustriels est vital, car cela limiterait la fréquence et l'intensité des événements extrêmes, tels que les fortes précipitations, les sécheresses, les inondations, l'acidification des océans, les extinctions d'espèces. De plus, l'adaptation humaine sera moins difficile.[2]

Bien que les combustibles fossiles soient appelés à rester une source importante d'énergie et de matériaux pendant des décennies, une révolution technologique est nécessaire pour passer à des sources d'énergie abordables, accessibles et durables. Les énergies renouvelables sont de bons candidats pour remplacer progressivement les combustibles fossiles, cependant, leur imprévisibilité et leur manque de fiabilité ont empêché leur utilisation. Par conséquent, ils auraient besoin ou au moins bénéficieraient de dispositifs de stockage d'énergie.[3] Le développement et l'intégration de dispositifs de stockage d'énergie sont cruciaux pour une utilisation efficace et une diffusion capillaire des énergies renouvelables, et parmi eux, les batteries représentent un excellent choix pour l'intégration avec des ressources renouvelables. Leur taille compacte les rend bien adaptés au transport; ils peuvent réduire les variations du rayonnement solaire local et atténuer les fluctuations du rendement dans les parcs éoliens. Bien que le coût élevé limite la pénétration du marché, la modularité et l'évolutivité des différents systèmes de batteries entraîneront certainement une baisse des coûts dans les années à venir. Plusieurs technologies de batteries intéressantes sont actuellement en train d'émerger ou d'être relancées pour des applications stationnaires en raison de leur faible coût potentiel (*redox-flow*) et de leurs performances améliorées (*lithium-ion*).[4]

De nos jours, des milliards de batteries lithium-ion (LIB) sont produites et régulièrement utilisées pour alimenter les smartphones, tablettes, ordinateurs portables et plusieurs autres appareils électroniques portables. Les LIB de pointe peuvent fournir une énergie volumétrique et gravimétrique jusqu'à 770 Wh L^{-1} et 260 Wh Kg^{-1}, respectivement. Cependant, la densité d'énergie des LIB conventionnelles est déjà proche de la limite (**Figure 10.2a**).[6] De plus, la sécurité des LIB est une préoccupation majeure, car la présence à la fois d'un électrolyte combustible et d'un agent oxydant présente un risque de réactions d'emballement thermique entraînant des incendies ou des explosions. Par conséquent, le milieu de la recherche a déjà commencé à regarder au-delà des LIB, confirmant ainsi que la quête pour une technologie de stockage d'énergie de nouvelle génération a commencé. Le remplacement de l'anode à base de graphite, couramment utilise dans les LIB, par du Li métallique peut doubler l'énergie spécifique, atteignant environ 440 Wh kg^{-1}. Le passage à de nouvelles chimies, telles que les systèmes Li-S et Li-air, peut encore augmenter l'énergie spécifique à ~ 650 Wh kg^{-1} et ~ 950 Wh kg^{-1}, respectivement (**Figure 10.2b**).[10] Cependant, plusieurs défis caractérisent l'utilisation du Li dans les batteries secondaires, dont la plupart sont liés à la sécurité et à la stabilité pendant le cycle de charge et de décharge, tels que le dépôt irrégulier et la formation de dendrites.

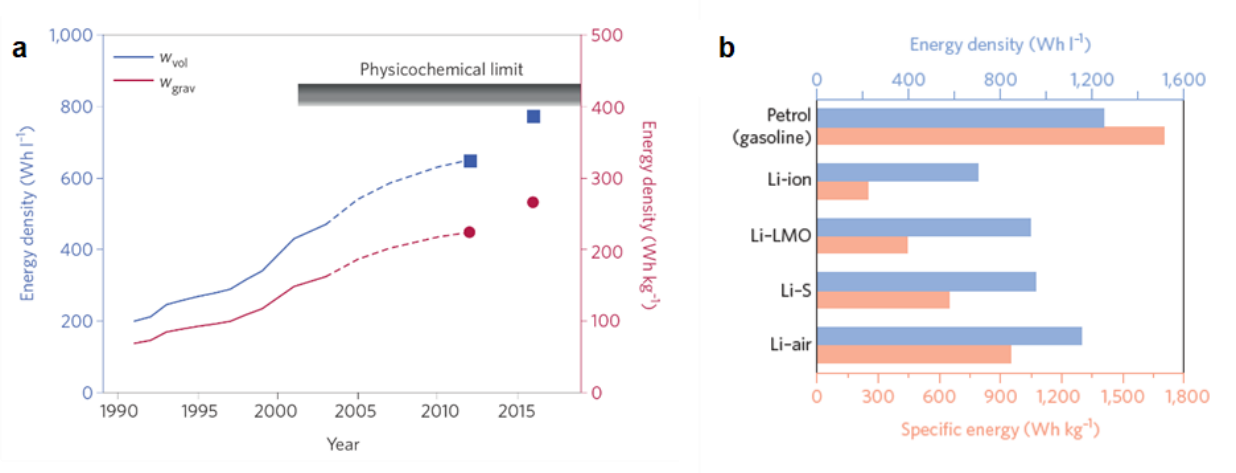

Figure 10.2 (a) Densité d'énergie de la cellule LIB cylindrique standard 18650 de 1991 à 2016. *Reproduction autorisée.*[6] *(Copyright 2016 Nature Publishing Group).* (b) Diagramme à barres montrant les densités d'énergie gravimétrique (rose) et volumétrique (bleu) de l'essence et des batteries au Li conventionnelles. *Reproduction autorisée.*[10] *(Copyright 2017 Nature Publishing Group).*

Une stratégie efficace pour surmonter ces problèmes consiste à remplacer l'électrolyte liquide par un matériau solide conducteur d'ions, qui peut empêcher mécaniquement la croissance dendritique ainsi que les changements de volume de Li. L'utilisation d'un électrolyte solide peut également simplifier la procédure d'assemblage et réduire les coûts, en plus d'être bénéfique pour diminuer à la fois le poids et le volume de la cellule. Le Li métallique peut être utilisés en toute sécurité comme anode et, associé à des morphologies de cathode plus denses, peut encore augmenter la densité d'énergie de la batterie. Les électrolytes solides destinés à des applications de batteries se répartissent principalement en deux catégories : les céramiques inorganiques et les polymères organiques. En général, le principal avantage des électrolytes céramiques réside dans les propriétés mécaniques. L'excellente résistance mécanique et la dureté extrême empêchent facilement la croissance dendritique ainsi que les éventuels courts-circuits. Ils se caractérisent également par une bonne stabilité thermique qui maintiennent ainsi les électrodes séparées même en cas d'emballement thermique. Concernant la conductivité ionique, des valeurs de plus en plus proches de ces des électrolytes liquides (10^{-3}–10^{-2} S cm^{-1}) ont été rapporté au cours des dernières décennies (**Figure 10.3**).

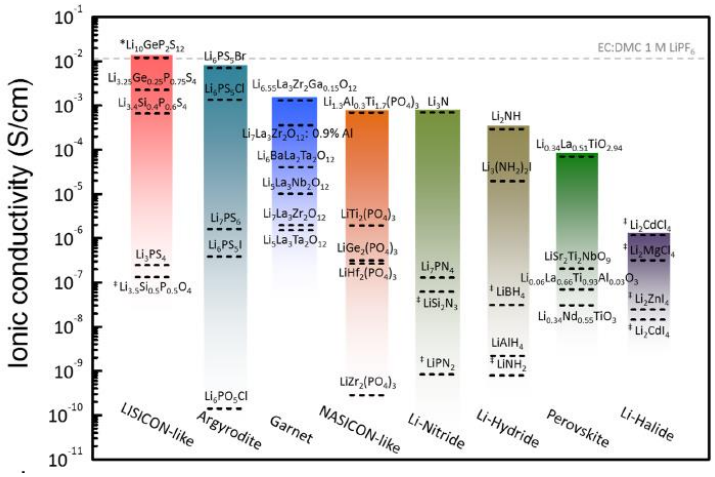

Figure 10.3 Conductivité ionique totale des conducteurs d'ions de lithium à l'état solide à température ambiante. *Reproduction autorisée.*[43] *(Copyright 2016 American Chemical Society).*

Toutefois, les électrolytes céramiques présentent encore quelques inconvénients majeurs qui doivent être résolus, par exemple, la stabilité chimique et électrochimique. Les processus de synthèse peuvent être très compliqué, car plusieurs matériaux seraient réactifs à l'humidité, mais le principal problème est sans doute la compatibilité interfaciale avec les électrodes. D'un point de vue mécanique, trouver un bon contact de surface entre deux matériaux solides est très difficile, et nécessite l'utilisation de traitements à haute pression et à haute température, qui augmentent considérablement les coûts. Sur cet aspect précis, les électrolytes polymères sont certainement plus efficaces, car leur flexibilité est bénéfique pour réaliser une interface optimale avec les électrodes. Toutefois, leur conductivité ionique à température ambiante est encore trop faible par rapport aux milieux liquides et leur résistance mécanique n'est pas suffisamment élevée pour empêcher la croissance dendritique de Li. C'est pourquoi, au cours des dernières décennies, un intérêt croissant de la recherche s'est tourné vers les électrolytes composites, qui visent à combiner les avantages et à éliminer les inconvénients des électrolytes solides inorganiques et organiques.

10.2 Objectives

Dans ce travail, des matériaux NASICON (*Na superionic conductors*) à base de Li sont synthétisés avec diverses méthodes pour obtenir différentes morphologies. Ensuite, ils sont proposés comme base pour développer des électrolytes solides afin de résoudre certains des principaux problèmes qui affectent encore les batteries au lithium à l'état solide. Le but de la thèse est décrit ci-dessous sous la forme d'une liste de différents objectifs:

1. **Amélioration de la synthèse à l'état solide du LATP.** Le LATP est un matériau conducteur d'ions Li^+ adapté au développement d'électrolytes denses entièrement inorganiques pour les batteries à base de lithium. Cependant, certains aspects fondamentaux de sa cristallisation sont encore inconnus et sa synthèse peut encore être optimisée, en réduisant par exemple le temps et la température de calcination et en améliorant la densité des pastilles avec différentes techniques.
2. **Effet de la morphologie des fibres sur les propriétés du LATP.** Une approche synthétique pour fabriquer des nanofibres de LATP, qui consiste à coupler sol-gel et électrospinning, a été sélectionnée après une recherche approfondie dans la littérature. Des études antérieures rapportent que la morphologie des fibres s'est avérée bénéfique pour obtenir des pastilles inorganiques plus denses, ainsi que pour améliorer les propriétés de l'électrolyte polymère lorsque des fibres céramiques sont utilisées comme charges.
3. **Amélioration des électrolytes polymères à base de PEO par l'addition de nanofibres de LAGP.** La méthode utilisée pour la fabrication des nanofibres de LATP n'était pas directement applicable au LAGP, ainsi une nouvelle approche synthétique à base de chlorure a été développée. Les nanofibres de LAGP ont été testées en tant que pastilles céramique nanofibreux et comme charges pour les électrolytes polymères, montrant des résultats prometteurs.
4. **Amélioration de la pureté et de la morphologie des nanofibres de LAGP par substitution de Ge par Ti.** La pureté et la morphologie des nanofibres de LAGP précédemment synthétisées pourraient être améliorées. Par conséquent, nous avons étudié l'effet d'une substitution partielle de Ge par Ti. L'ajout de butoxyde de Ti stabilisé, grâce à sa viscosité élevée, peut être bénéfique pour la stabilité du processus d'électrospinning, conduisant ainsi à une morphologie améliorée des fibres. De plus, cela pourrait aider à la cristallisation de la phase NASICON lors de l'étape de calcination.

La thèse est divisée en huit chapitres, qui sont organisés comme suit :

Chapitre 1 Le sujet de la crise énergétique est introduit. Des informations générales sur les LIB et les batteries à l'état solide sont fournies, avec un accent particulier sur l'utilisation de fibres céramiques conductrices d'ions pour développer des électrolytes solides.

Chapitre 2 Le but et les objectifs de la thèse sont présentés.

Chapitre 3 Les détails expérimentaux sont fournis. Les matériaux ainsi que les différentes méthodes de synthèse sont décrits en détail. Enfin, les techniques de caractérisation employées pour toutes les étapes de ce projet sont listées.

Chapitre 4 L'influence de l'utilisation des phases TiO_2 rutile et anatase sur la synthèse à l'état solide du LATP est étudiée.

Chapitre 5 L'effet de la pression sur les propriétés des nanofibres de LATP préparées par électrospinning et calcination subséquente est décrit.

Chapitre 6 Une nouvelle méthode de synthèse pour fabriquer des nanofibres de LAGP par électrospinning est introduite. La caractérisation des nanofibres céramiques obtenues en tant que pastille céramique nanofibreux et charges dans des électrolytes polymères à base de PEO est décrite.

Chapitre 7 L'effet de la substitution partielle de Ge par Ti sur les propriétés des fibres de LAGP est présenté. Ensuite, des nanofibres LAGP avec Ti ont été ajoutées comme charges dans des électrolytes polymères à base de PEO et leurs effets sont également discutés.

Chapitre 8 Ici, les conclusions et quelques perspectives sur les sujets de la thèse sont rapportées. De plus, un aperçu des futures études potentielles liées aux résultats de la thèse est proposé.

10.3 Partie expérimentale

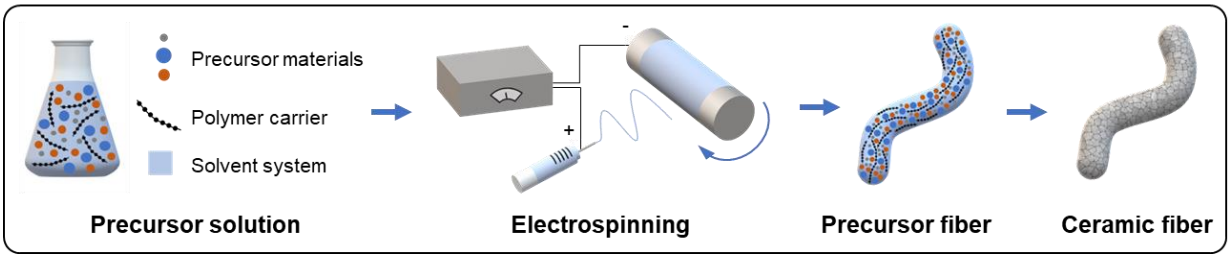

Figure 10.4 Illustration schématique du processus de synthèse des fibres céramiques par électrospinning.

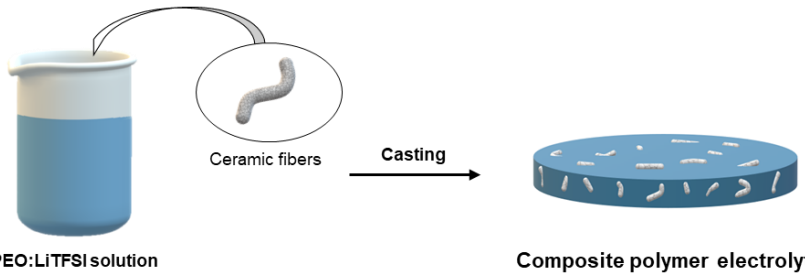

Figure 10.5 Illustration schématique de la préparation d'un électrolyte polymère composite avec des fibres céramiques comme charges.

10.4 Influence des précurseurs TiO_2 rutile et anatase sur la synthèse à l'état solide d'un électrolyte céramique de $Li_{1.5}Al_{0.5}Ti_{1.5}(PO_4)_3$

Dans cette étude, nous avons évalué comment différents polymorphes de TiO_2 peuvent affecter la synthèse et les propriétés d'un électrolyte $Li_{1.5}Al_{0.5}Ti_{1.5}(PO_4)_3$. Plus précisément, nous avons synthétisé le LATP par une méthode à l'état solide en utilisant l'anatase TiO_2 comme source de Ti, et ci-après dénommé aLATP. Nous avons reproduit la même synthèse, sauf en utilisant du rutile TiO_2 à la place (le produit final est désigné par rLATP). Nous avons étudié la cristallisation des deux matériaux en utilisant *in situ* HTXRD. En combinant les données obtenues par diffraction de rayon X à haute température (HTXRD), les images acquises par le microscope électronique à balayage (MEB) et les résultats de la spectroscopie d'impédance électrochimique (EIS), nous avons évalué l'influence des deux phases de TiO_2 sur la synthèse, ainsi que sur les propriétés et les performances des électrolytes de LATP synthétisés.

L'imagerie MEB a été utilisée pour étudier la morphologie de rLATP et aLATP (**Figure 10.6**). Les deux échantillons sont constitués de cristallites cubiques et irrégulières, qui ont tendance à former des agglomérats de plusieurs microns. La forme irrégulière est liée à la température utilisée pour la synthèse, c'est-à-dire 700 °C.[207,208] Lorsqu'une température de 950 °C est utilisée, les cristaux résultants sont principalement de forme cubique dans les deux échantillons (**Figure 10.6c,f**). L'analyse EDS des deux échantillons a confirmé la formation de LATP avec une distribution élémentaire uniforme sans ségrégation apparente des phases secondaires (**Figure 10.6g,h**). L'analyse HTXRD a été réalisé sur les deux échantillons pour avoir un aperçu approfondi de la cristallisation du LATP et de la manière dont elle est influencée par la présence de phases rutile et anatase. Lorsque la température augmente, les profils XRD des deux échantillons évoluent : les pics attribués au produit intermédiaire, comme le

Li_3PO_4 et le biphosphammite $(NH_4)H_2PO_4$ commencent à apparaître entre 100 et 200 °C dans les profils des deux échantillons.

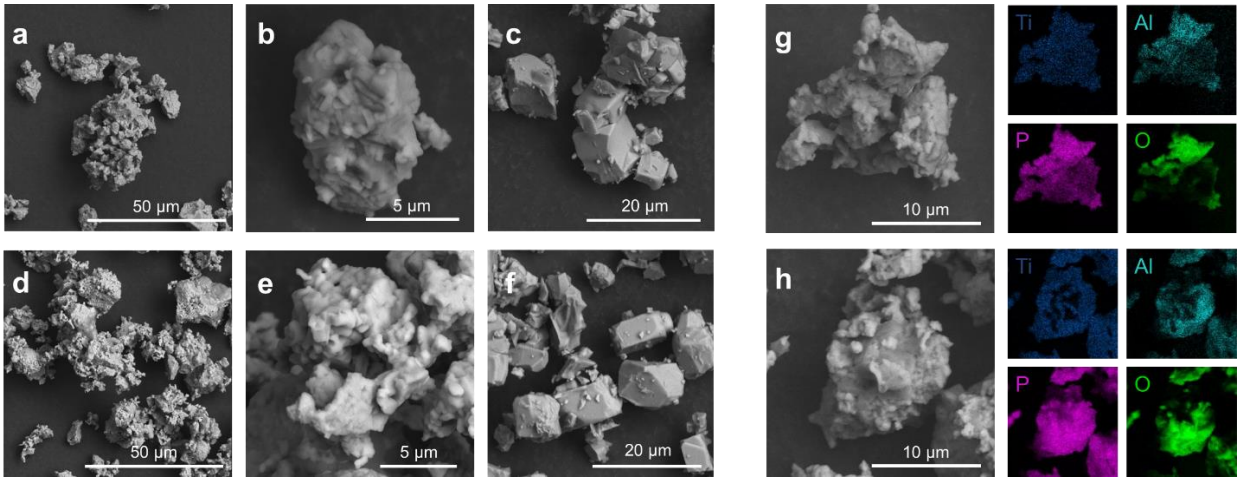

Figure 10.6 Images MEB d'aLATP synthétisé à (a,b) 700°C et (c) 950°C et de rLATP synthétisé à (d,e) 700°C et (f) 950°C. Analyse MEB-EDS et cartographie élémentaire correspondante de (g) aLATP et (h) rLATP.

Ensuite, les pics correspondant aux matériaux précurseurs, rutile et anatase inclus, commencent à diminuer d'intensité et la phase rhomboédrique de LATP apparaît. Plus précisément, dans le diffractogramme d'aLATP acquis à 378 °C, des pics correspondant à la phase NASICON (groupe d'espace $R\bar{3}c$) de $Li_{1.2}Al_{0.2}Ti_{1.8}(PO_4)_3$ (carte PDF : 01-084-5450) ont commencé à apparaître. Dans une plage de température similaire, aucun pic n'est détecté dans le profil de rLATP, comme illustré à la **Figure 10.7a**. Lorsque la température atteint 583 °C, nous avons observé l'apparition de la phase de LATP également dans le profil de rLATP, tandis que dans le profil de aLATP collecté dans la gamme 592-622 °C, les pics correspondants sont déjà très intenses (**Figure 10.7b**). Lorsque la température atteint 700 °C, la phase de aLATP est caractérisée par un degré de cristallinité plus élevé et moins de phases d'impuretés que le rLATP. Cependant, après 2 heures à 700 °C, le rLATP devient plus pur et plus cristallin, n'affichant que quelques pics de faible intensité attribuables à $Li_4P_2O_7$ et Li_3PO_4, tandis que plusieurs pics associés à $AlPO_4$ et $Li_4P_2O_7$ ont été identifiés dans le diffractogramme d'aLATP acquis après le plateau de 2 heures à 700 °C (**Figure 10.7c,d**). Les deux échantillons ont été refroidis à température ambiante pour les analyses XRD finales. Les profils n'ont pas changé de manière significative par rapport à leurs homologues à 700 ° C, ce qui vérifie leur stabilité (**Figure 10.7c,d**).

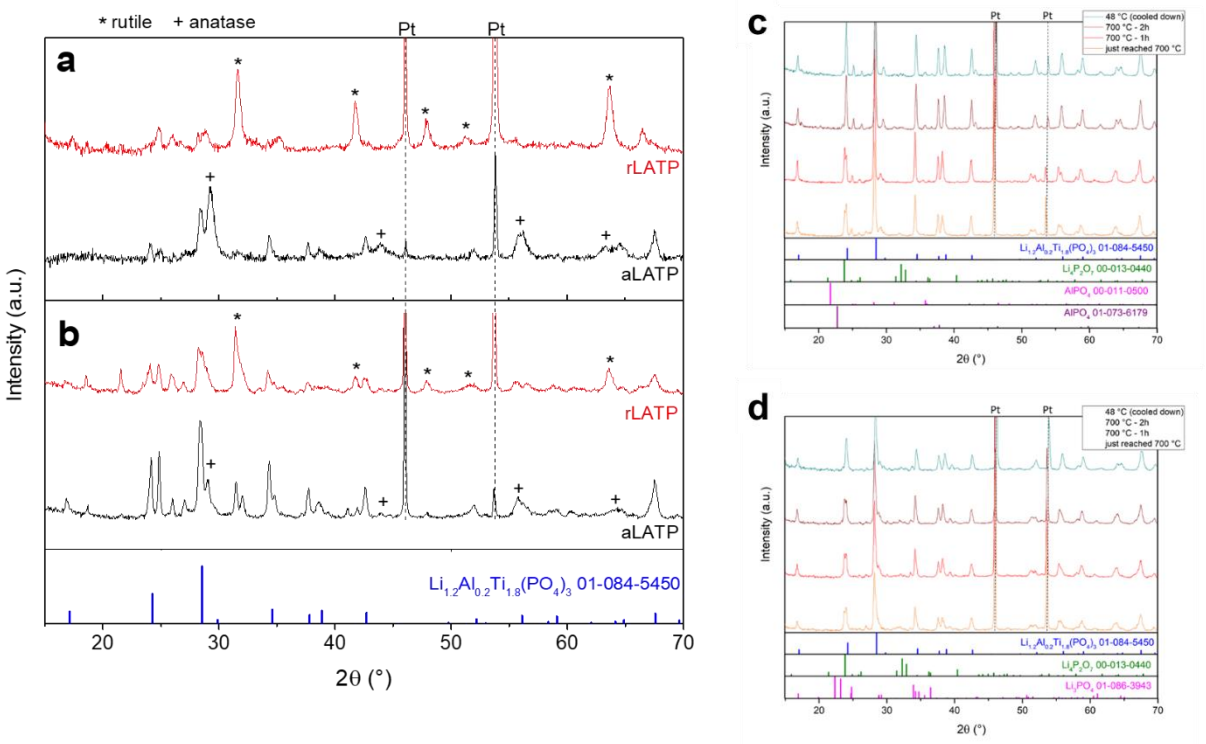

Figure 10.7 Profils XRD acquis dans une plage de température de (a) 378-408 °C pour aLATP et 370-400 °C pour rLATP, et (b) 592-622 °C pour aLATP et 583-613 °C pour rLATP. ((*) : TiO_2 rutile ; (+) : TiO_2 anatase ; les pics de Pt proviennent du creuset). Profils XRD acquis sur (c) aLATP et (d) rLATP, lorsque la température vient d'atteindre 700 ° C, après 1 et 2 heures à la même température et après refroidissement.

A 300 °C, seuls les profils XRD de TiO_2 apparaissent dans les échantillons. Ceci indique qu'à 300 °C tous les précurseurs sont devenus amorphes à l'exception de TiO_2, et que le TiO_2 est le dernier à réagir. L'utilisation de la phase anatase ou rutile du TiO_2 n'affecte pas les voies réactionnelles de la synthèse. Entre 127 et 327 °C, l'enthalpie de formation et l'énergie de Gibbs du TiO_2 anatase sont supérieures d'environ 6,2 kJ/mol à celles du TiO_2 rutile.[209] En supposant une vitesse de réaction de type Arrhenius, cette différence entraîne une cinétique quatre fois plus rapide pour les réactions de TiO_2 anatase à 327 °C, en bon accord avec notre observation selon laquelle le LATP apparaît plus tôt avec TiO_2 anatase qu'avec TiO_2 rutile. Des pastilles ont été préparées avec aLATP et rLATP en pressant à chaud les poudres correspondantes à 750 °C sous 56 MPa. La densité des pastilles d'aLATP et de rLATP, estimée en utilisant leur poids et leurs dimensions, s'est avérée égale à 90 % de la valeur théorique. Pour évaluer la conductivité ionique, chaque échantillon a été peint avec de l'encre d'argent et placé dans une pile bouton entre des électrodes blocants en acier inoxydable (**Figure 10.8a**). Les spectres EIS ont été acquis dans la plage de température de 20 à 80 °C. Les diagrammes de Nyquist résultants se composent de deux demi-cercles : le premier a été acquis à haute fréquence, tandis que le second

peut être observé dans la région des fréquences moyennes et basses et apparaît petit et partiellement convoluté avec la capacitance double couche des électrodes.

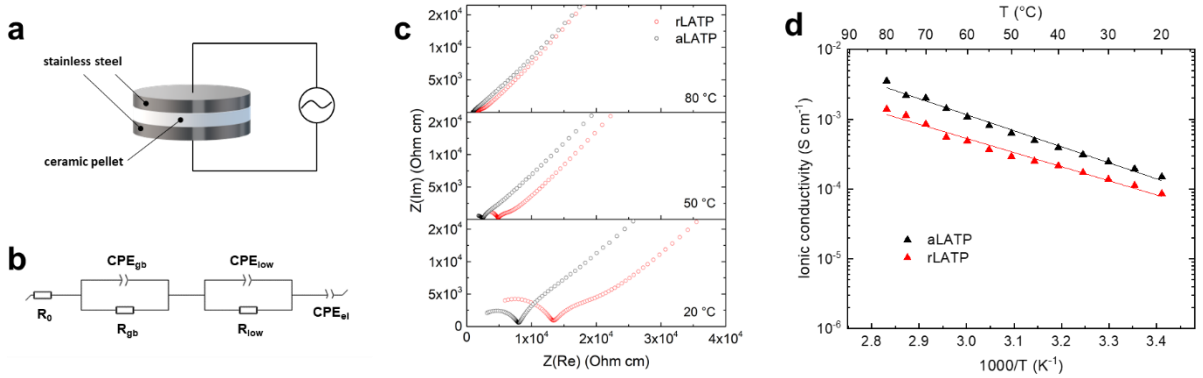

Figure 10.8 (a) Schéma de la configuration utilisée pour l'analyse EIS de aLATP et rLATP. (b) Circuit équivalent utilisé pour l'ajustement des données EIS. (c) Spectres EIS à 20, 50 et 80 ° C et (d) diagrammes d'Arrhenius dans une plage de température de 20 à 80 ° C de aLATP et rLATP.

Des résultats similaires ont été rapportés pour le LLZO pressé à chaud par Tenhaeff et al., qui n'ont pas pu associer ce petit demi-cercle à un phénomène distinct.[210] Ainsi, nous avons sélectionné un circuit équivalent composé de résistances (R) et d'éléments à phase constante (CPE), qui représentent les contributions résistives et capacitives non idéales de chaque phénomène. Plus précisément, le circuit équivalent $R_0(R_{gb}CPE_{gb})(R_{low}CPE_{low})CPE_{el}$ représenté sur la **Figure 10.8b**, a été utilisé pour modéliser les données expérimentales des deux échantillons, où R_0 est la résistance du circuit, externe à l'échantillon, R_{gb} et CPE_{gb} sont associés au transport ionique aux joints de grains, R_{low} et CPE_{low} représentent le demi-cercle non identifié à basse fréquence et CPE_{el} est lié à la capacitance double couche des électrodes. Nous pouvons exclure avec confiance la présence de contributions intra-grain, car il apparaît comme un consensus scientifique que la conductivité globale des matériaux NASICON ne peut être identifiée qu'à de très basses températures, de -100 à 10 °C.[85,87,211,212] De plus, la contribution capacitive du premier demi-cercle est égale à 10^{-9} F, ce qui se situe dans la plage typique des phénomènes aux joints de grains.[213] Sur ces prémisses, nous pouvons évaluer la conductivité ionique totale (σ), qui dérive principalement du transport ionique se produisant aux joints de grains pour les deux échantillons. La **Figure 10.8c** affiche les diagrammes de Nyquist représentatives résultant d'analyses EIS effectuées à 20, 50 et 80 °C. En les ajustant, nous pouvons calculer la conductivité ionique totale des pastilles de aLATP et rLATP. D'après les valeurs résultantes, présentées à la **Figure 10.8d** sous la forme d'un diagramme d'Arrhenius, aLATP apparaît plus conducteur que rLATP sur toute la plage de températures. La pente du diagramme d'Arrhenius

exprimée sous la forme linéaire $\ln(\sigma) = \ln(A) - Ea/RT$, a été utilisée pour calculer l'énergie d'activation, qui correspond à 0,44 (±0,01) eV et 0,40 (±0,02) eV pour aLATP et rLATP, respectivement. Les deux valeurs sont en bon accord avec celles rapportées dans la littérature.[212,214] La conductivité ionique de aLATP à 20 °C est égale à $1,5 \times 10^{-4}$ S cm^{-1}, soit environ le double de celle du rLATP ($8,5 \times 10^{-5}$ S cm^{-1}). Cette différence est principalement due à une conduction ionique moins efficace aux joints de grains de rLATP. L'origine de cette contribution différente pourrait être liée à une morphologie légèrement différente des particules. Comme discuté ci-dessus, aucune différence significative dans la morphologie des cristallites des deux échantillons n'a été observée. Cependant, comme le montre la **Figure 10.6**, les cristallites d'aLATP semblent légèrement plus uniformes dans la forme, ce qui pourrait être bénéfique pour obtenir un tassement plus serré. Pour vérifier cette hypothèse, nous avons pris des images MEB en coupe transversale sur des pastilles pressées à chaud de aLATP et rLATP. À faible grossissement (**Figure 10.9a,b**), nous n'avons observé aucune différence significative entre les deux pastilles. Par conséquent, nous avons acquis des images à fort grossissement en sélectionnant les zones les plus représentatives des deux échantillons. Cela nous a permis d'estimer la porosité locale des pastilles, qui est fortement liée à l'efficacité du processus de densification. De plus, on peut observer la présence potentielle de fractures, préjudiciables à la réalisation d'une conduction ionique rapide. Après avoir étudié plusieurs zones des deux échantillons, les plus représentatives sont présentées à la **Figure 10.9c,d**.

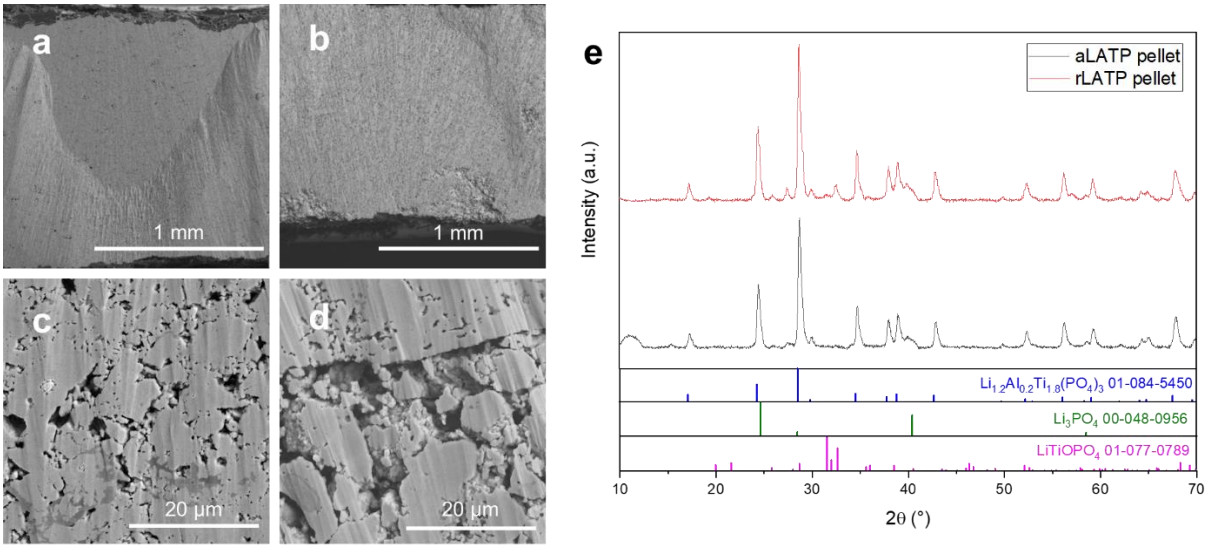

Figure 10.9 Images MEB en coupe transversale de pastilles de (a,c) aLATP et (b,d) rLATP densifiées à 750 °C par pressage à chaud, acquises après analyses EIS, et (e) profils XRD correspondants.

Alors que la porosité locale est similaire dans les deux échantillons, c'est-à-dire 9-10%, ce qui est bien corrélé à la densité des pastilles, la densification de aLATP apparaît plus uniforme, ce qui assure un meilleur contact entre les particules et par conséquent une conduction de lithium plus efficace à l'interface. Par ailleurs, le rLATP est caractérisé par des fractures et des pores plus grands, probablement dus à un tassement moins efficace des particules lors de l'étape de pressage à chaud. Les pores et les fractures pourraient provenir de la taille moyenne différente des particules, calculée à partir des données de diffraction des pastilles. En fait, rLATP est caractérisé par des particules légèrement plus grosses que celles de aLATP, c'est-à-dire 197 Å contre 76 Å, ce qui peut affecter négativement son processus de densification. Ce phénomène génère plusieurs goulots d'étranglement le long du trajet des ions Li, ralentissant ainsi leur transport entre les électrodes et affectant négativement la conductivité finale de la pastille de rLATP. Pour exclure toute influence potentielle de la composition des pastilles sur les valeurs de conductivité ionique, nous avons acquis les profils XRD des pastilles de aLATP et rLATP (**Figure 10.9e**). Nous n'avons observé aucune évolution inattendue des pics de LATP, cependant des pics associés aux phases d'impuretés de $LiTiOPO_4$ et Li_3PO_4 ont été détectés dans les deux échantillons. Les pics apparaissent légèrement plus intenses dans le profil de rLATP, ce qui correspond bien à sa faible conductivité ionique mesurée par EIS. Hupfer et al. ont rapporté que de petits pourcentages de $LiTiOPO_4$ peuvent être bénéfiques pour la conductivité ionique du LATP, en particulier lorsque de basses températures de frittage sont utilisées;[215] cependant, ce phénomène a été observé avec la présence simultanée de $AlPO_4$ comme phase d'impureté, que nous n'avons pas détectée. Étant donné que, dans notre étude, aLATP et rLATP affichent une composition similaire, nous pouvons affirmer que la principale contribution à la différence observée dans le comportement de conductivité ionique est probablement associée à leur morphologie, comme le démontre l'analyse MEB en coupe transversale.

Pour conclure, le TiO_2 anatase doit être choisie pour une température de synthèse inférieure et une conductivité plus élevée, tandis que le TiO_2 rutile est le choix pour les cristaux plus pur. Les tendances actuelles se concentrent sur l'optimisation des matériaux électrolytiques solides connus plutôt que sur la recherche d'alternatives. Dans ce cadre, chaque réalisation et chaque détail, par ex. la sélection des meilleurs matériaux précurseurs ainsi que la température de synthèse appropriée, peuvent être utiles pour réduire le coût et améliorer les méthodes synthétiques actuelles. Cet aspect est crucial pour l'échelle industrielle de la synthèse de l'électrolyte solide, qui constitue une étape obligatoire pour le déploiement futur de batteries entièrement solides.

10.5 Effet de la pression sur les propriétés de l'électrolyte solide constitué de nanofibres céramiques électrofilées de $Li_{1.3}Al_{0.3}Ti_{1.7}(PO_4)_3$

Nous adaptons ici la procédure de synthèse employée par Lancel et al. pour obtenir la stœchiométrie la plus conductrice : $Li_{1.3}Al_{0.3}Ti_{1.7}(PO_4)_3$. Dans le but de réduire la porosité de la membrane céramique, l'effet de l'application d'une pression de 150 MPa sur la membrane électrofilée, avant le traitement thermique a été étudié. Nous rapportons comment le processus de pressage affecte la morphologie de la membrane ainsi que la structure et les propriétés physico-chimiques du matériau céramique. Malgré la présence de certaines phases d'impuretés et une substitution moins homogène de Ti^{4+} par Al^{3+}, les nanofibres de LATP pressées ont montré une conductivité ionique accrue et une énergie d'activation beaucoup plus faible par rapport aux fibres de LATP non pressées.

À l'aide d'une presse hydraulique, diverses charges ont été appliquées à des échantillons empilés de fibres précurseurs pour identifier la valeur à laquelle la porosité est réduite sans compromettre la morphologie des fibres et l'intégrité mécanique de l'échantillon pendant le traitement thermique. Une valeur de compromis a été identifiée à 150 MPa, qui réduit la porosité de l'échantillon céramique de 85 % à 60 % sans affecter son intégrité et sa morphologie. L'application d'une pression supérieure à 150 MPa donne un échantillon plus dense, qui est cependant plus susceptible de se fracturer lors du traitement thermique. Les fractures pourraient provenir d'une capacité réduite à s'adapter à la diminution de volume, ainsi que de sous-produits gazeux générés à haute température essayant de s'échapper de l'échantillon. Après l'étape de pressage, les échantillons de pLATPnf ont été calcinés à 850 °C pendant 2h avec une vitesse de chauffage de 5 °C min^{-1}. La température et le temps sélectionnés ont permis d'obtenir une phase LATP presque pure avec la structure NASICON recherchée, sans compromettre la forme des fibres. Les résultats présentés et discutés ci-dessous pour pLATPnf sont comparés à ceux d'échantillons de nanofibres de LATP non pressés, simplement appelés LATPnf, qui ont été préparés en suivant la même procédure, à l'exception de l'étape de pressage. Les images acquises par le microscope électronique à balayage (MEB) des fibres précurseurs de LATP, LATPnf et pLATPnf sont rassemblées dans la **Figure 10.10**. Les fibres précurseurs tel que filées se caractérisent par un diamètre allant de 700 nm à 2 μm (**Figure 10.10a**). Après calcination, le diamètre des fibres a diminué jusqu'à 0,4–1 μm (**Figure 10.10b**). LATPnf a conservé la morphologie 1D car la séparation des fibres garantit que la croissance cristalline ne se produit qu'à l'intérieur de chaque fibre. Cela permet également de contrôler la taille des cristallites en utilisant le confinement des fibres comme matrice. La **Figure 10.10c** montre clairement comment la pression appliquée sur pLATPnf diminue fortement la porosité et augmente ainsi le nombre de points de contact entre les fibres, lesquels sont bénéfiques

pour la conductivité ionique du matériau final. En termes de morphologie, les nanofibres sont encore facilement discernables et la coalescence est minimisée. Cependant, il n'y a presque pas de séparation spatiale entre les nanofibres, la croissance cristalline n'est donc pas aussi confinée que pour LATPnf.

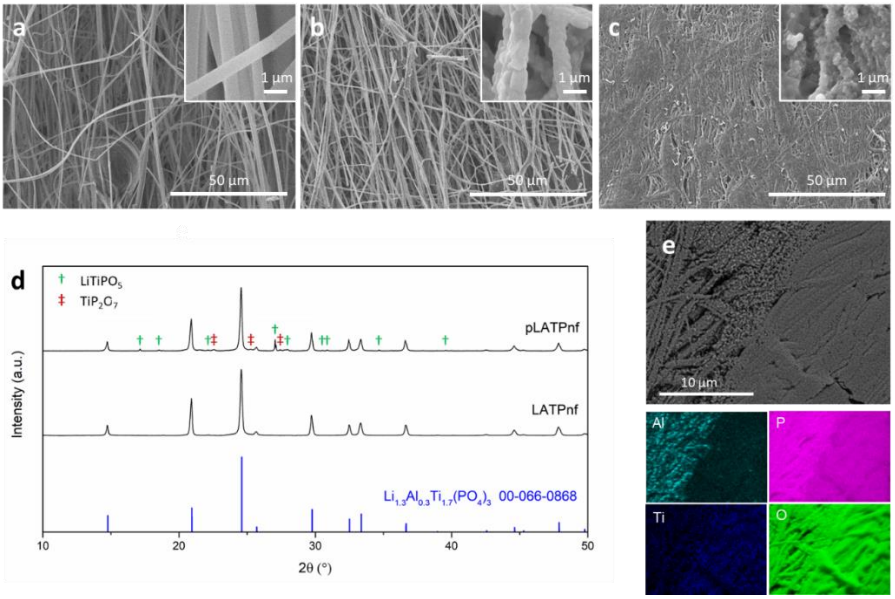

Figure 10.10 Images MEB de (a) fibres précurseurs de LATP, (b) LATPnf et (c) pLATPnf (grossissement correspondant dans l'encadré). (d) Profils XRD de pLATPnf et LATPnf. († : LiTiPO5 ; ‡ : TiP2O7). (e) Analyse MEB-EDS et cartes élémentaires correspondantes de pLATPnf.

Les profils XRD de LATPnf et pLATPnf sont rassemblés dans la **Figure 10.10d**. Les principaux pics dans les deux échantillons sont attribuables à la structure rhomboédrique de type NASICON (groupe d'espace $R\bar{3}c$) de $Li_{1.3}Al_{0.3}Ti_{1.7}(PO_4)_3$ (carte PDF 00-066-0868). L'absence d'une phase secondaire contenant de l'Al est la première preuve de la réussite de la substitution aliovalente de Ti^{4+} par Al^{3+}. Ni des phases secondaires ni des phases d'impuretés n'ont été détectées dans le profil de LATPnf, qui se compose donc de fibres LATP pures. Des pics de faible intensité ont plutôt été détectés dans le profil de pLATPnf et peuvent être attribués à de petites quantités de TiP_2O_7 et $LiTiPO_5$. Ce sont des produits secondaires fréquents dans les procédures de synthèse à haute température de LATP, résultant de la décomposition et de la réaction incomplète des matériau de départ.[197,218,219] $LiTiPO_5$ a une stœchiométrie similaire et est souvent considéré comme un intermédiaire réactionnel de $LiTi_2(PO_4)_3$.[220,221] La formation de TiP_2O_7, si TiO_2 est également détecté, pourrait être attribuée à une volatilisation partielle de Li_2O pendant le processus de chauffage,[218] cependant les conditions douces utilisées ne sont pas suffisantes pour provoquer une telle perte de lithium. Aucun pic lié à $AlPO_4$ et TiO_2 n'a été détecté, conformément aux rapports précédents sur les synthèses sol-gel de LATP.[222,223] Cet aspect confirme la substitution aliovalente réussie et suggère qu'aucune décomposition thermique

de la structure du LATP ne s'est produite. Comme indiqué précédemment, la porosité élevée des fibres précurseurs préparés par électrospinning est bénéfique pour réduire le temps et la température de calcination.[176,224] Cela a également été confirmé par la synthèse de LATPnf, qui a nécessité une étape de calcination d'à peine 2 heures à 850 °C pour obtenir une phase pure de NASICON, ce qui signifie un traitement thermique moins sévère par rapport aux études sur la synthèse sol-gel de LATP en vrac.[89,222,223] Les phases d'impuretés détectées dans pLATPnf sont probablement liées à sa densité plus élevée, qui nécessite des conditions de chauffage plus sévères pour obtenir le produit final. Augmenter la température et/ou le temps de calcination aurait sûrement été bénéfique en termes de pureté, cependant les fibres subissent une coalescence lorsque des conditions de chauffage sévères sont utilisées, conduisant à la perte complète de leur morphologie. À des fins de comparaison, nous avons décidé de maintenir les mêmes conditions de chauffage pour les deux échantillons, en tant que compromis entre la morphologie et la pureté. Pour mieux comprendre comment les différentes phases sont disposées dans la morphologie des fibres pLATPnf, nous avons acquis des cartes EDS. Nous avons observé une distribution élémentaire inégale dans le pLATPnf (**Figure 10.10e**). Plus précisément, la teneur en Al et Ti varie considérablement, ce qui signifie qu'il existe des différentes stœchiométries et/ou phases dans l'échantillon, en accord avec les profils XRD. Étant donné qu'aucune phase contenant de l'Al n'a été détectée par analyse XRD, la distribution inégale d'Al est vraisemblablement liée à différents degrés de substitution aliovalente de Ti^{4+} par Al^{3+}. Ceci est confirmé par la tendance opposée affichée pour la distribution de Ti dans la carte correspondante. La teneur en Al dans l'échantillon est fortement influencée par la densité des fibres. La **Figure 10.10e** montre que la substitution d'Al est moins significative dans les zones plus denses, où par conséquent, une teneur en Ti plus élevée est observée. Ainsi, les zones moins denses sont principalement constituées de LATP riche en Al, tandis que les plus denses, pauvres en Al, contiennent vraisemblablement des phases d'impuretés TiP_2O_7 et $LiTiPO_5$. Comme déjà rapporté, l'espace confiné de la fibre réduit la distance de diffusion des matériaux précurseurs, ce qui est bénéfique pour obtenir une distribution uniforme des espèces ioniques lors de l'étape de calcination.[176] Cet effet avantageux est minimisé par une certaine marge dans les zones pressées, où les fibres sont souvent fusionnées, ressemblant ainsi partiellement au matériau en vrac. L'analyse EIS des échantillons LATPnf et pLATPnf a été effectuée pour mesurer la conductivité ionique. Chaque échantillon a été placé dans une pile bouton entre des électrodes blocants en acier inoxydable (**Figure 10.11a**) et les données EIS ont été acquises à une température allant de 20 °C à 80 °C. L'ajustement des spectres EIS a été effectué en utilisant le circuit équivalent représenté sur la **Figure 10.11b**. Nous avons utilisé l'impédance totale

résultante pour calculer la conductivité ionique des deux échantillons à différentes températures, affichée sous forme de diagramme d'Arrhenius sur la **Figure 10.11d**. La pente des tracés d'Arrhenius a été utilisée pour calculer l'énergie d'activation de LATPnf et pLATPnf, donnant respectivement 0,37 ± 0,02 eV et 0,19 ± 0,02 eV. Les deux résultats sont en bon accord avec les valeurs rapportées dans la littérature pour le LATP.[67,223,227,228] La valeur la plus faible de pLATPnf pourrait être liée à un degré de substitution d'Al localement plus élevé ainsi qu'à la meilleure connexion entre les grains de LATP.[229–231] En ce qui concerne la conductivité ionique, LATPnf a montré une valeur égale à 5×10^{-7} S cm^{-1} à 25 °C, ce qui est légèrement supérieur à celui rapporté par Lancel et al.[197] La pression appliquée à pLATPnf s'est avérée très bénéfique pour la conductivité ionique de l'électrolyte final. En raison de la densité plus élevée et du plus grand nombre de points de contact, pLATPnf est caractérisé par une conductivité ionique supérieure de deux ordres de grandeur à 25 °C, c'est-à-dire 3×10^{-5} S cm^{-1}.

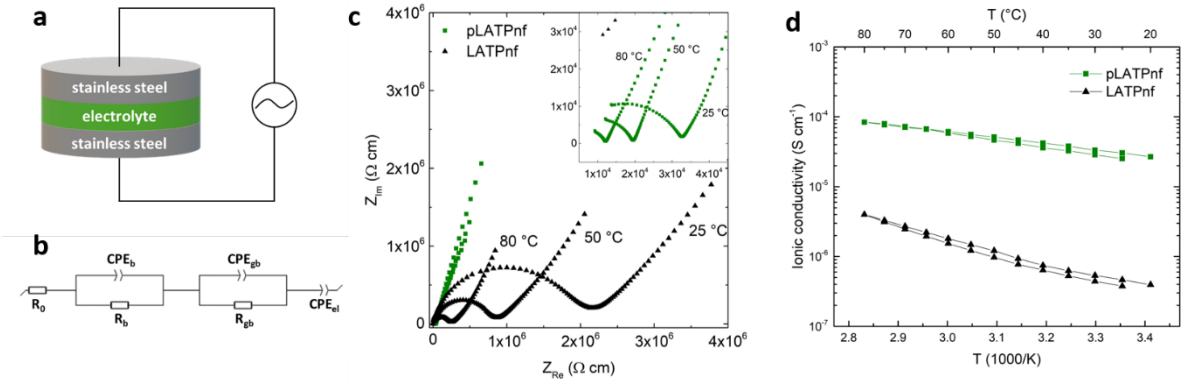

Figure 10.11(a) Schéma de la configuration d'analyse EIS. (b) Circuit équivalent utilisé pour ajuster les données EIS. (c) Spectres EIS de LATPnf et pLATPnf à 25 °C, 50 °C et 80 °C; un grossissement des données de pLATPnf à haute fréquence est montré dans l'encadré. (d) Diagramme d'Arrhenius comparant les conductivités ioniques de LATPnf et pLATPnf dans la plage de température de 20 à 80 °C. Deux balayages consécutifs dans des directions opposées ont été effectués.

Étant donné que les performances de LATPnf et pLATPnf ne sont pas comparables à celles d'une pastille dense de LATP, elles ne conviennent pas pour être testées dans une configuration de batterie à l'état solide. Cependant, les résultats obtenus sont prometteurs pour l'application future des fibres de NASICON à la fois comme base pour le développement d'électrolytes céramiques et comme charge/échafaudage actif pour les électrolytes polymères composites.

10.6 Propriétés et performances des fibres électrofilées de $Li_{1.5}Al_{0.5}Ge_{1.5}(PO_4)_3$ et leur application comme charge dans des électrolytes à base de PEO.

Des études antérieures sur la synthèse sol-gel de LAGP utilisaient divers matériaux précurseurs, à la fois organiques et inorganiques, comme source de Ge.[69,86,88,90,91,233–239] Parmi eux, l'oxyde de germanium a l'avantage d'être relativement peu coûteux et stable dans les conditions atmosphériques, cependant, sa faible solubilité dans l'eau et les solvants organiques le rend inadapté aux techniques d'électrospinning.[235,236] Les alcoxydes de Ge sont les précurseurs les plus fréquemment utilisés pour les synthèses sol-gel de LAGP, grâce à leur bonne solubilité dans divers solvants organiques, ce qui permet d'obtenir facilement une solution homogène.[69,88,90,91,233,234,237–239] Toutefois, leur réactivité à l'égard de l'eau limite fortement l'utilisation d'autres sels précurseurs aqueux, par exemple nitrates et acétates. Les alcoxydes subissent instantanément une réaction d'hydrolyse et de polycondensation en présence même de petites quantités d'eau, conduisant à la formation et à la précipitation d'oligomères Ge-O-Ge. Ces produits de polycondensation forment rapidement une suspension qui n'est pas adaptée à l'électrospinning car elle affecte négativement l'homogénéité de la solution, donc la pureté du matériau final.[240] Le chlorure de germanium a également été étudié comme source de Ge pour les méthodes de chimie douce. C'est une alternative valable aux alcoxydes surtout en raison de son faible coût, toutefois, il réagit avec l'eau aussi.[86] Les synthèses sol-gel de LAGP rapportées dans la littérature n'étaient pas directement applicables à l'électrospinning pour diverses raisons, par exemple la faible concentration et viscosité, les grandes quantités d'additifs, le manque d'homogénéité de la solution, l'incompatibilité avec les polymères filables. Après avoir testé différents matériaux à base de Ge, nous avons réussi à préparer une solution homogène et stable à base de précurseurs chlorures et adaptée à la synthèse de nanofibres de LAGP. Nous rapportons ici une procédure pour obtenir des nanofibres de LAGP par électrospinning, ainsi que leur application comme charge pour améliorer les performances d'un électrolyte à base de PEO:LiTFSI.

Des échantillons circulaires découpés dans la membrane électrofilée vierge ont été calcinés à 700 °C, 800 °C et 900 °C pendant deux heures sous un flux d'air constant. La température a eu un effet significatif sur la taille et la porosité des échantillons céramiques. Les échantillons de LAGP 700 affichaient des valeurs de porosité allant de 79 à 83% et leur aire s'est réduit d'environ 50% par rapport à celle des échantillons vierges correspondants. Les porosités du LAGP 800 étaient d'environ 60 % tandis que leur surface est devenue 25% de ce qu'elle était avant l'étape de calcination. Une température plus élevée s'est révélée préjudiciable à l'intégrité mécanique des échantillons calcinés : alors qu'une température de 700 °C n'a pas eu d'effet significatif sur l'intégrité des échantillons, à 800 °C, deux

échantillons sur trois présentent des fractures après traitement thermique. A 900 °C, tous les échantillons traités étaient endommagés ou cassés. Par conséquent, plus la température est élevée, plus la contraction est rapide et importante pendant l'étape de calcination, conduisant à des échantillons plus petits et moins poreux qui sont également plus susceptibles de se casser. La **Figure 10.12** montre l'évolution morphologique et structurale des fibres de LAGP calcinées à 700 °C, 800 °C et 900 °C. Le diamètre des fibres précurseurs filées (**Figure 10.12a**) varie de 300 à 800 nm. La gamme de diamètres ne change pas après traitement thermique à 700 °C. L'utilisation de températures de calcination plus élevées (800 °C et 900 °C) est préjudiciable à la morphologie de l'échantillon, car les fibres commencent à coalescer. À 800 °C, plusieurs fibres peuvent encore être identifiées par imagerie MEB, comme le montre l'encadré de la **Figure 10.12c**, tandis qu'une température de 900 °C donne un échantillon dense causé par la coalescence presque totale des fibres (**Figure 10.12d**). Bien que des températures de calcination plus élevées aient tendance à endommager la morphologie des fibres, elles sont bénéfiques pour la cristallisation du matériau et sa pureté, comme le montrent les profils XRD rassemblés dans la **Figure 10.12e**. Les principaux pics de chaque profil peuvent être attribués à la structure de type NASICON (groupe d'espace $R\bar{3}c$) de $Li_{1.5}Al_{0.5}Ge_{1.5}(PO_4)_3$ (carte PDF 04-022–7674). Ils deviennent plus aigus en augmentant la température de calcination, ce qui signifie que la cristallinité du LAGP s'améliore. Des pics mineurs dans les profils de LAGP 700 et LAGP 800 sont liés aux phases d'impuretés de $AlPO_4$, GeP_2O_7 et $Li_9Al_3(PO_4)_2(P_2O_7)_3$, tandis que seules des traces de $AlPO_4$ et GeP_2O_7 ont été obtenues lorsque la température de 900 °C est utilisée. La phase $Li_9Al_3(PO_4)_2(P_2O_7)_3$, riche en Li, a été rapportée antérieurement lorsqu'un dopage en Al de 0,7 et plus est utilisé. Cependant, ses pics sont plus intenses lorsque la température utilisée pour le traitement thermique est diminuée.[247] $AlPO_4$ est une phase d'impureté courante pour la synthèse sol-gel du LAGP[86,88,239,247] tandis que GeP_2O_7 est un produit intermédiaire de la cristallisation du LAGP.[248] Ces aspects sont compatibles avec la diminution de l'intensité des pics d'impuretés lorsque la température de calcination est augmentée. Pour étudier la distribution élémentaire et la localisation des phases détectées par XRD, une cartographie EDS de Al, Ge, P et O a été réalisée pour LAGP 700 et est affichée sur la **Figure 10.12e**. La distribution élémentaire apparaît homogène sur l'ensemble de l'échantillon. Les phases d'impuretés résultant de l'attribution des pics XRD ne peuvent pas être identifiées dans les cartes élémentaires, car aucune concentration locale de Ge ou Ti n'est évidente.

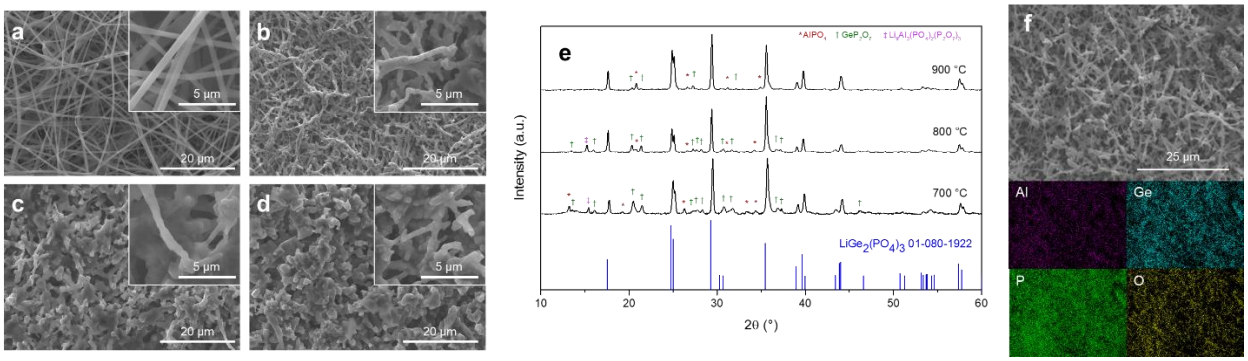

Figure 10.12 Images MEB de (a) fibres précurseurs de LAGP, (b) LAGP 700, (c) LAGP 800 et (d) LAGP 900 (détails à fort grossissement des fibres dans l'encadré). (e) Profils XRD de LAGP 700, LAGP 800 et LAGP 900. ((*) : $AlPO_4$; (†) : GeP_2O_7 ; (‡) : $Li_9Al_3(PO_4)_2(P_2O_7)_3$). (f) Analyse SEM-EDS et cartographie élémentaire correspondante du LAGP 700.

Pour évaluer la conductivité ionique des fibres céramiques de LAGP, une analyse EIS a été réalisée sur LAGP 700 et LAGP 800. L'impossibilité d'obtenir un échantillon de LAGP 900 intact nous empêche d'évaluer ses performances électrochimiques. Chaque échantillon céramique de LAGP a été placé dans une pile bouton entre des électrodes blocants en acier inoxydable (**Figure 10.13a**) pour évaluer l'impédance entre 20 °C et 80 °C. Les spectres EIS ont été ajustés en utilisant le circuit équivalent représenté sur la **Figure 10.13b** et l'impédance résultante a été utilisée pour calculer les valeurs de conductivité ionique affichées sur la **Figure 10.13c**. La conductivité ionique des deux échantillons suit la loi d'Arrhenius. La pente du diagramme d'Arrhenius exprimée sous la forme linéaire $\ln(\sigma) = \ln(A) - EA/RT$, a été utilisée pour calculer l'énergie d'activation, qui correspond à 0,407 (±0,003) eV pour LAGP 700 et 0,349 (± 0,007) eV pour LAGP 800. Les deux valeurs sont en bon accord avec celles rapportées dans la littérature.[252] Comme l'ont démontré Delaizir et al. l'énergie d'activation semble être indépendante de la densité,[233] tandis que Yang et al. observé qu'une densité plus élevée correspond à une énergie d'activation légèrement inférieure.[253] Par conséquent, la valeur que nous rapportons pour le LAGP 800 est certainement liée à sa densité plus élevée (env. 40 %) par rapport au LAGP 700 (env. 20 %), ainsi qu'à sa pureté plus élevée, telle qu'observée dans les résultats XRD (**Figure 10.12e**). Une densité et une pureté plus élevées sont bénéfiques pour la formation de nombreuses voies de percolation, conduisant ainsi à une conduction d'ions de lithium plus efficace. Les spectres EIS de LAGP 700 et LAGP 800 acquis à 20 °C, 50 °C et 80 °C sont rassemblés dans la **Figure 10.13e** à titre de comparaison. Les valeurs de conductivité ionique à 20 °C correspondent à $1,9 \times 10^{-8}$ S cm^{-1} et $1,5 \times 10^{-7}$ S cm^{-1} pour LAGP 700 et LAGP 800 respectivement. A 50 °C elles deviennent respectivement $8,5 \times 10^{-8}$ S cm^{-1} et $5,9 \times 10^{-7}$ S cm^{-1}, tandis qu'à 80 °C elles sont égales à $2,8 \times 10^{-7}$ S cm^{-1} et $1,6 \times 10^{-6}$ S cm^{-1}.

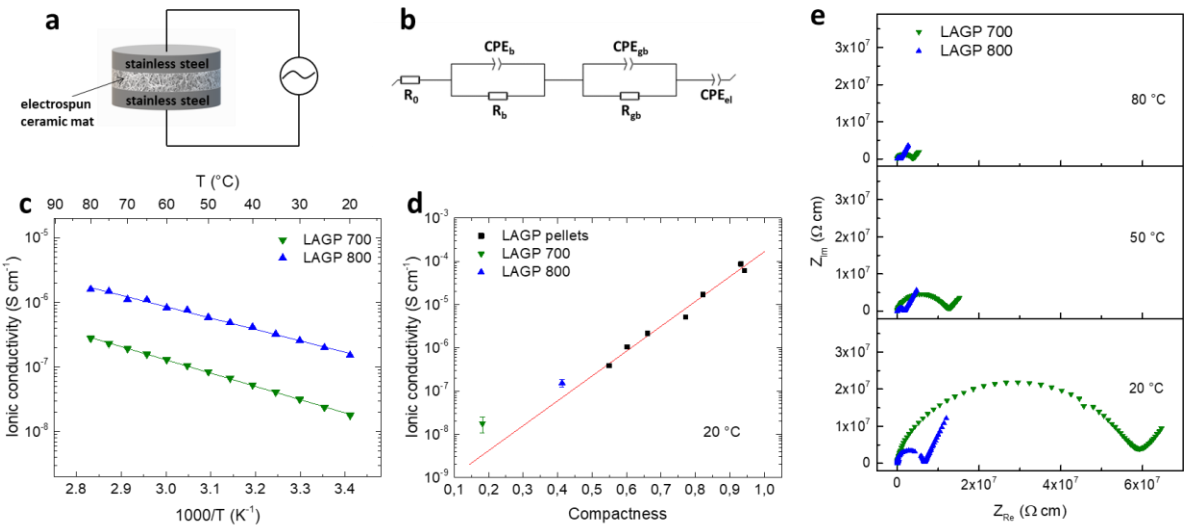

Figure 10.13 (a) Schéma de la configuration utilisée pour l'analyse EIS des LAGP 700 et LAGP 800. (b) Circuit équivalent utilisé pour l'ajustement des données EIS. (c) Diagramme d'Arrhenius représentatif de LAGP 700 et LAGP 800 dans une plage de température de 20 °C à 80 °C. (d) Conductivité ionique à 20 °C en fonction de la densité de LAGP 700 et LAGP 800 par rapport aux données obtenues avec les pastilles de LAGP par Delaizir et al.[233] (e) Spectres EIS de LAGP 700 et LAGP 800 à 20 °C, 50 °C et 80 °C.

Bien que la faible conductivité ionique à température ambiante les rende impropres à être utilisés tels quels comme électrolyte solide, leur faible densité doit être prise en compte. Comme en témoignent les données affichées sur la **Figure 10.13d**, où la conductivité ionique à 20 °C est tracée en fonction de la densité du matériau, les valeurs de conductivité LAGP 700 et LAGP 800 sont supérieures à celles estimées par un ajustement linéaire des données rapportées par Delaizir et al. pour les pastilles de LAGP ayant des densités comprises entre 50 et 100 % de la valeur théorique du LAGP.[233] Parmi toutes les applications potentielles des nanofibres céramiques conductrices d'ions, l'une des plus intéressantes est celle de charge dans les électrolytes polymères composites. Nous avons donc étudié l'effet des nanofibres de LAGP lorsqu'elles sont utilisées comme charge dans des électrolytes à base de PEO. Nous avons sélectionné le LAGP 700 malgré sa plus faible pureté car, étant caractérisé par une morphologie des fibres plus prononcée, il permet de souligner les effets attribués à la forme allongée par rapport à une charge conventionnelle en forme de particules. Des analyses EIS ont été effectuées sur des électrolytes composites (dénommes CE-LAGPf si avec fibres et CE-LAGPp si avec particules) et sur l'électrolyte polymère sans LAGP (dénommes PE) pour étudier l'effet de la présence de la charge et de la morphologie sur le transport d'ions lithium. L'électrolyte a été placé dans une pile bouton entre des électrodes blocants en acier inoxydable avant le test (**Figure 10.14a**). Les spectres EIS ont été acquis dans la plage de température de 20 °C à 80 °C et ajustés à l'aide du circuit équivalent illustré à la **Figure 10.14b**. L'addition de 10 % en poids de fibres de LAGP entraîne une valeur d'impédance

réduite de moitié à 20 °C, comme le montre la **Figure 10.14c** en comparant CE-LAGPf10 et PE, tandis que CE-LAGPp10 affiche la même valeur que l'électrolyte sans charge. Les données acquises entre 20 et 80 °C ont été utilisées pour tracer les diagrammes d'Arrhenius correspondantes. Les tracés de CE-LAGPf10, CE-LAGPp10 et PE sont comparés et illustrés à la **Figure 10.14d** pour mieux souligner les avantages de l'utilisation de fibres au lieu de particules comme charge. Les trois électrolytes montres ici présentent le comportement typique à 2 pentes en raison de la transition du PEO de semi-cristallin à amorphe.[256,257] La première section, en dessous du point de fusion du PEO, est caractérisée par une relation linéaire entre la conductivité et la température, ce qui signifie que la conduction des ions de lithium obéit à la loi d'Arrhenius, tandis que la deuxième région est liée au mouvement segmentaire des chaînes de PEO et est mieux ajustée en utilisant le équation de Vogel-Tammer-Fulcher.[256] La conductivité ionique du CE-LAGPf10 est supérieure à celle du PE et du CE-LAGPp10 dans toute la gamme de température, mais surtout à 20 °C où correspond à $7{,}14 \times 10^{-6}$ S cm^{-1}, soit le double de celui de PE ($3{,}42 \times 10^{-6}$ S cm^{-1}). L'amélioration observée est certainement due à la conductivité élevée à température ambiante de LAGP, rapportée à $2{,}8 \times 10^{-4}$ S cm^{-1} pour une pastille dense à 100 % (**Figure 10.13d**).[69,233] La distribution uniforme des fibres s'est avérée bénéfique pour empêcher la cristallisation du PEO et ainsi obtenir une conduction des ions de lithium plus rapide.[179,192,258,259] Dans la plage de 20 °C à 40 °C, la conductivité ionique du CE-LAGPp10 est à peu près la même que celle du PE, ce qui signifie que l'utilisation de particules de LAGP comme charge n'a eu aucun effet sur le mécanisme de conduction. Contrairement aux fibres qui fournissent un chemin de conduction continu, un saut constant d'ions Li de la chaîne polymère aux particules est nécessaire lorsque des charges en forme de particules sont utilisées.[177,178] Dans la plage de température de 50 °C à 80 °C, la conductivité ionique est plus faible que celle du PE. Cela peut être attribué au phénomène d'agglomération des particules, qui conduit à une conduction Li-ion inhomogène à travers l'électrolyte composite lorsque le PEO devient amorphe.[177,192,256] L'absence d'agglomérats dans le CE-LAGPf10 permet d'atteindre des valeurs de conductivité légèrement supérieures à celles du PE puisque les fibres uniformément dispersées n'entravent pas la mobilité des chaînes de PEO.

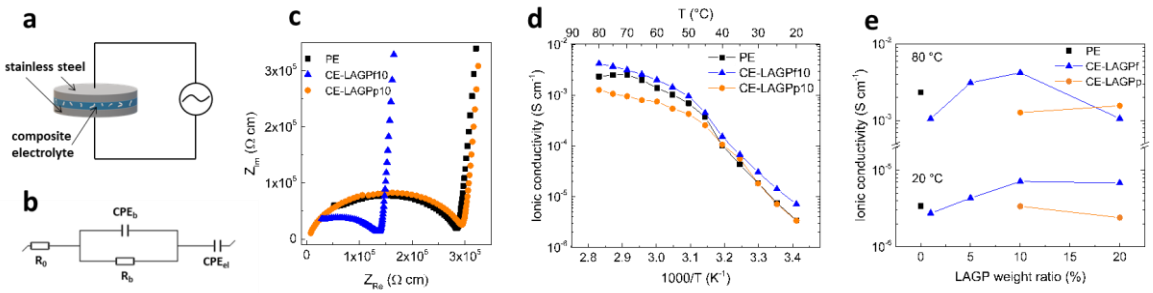

Figure 10.14 Schéma de la configuration utilisée pour l'analyse EIS des électrolytes polymères et composites. (b) Circuit équivalent utilisé pour l'ajustement des données EIS. (c) Spectres EIS à 20 °C et (d) diagrammes d'Arrhenius dans une plage de températures de 20 °C à 80 °C de CE-LAGPf10, CE-LAGPp10 et PE. (e) Conductivité ionique à 20 °C et 80 °C en fonction du rapport de pourcentage pondéral de LAGP.

Nous nous attendons à ce que la conductivité puisse être encore augmentée en optimisant la synthèse, obtenant ainsi des nanofibres de LAGP avec un degré de pureté plus élevé. Nous pensons que le processus rapporté ici peut être une contribution significative à l'optimisation des conditions des synthèses sol-gel de LAGP. De plus, l'ajout de nanofibres de LAGP à un électrolyte polymère à base de PEO a en outre démontré que les charges de forme allongée sont capables de fournir des performances améliorées par rapport à leur homologue en forme de particules, étant ainsi des candidats appropriés pour développer des électrolytes composites pour les batteries à l'état solide de nouvelle génération.

10.7 Propriétés et performances des nanofibres de $Li_{1.5}Al_{0.5}Ge_{1.5-x}Ti_x(PO_4)_3$ ($0.1 \leq x \leq 0.3$) : influence de la substitution de Ge^{IV} par Ti^{IV}

Sur la base des résultats de nos travaux précédents sur la synthèse de nanofibres de LAGP par électrospinning[199] et des données rapportées sur les fibres de LATP,[197,198] nous avons réussi à synthétiser des nanofibres de $Li_{1.5}Al_{0.5}Ge_{1.5-x}Ti_x(PO_4)_3$ ($0.1 \leq x \leq 0.3$) (LAGTP) pures et stables. Nous visons à mieux comprendre l'effet d'une substitution partielle de Ge par Ti sur la synthèse et les propriétés d'électrolytes à base de fibres $Li_{1.5}Al_{0.5}Ge_{1.5}(PO_4)_3$ (LAGP). Ainsi, nous avons étudié et comparé leur propriétés morphologiques et structurelles à celles des fibres de LAGP non substitué. De plus, nous proposons leur application comme charge pour améliorer les performances d'un électrolyte composite à base de PEO pour batteries au lithium métallique.

Après la réalisation des membranes électrofilées, des échantillons circulaires ont été découpés et calcinés à 700 °C pendant 2 heures sous flux d'air constant. Comme déjà observé pour le LAGP

brut,[199] la température affecte l'intégrité mécanique des échantillons. Après le traitement thermique à 700 °C, tous les échantillons restent intacts, alors que l'augmentation de la température à 800 °C tend à provoquer des fractures. Aucun échantillon intact n'a été obtenu à 900 °C. Les trois échantillons de céramique LAGTP calcinés à 700 °C sont caractérisés par une porosité égale à 93 ± 3 %. La **Figure 10.15** affiche les images MEB acquises sur les membranes précurseur et sur LAGTP01, LAGTP02 et LAGTP03 calcinées à 700 °C. Des images SEM de nanofibres LAGP de nos travaux précédents ont également été incluses (**Figure 10.15g**) à des fins de comparaison. Aucune différence pertinente ne peut être observée dans la morphologie des membranes précurseurs, ce qui signifie que les paramètres pour l'électrospinning des solutions précurseurs a été bien optimisé. L'effet de l'ajout de Ti peut être observé dans les échantillons calcinés. Comme pour le LAGP, aucune coalescence ne se produit en calcinant les échantillons à 700 °C. Cependant, les structures semblables à du corail qui caractérisent la morphologie du LAGP disparaissent lorsque Ti est ajouté, ce qui donne des fibres bien distinctes. La structure des échantillons de LAGTP a été étudiée par analyse XRD. Les profils correspondants sont rassemblés à la **Figure 10.15i** et comparés à ceux des nanofibres de LAGP. La phase principale de tous les échantillons de LAGTP correspond à la structure rhomboédrique typique des matériaux de type NASICON (groupe d'espace $R\bar{3}c$). Des pics mineurs peuvent être attribués à des composés à base de phosphate, tels que $Li_9Al_3(PO_4)_2(P_2O_7)_3$, $AlPO_4$, TiP_2O_7 et $Li_4P_2O_7$. Compte tenu de la basse température et du court temps de calcination, une grande amélioration en termes de pureté a été obtenue.

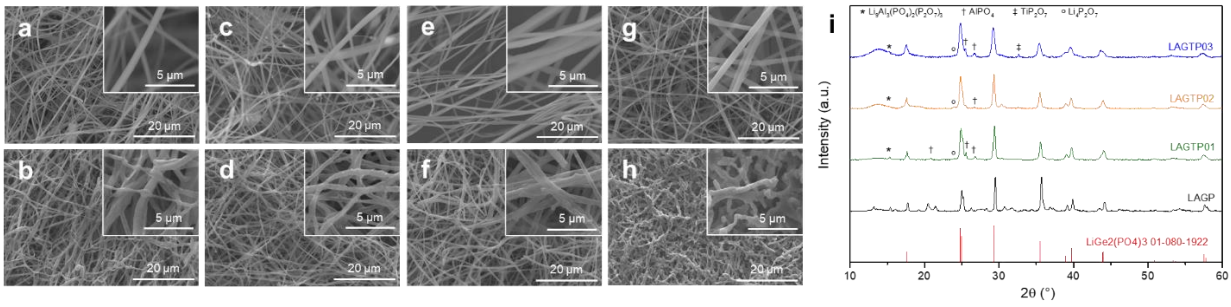

Figure 10.15 Images MEB des échantillons précurseurs et calcines de (a,b) LAGTP01, (c,d) LAGTP02, (e,f) LAGTP03 et (g,h) LAGP (détails à fort grossissement des fibres dans l'encadré). (i) Profils XRD de LAGP, LAGTP01 LAGTP02 et LAGTP03 calcinés à 700 °C. ((*) : $Li_9Al_3(PO_4)_2(P_2O_7)_3$; (†) : $AlPO_4$; (‡) : TiP_2O_7 ; (°) : $Li_4P_2O_7$).

En comparant les profils XRD des échantillons de LAGTP avec celui du LAGP préparé dans les mêmes conditions, on peut voir que, bien que certaines phases d'impuretés ($Li_9Al_3(PO_4)_2(P_2O_7)_3$ et $AlPO_4$) soient toujours présentes, leurs pics sont moins nombreux et moins intenses. Aucun pic

associé à GeP_2O_7 n'a été détecté. Un petit pic autour de 24° est probablement dû à la présence de traces de $Li_4P_2O_7$. Dans le profil de LAGPT03, le petit pic détecté autour de 32,6° est attribuable à une phase d'impureté de TiP_2O_7, probablement en raison de l'augmentation de la teneur en Ti, qui a provoqué une faible ségrégation de phase. $Li_4P_2O_7$ et TiP_2O_7 sont souvent signalés comme des phases secondaires communes des matériaux NASICON à base de Li.[247,264,265] De plus, en augmentant la quantité de Ti ajouté, les échantillons deviennent moins cristallins comme suggéré par l'élargissement des pics et l'apparition d'une petite bosse à environ 14°. Pour évaluer l'application potentielle des nanofibres de LAGTP en tant que charges, elles ont été ajoutées à une matrice de PEO:LiTFSI pour obtenir les électrolytes composites correspondants, c'est-à-dire CE-LAGTP01, CE-LAGTP02 et CE-LAGTP03. Les dimensions des nanofibres et leur distribution dans la matrice polymère ont été étudiées au MEB. Les images sont rassemblées dans la **Figure 10.16a-e** avec celles de CE-LAGP et CE-LATP. Comme mentionné ci-dessus, tout en discutant des images MEB des fibres céramiques de LAGTP (**Figure 10.15**), l'ajout de Ti a été bénéfique pour la morphologie des fibres. Cette morphologie améliorée, leur permet de conserver leur intégrité lors de la dispersion dans la bouillie d'électrolyte. Les charges de LAGTP sont en effet caractérisées par une forme allongée prononcée qui ressemble mieux aux fibres par rapport aux charges de LAGP (**Figure 10.16a**). De plus, les fibres de LAGTP semblent plus longues que leurs homologues de LAGP, approchant une longueur d'environ 20 μm. Ces aspects sont d'une grande importance en ce qui concerne les performances électrochimiques des électrolytes. Des fibres plus longues et de forme plus uniforme peuvent fournir des chemins rapides et continus pour le transport ionique entre les électrodes, améliorant ainsi les performances de l'électrolyte à température ambiante. Pour déterminer si la morphologie et la pureté améliorées entraînaient une conduction ionique plus rapide, des analyses EIS ont été effectuées sur des électrolytes composites à base de LAGTP. Les résultats ont été comparés à ceux obtenus avec CE-LAGP et PE que nous avons précédemment rapportés,[199] et avec CE-LATP, spécifiquement préparé comme référence. Chaque électrolyte a été placé dans une pile bouton entre des électrodes blocants en acier inoxydable, conformément à la configuration illustrée à la **Figure 10.16f**. Les spectres EIS, acquis entre 20 et 80 °C, ont été ajustés à l'aide du circuit équivalent représenté sur la **Figure 10.16g**. Les données résultantes sont affichées sous la forme d'un diagramme d'Arrhenius dans la **Figure 10.16h,i**. La **Figure 10.16h** montre comment la conductivité ionique des échantillons de LAGTP change avec la température. Tous les tracés ont le comportement caractéristique à deux pentes, typique des électrolytes polymères à base de PEO, où les deux sections sont divisées par le point de fusion du PEO. Le plus performant des trois électrolytes composites à base de LAGTP, c'est-

à-dire CE-LAGTP03, a été sélectionné et comparé avec CE-LAGP, CE-LATP et PE (**Figure 10.16i**). A 20 °C, CE-LAGP, semble être le plus conducteur, tandis que CE-LAGTP03 est, comme prévu, juste entre CE-LAGP et CE-LATP, avec une conductivité ionique de 5,3 × 10^{-6} S cm^{-1}. A 40 °C, le CE-LAGTP03 se caractérise par une conductivité ionique plus élevée (2,2 × 10^{-4} S cm^{-1}) par rapport au CE-LAGP et au CE-LATP, qui reste supérieure jusqu'à 80 °C, où elle est égale à 7,5 × 10^{-3} S cm^{-1}.

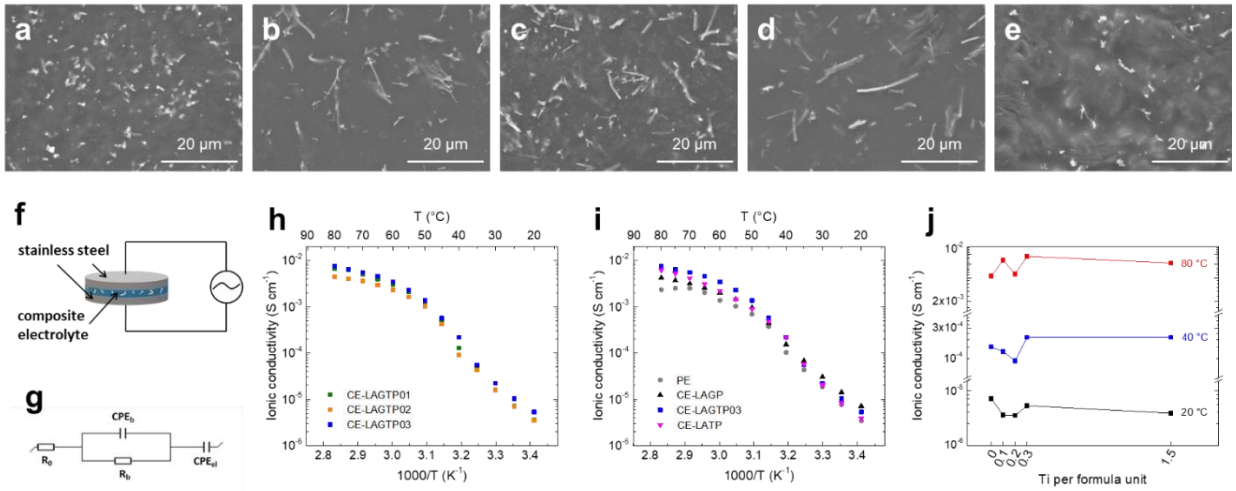

Figure 10.16 Images MEB de (a) CE-LAGP, (b) CE-LAGTP01, (c) CE-LAGTP02, (d) CE-LAGTP03 et (e) CE-LATP. (f) Schéma de la configuration utilisée pour l'analyse EIS des électrolytes composites et polymères. (g) Circuit équivalent utilisé pour l'ajustement des données EIS. Diagrammes d'Arrhenius représentatives dans une plage de température de 20 à 80 ° C des électrolytes (h) CE-LAGTP et (i) LAGTP03 comparé à PE, CE-LAGP et CE-LATP. (j) Conductivité ionique à 20, 40 et 80 °C en fonction de la teneur en Ti.

La présence de Ti semble affecter positivement le transport ionique au-dessus de 40 °C. Cet aspect est plus apparent sur la **Figure 10.16j**, où la conductivité ionique à 20, 40 et 80 °C est tracée en fonction de la teneur en Ti par unité de formule. Alors que CE-LAGTP01 et CE-LAGTP02 se caractérisent par des conductivités ioniques inférieures à celles de CE-LAGP, notamment à basse température, la substitution de 20% de Ge par Ti améliore le transport ionique. L'effet est encore plus marqué à des températures plus élevées et confirmé par les valeurs obtenues avec CE-LATP. La substitution partielle de Ge par Ti n'a pas entraîné d'amélioration significative de la conductivité ionique, par rapport au LAGP non substitué. Ceci était attendu puisque la plupart des structures $Li_{1+x}Al_xGe_yTi_{2-x-y}(PO_4)_3$ rapportées sont caractérisées par des valeurs de conductivité ionique inférieures à celles rapportées pour $Li_{1.5}Al_{0.5}Ge_{1.5}(PO_4)_3$ et $Li_{1.3}Al_{0.3}Ti_{1.7}(PO_4)_3$ structures parents.[70,72,266]

Bien qu'aucune amélioration significative ne soit observée du point de vue des performances, nous pensons qu'une substitution partielle de Ge par Ti peut être une stratégie appropriée pour améliorer la pureté du LAGP synthétisé par des méthodes en solution, telles que le sol-gel. De plus, la présence

de Ti affecte la cristallisation de la phase NASICON, comme le démontre la morphologie améliorée des fibres, ce qui peut être bénéfique pour le développement futur des méthodes de synthèse des électrolytes à base de NASICON.

10.8 Conclusions et perspectives futures

De nos jours, l'effort de recherche est principalement axé sur la découverte de l'électrolyte solide définitif. Cependant, tous les matériaux proposés jusqu'à présent se caractérisent par des avantages mais aussi des inconvénients qui doivent être abordés. Cela signifie que davantage de ressources devraient être investies dans l'optimisation des matériaux actuellement connus, et en particulier dans la recherche de solutions adaptées à tous les problèmes et défis qu'ils présentent. Malgré les électrolytes solides céramiques sont la classe la plus prometteuse de matériaux conducteurs de Li pour les dispositifs de stockage d'énergie de nouvelle génération, ils sont toujours caractérisés par des problèmes intrinsèques qui doivent être résolus afin de parvenir au déploiement commercial des ASSLB. Récemment, des matériaux caractérisés par des conductivités ioniques comparables aux électrolytes liquides ont été signalés, ce qui représente des découvertes révolutionnaires ; cependant, d'autres aspects sont cruciaux pour parvenir à leur production industrielle ainsi qu'une batterie parfaitement opérationnelle, qui sont souvent négligés. Par exemple, alors que la plupart des chercheurs s'efforcent d'atteindre la conductivité ionique la plus élevée, une plus grande attention devrait être accordée à l'amélioration de l'interface entre l'électrolyte solide et les électrodes, ce qui est probablement le problème le plus grave des technologies à l'état solide. Sur cet aspect, une stratégie efficace pour obtenir un meilleur contact entre l'électrolyte et les électrodes, est le développement d'un électrolyte polymère composite. Les polymères, pour leurs propriétés physiques intrinsèques, telles que la flexibilité et la résistance mécanique, sont optimaux pour obtenir une interface stable et homogène avec la surface de l'électrode. Appliquer des revêtements de différents matériaux sur la pastille de céramique pour former une couche intermédiaire entre l'électrolyte et l'électrode peut également être une stratégie appropriée.

Dans ce cadre, les matériaux 1D ou, plus généralement, les matériaux nanostructurés, peuvent fournir des propriétés particulières pour le développement de matériaux fonctionnels avancés. L'utilisation de nanofibres et de nanofils comme charges actives pour le développement d'électrolytes polymères composites est déjà une pratique courante. Ils se sont avérés bénéfiques pour l'amélioration des

propriétés mécaniques et électrochimiques de l'électrolyte. Par ailleurs, il existe plusieurs applications potentielles pour les matériaux céramiques nanostructurés. Les tapis nanofibreux en céramique, par exemple, peuvent être utilisés comme échafaudage de renforcement dans les électrolytes et les électrodes, et en même temps, ils peuvent fournir des chemins rapides et continus pour la conduction des ions Li. Les nanofils peuvent être utilisés comme base pour développer des électrolytes denses entièrement en céramique, car ils se sont avérés efficaces pour obtenir des tassements plus efficaces et donc des densités plus élevées.

Par ailleurs, divers procédés de synthèse doivent être repensés en tenant compte de leur potentiel de montée en gamme industrielle. La plupart des procédés utilisés pour la synthèse des matériaux céramiques impliquent de longues étapes à haute température et des techniques de mélange à haute énergie, qui ne sont pas adaptées aux productions à grande échelle. Par conséquent, les voies de synthèse déjà connues doivent être optimisées, tandis que de nouvelles approches impliquant des étapes plus simples et moins coûteuses doivent être développées.

11 Appendix II: Original contributions

11.1 First authored publications

1. A. La Monaca, G. Girard, S. Savoie, R. Veillette, A. Vijh, F. Rosei, A. Paolella, Influence of Ti^{IV} substitution on the properties of a $Li_{1.5}Al_{0.5}Ge_{1.5}(PO_4)_3$ nanofiber-based solid electrolyte, *Nanoscale*, **2022**, 14, 5094-5101, DOI: 10.1039/D2NR00017B

2. A. La Monaca, W. Zhu, Z. Feng, G. Bertoni, D. Campanella, G. Girard, S. Savoie, A. G. Nita, D. Clement, H. Demers, A. Vijh, F. Rosei, A. Paolella, Influence of Rutile and Anatase TiO_2 Precursors on the Synthesis of a $Li_{1.5}Al_{0.5}Ti_{1.5}(PO_4)_3$ Electrolyte for Solid-State Lithium Batteries, *Journal of the Electrochemical Society*, **2022**, 169 (4), 040515, DOI: 10.1149/1945-7111/ac6325

3. A. La Monaca, G. Girard, S. Savoie, G. Bertoni, S. Krachkovskiy, A. Vijh, F. Pierini, F. Rosei, A. Paolella, Synthesis of Electrospun NASICON $Li_{1.5}Al_{0.5}Ge_{1.5}(PO_4)_3$ Solid Electrolyte Nanofibers by Control of Germanium Hydrolysis, *Journal of the Electrochemical Society*, **2021**, 168 (11), 110512, DOI: 10.1149/1945-7111/ac334a

4. A. La Monaca, G. Girard, S. Savoie, H. Demers, G. Bertoni, S. Krachkovskiy, S. Marras, E. Mugnaioli, M. Gemmi, D. Benetti, A. Vijh, F. Rosei, A. Paolella, Effect of pressure on the properties of a NASICON $Li_{1.3}Al_{0.3}Ti_{1.7}(PO_4)_3$ nanofiber solid electrolyte, *Journal of Material Chemistry A*, **2021**, 9, 13688–13696, DOI: 10.1039/D1TA01143J

5. A. La Monaca, A. Paolella, A. Guerfi, F. Rosei, K. Zaghib, Electrospun Ceramic Nanofibers as 1D Solid Electrolytes for Lithium Batteries, *Electrochemistry Communications*, **2019**, 104, 106483, DOI: 10.1016/j.elecom.2019.106483